2023-05-01

Characterization And Modeling Of Unbound And Cementitiously Stabilized Materials For Structural Analysis Of Multilayer Pavement Systems

Edgar Daniel Rodriguez Velasquez
University of Texas at El Paso

CHARACTERIZATION AND MODELING OF UNBOUND AND CEMENTITIOUSLY STABILIZED MATERIALS FOR STRUCTURAL ANALYSIS OF MULTILAYER PAVEMENT SYSTEMS

EDGAR DANIEL RODRIGUEZ VELASQUEZ

Doctoral Program in Civil Engineering

APPROVED:

Reza Ashtiani, Ph.D., Chair

Vivek Tandon, Ph.D.

Vladik Kreinovich, Ph.D.

Jose Hurtado, Ph.D.

Brian Diefenderfer, Ph.D.

Stephen L. Crites, Jr., Ph.D.
Dean of the Graduate School

Dedication

I dedicate this dissertation to my beloved wife, Carolina, and my dear son, Luciano, whose love and constant support have been a source of inspiration throughout my academic journey.

CHARACTERIZATION AND MODELING OF UNBOUND AND CEMENTITIOUSLY STABILIZED MATERIALS FOR STRUCTURAL ANALYSIS OF MULTILAYER PAVEMENT SYSTEMS

by

EDGAR DANIEL RODRIGUEZ VELASQUEZ, MSCE

DISSERTATION

Presented to the Faculty of the Graduate School of

The University of Texas at El Paso

in Partial Fulfillment

of the Requirements

for the Degree of

DOCTOR OF PHILOSOPHY

Department of Civil Engineering

THE UNIVERSITY OF TEXAS AT EL PASO

May 2023

Acknowledgements

I am grateful for the unwavering support, guidance, and inspiration provided by my mentor, Dr. Reza Ashtiani, who gave me the chance to be part of his research team and grow academically and personally. I extend my sincere thanks to my dissertation committee members, Dr. Vivek Tandon, Dr. Vladik Kreinovich, Dr. Jose Hurtado, and Dr. Brian Diefenderfer, for their valuable feedback and guidance throughout the research process. I would like to acknowledge the contribution of Dr. Brian Diefenderfer, Dr. Nelson Gibson, and Mr. Randy Weingart, for generously sharing the relevant data of the full-scale inverted pavement section constructed in Virginia. Lastly, I express my heartfelt gratitude to my family, including my father, mother, and two sisters, for their unwavering love, support, encouragement, and patience during my graduate studies.

Abstract

The incorporation of cement for soil improvement is a sustainable solution for utilizing marginal materials in the construction of new pavements and the rehabilitation of existing roadway systems. To effectively design and assess the performance of pavement structures, it is crucial to determine the strength and resilient properties of cementitiously stabilized aggregates. Accurate determination of the Unconfined Compressive Strength (UCS), tensile strength, and Resilient Modulus (M_r) is of utmost importance for thoroughly characterizing the structural capacity of pavement layers through a mechanistic approach.

The tensile strength of stabilized materials can be assessed in a laboratory setting through the implementation of two widely employed testing techniques: the flexural beam test and the Indirect Diametrical Tensile (IDT) strength test. Previous studies have shown that the split tension-type testing setup is a more reliable method compared to the traditional bending beam test due to its practicality, consistency of results, adherence to theoretical principles, ease of specimen preparation, and uniform distribution of the stabilizer (Wang & Huston 1972, Kennedy & Hudson 1973, Dempsey et al. 1984, Thompson 1965a, Piratheepan & Gnanendran 2008, Gnanendran & Piratheepan 2010, Ashtiani & Tarin 2016). The resilient characteristics of stabilized materials can be evaluated through stress-path laboratory testing, which is a complex, time-consuming, and costly procedure. The testing involves exposing specimens to uniform static confining stresses and axial cyclic loading within a triaxial chamber, while monitoring stresses and strains to determine the resilient behavior of the cement-treated samples (Lee et al. 1997, Hossain & Kim 2015).

Due to the increasing demand for accelerated mixture design methods and the resource-intensive nature of conducting a full set of laboratory tests, many transportation agencies do not conduct all of the recommended tests to accurately determine the material properties required for

design input parameters. As a result, pavement engineers often rely on past experiences or readily accessible correlation equations to design and analyze cementitiously stabilized layers.

This dissertation sheds light on the relationship between the IDT strength and the UCS, as well as the correlations between the M_r and the UCS of cementitiously stabilized virgin and reclaimed materials from various aggregate sources, under varying stabilizer content and moisture susceptibility conditions. The results of this study will prove valuable for engineers and design agencies as they aim to enhance their predictions of the IDT strength and M_r of virgin and reclaimed materials stabilized with cement.

A parallel aspect of this dissertation is related to the laboratory preparation of cement-treated specimens. Proper compaction of these specimens is essential for obtaining accurate and reliable strength and resilient property measurements of both unbound and cementitiously stabilized materials. The commonly used method for preparing specimens in the laboratory is a variation of the Proctor compaction procedure, which is widely adopted by design practitioners and pavement agencies (Browne 2006, Cerni & Camilli 2011, Arabali et al. 2018, Yaghoubi et al. 2018). Despite some variations in details such as mold geometry, hammer weight, number of layers, and number of blows per layer (Du et al. 2018), the fundamental mechanism of Proctor compaction, which involves the application of loads imparted by an impact hammer, remains consistent across different pavement design agencies.

It is widely acknowledged that laboratory compaction procedures, which involve the use of impact energy, diverge greatly from the traditional compaction methods employed in the field (Sebesta & Liu 2008). The compaction of pavement layers during construction is accomplished through a combination of kneading, vibration, and static pressure (Browne 2006). However, the

Proctor compaction method in the laboratory imitates field compaction by dropping a hammer from a specified height (Cerni & Camilli 2011).

The aim of this dissertation is to explore the effect of laboratory compaction methods on the pore structure and strength properties of cementitiously stabilized materials. The homogeneity, quality, and distribution of pores in laboratory-compacted specimens can greatly impact the reliability of data used for the design and analysis of pavement structures. To address this issue, the study focuses on the examination of virgin and reclaimed aggregates stabilized with cement from various sources. The investigation aims to determine the interaction between material type, cement content, and compaction energy on the orthogonal strength properties of the cementitiously stabilized mediums.

The main final aspect of this dissertation is concerned with the study of the structural behavior of a particular type of multilayer pavement system known as inverted pavement, which comprises a cementitiously stabilized layer within its structure. This type of multilayer pavement structure consists of an asphalt-wearing course, an unbound aggregate layer at the bottom, and an underlying cement-treated layer placed on top of the subgrade soil. Unlike traditional pavements, where the stiff layer is located near the surface, the location of the cement-treated layer in an inverted pavement system results in unique interaction between layers of varying rigidity when subjected to traffic-induced stress paths and environmental conditions.

To fill the gap in the limited number of studies about the design, mechanical response, and performance of inverted pavement structures, this dissertation presents and analyzes the non-destructive in-situ test results from full-scale inverted pavements constructed on Bull Run Route 659 in Virginia. Ground Penetrating Radar (GPR) was utilized to verify the layer thicknesses, while Dynamic Cone Penetrometer (DCP) and Falling Weight Deflectometer (FWD) testing was

performed to analyze and compare the deformation characteristics of inverted and conventional pavement structures loaded under controlled conditions. Moreover, the stiffness properties of the unbound granular layer of the inverted layered system were studied based on the DCP results.

In addition to the DCP and FWD testing, the inverted section and adjacent conventional road segment were instrumented with different sensing devices embedded within the pavement structures. The instrumentation plan aimed to monitor the mechanical responses of the layers under controlled traffic loading conditions at certain critical depths. Lastly, a backcalculation analysis was carried out, using the deflection values obtained from the in-situ FWD testing to calculate the modulus values of each layer of the inverted pavement. The collected data from the in-situ testing was used to conduct a finite element (FE) numerical analysis that compared the mechanical response of the Virginia inverted pavement section to an equivalent conventional design, where the order of the two layers located beneath the asphalt concrete layer was switched.

The numerical simulations performed based on the Virginia inverted pavement were replicated on another inverted pavement section built on State Highway SH-123 in Texas, which had a different layer arrangement and unique material characteristics. The layer thicknesses were obtained through in-situ GPR testing and the Modulus values of each pavement layer were estimated from FWD test outcomes. The Texas inverted structure was compared to an equivalent conventional design obtained by rearranging the order of the two layers located below the bituminous superficial layer of the inverted pavement. Two distinct loading scenarios were considered for the Texas inverted pavement section: conventional heavy vehicles and Super Heavy Loads.

Table of Contents

Dedication iii

Acknowledgements v

Abstract vi

Table of Contents x

List of Tables xiii

List of Figures xv

Chapter 1: Introduction 1

1.1. Problem Statement 4

1.2. Research Objectives 6

1.2.1. Material Models for the Design of Cementitiously Stabilized Layers 6

1.2.2. Influence of Laboratory Compaction Methods on the Microstructure and Strength Properties of Cementitiously Stabilized Materials 7

1.2.3. Numerical Modeling and Mechanistic Analysis of Inverted Pavement Structures 7

1.3. Dissertation Outline 8

Chapter 2: Literature Review 11

2.1. Material Models for The Design of Cementitiously Stabilized Layers 11

2.2. Influence of Laboratory Compaction Methods on The Microstructure and Strength Properties of Cementitiously Stabilized Materials 14

2.3. Numerical Modeling and Mechanistic Analysis of Inverted Pavements 16

Chapter 3: Development and Implementation of Experimental Program 25

3.1. Material Characterization 25

3.2. Laboratory Compaction Methods 27

3.3. Curing, Moisture Conditioning, and Mechanical Testing 29

3.4. Microstructural Analysis 31

Chapter 4: Material Models for the Design of Cementitiously Stabilized Layers.....33
4.1. UCS and IDT Strength Relationships.....33
4.2. UCS and M_r Relationships.....36
4.3. Material Models for Cementitiously Stabilized Materials.....39
Chapter 5: Influence of Laboratory Compaction Methods on the Microstructure and Strength Properties of Cementitiously Stabilized Materials.....41
5.1. Influence of Compaction on the Microstructure.....41
5.2. Influence of Compaction on the Strength Properties.....45
Chapter 6: The Bull Run Inverted Pavement Road Test: Deflection Analysis and Deformation Characterization from Field Testing Responses.....53
6.1. DCP Testing Results and Analysis.....61
6.2. FWD Testing Results and Analysis.....70
Chapter 7: Numerical Analysis of the Virginia Inverted Pavement Structure.....82
7.1. Backcalculation Analysis.....82
7.2. Loading Conditions.....85
7.3. Numerical Simulation.....86
7.3.1. Isotropic Analysis.....87
7.3.2. Anisotropic Analysis.....98
7.3.3. Model validation with field measurements.....103
Chapter 8: Numerical Analysis of the Texas Inverted Pavement Structure.....115
8.1. Field Data Testing Results.....115
8.2. Numerical Analysis Considerations.....118
8.3. Isotropic Analysis.....119
8.4. Anisotropic Analysis.....127

Chapter 9: Stability Analysis of Unbound Granular Mediums in Pavement Structures.....133
9.1. Numerical Simulations.....134
9.2. Stress-Induced Anisotropy.....137
9.3. Stress-Path Analysis.....139
9.3.1. Virginia Inverted Pavement Section Stress Path Analysis 140
9.3.2. Texas Inverted Pavement Section Stress Path Analysis for Conventional Loads.....145
9.3.3. Texas Inverted Pavement Section Stress Path Analysis for Super Heavy Loads.....150
9.4. Failure Function Analysis.....154
9.4.1. Virginia Inverted Pavement Section Failure Function Analysis..... 156
9.4.2. Texas Inverted Pavement Section Failure Function Analysis for Conventional Loads 159
9.4.3. Texas Inverted Pavement Section Failure Function Analysis for Super Heavy Loads 162
Chapter 10: Summary of Findings and Conclusions 165
10.1. Material Models for the Design of Cementitiously Stabilized Layers 165
10.2. Influence of Laboratory Compaction Methods on the Microstructure and Strength Properties of Cementitiously Stabilized Materials.....167
10.3. The Bull Run Inverted Pavement Road Test: Deflection Analysis and Deformation Characterization from Field Testing Responses.....169
10.4. Numerical Analysis of Inverted Pavement Structures.....171
10.4.1. Isotropic Analysis 172
10.4.2. Anisotropic Analysis.....174
10.5. Stability Analysis of Unbound Aggregate Systems in Pavement Structures.....176
References.....180
Vita.....188

List of Tables

Table 2.1: Summary of equations correlating UCS (psi) to IDT strength (psi).....11

Table 2.2: Summary of equations correlating UCS (psi) to M_r (ksi).....12

Table 2.3: Inverted pavement layer configurations of relevant full-scale research projects 22

Table 3.1: Optimum moisture contents and maximum dry densities of virgin and reclaimed materials fabricated using impact, vibratory, and gyratory compaction procedures 27

Table 4.1: Regression coefficients and associated statistical parameters of IDT strength models.....40

Table 4.2: Regression coefficients and associated statistical parameters of M_r models.....40

Table 5.1: Average, minimum, maximum, and standard deviation of the porosity of cementitiously stabilized limestone specimens fabricated using impact, vibratory, and gyratory compaction methods.....44

Table 5.2: Calculations for the determination of the impact compaction energy and vibratory compaction energy imparted during the fabrication of the cementitiously stabilized cylindrical specimens in the laboratory. 48

Table 6.1: Values and statistics of the slopes of the trendlines of the primary and secondary deflection basins at the Virginia conventional pavement structure. 80

Table 6.2: Values and statistics of the slopes of the trendlines of the primary and secondary deflection basins at the Virginia inverted pavement structure.....81

Table 7.1. Weight and geometric characteristics of the axle configuration from the aggregate haul truck used at the road test in Virginia.....86

Table 7.2. Comparison of calculated and measured longitudinal strains at the bottom of the AC layer of the Virginia inverted pavement section 109

Table 7.3. Data measured by pressure cells installed at the top and bottom of the UAB layer of the Virginia inverted pavement section.....111

Table 7.4. Comparison of calculated and measured vertical stresses at the top of the UAB layer of the Virginia inverted pavement section.....112

Table 7.5. Comparison of calculated and measured vertical stresses at the bottom of the UAB layer of the Virginia inverted pavement section.....114

List of Figures

Figure 1.1: Typical layer configuration of a traditional pavement structure (a) and an inverted pavement structure (b) 3

Figure 3.1: Experimental matrix for comprehensive laboratory testing 26

Figure 3.2: Grain size distribution characteristics of virgin and reclaimed aggregates 26

Figure 3.3: (a) Impact hammer, (b) vibratory hammer, (c) Texas Gyratory Compactor, and (d) SuperPave Gyratory Compactor used for compaction in the laboratory 28

Figure 3.4: (a) UCS, (b) IDT strength, and (c) submaximal modulus laboratory testing apparatus....31

Figure 3.5: X-ray CT system used to analyze the cylindrical samples placed inside sealed PVC pipe caps used for protecting specimens during transport to the testing facilities. 32

Figure 4.1: Correlations between UCS and IDT strength for cement-treated materials. 34

Figure 4.2: UCS-IDT strength relationships for cementitiously stabilized materials clustered based on specimen height-to-diameter ratio 35

Figure 4.3: UCS-IDT strength relationships for cementitiously stabilized materials clustered based on compaction method. 36

Figure 4.4: Correlations between UCS and M_r for cement-treated virgin and reclaimed materials. 37

Figure 4.5: UCS-M_r relationships for stabilized materials categorized based on cement dosage. 38

Figure 4.6: UCS-M_r relationships for stabilized materials categorized based on cement dosage. 38

Figure 5.1: X-ray computerized tomographic images of the longitudinal cross-sectional areas throughout the center of cement-treated limestone specimens fabricated using (a) impact, (b) vibratory, and (c) gyratory compaction mechanisms. 42
Figure 5.2: Distribution of porosity in cross-sectional views along the height of cementitiously stabilized limestone specimens fabricated using the IH, VH, and SGC. 43
Figure 5.3: Distribution of porosity in various central longitudinal views of cementitiously stabilized limestone specimens fabricated using the IH, VH, and SGC. 44
Figure 5.4: UCS values of cementitiously stabilized virgin and reclaimed materials compacted with the application of impact compaction energy and gyratory compaction energy. 47
Figure 5.5: UCS values of cementitiously stabilized virgin and reclaimed materials compacted with the application of impact compaction energy and vibratory compaction energy 50
Figure 5.6: IDT strength values of cementitiously stabilized virgin and reclaimed materials compacted with the application of impact compaction energy and vibratory compaction energy 52
Figure 6.1: Location of inverted and conventional pavement sections at Bull Run Route 659. 53
Figure 6.2: Layer configuration of the inverted pavement structure (a) and the conventional pavement structure (b) constructed at Bull Run Route 659. 54
Figure 6.3: Falling Weight Deflectometer (a) and Dynamic Cone Penetrometer (b) used for in-site evaluation of the pavement structures at Bull Run Route 659 56
Figure 6.4: Plan and side views of sensors installed in the Virginia inverted pavement structure 57

Figure 6.5: Plan and side views of sensors installed in the Virginia conventional pavement structure.....57
Figure 6.6: H-bar-type strain gauges being placed in the Virginia inverted pavement structure.....59
Figure 6.7: Pressure cell installed at the interface between the CTB layer-SG soil (a) and AC-UAB layers (b) in the Virginia inverted pavement structure. 60
Figure 6.8: Longitudinal, transversal, and vertical LVDTs installed at the bottom of the UAB layer next to a pressure cell at the Virginia inverted pavement section. 61
Figure 6.9: Progression of the cumulative penetration with increasing blow applications per type of lane (a) and per station (b) within the UAB layer at the Virginia inverted pavement section.....62
Figure 6.10: Variation of the penetration depth with increments in the number of blows at the top, middle, and bottom portions of the UAB layer during DCP testing at Northbound lanes 63
Figure 6.11: Variation of the penetration depth with increments in the number of blows at the top, middle, and bottom portions of the UAB layer during DCP testing at Southbound lanes 64
Figure 6.12: Variation of penetration rates at the top, middle, and bottom sublayers of the UAB layer at the Southbound and Northbound lanes.....66
Figure 6.13: Variation of the average penetration rates (a) and average Moduli (b) at the top, middle, and bottom sublayers of the UAB layer at Southbound and Northbound lanes 67
Figure 6.14: Penetration depths (a) and percentages of total penetration (b) achieved in the top, middle, and bottom parts of the UAB layer.....69
Figure 6.15: Surface deflections measured at the center of the loading plate during FWD testing on the (a) inverted pavement and (b) conventional pavement 71

Figure 6.16: Deflection-based indices computed from the FWD data measured on the Virginia inverted pavement structure. 73
Figure 6.17: Deflection-based indices computed from the FWD data measured on the Virginia conventional pavement structure. 74
Figure 6.18: AREA value and constraint deflection basin surface from the FWD data measured on the Virginia inverted pavement structure. 76
Figure 6.19: AREA value and constraint deflection basin surface from the FWD data measured on the Virginia conventional pavement structure. 77
Figure 6.20: Trendline equations of deflections calculated as an example for Station 8 of the inverted pavement (a) and Station 19 of the conventional pavement (b). 79
Figure 7.1: Progression of surface deflections measured under the load plate center and resulting backcalculated Moduli of the subgrade soil at the Virginia inverted pavement section. 83
Figure 7.2: Progression of Moduli at the AC layer, UAB layer, CTB layer, and SG soil from the Virginia inverted section (a) and resulting average backcalculated Modulus values (b) 84
Figure 7.3: 3-D representation of an aggregate haul truck featuring the same axle configuration as the vehicle used at the road test in Virginia. Source: Hum3D. 85
Figure 7.4: Mesh, 20-node brick element, boundaries, and loading conditions considered in the simulation of the Virginia inverted and conventional pavement structures. 88
Figure 7.5: Tensile stresses developed at the bottom of the AC layer in the Virginia inverted and conventional pavement structures considering a full truck analysis (a) and axle analysis (b) 88
Figure 7.6: Tensile strains developed at the bottom of the AC layer in the Virginia inverted and conventional pavement structures considering a full truck analysis (a) and axle analysis (b) 89

Figure 7.7: Compressive stresses developed at the top of the SG soil in the Virginia inverted and conventional pavement structures considering a full truck analysis (a) and axle analysis (b) 90
Figure 7.8: Compressive strains developed at the top of the SG soil in the Virginia inverted and conventional pavement structures considering a full truck analysis (a) and axle analysis (b) 91
Figure 7.9: Vertical deformation at the top of the AC layer in the Virginia inverted and conventional pavement structures considering a full truck analysis (a) and axle analysis (b) 92
Figure 7.10: Vertical stresses at the top of the UAB layer in the Virginia inverted and conventional pavement structures.....93
Figure 7.11: Contrasting extent of the pressure bulbs evident at the surface of the UAB layer in the Virginia inverted (a) and conventional (b) pavement structures. 95
Figure 7.12: Longitudinal shear stresses at the top of the UAB layer beneath one set of tires for all axles in the Virginia inverted (a) and conventional (b) pavement structures.....96
Figure 7.13: Transversal shear stresses at the top of the UAB layer beneath the tires of one set of dual axles in the Virginia inverted (a) and conventional (b) pavement structures.....96
Figure 7.14: Vertical stress distribution within the UAB layer of the Virginia inverted (a) and conventional (b) pavement structures. 97
Figure 7.15: Horizontal stress distribution within the UAB layer of the Virginia inverted (a) and conventional (b) pavement structures. 98
Figure 7.16: Vertical stress distribution within the UAB layer of Virginia the inverted pavement beneath the dual axle assuming E_x/E_y=1.0 (a), E_x/E_y=0.5 (b), and E_x/E_y=0.4 (c). 101
Figure 7.17: Vertical stress distribution within the UAB layer of the Virginia conventional pavement beneath the dual axle assuming E_x/E_y=1.0 (a), E_x/E_y=0.5 (b), and E_x/E_y=0.4 (c).....102

Figure 7.18: Horizontal stress distribution within the UAB layer of the Virginia inverted pavement beneath the dual axle assuming E_x/E_y=1.0 (a), E_x/E_y=0.5 (b), and E_x/E_y=0.4 (c).....104
Figure 7.19: Data measured by SG-6 placed longitudinally to the traffic flow below the AC layer of the Virginia inverted pavement section during Runs 2 and 3. 105
Figure 7.20: Data measured by SG-4 placed longitudinally to the traffic flow below the AC layer of the Virginia inverted pavement section during Run 1 (a), Run 2 (b), and Run 3 (c). 106
Figure 7.21: Data measured by SG-2 placed longitudinally to the traffic flow below the AC layer of the Virginia inverted pavement section during Run 1 (a), Run 2 (b), and Run 3 (c). 107
Figure 7.22: Calculated horizontal longitudinal strains developed at the bottom of the AC layer of the Virginia inverted pavement structure. 108
Figure 7.23: Data measured by the following pressure cells installed at the top of the UAB layer of the Virginia inverted pavement section: (a) PC-1/Run 2, (b) PC-1/Run 3, and (c) PC-6/Run 1. 110
Figure 7.24: Calculated vertical stresses developed at the top of the UAB layer of the Virginia inverted pavement structure.....112
Figure 7.25: Calculated vertical stresses developed at the bottom of the UAB layer of the Virginia inverted pavement structure.....113
Figure 8.1: Location of SH-123 between Karnes City and San Marcos in Texas. 116
Figure 8.2: Data sample from GPR readings performed in the Texas inverted pavement structure. 117
Figure 8.3: Backcalculated Modulus values of each layer of the Texas inverted and conventional pavement sections. 118

Figure 8.4: Tensile stresses (a) and strains (b) developed at the bottom of the AC layer in the Texas inverted and conventional pavement structures considering a full truck analysis. 120
Figure 8.5: Compressive stresses (a) and strains (b) developed at the top of the SG soil in the Texas inverted and conventional pavement structures considering a full truck analysis. 121
Figure 8.6: Vertical deformation at the top of the AC layer in the Texas inverted and conventional pavement structures considering a full truck analysis.....122
Figure 8.7: Vertical stresses at the top of the UAB layer in the Texas inverted and conventional pavement structures. 123
Figure 8.8: Longitudinal shear stresses at the top of the UAB (a) and transversal shear stresses at the top of the UAB (b) in the Texas inverted and conventional pavement structures. 124
Figure 8.9: Vertical stress distribution within the UAB layer of the Texas inverted (a) and conventional (b) pavement structures. 125
Figure 8.10: Horizontal stress distribution within the UAB layer of the Texas inverted (a) and conventional (b) pavement structures. 126
Figure 8.11: Vertical stress distribution within the UAB layer of the Texas inverted pavement structure beneath the last dual axle assuming E_x/E_y=1.0 (a), E_x/E_y=0.5 (b), and E_x/E_y=0.25 (c). 128
Figure 8.12: Vertical stress distribution within the UAB layer of the Texas conventional pavement beneath the dual axle assuming E_x/E_y=1.0 (a), E_x/E_y=0.5 (b), and E_x/E_y=0.25 (c).....129
Figure 8.13: Horizontal stress distribution within the UAB layer of the Texas inverted pavement beneath the dual axle assuming E_x/E_y=1.0 (a), E_x/E_y=0.5 (b), and E_x/E_y=0.25 (c). 130

Figure 8.14: Horizontal stress distribution within the UAB layer of the Texas conventional pavement beneath the dual axle assuming E_x/E_y=1.0 (a), E_x/E_y=0.5 (b), and E_x/E_y=0.25 (c) 131
Figure 8.15: Vertical and horizontal strain at the top of the UAB layer of the Texas inverted pavement structure for all axles at isotropic and anisotropic conditions. 132
Figure 9.1: Mesh of the Texas inverted pavement model in Abaqus generated using 2.67-in sided cubic elements. 136
Figure 9.2: Rotation of the principal plane at the top of the UAB layer for the Virginia (a) and Texas (b) inverted and conventional pavement structures. 139
Figure 9.3: Schematic of the 189 nodes distributed in Planes 1, 2, and 3, respectively located beneath, at the edge, and at 3 in away from the tire contact area highlighted in yellow. 141
Figure 9.4: P-q plot from the stresses calculated at three transversal planes within the UAB layer of the Virginia inverted pavement structure. 142
Figure 9.5: P-q plot from the stresses calculated within the UAB layer of the Virginia inverted and conventional pavement structures.....143
Figure 9.6: I_1-J_2 plots from the stresses calculated within the UAB layer of the Virginia inverted pavement structure for Plane 1 (a), Plane 2 (b), and Plane 3 (c). 144
Figure 9.7: I_1-J_2 plots from the stresses calculated within the UAB layer of the Virginia inverted and conventional pavement structures compared to (a) AASHTO T-307 and (b) NCHRP 1-28A. 145
Figure 9.8: Schematic of the 252 nodes distributed in Planes 1, 2, and 3, respectively located beneath, at the edge, and at 3 in away from the tire contact area highlighted in yellow. 146

Figure 9.9: P-q plot from the stresses calculated at three transversal planes within the UAB layer of the Texas inverted pavement structure. 147
Figure 9.10: P-q plot from the stresses calculated within the UAB layer of the Texas inverted and conventional pavement structures. 148
Figure 9.11: I_1-J_2 plots from the stresses calculated within the UAB layer of the Texas inverted pavement structure for Plane 1 (a), Plane 2 (b), and Plane 3 (c). 149
Figure 9.12: I_1-J_2 plots from the stresses calculated within the UAB layer of the Texas inverted and conventional pavement structures compared to (a) AASHTO T-307 and (b) NCHRP 1-28A. 150
Figure 9.13: P-q plots from the stresses calculated at three transversal planes within the UAB layer of the Texas inverted pavement structure subjected to conventional loads (a) and SHLs (b). 151
Figure 9.14: P-q plots from the stresses calculated within the UAB layer of the Texas inverted and conventional pavement structures subjected to conventional loads (a) and SHLs (b). 152
Figure 9.15: I_1-J_2 plots from the stresses calculated within the UAB layer of the Texas inverted pavement structure subjected to SHLs for Plane 1 (a), Plane 2 (b), and Plane 3 (c). 153
Figure 9.16: I_1-J_2 plots from the stresses calculated within the UAB layer of the Texas inverted and conventional pavement structures subjected to SHLs compared to (a) AASHTO T-307 and (b) NCHRP 1-28A. 154
Figure 9.17: Failure function f values in the three planes of analysis within the UAB layer of the Virginia inverted pavement section assuming material properties of c = 8 psi and φ = 32° 157
Figure 9.18: Failure function f values in Plane 1 within the UAB layer of the Virginia inverted and conventional pavement sections assuming material properties of c = 3.5 psi and φ = 35°. .158

Figure 9.19: Influence of c and φ on the failure function f values in a point located at 0-in depth and 0-in offset from the tire contact area within the UAB layer of the Virginia inverted section. 159
Figure 9.20: Failure function f values in the three planes of analysis within the UAB layer of the Texas inverted pavement section assuming material properties of c = 5 psi and φ = 33° 160
Figure 9.21: Failure function f values in Plane 1 within the UAB layer of the Texas inverted and conventional pavement sections assuming material properties of c = 3.5 psi and φ = 35° 161
Figure 9.22: Influence of c and φ on the failure function f values in a point located at 0-in depth and 0-in offset from the tire contact area within the UAB layer of the Texas inverted section. 162
Figure 9.23: Failure function f values in Plane 1 within the UAB layer of the Texas inverted pavement section subjected to conventional loads and SHLs assuming material properties of cohesion and angle of internal friction of 5 psi and 33°, respectively. 163
Figure 9.24: Failure function f values in Plane 1 within the UAB layer of the Texas inverted pavement section subjected to conventional loads and SHLs assuming material properties of cohesion and angle of internal friction of 3 psi and 30°, respectively. 164

Chapter 1: Introduction

Chemical stabilization by means of adding cement is a classical method used to enhance the mechanical and durability properties of granular materials in multilayer pavement structures. The design of cementitiously stabilized layers demands the estimation of specific laboratory-derived properties to characterize their strength and resilient behavior under loading. As a more attainable option in lieu of typical experimental procedures dependent on the availability of resources (i.e., time, budget, qualified personnel, and specialized equipment, among others) practical correlation equations were explored. Two sets of material models were developed to forecast the tensile strength and resilient modulus of virgin and reclaimed cement-treated materials. The first set of models considers the cement content, UCS, and height-to-diameter ratio to predict the IDT strength using different compaction methods. The second set of models predicts the M_r in terms of the cement content, UCS, and strength ratio (SR).

If laboratory testing results in being a viable alternative for estimating the strength and resilient properties of cementitiously stabilized layers, the compaction method selected for the fabrication of the specimens to be tested will be determinant for a realistic characterization of the material. The mechanism of application of compaction energy in the field significantly influences the particle orientation, pore structure distribution, level of anisotropy, hydraulic conductivity, and orthogonal strength properties of unbound and cement-treated pavement layers. The specimen fabrication process in the laboratory must reflect the conditions experienced by a material during in-situ compaction to ensure a reliable and accurate design of the pavement layered system. Thus, cement-treated virgin and reclaimed specimens were prepared in the laboratory using impact, vibratory, and gyratory methods to investigate the influence of aggregate type, cement dosage, and laboratory compaction mechanism on their microstructure, UCS, and IDT strength.

Besides the study of the interrelations between laboratory compaction methods, mixture design parameters, intergranular structure, strength characteristics, and resilient behavior in cementitiously stabilized virgin and reclaimed materials, one unconventional type of asphalt concrete pavement configuration known as inverted pavements was also explored.

The standard order of the layers in conventional asphalt pavements starts with an asphalt concrete layer at the surface, followed by a stabilized granular layer, and ends with an underlying unbound granular layer placed on top of the subgrade soil. The rationale of traditional pavement designs is based on protecting the lower layers. As shown in Figure 1.1, the subgrade soil in a typical asphalt concrete pavement is protected by layers of increasing load distribution capacity and better-quality materials. In an inverted pavement, the conventional order of the two layers located below the asphalt concrete layer is switched; the second-lower layer is unbounded, while the third-lower layer is stabilized with cement. The unbound granular layer is placed between a lower cement-treated granular layer and an upper asphalt concrete layer, as depicted in Figure 1.1. The varying stiffness values or modular ratios between consecutive layers in an inverted pavement influence the stress-strain behavior of the structure subjected to cyclic traffic loads.

Inverted pavement designs have been shown to be a superior alternative to traditional asphalt concrete pavements, according to limited yet credible full-scale experimental research. Compared to conventional pavements, inverted structures offer improved mechanical performance, extended service life, and decreased lifecycle costs (Rasoulian 2000, Tutumluer 2013, Papadopoulos & Santamarina 2017). The increased load-bearing capacity of inverted pavements, which results in a longer service life, can provide substantial cost savings over the lifecycle of the infrastructure (Titi et al. 2003, Buchanan 2010, Cortes & Santamarina 2013).

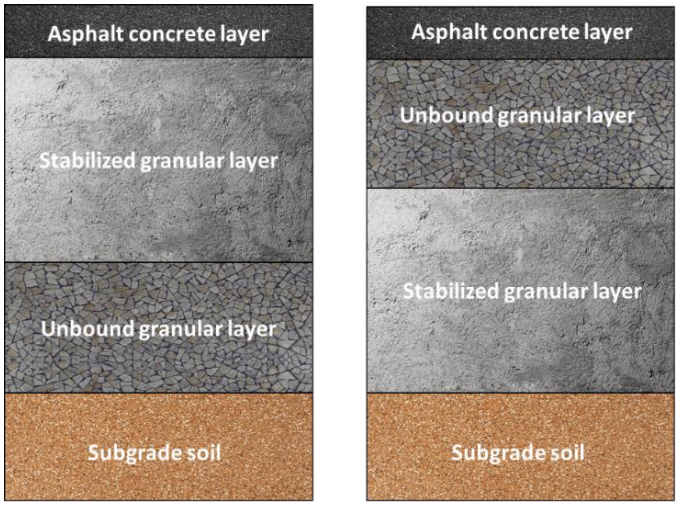

Figure 1.1: Typical layer configuration of a traditional pavement structure (a) and an inverted pavement structure (b).

In an effort for continuing the contribution to knowledge in this novel design philosophy, an inverted pavement test section built on Route 659 (Virginia) was studied. The testing site consisted of a 900 ft-length two-lane road subdivided into a 500 ft-length inverted pavement segment and a 400 ft-length conventional pavement segment. GPR, FWD, and DCP test results were analyzed including data measured by different sensing devices (e.g., strain gauges, pressure cells, linear variable differential transformers, thermocouples, and moisture sensors) installed throughout 50 ft at specific depths within each pavement structure.

According to the field data collected from the testing site, the Virginia inverted pavement section was simulated based on a three-dimensional FE model. Critical mechanical responses from the simulation were validated with field measurements registered by the sensors installed during the instrumentation plan. The validated model was used to simulate a conventional pavement structure equivalent to the inverted one for comparison purposes. The numerical analysis was reproduced for a 4.4-mile-long inverted pavement test section constructed in SH-123 (Texas) based on available field data extracted from FWD and GPR testing.

1.1. PROBLEM STATEMENT

Cement stabilization of marginal materials provides a sustainable means for the construction of new roadways and the rehabilitation of old pavement structures. The strength and resilient properties of cement-treated materials are essential for the design and performance evaluation of roadways. The UCS, tensile strength, and the M_r are critical properties derived from laboratory testing used to characterize the orthogonal load-bearing capacity of cementitiously stabilized layers. Given the increasing demand for quick design solutions, it is not always feasible to determine all necessary design parameters through comprehensive laboratory testing. As a result, pavement engineers often resort to relying on their prior experience or established correlations when estimating material properties, as laboratory testing can be time-consuming and expensive. However, while there are numerous correlations available for virgin materials, there are only a limited number of correlations that can be applied to reclaimed materials that have undergone cement treatment. In this dissertation, the relationship between the strength and resilient properties of cement stabilized virgin and reclaimed materials are studied to develop a set of models capable of capturing the influence of UCS, specimen geometry, cement content, and strength ratio (SR) on the IDT strength and M_r of laboratory-compacted samples fabricated using virgin and reclaimed aggregates treated with different amounts of cement dosages.

A crucial factor that influences the mechanical responses of cementitiously stabilized pavement layers is the adequate compaction of specimens in the laboratory during the mixture design and strength characterization of the materials. The reliability of laboratory-compacted material properties is often affected by issues related to the quality, uniformity, boundaries, and internal pore structure of the specimens. Commonly used Proctor tests tend to result in specimens with high levels of non-uniformity due to the way compaction energy is applied, compromising

the accuracy of laboratory test results (Ping et al. 2003, Kaya et al. 2012). This disparity in laboratory test results has significant implications for the mix design and the physical and mechanical characterization of pavement materials. The systematic bias caused by the specimen compaction process results in inaccuracies that can lead to major complications for both pavement agencies and private laboratories that routinely compare their results for unbound and stabilized pavement materials (Sebesta & Harris 2005). For example, unreliable compressive strength results could result in selecting the wrong amount of stabilizer, leading to a shorter pavement service life and potential failure of the stabilized layers. This dissertation, therefore, concentrates on examining how laboratory compaction techniques impact the internal porosity and compressive and tensile strength of cementitiously stabilized pavement materials.

Proper compaction during the fabrication of cementitiously stabilized specimens in the laboratory for subsequent strength and resilient characterization is crucial for the design of multilayer pavement systems containing cement-treated layers. The last main focus of this dissertation is centered on the study of an unconventional multilayer system adequate for traffic load dissipation known as inverted pavement. Although the literature has evidenced the cost-effectiveness of inverted structures in providing highly serviceable pavements, the analysis and construction of inverted pavements in the United States is not a widespread practice among design engineers. Stakeholders of transportation facilities have not formally included inverted pavements in their toolbox for road infrastructure design due to the lack of research and full-scale experiments needed to comprehensively understand the mechanical behavior of the structures under local conditions and typical construction techniques. To overcome the limited amount of data associated with the design and performance of inverted pavements, this dissertation aims to describe the responses under loading of a full-scale inverted pavement section constructed on Bull Run Route

659 located in Chantilly (Virginia) based on a mechanistic approach. Inverted pavement responses were compared to the behavior of a typical conventional pavement section loaded under the same conditions. Moreover, backcalculated Modulus values of the different pavement layers were used as input data for the development of a series of numerical simulations of inverted and conventional pavement structures based on the FE method. The Virginia inverted pavement section and an additional inverted pavement design from a road segment of SH-123 in Corpus Christi (Texas) were considered for the numerical simulation, including their equivalent conventional designs.

1.2. RESEARCH OBJECTIVES

The research objectives of this dissertation have been categorized into three main components: 1) Material models for the design of cementitiously stabilized layers; 2) Influence of laboratory compaction methods on the microstructure and strength properties of cementitiously stabilized materials; and 3) Numerical modeling and mechanistic analysis of inverted pavement structures. Under each main component, specific objectives were set and are indicated as follows:

1.2.1. Material Models for the Design of Cementitiously Stabilized Layers

Develop correlations between tensile and compressive strength properties, as well as predictive relationships between resilient and compressive strength properties of cement-treated materials, taking into consideration a variety of virgin and reclaimed aggregate sources, three levels of stabilizer content, particular curing and durability conditions, different specimen sizes, and distinct laboratory compaction methods.

Develop a set of mathematical regression models to forecast the IDT strength and the M_r based on the UCS and the previously mentioned mixture design variables, including the aggregate type, cement content, curing and durability conditions, sample size, and laboratory compaction procedures.

1.2.2. Influence of Laboratory Compaction Methods on the Microstructure and Strength Properties of Cementitiously Stabilized Materials

Investigate the influence of impact, vibratory, and gyratory compaction methods on the microstructure of cementitiously stabilized limestone specimens based on an X-ray Computed Tomography (CT) analysis.

Study the influence of impact, vibratory, and gyratory compaction energy on the UCS and IDT strength properties of cementitiously stabilized virgin and reclaimed materials. Different aggregate sources and cement contents will be considered.

1.2.3. Numerical Modeling and Mechanistic Analysis of Inverted Pavement Structures

Describe the full-scale pavement testing site constructed in Virginia based on field data pertaining to the cumulative deformation collected from DCP testing performed at the top of the unbound granular layer of the inverted pavement structure.

Analyze data from non-destructive field testing by means of the FWD executed at the subgrade soil and wearing course of the Virginia inverted and conventional pavement structures. The resulting FWD data associated with the deflections registered at predefined distances measured from the point of application of the load will also be incorporated into the descriptive study. The data will be used to evaluate the deformation potential and rigidity properties of the unbound granular layer from the inverted pavement structure influenced by the underlying rigid cement-treated granular layer.

Execute a backcalculation analysis taking into consideration the deflection data collected from the field during FWD testing in the Virginia inverted pavement structure. The purpose of this analysis is to estimate the Moduli values of each layer of the structure, including the subgrade soil

that supports the layered system. The pavement analysis program selected to perform the structural assessment is Elmod 6 (Evaluation of Layer Moduli and Overlay Design), developed by Dynatest.

Perform the postprocessing of the data (i.e., filtering, correlation, and interpretation) collected by the different sets of sensors installed within the Virginia inverted pavement section for subsequent comparison against the simulated pavement responses from the numerical model.

Create numerical models of the Virginia inverted pavement section based on the data collected from the field. Texas inverted pavement section will also be modeled based on the mechanical properties from in-situ GPR and FWD testing. The FE-based program Abaqus will be used to simulate the behavior of the pavement structures subjected to different truck configurations. The following mechanical responses will be evaluated:

- Tensile strains and stresses at the bottom of the asphalt concrete layer.
- Compressive strains and stresses at the top of the subgrade soil.
- Variation of shear stresses at the top of the unbound granular layer.
- Variation of vertical and horizontal stresses and strains at the top and bottom of the unbound granular layer.
- Vertical and horizontal distribution of stresses within the unbound granular layer.
- Anisotropic behavior analysis of the unbound granular layer based on the stress path and material stability approaches.

1.3. DISSERTATION OUTLINE

The thesis has been structured in 10 chapters.

In Chapter 1, the dissertation begins with an introduction that outlines the problem statement and research objectives. The chapter presents the three main areas of study that the dissertation focuses on, which include: developing material models for designing cementitiously

stabilized layers, investigating the impact of laboratory compaction methods on the microstructure and strength properties of cementitiously stabilized materials, and utilizing numerical modeling and mechanistic analysis to evaluate the performance of inverted pavement structures.

In Chapter 2, a comprehensive literature review was conducted, and the most pertinent publications pertaining to the problem statement of this proposal were identified and analyzed in detail. The literature review focused on three primary areas, namely modeling the strength and resilient properties of cementitiously stabilized materials, laboratory compaction of cement-treated specimens, and the structural behavior of inverted pavement structures.

Chapter 3 of this dissertation presents the laboratory testing program that was designed to investigate the strength and resilient properties of cementitiously stabilized virgin and reclaimed specimens, as well as the influence of laboratory compaction methods on their internal structure and mechanical properties. The experimental program was carefully planned to ensure that reliable data could be obtained to achieve the research objectives.

Chapter 4 presents the analysis of results obtained from various laboratory tests, including the UCS test and IDT strength test. The objective of the analysis is to investigate the impact of factors such as compaction, curing/conditioning procedures, specimen geometry, and cement content on the relationship between UCS and IDT strength. Additionally, the study also focuses on the influence of the curing/conditioning procedures, cement content, and strength ratio of the submaximal modulus test on the relationship between UCS and M_r. The results of the analysis help establish material models that can predict IDT strength and M_r based on the different mixture design variables considered during laboratory testing.

Chapter 5 presents an analysis of the results obtained from the X-ray CT, UCS, and IDT strength tests, highlighting the impact of impact, vibratory, and gyratory compaction methods on

the microstructure and strength properties of cement stabilized limestone materials. Furthermore, a comparison is made between the UCS and IDT strength of cementitiously stabilized virgin and reclaimed materials treated with various cement contents and fabricated using diverse laboratory compaction methods.

Chapter 6 involved the analysis of data obtained from in-situ tests conducted on both the Virginia inverted and conventional pavement sections. The field data included penetration results obtained from DCP tests carried out at the top of the unbound aggregate base layer of the inverted structure during construction. In addition, surface deflections collected using the FWD upon the completion of both inverted and conventional pavements were analyzed.

Chapters 7 and 8 will involve the creation of numerical models using the Finite Element method to evaluate the mechanical behavior of inverted and conventional pavement structures under different loading conditions. In Chapter 7, the inverted pavement at Bull Run Route 659 in Chantilly, Virginia, will be modeled, while Chapter 8 will focus on the inverted pavement constructed at State Highway SH-123 in Corpus Christi, Texas. The models will take into account various material properties and loading conditions to assess the behavior of the pavement structures.

Chapter 9 will analyze the unbound granular base layer of the Virginia and Texas pavement sections by examining the stress states using p-q and I_1 vs. J_2 plots. Additionally, a stability analysis will be conducted using a failure function that relates stress invariants to strength properties such as cohesion and angle of internal friction.

The final chapter of the dissertation, Chapter 10, serves as the conclusion. It provides a summary of all the relevant findings obtained throughout the research, highlighting the conclusions derived from these results.

Chapter 2: Literature Review

2.1. MATERIAL MODELS FOR THE DESIGN OF CEMENTITIOUSLY STABILIZED LAYERS

A comprehensive review of the literature was conducted in this dissertation to study the most relevant empirical relationships between the UCS, IDT strength, and M_r of low-quality materials treated with cement. Table 2.1 summarizes a series of equations developed by selected authors to estimate the IDT strength of stabilized mediums in terms of the UCS for specific types of pavement materials and stabilizer agents.

Table 2.1: Summary of equations correlating UCS (psi) to IDT strength (psi).

Correlation equations	Materials	Stabilizers	Reference
IDT = 0.09 to 0.18 UCS	Silt	Cement	Wang and Huston (1972)
IDT = 0.1242 UCS	Gravel	Cement	Babic (1987)
IDT = 0.1300 UCS	A-6 and A-7-6	Lime	Thompson (1965a)
IDT = 0.1880 UCS	Clayey sand	Lime	Arabani and Karami (2007)
IDT = 0.1600 UCS	Silt	Lime	Arrieta et al. (2018)
IDT = 0.1766 UCS + 9.3056	Full-depth reclaimed material	Cement	Scullion et al. (2012)
IDT = 0.1200 UCS	Clay, silt, sand, and gravel	Cement, lime, class C fly ash	Wen et al. (2014)
IDT = 0.1205 UCS	Limestone, gravel, and sandstone	Cement	Rashidi et al. (2018)

The results presented in Table 2.1 show that the ratio of IDT strength to UCS ranges from 0.09 to 0.22. This variation can be attributed to a variety of factors, including the type and amount of stabilizer used, compaction method, specimen size, curing and conditioning procedures, among other mixture design variables considered in the laboratory testing programs of each study.

Most of the studies listed in Table 2.1 focused on the stabilization of virgin granular materials, except for the study conducted by Scullion et al. (2012), which investigated the impact of incorporating cement on the mechanical properties of reclaimed materials. The study concluded that there was a strong correlation between the IDT strength and the UCS of cement-treated full-

depth reclaimed (FDR) materials. In a similar effort to establish the relationship between tensile and compressive strength characteristics of stabilized materials, Arrieta et al. (2018) carried out an experimental program which involved the preparation of cylindrical lime-treated specimens. The specimens were compacted statically and cured in a humidity room at a temperature of 25°C for varying durations of 15, 30, 60, 90, and 180 days. These compaction and curing procedures differed from the commonly used methods, such as impact compaction and 7-day curing, adopted by other researchers in the field. Lastly, other significant studies have investigated the impact of moisture exposure on the relationship between IDT strength and UCS. For instance, Rashidi et al. (2018) conducted an experiment where cement-treated specimens underwent a 10-day capillary soak, while Scullion et al. (2012) subjected cement stabilized samples to both a 10-day capillary rise and four hours of water immersion at room temperature.

Table 2.2 presents a compilation of formulas that link the M_r to the UCS for specific materials and calcium-based stabilizers. The varying forms of the correlation equations reflect the different mix design variables and testing methodologies utilized in the experimental studies of each investigation.

Table 2.2: Summary of equations correlating UCS (psi) to M_r (ksi).

Correlation equations	Materials	Stabilizers	Reference
$M_r = 0.1235$ UCS + 9.9786	A-7-6, A-6, A-4	Lime	Thompson (1965b)
$M_r = 1.2$ UCS	Coarse-grained sandy soil	Cement	Barenberg (1977)
$M_r = 0.467$ UCS – 45.977 for UCS range from 0.145 to 0.254 ksi $M_r = 0.974$ UCS – 174.6258 for UCS range from 0.254 to 0.5511 ksi	Sand, clay, and loamy sand	Lime	Little et al. (1994)
$M_r = 0.4958$ UCS – 5.244	Soft clays	Fly ash	Kang et al. (2014)
$M_r = 10.33$ UCS – 2,622 for a SR of 20% $M_r = 7.40$ UCS – 1,940 for SRs of 40% and 60%	Limestone, gravel, and sandstone	Cement	Rashidi et al. (2018)

In a significant study, Thompson (1965b) conducted a linear regression analysis that compared the resilient and compressive strength properties of lime-soil mixtures. The resulting equation relates the M_r, which was measured using an unconsolidated-undrained triaxial compression test at a confining pressure of 15 psi and a constant loading rate of 0.4 in/min, to the UCS of 7-day cured cylindrical specimens that were compacted by impact to achieve a height-to-diameter (H/D) ratio of 2. Likewise, Little et al. (1994) estimated the M_r of lime-treated subgrade materials using field data from FWD testing. The UCS values were derived from cylindrical specimens that were compacted by impact in the laboratory, with H/D ratios of 1.33 and a curing period of 28 days before testing. The results indicated that, for the evaluated range of UCS, the linear growth of the M_r was approximately double once the compressive strength reached 254 psi.

Kang et al. (2014) performed a correlation analysis between the 28-day UCS and the M_r of stabilized base materials. Their study involved using triaxial compression tests to estimate the resilient behavior of class C fly ash-treated specimens subjected to five different deviatoric stresses and three different confining pressures. The samples were compacted into cylindrical shapes with H/D ratios of 2 and statically compressed. The results of the linear regression analysis were complemented with an investigation of the effect of confining pressure, curing time, permanent strain, and deviatoric stress on the M_r of the stabilized specimens.

Rashidi et al. (2018) established linear correlation equations between the UCS and the M_r of virgin materials stabilized with varying amounts of cement. The M_r was determined using a submaximal test at strength ratios of 20%, 40%, and 60% of the UCS values of the materials. The cylindrical specimens, compacted using the Proctor method and with a H/D ratio of 2, were subjected to two different curing and conditioning procedures: 7-day curing and 10-day capillary

rise. The authors also investigated the relationship between M_r and the cement content, strength ratio (SR), and material type.

The studies carried out by the previously mentioned authors highlight the significant interest among the academic community in determining the strength and durability of cement-treated materials for effective pavement structure design. The compaction energy used during the laboratory fabrication of specimens has an impact on the mechanical characterization of cement-stabilized systems. Thus, an additional area of interest in this dissertation is referred to the influence of compaction during the laboratory fabrication of cement-treated specimens on the microstructure of the sample and its effect on the compressive and tensile strength properties of the stabilized medium.

2.2. INFLUENCE OF LABORATORY COMPACTION METHODS ON THE MICROSTRUCTURE AND STRENGTH PROPERTIES OF CEMENTITIOUSLY STABILIZED MATERIALS

Proper compaction during specimen preparation in the laboratory is crucial for obtaining accurate estimations of the strength properties of stabilized systems. The most commonly used procedure for compacting specimens in the laboratory is the impact hammer compaction. However, the quality, uniformity, boundary conditions, and microstructure of specimens prepared using the Proctor test can have a significant influence on the reliability of the material properties obtained in the laboratory. The application of compaction energy using impact compaction often leads to high levels of non-uniformity in the specimens, which can affect the accuracy of laboratory performance test results (as noted by Ping et al. 2003 and Kaya et al. 2012). This can result in discrepancies between records from different state agencies and private laboratories for routine mechanical tests of unbound and stabilized pavement materials. Systematic errors associated with specimen preparation can have major consequences for mixture design and the determination of

the physical and mechanical properties of granular materials used in pavement design (as highlighted by Sebesta & Harris 2005). For example, the repeatability and accuracy of compressive strength results for base and subbase materials can result in the incorrect selection of the optimal stabilizer content, leading to premature failure of treated pavement layers.

Several researchers have pointed out the issues with the low quality of specimens prepared using impact compaction. For instance, Arabali et al. (2018) noted that Proctor compaction with an impact hammer can result in large variations in strength test results of laboratory-compacted specimens due to barriers at layer interfaces. Lee et al. (2019) similarly noted that the precision of compressive strength results of specimens compacted using impact compaction poses a major problem for the design of stabilized pavement layers.

Due to the issues surrounding the impact hammer compaction method, there is a growing body of literature advocating for improvements to Proctor compaction procedures or the adoption of new methods to produce specimens that accurately replicate the internal structure and mechanical properties of pavement materials in the field. For example, Sebesta et al. (2008) conducted a study comparing the effects of impact compaction and vibratory compaction on the strength, performance, and fabric of two different base materials. The results showed that specimens prepared using vibratory compaction had better mechanical properties (such as higher triaxial strength and higher seismic modulus) and better performance (such as lower moisture susceptibility and lower rut depth) compared to specimens compacted using the impact hammer. However, Computed Tomography results were not conclusive in determining the superiority of a specific compaction method.

In addition to vibratory and impact compaction methods, researchers have also investigated the use of the SuperPave Gyratory Compactor (SGC) for preparing cement-stabilized specimens

in the laboratory. Du et al. (2018) compared the performance of specimens produced using gyratory compaction with those produced using impact compaction and vibratory compaction. The findings showed that gyratory compaction had a lesser impact on aggregate degradation and was better able to preserve the original gradation structure. Additionally, the SGC was not as effective as vibratory compaction but was better than impact compaction in terms of compressive strength and dry/temperature shrinkage values. The authors emphasized the need to use X-ray methods to study the grain size distribution of cement-stabilized mixtures compacted using different techniques.

The set of researchers mentioned previously has emphasized the significance of compaction in preparing cement-stabilized specimens in the laboratory for determining their strength and resilient properties. Properly fabricating and testing these specimens is crucial in order to determine the optimal amount of stabilizer to be added to the mixture and to design multi-layer pavement systems. The last fundamental area of interest in this dissertation encompasses the study of a non-traditional and novel type of pavement structure known as inverted pavement. Since inverted pavements include a cement-treated layer within their structure, proper compaction during the mixture design of that stabilized system is necessary to forecast the material properties expected in the field after construction.

2.3. NUMERICAL MODELING AND MECHANISTIC ANALYSIS OF INVERTED PAVEMENTS

Trial projects were conducted in a reduced number of states to study the structural behavior of inverted pavements and contribute to increasing the narrow amount of research regarding the construction and performance of inverted pavement structures. Such is the case of a full-scale experiment located on Interstate Highway I-10, at Road Forks-East, New Mexico (Johnson 1960). In this experimental study, three inverted pavements were constructed and compared against six

pavement design configurations consisting of a 3-in asphalt concrete layer placed on top of specific sublayer systems, including untreated and cement-treated granular layers with different thicknesses. After one year of heavy traffic loading, no reflective cracking and no distortions were evidenced on the inverted pavement structures. Additionally, two inverted structures presented the lowest permanent deformation exhibiting an average rut depth of 125 mils.

A similar experimental project took place on Route 64, North of Santa Fe, New Mexico (Johnson 1960). In this study, two inverted pavements were constructed and compared to seven pavement design configurations consisting of a 3-in asphalt concrete layer placed on top of specific sublayer systems, including untreated layers with plastic and non-plastic aggregates as well as cement- and asphalt-treated granular layers with different thicknesses. Six years after subjecting the highway to heavy traffic loads, the surface roughness and deflections were measured using the Bureau of Public Roads roughometer and the Benkelman beam. The inverted pavement structures exhibited the lowest average roughness values (44.35 in/mile) and the lowest average deflections (14.47 mils) under a load application of 10.8 kips.

In 1971, the structural responses of an inverted pavement and three different types of pavement structures, all trafficked under controlled loading conditions, were investigated at the U.S. Army Engineer Waterways Experiment Station in Vicksburg, Mississippi (Grau 1973). The inverted pavement was compared to a pavement structure consisting of a 3-in asphalt concrete layer, a 6-in crushed stone base layer, and a 15-in lean clay subbase layer stabilized with 3.5% of lime. Both structures were trafficked to failure using three test carts, including a 359.35-kips 12-wheel assembly, a 161-kip twin-tandem assembly, and a 50.7-kips single-wheel assembly. A pavement was considered to fail if one of the upcoming conditions were met: (a) upheaval at the surface adjacent to the traffic lane greater than 1 in and (b) loss of waterproofing properties of the

pavement surface due to excessive cracking. At the moment failure was reached, the total deflection on the inverted pavement (0.45 in) was slightly higher compared to the other pavement structure (0.42 in). However, the inverted pavement could sustain more coverages (1,200 coverages for the 12-wheel cart, 1,000 coverages for the twin-tandem cart, 120 coverages for the single-wheel cart) than the other pavement structure (198 coverages for the 12-wheel cart, 140 coverages for the twin-tandem cart, 40 coverages for the single-wheel cart). Coverages were defined as the number of wheel load repetitions for the entire tire print width on any given pavement surface.

In 1983, the Georgia Department of Transportation and the Federal Highway Administration (FHWA) sponsored a full-scale research project that involved the construction and testing of 12 pavement structures in a laboratory facility under strictly controlled loading and climatic conditions (Barksdale 1984). Two inverted pavement structures were compared to five crushed stone bases, consisting of a 3.5-in asphalt concrete layer placed on top of an 8-in or a 12-in unbound granular base layer, and five different types of full-depth asphalt concrete pavements with thicknesses of 6.5 in, 7 in, and 9 in. The subgrade soil considered in the experimental project consisted of a non-plastic micaceous silty sand overlying a concrete slab. Loading conditions included the application of 6.5 kips uniformly distributed over a 9-in diameter circular area at seven different positions, including a main central circle and six secondary overlapping circles about the central circular area. Pavements were tested until reaching failure and instrumented using strain sensors, pressure cells, and linear variable differential transducers. The most relevant results showed that the inverted pavements failed at a number of load repetitions of 3.6 and 4.4 million compared to all the other structures that failed within the range of 0.01 to 3.5 million. Furthermore, the inverted pavements exhibited, on average, 27% less tensile strain at the bottom of the asphalt

concrete layer, 65% less vertical stress at the top of the subgrade, and 69% less surface deflection compared to the crushed stone bases and full-depth asphalt concrete pavements.

Another noteworthy full-scale experience was developed in 1989 on Route 59, Northeast Texas (Hoskins et al. 1991, Moody 1994). An inverted pavement structure was one of the six rehabilitation strategies constructed at the testing site to evaluate their effectiveness in reducing reflective cracking in asphalt concrete overlays placed on top of jointed concrete pavements. The other six strategies involved full-depth repair, crack and seat, open-graded asphalt concrete interlayer, styrene-butadiene-styrene modified seal coat interlayer and two types of mixture designs for asphalt concrete overlays. After two years of annual application of 2.3 million Equivalent Single Axle Loads (ESALs), the inverted pavement showed the lowest progression of reflecting cracking from transverse joints. It resulted in being the third most economical alternative ($1.67/ft^2) regarding construction and maintenance costs for a design period of 30 years. The strategy with the lowest cost corresponded to a 3-in asphalt concrete overlay with $1.08/ft^2.

In 1991, an in-situ full-scale research study was initiated on State Route LA-97 close to Jennings, Louisiana (Rasoulian et al. 2000, Titi et al. 2003). The performances of an inverted and a conventional pavement structure were evaluated during 10.2 years of service. The conventional structure consisted of a 3.5-in asphalt concrete layer placed on top of an 8.50-in cement-treated base layer. The top 12 in of the A-4 subgrade soil was treated with lime to provide a stable foundation for both pavement structures. Roughness, rutting, and deflections were measured using the Mays Ride Meter, a high-speed road profiler, and a dynamic non-destructive testing device. Results from the long-term monitoring program showed that the inverted pavement, compared to the conventional pavement, developed lower International Roughness Index values (i.e., 65 in/mile for the inverted structure versus 79 in/mile for the conventional structure), similar average rut

depths (i.e., 149.6 mils for the inverted structure versus 130 mils for the conventional structure), less total cracking lengths (i.e., 338 ft for the inverted structure versus 764 ft for the conventional structure), and similar variation of Structural Numbers (i.e., from 4.1 to 7.2 for the inverted structure versus 4.2 to 7.1 for the conventional structure). The structural performance of the pavements was measured using an Accelerated Loading Facility with the capacity of applying 11,200 to 160,000 ESALs per day. The inverted pavement could withstand approximately four times more ESALs than the conventional pavement (i.e., 1.29 million ESALs for the inverted structure versus 0.31 million ESALs for the conventional structure).

An inverted pavement section was constructed in 2001 on a haul road at the Lafarge Building Materials quarry in Morgan County, Georgia (Lewis 2006, Georges, 2007, Lewis et al., 2012). The inverted structure was compared to a conventional pavement structure consisting of a 3-in asphalt concrete layer, an 8-in granular aggregate base layer, a 6-in surge stone layer, and a 2-in granular layer placed on top of a granite subgrade soil. Pavements were subjected to approximately 854,000 ESALs throughout five years of service and evaluated based on imaging surface distress inspections and FWD testing. The average rut depth registered on the inverted pavement structure was 146 mils, ranging from 63 mils to 378 mils, while the average rut depth recorded on the conventional pavement structure was 275 mils, ranging from 63 mils to 1,008 mils. The data collected also revealed that no cracking was exhibited on the surface layer of the inverted pavement, while extensive cracking was exhibited on the surface layer of the conventional pavement. Taking into consideration the influence of rutting and cracking, the remaining life of the structures was computed in terms of a percentage of the initial pavement life. Results showed that the remaining life of the inverted pavement was 99.34% of the original design life, whereas the remaining life of the conventional structure was 67.92% of the initial pavement life.

An additional relevant inverted pavement test section was constructed in 2008 at the South Lagrange loop in Troup County, Georgia (Lewis et al. 2012). The inverted structure was compared to a conventional Portland cement concrete pavement consisting of a 9.5-in concrete slab and a 10-in graded aggregate base layer placed on top of 6-in subgrade soil with a minimum California Bearing Ratio (CBR) of approximately 15%. A 30-year life cycle cost analysis showed that the inverted pavement resulted in net savings of $139,000 compared to the rigid pavement structure (Buchanan 2010). After one year of service, FWD testing was performed on the inverted pavement under load applications of 9 kips. The pavement showed a remarkable structural performance evidenced by an average deflection of 8.54 mils at the sensor below the loading plate. Furthermore, the inverted pavement exhibited prolonged remaining lives exceeding 10 years, considering the impact of the progression of rutting and cracking on the road performance.

One of the most recently developed full-scale inverted pavement testing sites was constructed on Pit Highway 659 in North Carolina (Weingart 2018). The inverted pavement structure was compared to a conventional pavement consisting of a 6-in asphalt concrete layer and a 10-in unbound granular base layer placed on the subgrade soil. Economic analysis showed that the inverted pavement incurred construction costs equal to $\$2.79/ft^2$, resulting in approximately 11.3% cost savings compared to the conventional pavement, which incurred construction costs equivalent to $\$3.15/ft^2$. FWD testing was also performed on both pavement structures, resulting in lower average deflections measured on the inverted pavement (7 mils) compared to the average deflections measured on the conventional pavement (15 mils).

Table 2.3 summarizes the thicknesses of the system of layers corresponding to the different inverted pavement structures covered in the literature review of the present study constructed as part of full-scale testing programs in the U.S. Additional information related to the strength

characteristics of pavement layers and the general properties of subgrade soils is also included in the table.

Table 2.3: Inverted pavement layer configurations of relevant full-scale research projects.

Project name or location	Inverted pavement structure	Reference
Interstate Highway I-10, New Mexico	3-in asphalt concrete layer 6-in unbound aggregate base layer 6-in subbase layer stabilized with 3% cement 2-in, 3-in, and 9-in unbound aggregate subbase layer	Johnson (1960)
Route 64, New Mexico	3-in asphalt concrete layer 6-in unbound aggregate base layer consisting of either plastic or non-plastic aggregates 6-in subbase layer stabilized with 4% cement	Johnson (1960)
U.S. Army Engineer Waterways Experiment Station, Mississippi	3.5-in asphalt concrete layer 6-in unbound limestone base layer with a California Bearing Ratio (CBR) of 180% 15-in clay subbase layer stabilized with 10% cement High plastic clayey subgrade with a CBR of 4%	Grau (1973)
Georgia	3-in asphalt concrete layer 8-in unbound well-graded granitic gneiss base layer 6-in cement-treated subbase layer consisting of either crushed stone or silty sand 44-in micaceous non-plastic silty sand subgrade placed on top of a concrete slab	Barksdale (1984)
Route 59, Texas	3-in asphalt concrete layer 8-in unbound aggregate base layer 2-in asphalt concrete layer placed over an existing jointed concrete pavement	Hoskins et al. (1991), Moody (1994)
State Route LA-97, Louisiana	3-in asphalt concrete layer 4-in unbound limestone base layer 6-in cement-treated granular subbase layer 12-in A-4 soil stabilized with lime A-4 subgrade soil	Rasoulian et al. (2000), Titi et al. (2003)
Lafarge Building Materials quarry, Georgia	3-in asphalt concrete layer 6-in unbound aggregate base layer with 86.4% of apparent density and 146.32 pcf of unit weight 8-in subbase layer stabilized with 4% to 5% cement 2-in unbound aggregate subbase layer Granitic subgrade with a minimum CBR of 15%	Lewis (2006), Georges (2007), Lewis et al. (2012)

Project name or location	Inverted pavement structure	Reference
South Lagrange loop, Georgia	1.5-in riding surface layer 2-in asphalt concrete layer 6-in unbound aggregate base layer with an apparent specific gravity of 86% 10-in subbase layer stabilized with 4% cement and presenting a minimum Unconfined Compressive Strength (UCS) of 450 psi 6-in stabilized subgrade soil with a Soil Support Value of 5% (similar to a CBR value of 15%)	Lewis et al. (2012), Buchanan (2010)
Pit Highway 659North Carolina	2.5-in asphalt concrete layer 6-in unbound aggregate base layer with an apparent density of 86.4% 8-in cement-treated subbase layer with a UCS of 1.56 ksi	Weingart (2018)

This dissertation aims to describe the full-scale inverted pavement constructed in Virginia. The description of the road test was based on cumulative deformation data collected from in-situ DCP testing executed at the top of the unbound granular layer of the inverted pavement section. Additionally, FWD deflection data from non-destructive field testing performed at the top of the subgrade soil and wearing courses of inverted and conventional pavement sections were also considered in the scope of the dissertation. Finally, DCP test results were examined to estimate the deformation potential and stiffness properties of the unbound granular layer of the inverted pavement section, while FWD test results were used to evaluate the deflection characteristics and homogeneity of compaction of the same unbound granular layer.

This dissertation also aims to perform a numerical analysis of two inverted pavement sections and their corresponding equivalent conventional designs. The inverted pavements selected for analysis were the Virginia inverted section and one inverted pavement constructed in Texas. The set of inverted and conventional pavement structures was simulated using the FE method based on the material properties derived from in-situ FWD and GPR testing. The Virginia

inverted pavement section results were validated with field responses collected by different sensing devices installed within the structure to capture the pavement behavior under loading. The same modeling considerations used to develop the Virginia inverted pavement section were applied to the analysis of the Texas inverted pavement section.

Chapter 3: Development and Implementation of Experimental Program

A laboratory testing program was established to investigate the strength and resilient properties of virgin and reclaimed specimens that were stabilized with cement and the influence of compaction on their internal structure and mechanical properties. The study involved the preparation and testing of 507 samples using the impact hammer, vibratory hammer, Texas Gyratory Compactor (TGC), and SuperPave Gyratory Compactor (SGC). Four different base aggregate sources were chosen for the study, including gravel and limestone, as virgin materials, and FDR material and recycled concrete aggregate (RCA), as reclaimed pavement materials. The study used three levels of cement dosage (2%, 3%, and 4% cement). After stabilization and compaction, the specimens were subjected to different curing/conditioning procedures, and some were also tested with X-ray CT, compressive testing, tensile testing, and submaximal modulus testing. The experimental design matrix, shown in Figure 3.1, included a series of tests to determine the microstructure, compressive and tensile strength, and the M_r of the cement-treated specimens using four aggregate sources, three cement contents, four compaction methods, two curing/conditioning procedures, and four specimen sizes.

3.1. MATERIAL CHARACTERIZATION

The grain size distribution and moisture-density relations of the virgin and reclaimed materials were analyzed. The particle size gradation for each material is presented in Figure 3.2. To determine the optimum moisture content and maximum dry density, cylindrical specimens with dimensions of 6 in in diameter and 8 in in height were compacted using the impact and vibratory hammers, while cylindrical specimens with dimensions of 6 in in diameter and 6 in in height were compacted using the SGC.

Compaction method	Moisture conditioning	Laboratory tests	Aggregate type and number of specimens per test												Sub Total	Total
			Limestone			Gravel			RCA			FDR				
			Cement content (%)													
			2	3	4	2	3	4	2	3	4	2	3	4		
Impact Hammer	7-day curing	UCS[a]	8	8	8	8	8	8	8	8	8	8	8	8	96	169
		IDT strength[b]	2	2	2	2	2	2	2	2	2	2	2	2	24	
		Submaximal[c] SR=25%	2	2	2	2	2	2	2	2	2	2	2	2	24	
		Submaximal[c] SR=50%	2	2	2	2	2	2	2	2	2	2	2	2	24	
		X-ray CT[d]		1											1	
	Tube Suction Test	UCS[e]	6	6	6	6	6	6	6	6	6	6	6	6	72	144
		IDT strength[b]	2	2	2	2	2	2	2	2	2	2	2	2	24	
		Submaximal[c]: SR=25%	2	2	2	2	2	2	2	2	2	2	2	2	24	
		Submaximal[c]: SR=50%	2	2	2	2	2	2	2	2	2	2	2	2	24	
Texas Gyratory Compactor	7-day curing	UCS[b]	2	2	2	2	2	2	2	2	2	2	2	2	24	48
		IDT strength[b]	2	2	2	2	2	2	2	2	2	2	2	2	24	
	Tube Suction Test	UCS[b]	2	2	2	2	2	2	2	2	2	2	2	2	24	48
		IDT strength[b]	2	2	2	2	2	2	2	2	2	2	2	2	24	
Vibratory Hammer	7-day curing	UCS[c]	2	2	2	2	2	2	2	2	2	2	2	2	24	49
		IDT strength[b]	2	2	2	2	2	2	2	2	2	2	2	2	24	
		X-ray CT[d]		1											1	
Superpave Gyratory Compactor	7-day curing	UCS[d]	2	2	2	2	2	2	2	2	2	2	2	2	24	49
		IDT strength[b]	2	2	2	2	2	2	2	2	2	2	2	2	24	
		X-ray CT[d]		1											1	
															Total number of specimens	507

[a]Specimen sizes (diameter x height): 4 in x 4 in, 4 in x 6 in, 6 in x 6 in, 6 in x 12 in.

[b]Specimen size (diameter x height): 4 in x 4 in.

[c]Specimen size (diameter x height): 6 in x 12 in.

[d]Specimen size (diameter x height): 6 in x 6 in.

[e]Specimen sizes (diameter x height): 4 in x 4 in, 4 in x 6 in, 6 in x 12 in.

Figure 3.1: Experimental matrix for comprehensive laboratory testing.

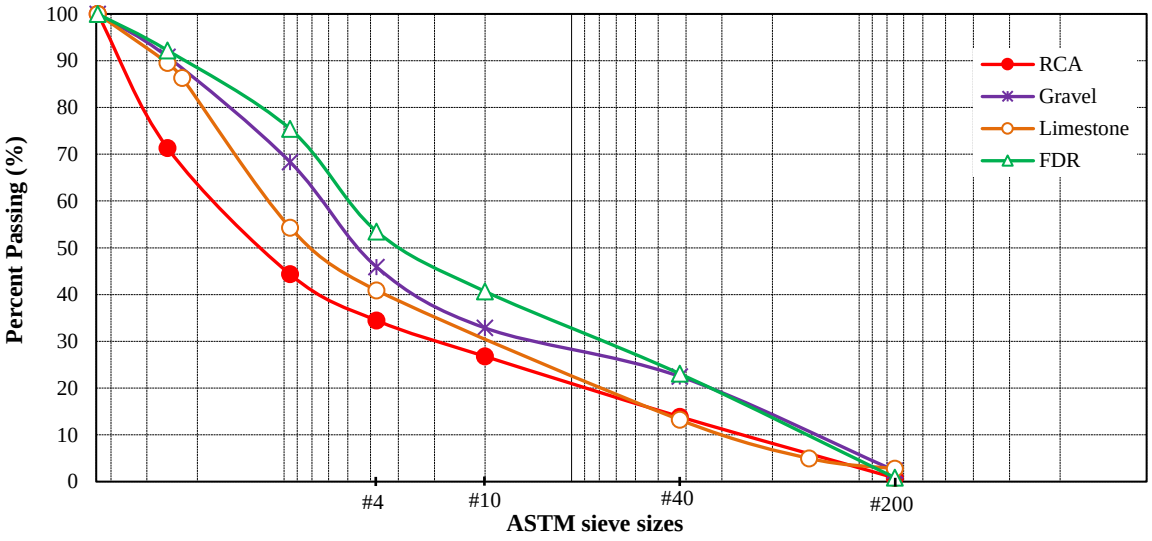

Figure 3.2: Grain size distribution characteristics of virgin and reclaimed aggregates.

The optimum moisture content (OMC) and maximum dry density (MDD) for each of the base aggregate materials were recorded in Table 3.1 after compacting cylindrical specimens with the Impact Hammer (IH), Vibratory Hammer (VH), and SuperPave Gyratory Compactor (SGC). Cement was added in increasing amounts of 2%, 3%, and 4% to create lightly and moderately stabilized specimens. The fabrication of cylindrical stabilized specimens at their optimum conditions (MDD and adjusted OMC) was performed using various compaction methods, including the IH, VH, Texas Gyratory Compactor (TGC), and SGC, for each combination of aggregate type and cement content.

Table 3.1: Optimum moisture contents and maximum dry densities of virgin and reclaimed materials fabricated using impact, vibratory, and gyratory compaction procedures.

Compaction Methods	**Properties**	**OMC (%) and MDD (pcf) values for different materials**			
		Limestone	**Gravel**	**RCA**	**FDR**
Impact	OMC	6.40	8.20	7.50	6.30
	MDD	146.08	124.86	126.10	129.85
Vibratory	OMC	6.50	9.60	10.8	8.30
	MDD	142.96	123.61	120.49	122.36
Gyratory	OMC	5.30	7.70	6.40	5.60
	MDD	142.96	131.72	134.84	133.60

3.2. LABORATORY COMPACTION METHODS

The cement-stabilized specimens were prepared using impact, vibratory, and gyratory compaction methods. The instruments used for compaction are depicted in Figure 3.3. The impact compaction process involved applying compaction energy to the stabilized specimens by dropping a 10-lb impact hammer from a height of 18 in onto the specimens, which were placed in cylindrical rigid molds. The compaction was performed in layers of 2 in in thickness, with 50 uniform hammer blows applied to each layer. The Soil Compactor Analyzer was utilized to provide the impact compaction energy in the laboratory. The weight of the hammer and the number of hammer blows

per layer were adjusted to ensure that the same compaction energy was applied to all specimens, regardless of size, as outlined in the experimental matrix in Figure 3.1.

Vibratory energy was applied to the cementitiously stabilized virgin and reclaimed materials during the compaction process using a vibratory hammer. The specimens were compacted in layers of 2 in in thickness, and the application of vibration sequences per layer was performed with a circular steel tamping plate attached to the hammer via a steel shaft. The vibration time was adjusted to ensure that the same energy was applied during the compaction of all the specimen sizes specified in the experimental design matrix shown in Figure 3.1.

Figure 3.3: (a) Impact hammer, (b) vibratory hammer, (c) Texas Gyratory Compactor, and (d) SuperPave Gyratory Compactor used for compaction in the laboratory.

Gyratory compaction was applied to the cement stabilized virgin and reclaimed specimens in the laboratory using the TGC and the SGC. The compaction process was achieved by imposing compressive pressure and shearing forces to the material through the kneading motion created by the gyrations of the cylindrical mold around its longitudinal axis. This study followed the laboratory procedure outlined in the testing protocol established by the Texas Department of Transportation (TxDOT 2008) for compaction with the TGC. For the case of compaction with the SGC, the compaction parameters were chosen based on a previous study by Ashtiani et al. (2020) that analyzed the effect of the number of gyrations, gyration angle, and compaction pressure on the height, density, and strength of compacted specimens. In this research study, the materials were compacted with 87 psi compaction pressure, a 1.25º gyration angle, and 120 gyrations to ensure proper packing and interlocking of the granular system. In order to reach the highest possible strength and density in a specimen, compaction and rearrangement of solid particles leads to an increase in interparticle contact and a reduction of air voids (Ashtiani 2009). The compaction pressure was limited to 87 psi as higher values were deemed to be outside of typical field compaction conditions and could result in increased particle disintegration compared to lower magnitudes. It is important to note that the gyratory compaction parameters used in this study align with the methodology and suggestions put forth in prior research studies (Browne 2006, Kim and Labuz 2007, Mokwa et al. 2008, Lee et al. 2019).

3.3. CURING, MOISTURE CONDITIONING, AND MECHANICAL TESTING

Following the compaction process, the laboratory-prepared specimens underwent two distinct curing and conditioning procedures to assess the impact of moisture intrusion on their strength and stress-strain behavior. All samples were first cured for seven days in a controlled environment at a temperature of 23°C and relative humidity of 95%. Subsequently, as per the Tube

Suction Test procedure, a set of specimens compacted using IH and TGC were subjected to a 10-day capillary soak to evaluate the effects of water penetration via capillary action through the internal structure of the stabilized material. Finally, the specimens underwent the UCS test, IDT strength test, and submaximal modulus test to determine their mechanical properties.

The cylindrical specimens of cementitiously stabilized materials were subjected to uniaxial compression tests to determine their compressive strength. The specimens were fabricated using impact, vibratory, and gyratory compaction methods and were loaded in a perpendicular direction to their cross-sections with a strain rate of 2% per minute until failure. The sizes of the specimens varied depending on the compaction method used. The impact-compacted specimens had H/D ratios of 1 (4 in diameter by 4 in height and 6 in diameter by 6 in height), 1.5 (4 in diameter by 6 in height), and 2 (6 in diameter by 12 in height). The vibratory-compacted specimens had a H/D ratio of 2 (6 in diameter by 12 in height). Finally, the specimens compacted with the TGC and SGC had H/D ratios of 1 (4 in diameter by 4 in height and 6 in diameter by 6 in height, respectively).

The strain-controlled IDT strength tests were carried out on cylindrical specimens of cement-treated materials with a diameter of 4 in and a height of 4 in. The specimens were subjected to a constant strain rate of 40 mils/min and the same specimen size was used for all compaction methods. The load was applied in the direction of the vertical diameter of the sample to cause uniform tension until failure was reached.

The submaximal modulus tests were conducted to determine the M_r of 6 in diameter by 12 in height cylindrical cement-treated specimens that were compacted using the Proctor method. The tests were performed under stress-controlled conditions and were designed to estimate the M_r at two different stress ratio levels. The cyclic stress amplitudes applied to each specimen were

calculated based on its UCS value. The dynamic load was applied at two submaximal levels, representing 25% and 50% of the compressive strength, and subjected to a specific number of cycles, with 5,000 repetitions per submaximal load level. The tests were conducted at a frequency of 1 Hz and involved the application of a haversine-shaped axial compressive load pulse, lasting for 0.1 seconds, with a rest period of 0.9 seconds.

Figure 3.4 displays the UCS, IDT strength, and submaximal modulus testing devices used to characterize the strength and resilient properties of cementitiously stabilized virgin and reclaimed materials in the laboratory.

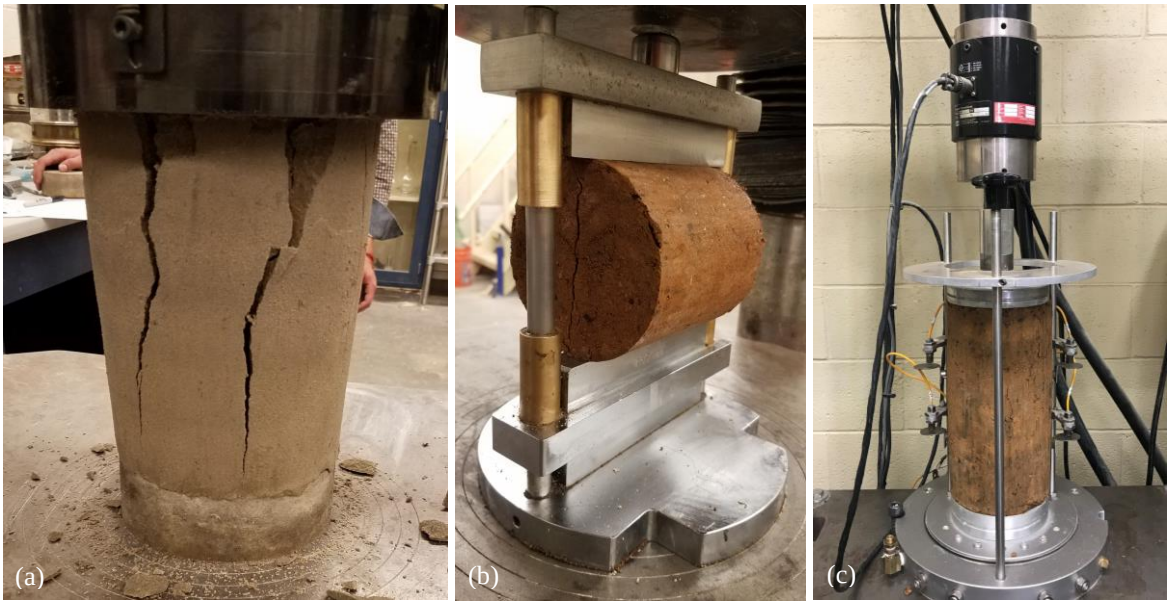

Figure 3.4: (a) UCS, (b) IDT strength, and (c) submaximal modulus laboratory testing apparatus.

3.4. MICROSTRUCTURAL ANALYSIS

An X-ray computed tomographic imaging technique was employed to examine the internal pore structure of cylindrical specimens consisting of limestone material mixed with 3% cement. The samples, with a diameter of 6 in and a height of 6 in, were fabricated using impact, vibratory, and gyratory compaction methods, and all were prepared at their OMC and MDD. The tomographic analysis aimed to evaluate the distribution of void structure throughout the height of

each specimen and assess its non-uniformity resulting from the different compaction methods. The specimens were positioned on a turntable, rotated, and moved vertically across the detector field during the acquisition of X-ray projections. Approximately 1,800 cross-sectional CT images of each specimen were taken at different heights to compare the variations in pore structure between the three laboratory-compacted samples. The porosity distributions were calculated in two directions, one perpendicular and one parallel to the central longitudinal axis of the cylindrical specimens. Figure 3.5 displays the helical scanner used to perform the X-ray CT scans on the cementitiously stabilized samples.

Figure 3.5: X-ray CT system used to analyze the cylindrical samples placed inside sealed PVC pipe caps used for protecting specimens during transport to the testing facilities.

Chapter 4: Material Models for the Design of Cementitiously Stabilized Layers

The laboratory findings from the UCS and IDT strength tests were analyzed to highlight the effect of compaction method, curing and conditioning procedures, specimen dimensions, and cement content on the relationship between UCS and IDT strength. Additionally, the results from the submaximal modulus test and UCS test were evaluated to underline the impact of curing and conditioning procedures, cement content, and the strength ratio from the submaximal modulus test on the relationship between M_r and UCS.

In this dissertation, the relationships between the tensile and compressive strength properties, as well as the correlations between the resilient and compressive strength characteristics of cement-treated materials were studied. The investigation encompassed a range of virgin and reclaimed aggregate sources, varying dosages of cement, specific curing and durability conditions, diverse specimen sizes, and various laboratory compaction techniques. The mixture design parameters and the UCS data were analyzed to establish a set of material models for predicting the IDT strength and the M_r of cementitiously stabilized virgin and reclaimed base materials.

4.1. UCS AND IDT STRENGTH RELATIONSHIPS

Figure 4.1 shows the correlation between the compressive and tensile strength of 288 cement-treated specimens compacted using the IH compaction method. The data points are color-coded based on the type of aggregate used and show a positive relationship between the UCS and IDT strength, indicated by the ascending trend of the best-fit line represented by a dashed line in the graph. The figure also displays the overall linear regression equation, considering all 144 data points, as well as linear regression models for each material type, with a zero intercept. The IDT strength of limestone, gravel, RCA, and FDR materials was found to be 7.7%, 16.7%, 17.2%, and 26.1% of their respective UCS values. The results highlight the differences in the compressive and

tensile strengths of virgin and reclaimed materials, with virgin materials exhibiting higher strength values than the reclaimed aggregates. These findings highlight the impact of aggregate source on the orthogonal strength properties of stabilized layers and can provide valuable information for optimizing the blend ratios of marginal materials in the design of stabilized layers.

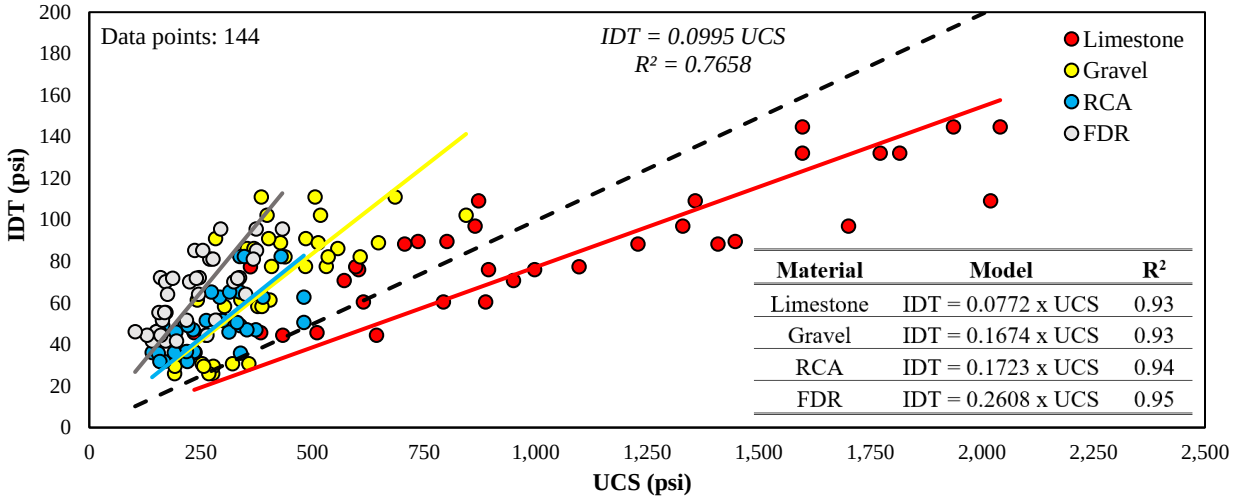

Figure 4.1: Correlations between UCS and IDT strength for cement-treated materials.

Figure 4.2 displays the relationship between the compressive and tensile strengths of cement-stabilized specimens that were categorized based on the H/D ratio of the cylindrical samples produced in the laboratory, which is a crucial factor that has a significant impact on the results of the compressive strength test. As depicted in the figure, the trendline for a H/D ratio of 1 has a flatter slope compared to the trendlines of the other specimen shapes. This trend highlights that the dimensions used in the compaction of the cylindrical specimens significantly affect the correlation between the UCS and IDT strength for the various types of virgin and reclaimed cementitiously stabilized materials.

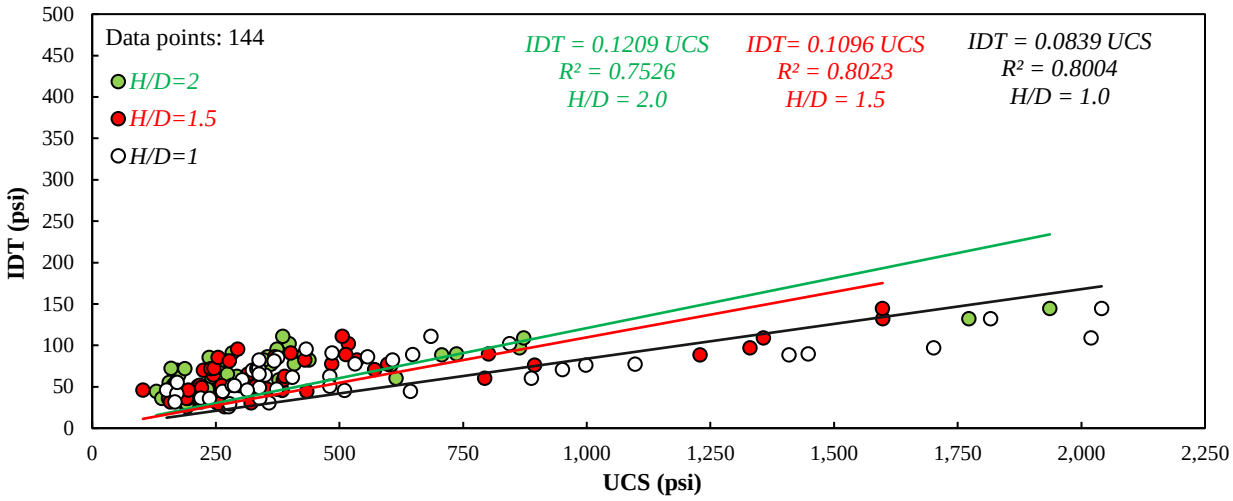

Figure 4.2: UCS-IDT strength relationships for cementitiously stabilized materials clustered based on specimen height-to-diameter ratio.

The experimental investigation considered four compaction methods to fabricate the cementitiously stabilized specimens. Figure 4.3 displays the relationship between compressive and tensile strength categorized based on the equipment used for the application of the compaction energy. The results indicate that the increase rate of IDT strength at increasing UCS values was similar and steeper when the cement-treated specimens were compacted using the VH and SGC. On the other hand, the rate of change of the IDT strength at increasing compressive strength levels was similar and flatter when the cement stabilized specimens were fabricated using the IH and TGC. These findings emphasize the influence of specimen size on the strength relationships of cement-treated specimens.

Figure 4.3 shows the relationship between the compressive and tensile strength of the cementitiously stabilized specimens categorized based on the compaction method used. The results indicate that the increase rate of IDT strength with increasing UCS values was steeper when the specimens were compacted using the VH and SGC. However, the rate of change of the IDT strength at increasing compressive strength levels was flatter when the specimens were compacted

using the IH and the TGC. These findings highlight the significant impact of compaction method on the strength relationships of cementitiously stabilized specimens.

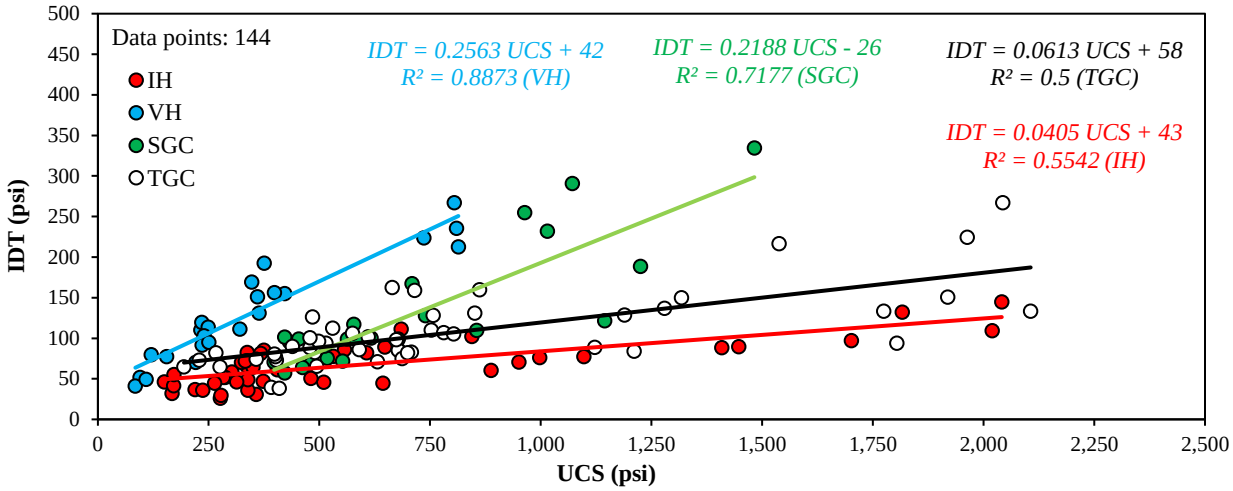

Figure 4.3: UCS-IDT strength relationships for cementitiously stabilized materials clustered based on compaction method.

4.2. UCS AND M_R RELATIONSHIPS

The relationship between the UCS and the M_r of 192 specimens compacted using the Proctor method is shown in Figure 4.4. The specimens are categorized based on their material type, represented by different colors. The figure includes data for specimens with H/D ratios of 1.5 and 2, and M_r values determined from 25% and 50% SRs. The graph shows a positive correlation between UCS and M_r, implying that specimens with higher compressive strength also have higher resilient modulus values compared to their counterparts. The figure also presents the general correlation equation considering all 96 data points, as well as the trendline equations for each aggregate type with the intercept set to zero. It is worth noting that the range of UCS and M_r values obtained from the reclaimed materials was smaller compared to that of the virgin aggregates, demonstrating the influence of the mineralogical and surface properties of virgin and reclaimed

aggregates on the compressive strength and resilient properties of cementitiously stabilized systems.

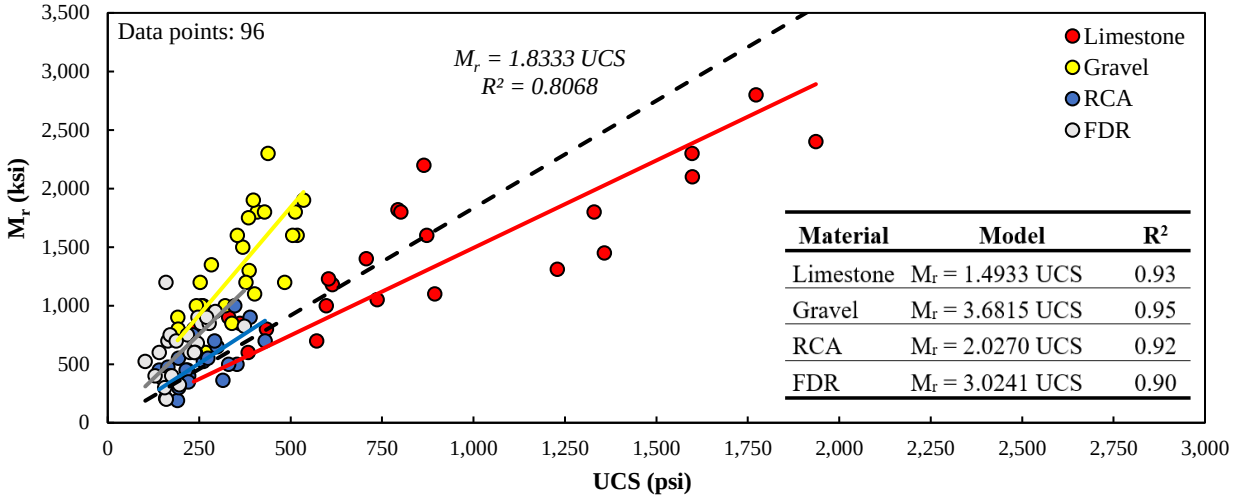

Figure 4.4: Correlations between UCS and M_r for cement-treated virgin and reclaimed materials.

In Figure 4.5, the influence of cement dosage on the relationship between UCS and M_r of cementitiously stabilized materials is depicted. The scatterplot highlights that as the amount of stabilizer in the mix increased, both the compressive strength and resilient modulus of the specimens improved. The increase in cement content also resulted in a wider spread of the data, as seen by a rise in the coefficient of variation (COV) for both the UCS and M_r values. For cement dosages of 2%, 3%, and 4%, the COV of the UCS was 47%, 64%, and 82%, respectively, while the COV for the M_r values was 44%, 46%, and 49%. This variability can be attributed to the mineralogical properties of the virgin and reclaimed aggregates, their varying strength behavior, and the potential for high stabilizer content to cause micro-cracks in overly stiff cementitiously stabilized specimens.

Figure 4.6 displays the relationship between the compressive strength and the M_r of cementitiously stabilized systems when subjected to different stress SR levels of 25% and 50%. The resilient modulus depends on the loading protocol during the testing and therefore, it is crucial

to consider the stress ratio when evaluating the resilient properties of cement stabilized systems. The trendlines in the figure suggest that applying dynamic stresses equal to 25% of the UCS will result in higher M_r values as it causes lower strain levels to the cement-treated specimens. On the other hand, when subjected to cyclic stresses equal to 50% of the UCS, the specimens experience high strain levels leading to lower M_r values. This information can be valuable for pavement design engineers who are looking to mitigate infrastructure distress in corridors subjected to super heavy loads.

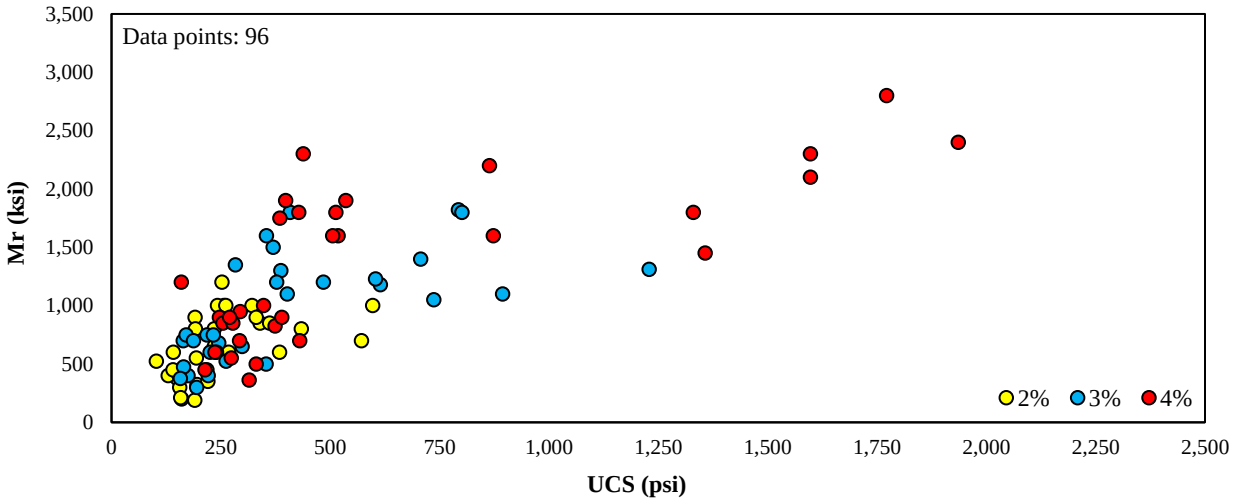

Figure 4.5: UCS-M_r relationships for stabilized materials categorized based on cement dosage.

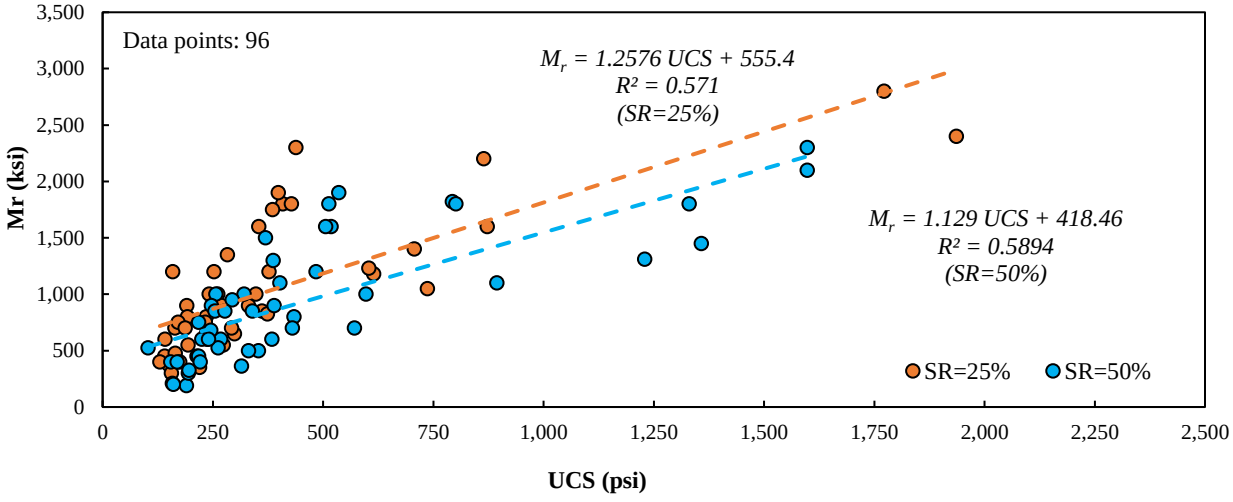

Figure 4.6: UCS-M_r relationships for stabilized materials categorized based on cement dosage.

4.3. MATERIAL MODELS FOR CEMENTITIOUSLY STABILIZED MATERIALS

The results of the experimental investigation led to the development of two sets of material models in this study. The first model predicts the IDT strength of virgin and reclaimed cement-treated specimens fabricated using different compaction methods, taking into consideration the UCS, H/D ratio, and stabilizer content as predictive variables. The second model predicts the M_r of virgin and reclaimed stabilized samples based on the UCS, cement content, and SRs of the submaximal modulus test. Both models were developed through a non-linear regression analysis that utilized the robust fitting weight functions incorporated in Matlab.

The general form of the IDT strength predictive models for cementitiously stabilized virgin and reclaimed materials is presented in Equation 4.1. The regression coefficients vary based on the curing/conditioning and compaction methods used in the fabrication of cement-treated specimens and reflect the impact of predictor variables on the IDT. The performance of the models is evaluated using statistical parameters such as the coefficient of determination (R^2), coefficient of correlation (R), root mean squared error (RMSE), and regression coefficients, which are summarized in Table 4.1. These values demonstrate the strong predictive capability of the proposed IDT strength models.

$$IDT = a\ UCS^b\ (H/D)^c C^d \tag{4.1}$$

Where:

IDT: Indirect diametrical tensile strength (psi)

UCS: Unconfined compressive strength (psi)

H/D: height-to-diameter ratio

C: percent cement in its decimal form

a, b, c, d: regression coefficients

Table 4.1: Regression coefficients and associated statistical parameters of IDT strength models.

Compaction / curing or conditioning process	Regression coefficients				Statistics		
	a	b	c	d	R^2	R	RMSE
IH / 7-day curing	406.28	0.18285	0.12647	0.85010	0.83	0.91	12.198
IH / TST	90.182	0.33357	0.16267	0.66234	0.84	0.92	16.076
VH / 7-day curing	1.5923	0.70208	0.00000	-0.09706	0.94	0.97	18.987
SGC / 7-day curing	0.0223	1.27760	0.00000	-0.07392	0.80	0.90	40.989
TGC / 7-day curing	115.98	0.20220	0.00000	0.41385	0.56	0.75	26.155
TGC / TST	4.0084	0.68687	0.00000	0.35195	0.87	0.93	25.847

Equation 4.2 presents the general form of the models for predicting the M_r in cementitiously stabilized specimens. The regression coefficients displayed in the equation are influenced by the curing/conditioning procedures employed during the fabrication of the Proctor-compacted specimens. The exponent representing the influence that the UCS and cement content exert on the M_r was found to be 0.5 for both predictors. The R^2, R, RMSE, and regression coefficients related to the forecasting models are summarized in Table 4.2. The statistical parameters demonstrate the ability of the proposed models to generate accurate predictions.

$$M_r = a\sqrt{(UCS)(C)}\,SR^b \tag{4.2}$$

Where:

M_r: Resilient Modulus (ksi)

UCS: Unconfined compressive strength (psi)

C: percent cement in its decimal form

SR: strength ratio of submaximal modulus test

a, b: regression coefficients

Table 4.2: Regression coefficients and associated statistical parameters of M_r models.

Curing or conditioning process	Regression coefficients		Statistics		
	a	b	R^2	R	RMSE
7-day curing	199.17	-0.39021	0.63	0.79	373.81
TST	242.91	-0.13809	0.80	0.89	352.11

Chapter 5: Influence of Laboratory Compaction Methods on the Microstructure and Strength Properties of Cementitiously Stabilized Materials

In this dissertation, impact, vibratory, and gyratory compaction methods were studied to understand their effect on the microstructure and strength properties of cementitiously stabilized virgin and reclaimed materials. A systematic and comprehensive experimental program was designed, taking into consideration variables such as aggregate source, cement content, and compaction energy application. One set of limestone specimens treated with cement were compacted using the IH, VH, and SGC, and then subjected to an X-ray CT analysis for microstructural examination. A different set of virgin and reclaimed stabilized specimens fabricated in the laboratory based on impact, vibratory, and gyratory compaction methods underwent mechanical testing under unconfined compression and indirect diametrical tension to assess the compressive and tensile strength properties of the cement-treated systems.

5.1. INFLUENCE OF COMPACTION ON THE MICROSTRUCTURE

Figure 5.1 provides a visualization of X-ray CT scans of the cylindrical cement stabilized limestone specimens, which were fabricated using different compaction methods. The longitudinal cross-sections along the center of the cylindrical specimens were analyzed to determine the uniformity of the samples. The images reveal that specimens compacted using the impact and vibratory hammers contained more entrapped air voids and non-uniform areas, while the specimen compacted with the SGC demonstrated a relatively uniform structure throughout its height.

The comparison of specimens was conducted using a rigorous and quantitative approach, relying on objectively measurable criteria, such as the variation in the percentage of voids along the height of the specimens. This approach enabled a more precise and reliable assessment of the internal structure of the cement-treated specimens. By analyzing the porosity variations with

height, it was possible to identify significant differences in the compaction quality and homogeneity of the specimens, and to draw meaningful conclusions about the effect of the different compaction methods on the resulting material properties.

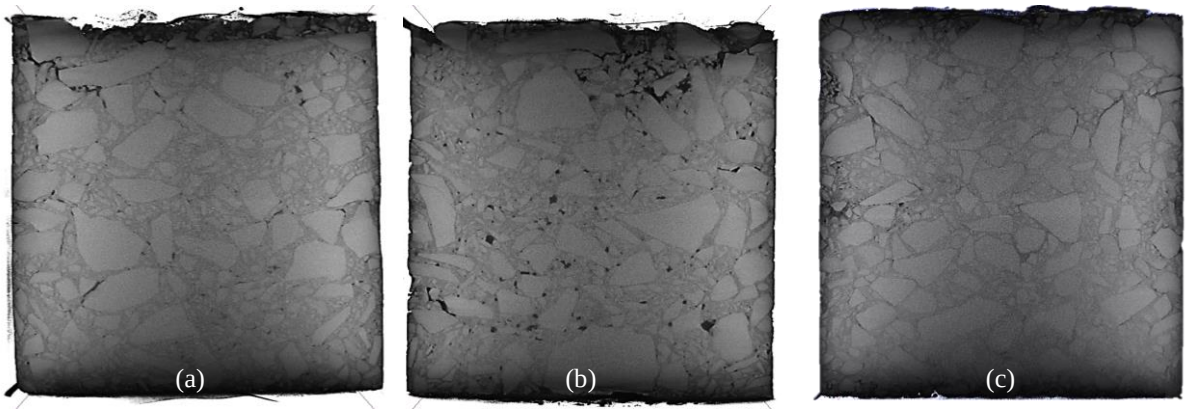

Figure 5.1: X-ray computerized tomographic images of the longitudinal cross-sectional areas throughout the center of cement-treated limestone specimens fabricated using (a) impact, (b) vibratory, and (c) gyratory compaction mechanisms.

In Figure 5.2, the distribution of porosity along the height of the three cementitiously stabilized limestone specimens is depicted, with images of the cross-sectional area of the specimen presented at particular points along its height. The graphs reveal significant porosity variations and porosity gradients along the height of the specimens that were compacted using the impact and vibratory methods. In contrast, the porosity distribution of the specimen compacted with the SGC was relatively uniform, with minimal variations throughout its height. In Figure 5.3, the porosity distributions of central longitudinal sections of the cylindrical specimens are presented at different rotation angles. The graph clearly shows that the specimens compacted with the impact and vibratory methods have significantly higher variations in air void distributions compared to those compacted with the SGC. Moreover, the specimen compacted with the gyratory method exhibited lower porosity variations among the analysis planes of the cementitiously stabilized specimen.

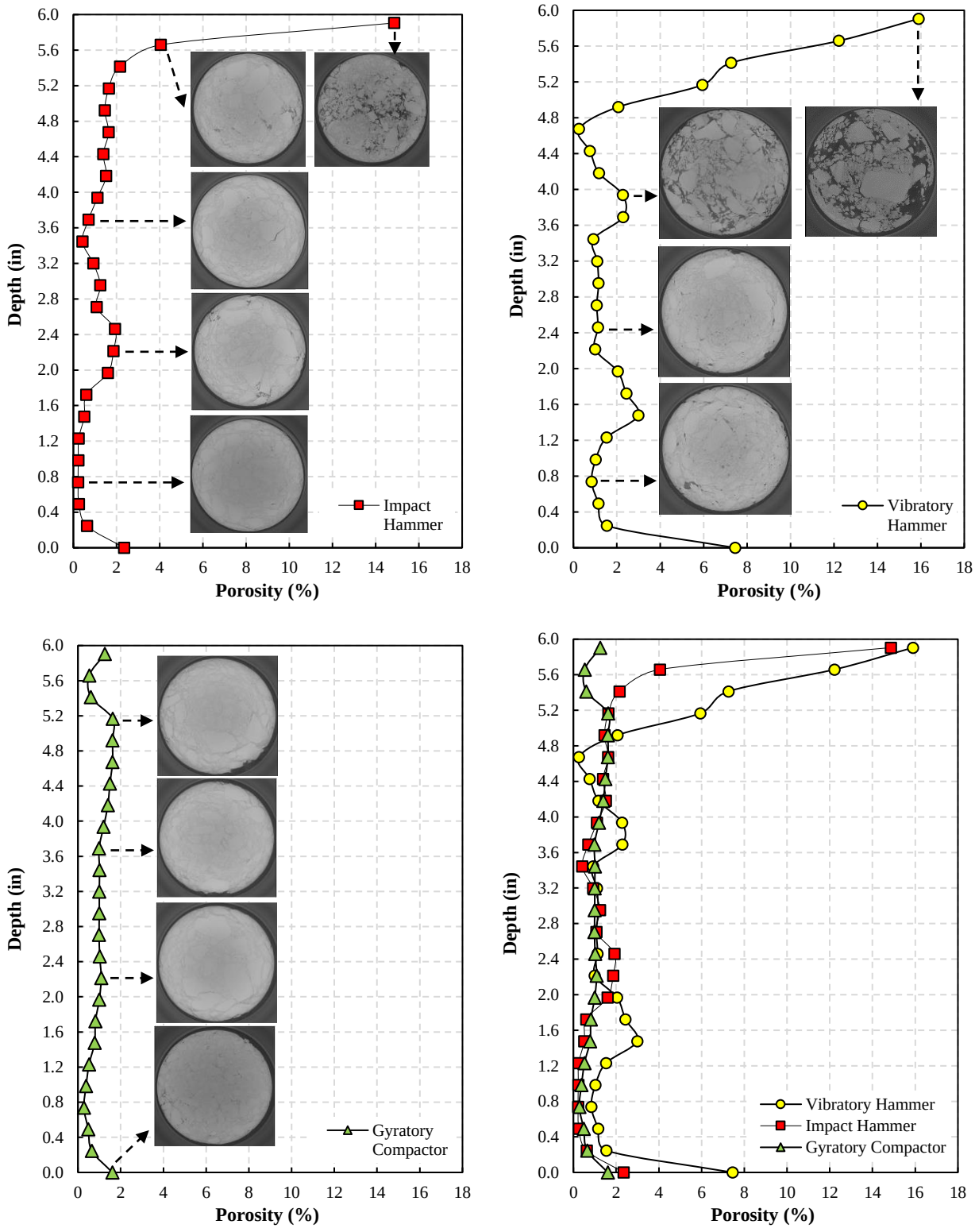

Figure 5.2: Distribution of porosity in cross-sectional views along the height of cementitiously stabilized limestone specimens fabricated using the IH, VH, and SGC.

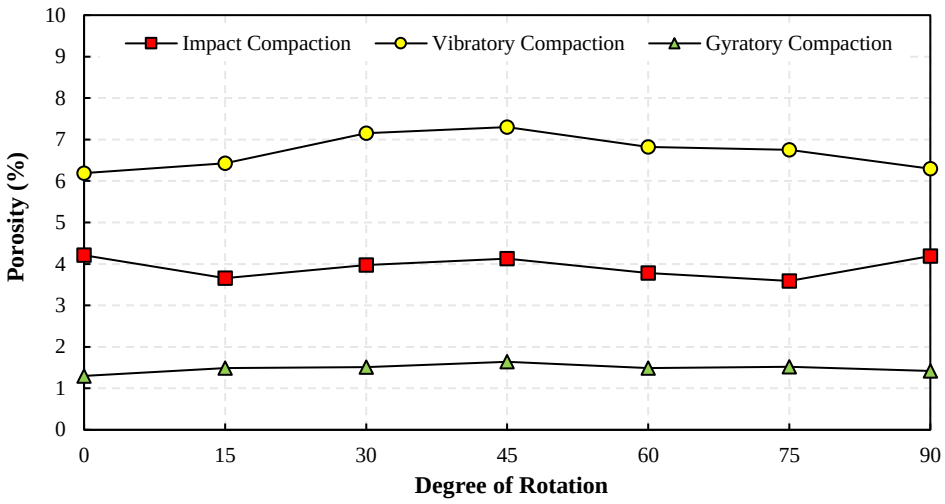

Figure 5.3: Distribution of porosity in various central longitudinal views of cementitiously stabilized limestone specimens fabricated using the IH, VH, and SGC.

Table 5.1 displays the average, minimum, and maximum values, along with the standard deviation, for the computed porosity of cementitiously stabilized limestone specimens prepared by means of impact, vibratory, and gyratory laboratory compaction techniques. The table depicts the divergence in porosity values between cross-sectional planes at various heights of the specimens and between longitudinal planes located at the core of the specimens, which are rotated at different angles.

Table 5.1: Average, minimum, maximum, and standard deviation of the porosity of cementitiously stabilized limestone specimens fabricated using impact, vibratory, and gyratory compaction methods.

Compaction Methods	**Type of Analysis**	**Porosity (%)**			
		Average	**Minimum**	**Maximum**	**Standard Deviation**
IH	Cross-sectional areas	1.79	0.22	14.86	2.86
	Central longitudinal areas	3.93	3.59	4.21	0.62
VH	Cross-sectional areas	3.10	0.26	15.90	3.85
	Central longitudinal areas	6.71	6.19	7.30	1.11
SGC	Cross-sectional areas	1.00	0.28	1.63	0.41
	Central longitudinal areas	1.48	1.30	1.64	0.34

As demonstrated in Table 5.1, the average porosity values of specimens compacted with the VH were the highest, followed by specimens compacted with the IH. In contrast, specimens fabricated with the SGC exhibited both the lowest average porosity values and the lowest variability of porosity values. The comparison of cross-sectional planes revealed that the maximum porosity values of specimens compacted with impact and vibratory hammers were around ten times higher than those of specimens compacted with the SGC. Similarly, the comparison of central longitudinal planes showed that the maximum porosity values of specimens compacted with the impact and vibratory hammers were five and three times higher, respectively, than those of specimens compacted with the SGC. These results provide crucial insights into the superior performance of the gyratory compaction method over the impact and vibratory compaction methods in terms of producing more uniform specimens.

5.2. INFLUENCE OF COMPACTION ON THE STRENGTH PROPERTIES

The mechanical testing developed in this dissertation pertained to determining the compressive and tensile strength properties of cementitiously stabilized aggregate base materials compacted using the IH, VH, and SGC. Gravel, limestone, RCA, and FDR materials were mixed with 2%, 3%, and 4% cement to account for lightly and moderately cement stabilized systems. An additional replicate was prepared for each blend all fabricated at their optimum conditions i.e., OMC and MDD. The laboratory-compacted specimens were placed in a curing chamber for seven days at 23°C, and 95% relative humidity. Subsequent to the curing process, the UCS and IDT strength methods were adopted for mechanical testing of the cement-treated mediums.

For the UCS testing, three sets of specimens were fabricated with a diameter of 6 in and heights of 6 in and 12 in, as well as 4 in diameter by 4 in tall cylinders. For the IDT strength testing, one set of specimens was fabricated with a diameter of 4 in and a height of 4 in. As a final analysis,

the compaction energies imparted by impact, vibratory, and gyratory procedures were computed and compared to the strength results obtained after testing the laboratory-compacted specimens.

The UCS test results of different cementitiously stabilized specimens fabricated using impact and gyratory compaction methods are plotted in Figure 5.4. The strength values of 4 in diameter by 4 in tall specimens fabricated using the IH were compared to the strength values of 6 in diameter by 6 in tall specimens fabricated using the SGC. A noteworthy observation in the plot is the drastic underperformance of cement-treated base materials compacted with the IH. For instance, the UCS of impact-compacted FDR specimens stabilized with 2% cement and the UCS of impact-compacted RCA specimens stabilized with 4% cement improved by more than 100% in both materials when the SGC was used for compaction. This trend of lower UCS values in specimens compacted with the IH was valid for almost all permutations except for the 4% cementitiously stabilized limestone specimens. One reasonable explanation for this behavior is the shrinkage cracking in stiff cement-treated systems that could have lowered the UCS of limestone specimens compacted with the SGC.

Figure 5.4 also presents the estimated values for the compaction energy imparted by means of the IH and the SGC during the fabrication of the cementitiously specimens in the laboratory. The impact compaction energy was computed in terms of the hammer weight, height drop, number of drops, number of layers, and specimen volume (TxDOT 2011), as indicated in Table 5.2. Findings showed that the IH imparted a compaction energy of 22,918 lb-ft/ft^3 to the 4 in diameter by 4 in tall cylindrical specimens. For the case of the SGC, the gyratory compaction energy was calculated based on Equation 5.1, adapted from Li et al. (2015).

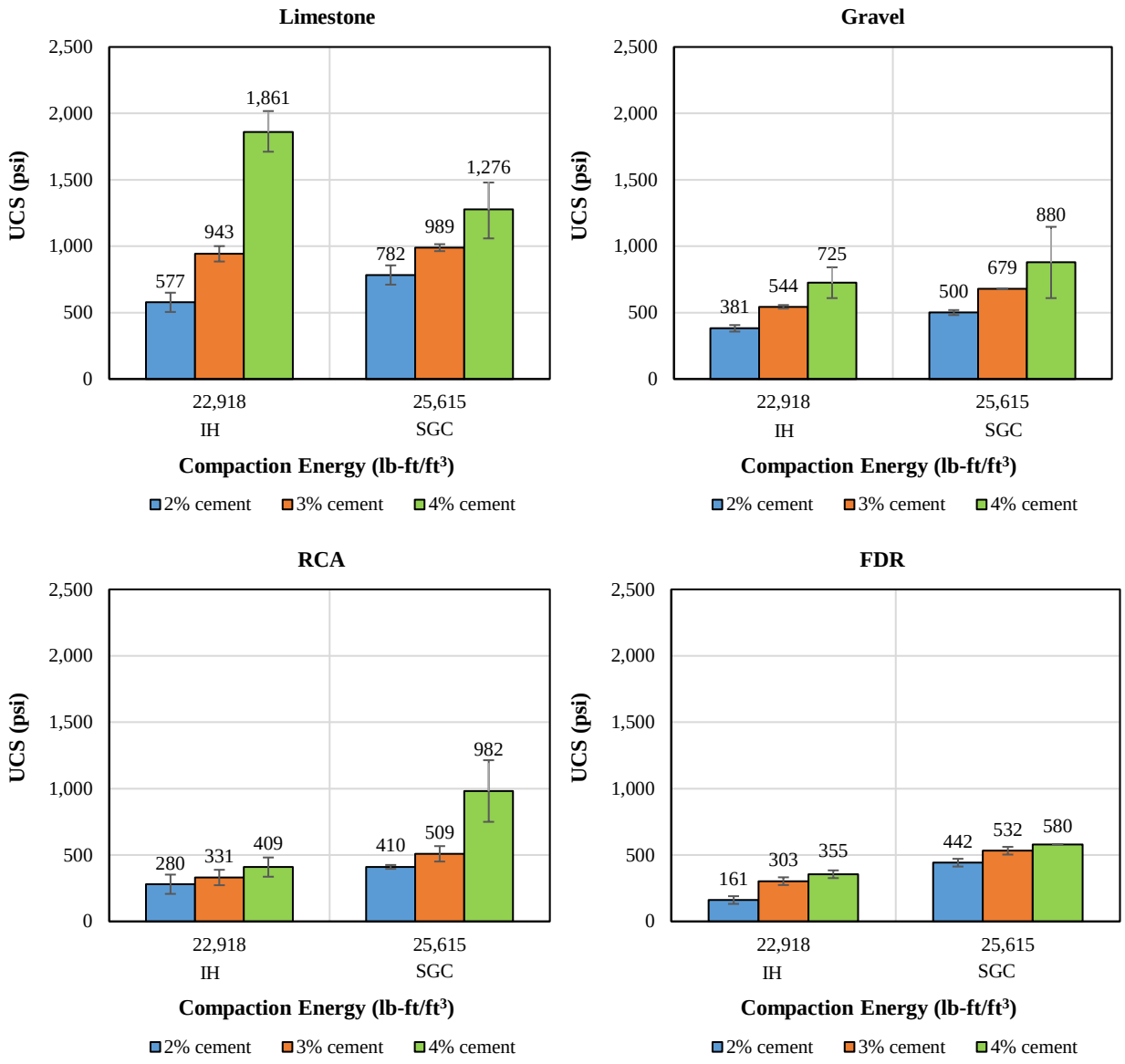

Figure 5.4: UCS values of cementitiously stabilized virgin and reclaimed materials compacted with the application of impact compaction energy and gyratory compaction energy.

Table 5.2: Calculations for the determination of the impact compaction energy and vibratory compaction energy imparted during the fabrication of the cementitiously stabilized cylindrical specimens in the laboratory.

Compaction Methods	**Compaction Energy (CE) lb-ft/ft^3**	**Compaction Energy Equation**	**Parameters and values**
Impact	22,918	$CE = \frac{H_d \cdot W_h \cdot N_d \cdot N_l}{V}$	H_d drop height: 18 in W_h hammer weight: 4.4$^{\Omega}$ lb 10.0$^{\epsilon}$ lb N_d number of drops: 50 N_l number of layers: 2$^{\Omega}$ or 6$^{\epsilon}$ V volume of mold: 48$^{\Omega}$ in^3 323.5$^{\epsilon}$ in^3
Vibratory	130,818	$CE = \frac{W \cdot e \cdot f_s \cdot t \cdot N_l}{V}$	W electrical input: 1.48 hp e equipment efficiency: 0.5 f_s percent of energy imparted into the soil: 0.5 t vibration time per layer: 9$^{\Omega}$ sec 20$^{\epsilon}$ sec N_l number of layers: 2$^{\Omega}$ or 6$^{\epsilon}$ V volume of mold: 48$^{\Omega}$ in^3 323.5$^{\epsilon}$ in^3

$^{\Omega}$*Values adopted for the compaction of 4 in diameter by 4 in tall cylindrical specimens.*
$^{\epsilon}$*Values adopted for the compaction of 6 in diameter by 12 in tall cylindrical specimens.*

In Equation 5.1, the work generated by both the vertical compaction pressure as well as the shear force is taken into consideration for the calculation of the compaction energy (Ping et al. 2003, Li et al. 2015). The gyratory compaction energy imparted to the 6 in diameter by 6 in tall specimens was 25,615 lb-ft/ft^3 on average. According to the results indicated in Figure 5.4, it is important to note that except for limestone material stabilized with 4% cement, all the rest of the materials that were fabricated with the application of higher compaction energy (i.e., using the SGC) resulted in specimens with higher UCS values.

$$CE_{gyratory} = \frac{pA(H_0 - H_{120})}{V_{120}} + \frac{4\theta \sum_{j=1}^{120} R_j e_j}{V_{120}} \quad (5.1)$$

Where:

$CE_{gyratory}$: compaction energy imparted by the SGC (lb-ft/ft^3)

p: compaction pressure of 87 (psi)

A: cross-sectional area of the specimen (in^2)

H_0: initial height of the specimen previous to the first gyration (in)

H_{120}: final height of the specimen after the 120th gyration (in)

θ: angle of gyration (radians)

R_j: resultant load for each gyration j (lb)

e_j: eccentricity of the resultant load for each gyration j (in)

V_{120}: volume of the specimen after the 120th gyration (in^3)

As a continuation of the analysis, the differences between the UCS results of impact-compacted specimens and vibratory-compacted specimens were evaluated. The strength values of 6 in diameter by 12 in tall specimens fabricated using the IH were compared to the strength values of specimens of the same size but fabricated using the VH. As observed in Figure 5.5, it is not possible to establish a clear tendency to state the superiority of impact compaction over vibratory compaction (or vice versa) in terms of the UCS values. All the studied permutations showed comparable UCS results for impact-compacted and vibratory-compacted specimens with differences that could be considered acceptable according to the margin of error of the test.

Figure 5.5 also presents the estimated values for the compaction energy imparted by means of the IH and the VH during the fabrication of cement-treated specimens in the laboratory. The vibratory compaction energy was calculated in terms of the electrical input, equipment efficiency, vibration time, number of layers, and specimen volume (Arcement and Wright 2001), as indicated in Table 5.2. Results showed that the VH imparted a compaction energy of 130,818 lb-ft/ft^3 to the

6 in diameter by 12 in tall specimens. For the case of the IH, the compaction energy imparted to the 6 in diameter by 12 in tall specimens was 22,918 lb-ft/ft^3. It is evident from the compaction energy estimations and UCS test results that despite the fact that the energy generated by the VH was 5.7 times higher than the IH, the UCS values of the majority of vibratory-compacted specimens were lower than the strength results obtained in specimens compacted with less energy (i.e., specimens compacted with the IH).

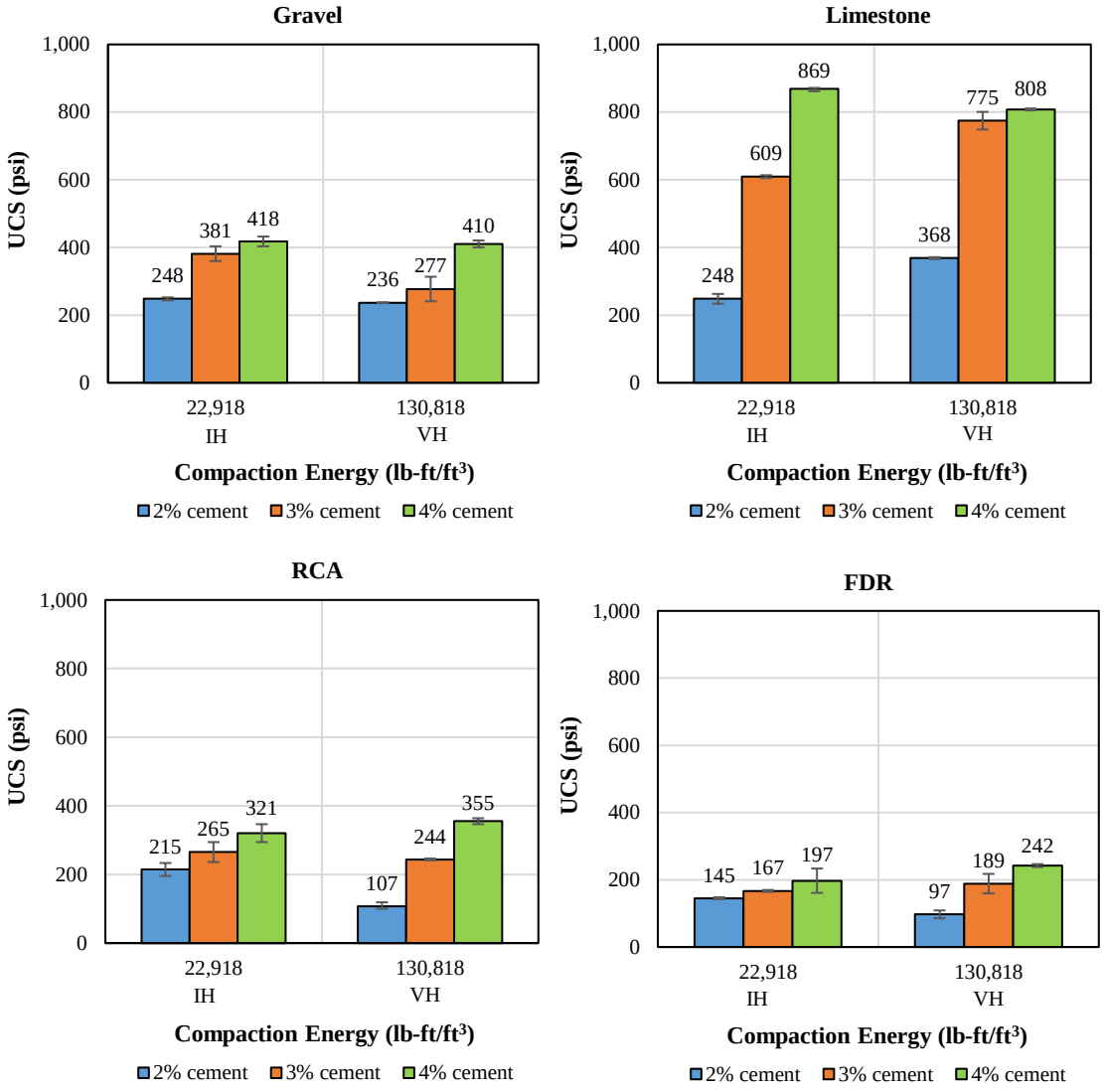

Figure 5.5: UCS values of cementitiously stabilized virgin and reclaimed materials compacted with the application of impact compaction energy and vibratory compaction energy.

Strain-controlled IDT strength tests were conducted on cementitiously stabilized specimens fabricated using impact, vibratory, and gyratory compaction methods. The experimental IDT strength results are graphically summarized in Figure 5.6. All impact-compacted specimens exhibited the lowest tensile strength values in comparison to specimens compacted with the VH and SGC. For instance, the tensile strength of RCA specimens stabilized with 2% cement and compacted with the IH was 36 psi. Under the same cement content, cement-treated specimens fabricated with the SGC and the VH resulted in approximately 138% and 83% improvement in their IDT strength values, respectively.

Figure 5.6 also shows the estimated values for the compaction energy imparted by means of the IH, VH, and SGC during the fabrication of 4 in diameter by 4 in tall cement-treated specimens in the laboratory. The energies imparted to impact-compacted, gyratory-compacted, and vibratory-compacted specimens were 22,918 lb-f/ft^3, 86,453 lb-f/ft^3, and 130,818 lb-f/ft^3, respectively. It is evident from the test results that specimens constituted by gravel stabilized with 2%, 3%, and 4% cement, limestone stabilized with 2% cement, as well as RCA stabilized with 3% cement experienced an increase in the IDT strength due to an increase in the compaction energy. In other words, the tensile strength values that corresponded to specimens compacted with the VH were higher than that of specimens compacted with the SGC and the IH.

For the remaining permutations (86% of the total permutations) and cement contents, an increase in compaction energy does not necessarily correlate with higher IDT strength values. The maximum IDT strength results corresponded to specimens compacted with the SGC. Compaction efforts higher than the energy imparted by the SGC (i.e., compaction energy imparted by the VH) resulted in specimens with lower tensile strengths. The data obtained from the IDT strength testing, highlight the influence of compaction mechanisms on the tensile strength properties of virgin and

reclaimed aggregate base materials in the laboratory. It is important to underscore the fact that modifications in the compaction procedures will naturally lead to differences in the pore-structure distribution, particle size gradation, and orthogonal strength properties of the mixtures.

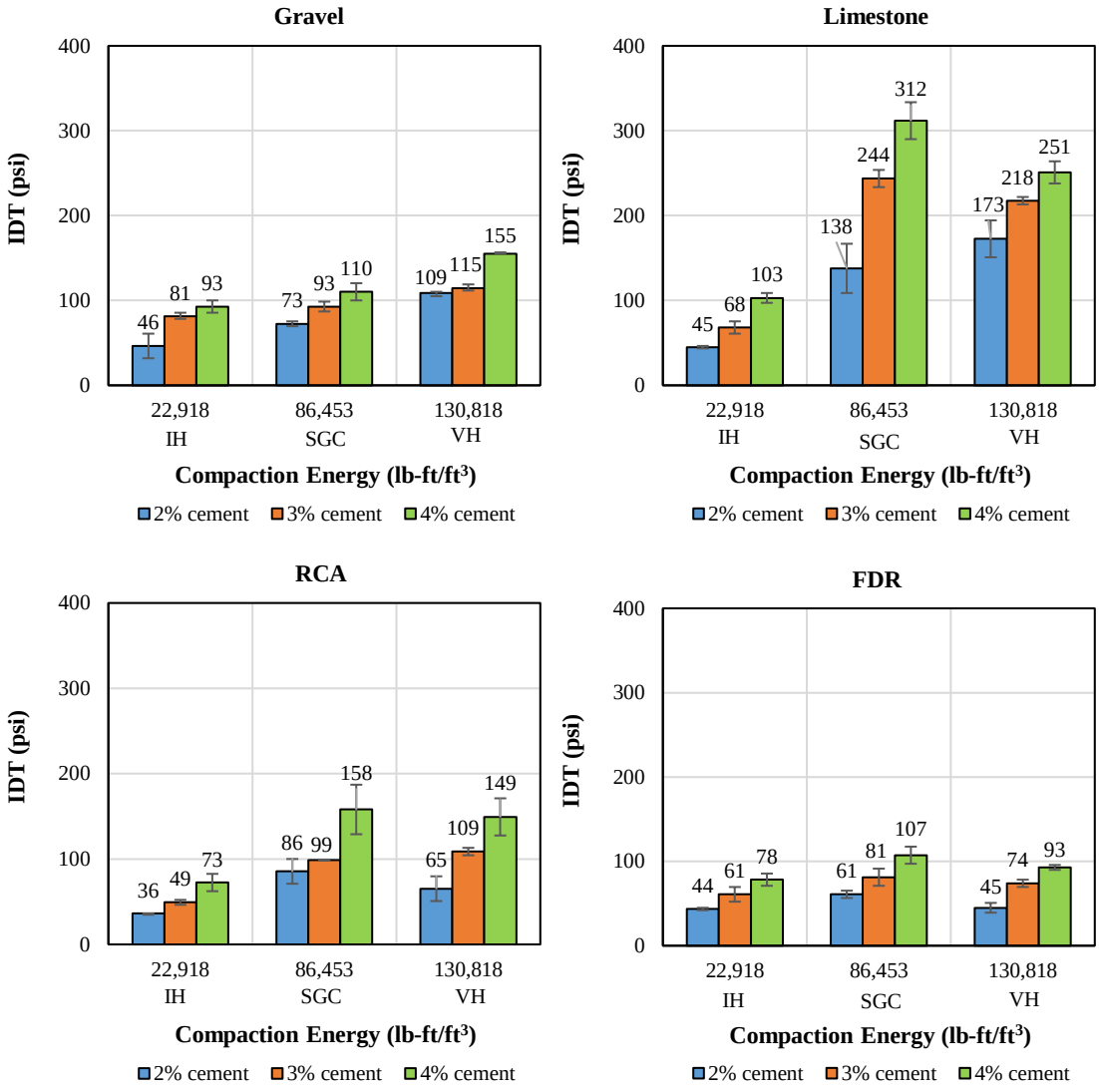

Figure 5.6: IDT strength values of cementitiously stabilized virgin and reclaimed materials compacted with the application of impact compaction energy and vibratory compaction energy.

Chapter 6: The Bull Run Inverted Pavement Road Test: Deflection Analysis and Deformation Characterization from Field Testing Responses

In 2010, a full-scale testing site consisting of a two-lane road segment of an inverted pavement structure followed by a two-lane conventional pavement section was constructed along Route 659 in Chantilly, Virginia. The project involved the participation of Luck Stone, Texas A&M University, FHWA's Office of Infrastructure Research and Development, the Virginia Department of Transportation (VDOT), and the Virginia Transportation Research Council. The specific pavement section in question was designed using the International Center for Aggregates Research (ICAR) model, and the material characterization was carried out by Texas A&M University and the Texas Transportation Institute.

The road lengths of inverted and conventional pavement sections were approximately 500 ft and 400 ft, respectively. The complete road test was located on a continuous section with no cuts and a straight alignment. Figure 6.1 illustrates the approximate starting and ending points of the inverted and conventional pavements highlighting the latitude and longitude of each point using a Mercator projection based on the World Geodetic System (WGS) 1984 geographic coordinate system (datum).

Figure. 6.1: Location of inverted and conventional pavement sections at Bull Run Route 659.

The inverted pavement structure consisted of a 5-in asphalt concrete (AC) layer, a 6-in 21-A type unbound aggregate base (UAB) layer, and a 10-in 21-B type cement-treated base (CTB) layer placed on top of a sandy fill subgrade soil. The conventional pavement structure consisted of a 1.5-in SM-9.5D type surface mix (SM), a 2-in IM-19.0A type intermediate mix (IM), a 7-in BM-25.0 type base mix (BM), a 3-in open-graded drainage layer (OGDL), and an 8-in 21-B type CTB placed on top of the same sandy fill material. The properties of the different types of pavement layers are described in standard specifications published by the Virginia Department of Transportation (VDOT 2022). Figure 6.2 shows the layer configuration of the inverted and conventional pavement structures constructed at Bull Run Route 659.

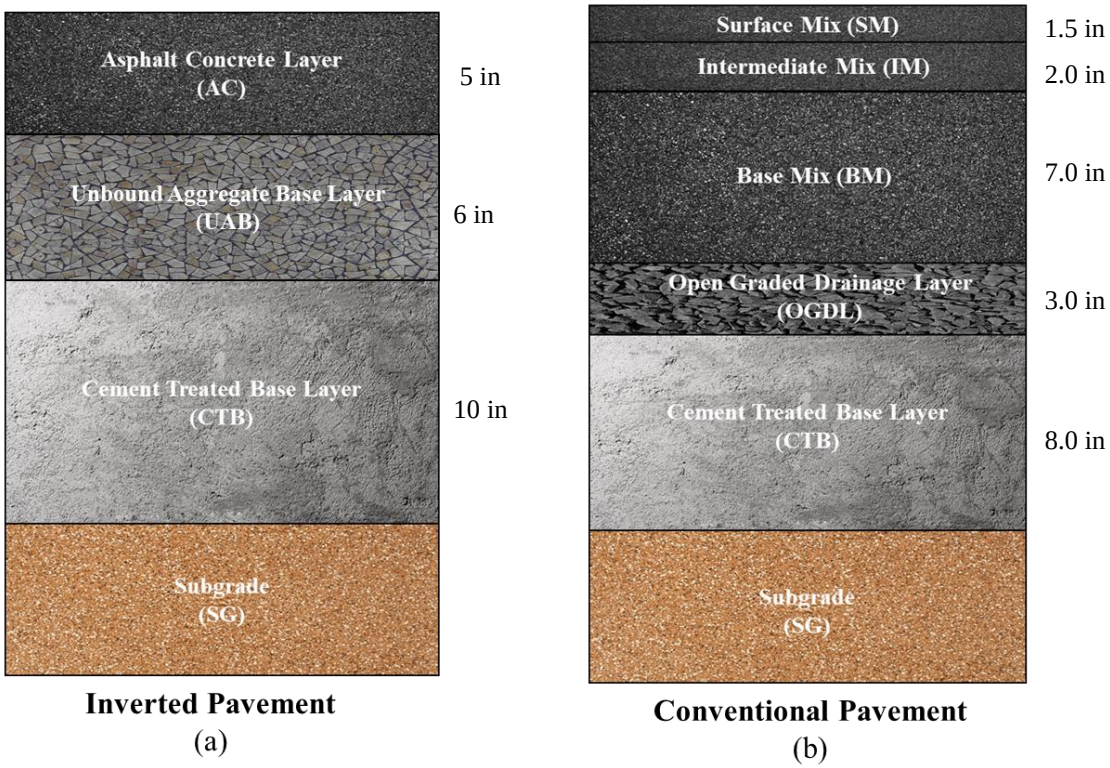

Figure 6.2: Layer configuration of the inverted pavement structure (a) and the conventional pavement structure (b) constructed at Bull Run Route 659.

The mechanical properties of the inverted and conventional pavement structures from Bull Run Route 659 were evaluated through DCP and FWD tests. After the construction of the UAB layer of the inverted pavement structure, DCP testing was conducted in four stations of the road segment, named Station 54, Station 55, Station 56, and Station 57, with two DCP test points selected at each station, one at the Northbound lane and another at the Southbound lane. The distance between consecutive stations was 100 ft. The DCP test was conducted manually by penetrating a hardened 60° cone into the UAB layer using a 17.6-lb hammer dropped from a height of 22.6 in. At the Southbound and Northbound lanes of Station 54 and the Northbound lane of Station 55, the total cumulative penetration with the DCP reached depths located at 0.748 in, 0.984 in, and 0.374 in above the UAB-CTB interface, respectively, while at the remaining five DCP testing points, the total cumulative penetration depth was equal to or greater than 6 in, which corresponded to the entire thickness of the UAB layer. Figure 6.3 shows a similar manually operated DCP testing device used in the field for data collection.

Following the construction of the most superficial asphalt concrete layer, a non-destructive structural evaluation of the inverted and conventional layered systems was performed based on pavement deflection data measured using the FWD. The evaluation was based on vertical deformations recorded by nine geophones positioned at lateral offset values of 0, 8, 12, 18, 24, 36, 48, 60, and 72 in from the center of the 11.81-in diameter load plate. In the case of the inverted pavement, a total of 20 stations were evaluated, covering a road segment length of 38 ft. For each station, a single drop of approximately 82 psi was applied during FWD testing. In the case of the conventional pavement, a total of 24 stations were evaluated, covering a road segment length of 290 ft. For each station, two drops of approximately 77 psi were applied during FWD testing. The equipment employed in the field during in-situ testing is displayed in Figure 6.3.

Figure 6.3: Falling Weight Deflectometer (a) and Dynamic Cone Penetrometer (b) used for in-site evaluation of the pavement structures at Bull Run Route 659.

Besides conducting DCP and FWD tests, 30 and 22 sensors were respectively installed into the inverted and traditional road sections, spanning 50 ft, at particular depths within the pavement structure. The inverted and conventional sections were embedded with various sensing instruments such as pressure cells (PC), linear variable differential transformers (LVDT), thermocouples (TC), strain gauges (SG), and moisture sensors (TDR). Figures 6.4 and 6.5 display the plan and side views of the complete set of instruments installed in the inverted and conventional pavement sections. As illustrated in the figures, the installed sensing devices, including SGs, PCs, and LVDTs, were aligned in the outer wheel path (OWP) to avoid direct contact with the paver.

In this dissertation, a subset of sensors that were installed in the Virginia inverted pavement section was studied to refine the simulated FE model created based on the layers configuration and material properties of the inverted pavement structure. The following lines will offer a concise summary of the sensors covered in this dissertation, focusing solely on the relevant instruments whose measurements were utilized in the study for model validation.

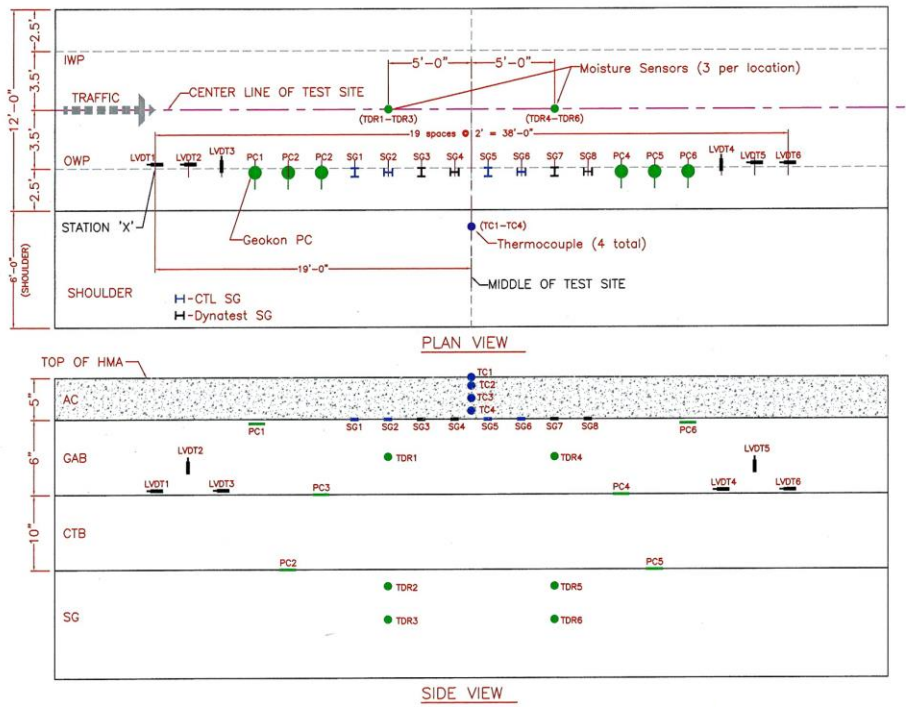

Figure 6.4: Plan and side views of sensors installed in the Virginia inverted pavement structure.

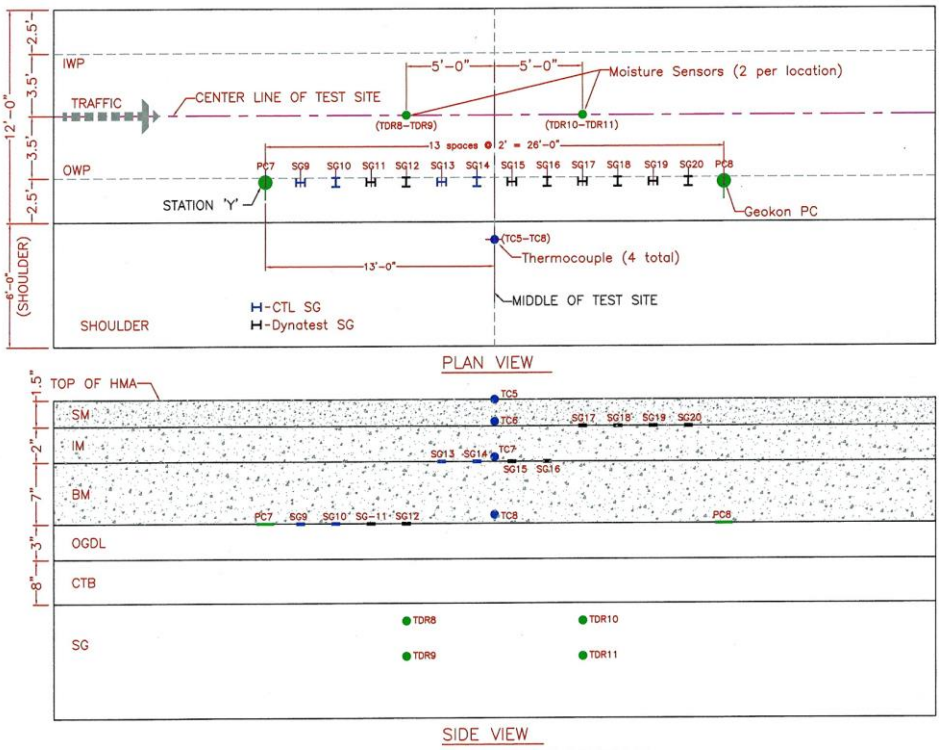

Figure 6.5: Plan and side views of sensors installed in the Virginia conventional pavement structure.

The asphalt strain gauges used in the study were installed in the inverted pavement section, with placement at the bottom of the 5-in asphalt concrete layer. Specifically, the gauges were H-bar-type sensors that measured the pavement strain response on the pavement structure. The performance of the strain gauges at the testing site was very good regarding survivability, reliability, and repeatability, with two brands of SGs utilized: Dynatest and CTL. To ensure proper installation, a thin layer of CSS1-type asphalt primer was applied to the compacted and leveled UAB layer at each location. A mastic mix consisting of type CSS1 bitumen and aggregate passing the No. 10 sieve in a 1:2 ratio was then prepared and applied in an approximately 6 in^2 area to each gauge location after the primer had cured. The gauge was then placed into the mastic mix by gently pressing the gate and anchors until the SG came into full contact with the mix. To ensure accurate measurement at the level of interest, the gauge was placed so that the strain gauge bar was at the interface between the AC and UAB layers. The strain gauges had two possible orientations: one with the leads parallel to the direction of traffic and the other with the leads perpendicular to the direction of traffic. A trench of approximately 4 in depth and 2 in wide was excavated from each SG to a nearby common trench leading to the shoulder edge, and the gauge lead wires were placed in the excavation. Prior to paving, a protective layer of hot mix asphalt was placed over and around the gauges, which was compacted using a steel plate. The first lift of asphalt concrete was then compacted in the direction of the lead wires extending from the gauge, striving for accurate measurements of pavement strain response in the inverted pavement section. Figure 6.6 shows the two consecutive SGs being installed at the top of the UAB layer of the inverted pavement section.

To accurately measure the vertical stresses within the Virginia inverted pavement section, earth pressure cells of the Geokon brand were strategically installed at critical levels. The PCs, with a diameter of 9 in, were placed at the top and bottom of the UAB layer, as well as at the top

of the subgrade (SG) soil. To install the cells at the interface between the UAB-CTB layers and CTB layer-SG soil, a small shovel was used to excavate a shallow, circular hole at the proposed location, followed by a trench of approximately 3 in wide and 15 in long for the transducer housing. The bottom of the hole was cleared of any particles larger than ¼ in diameter, and a smooth surface was prepared by tamping the soil with an 8-in^2 steel plate temper. A thin layer of sand was then placed at the bottom of the hole and compacted with the temper. The cell was placed on top of the sand layer, ensuring good contact between the cell face and the sandy material. The orientation of the fluid tube transducer housing was kept parallel to the wheel pass, and the cell was appropriately leveled before placing sand over it and compacting it by hand. Finally, a trench of approximately 4.5 in-depth was excavated from each SG to the nearby common trench leading to the shoulder edge. For the case of pressure cells installed at the interface between the AC-UAB layers, the same bituminous materials and compaction method used for the installation of the SGs were applied to accommodate the PCs. Figure 6.7 depicts the installation process of two pressure cells at the interface between the CTB layer-SG soil and AC-UAB layers, one at each level.

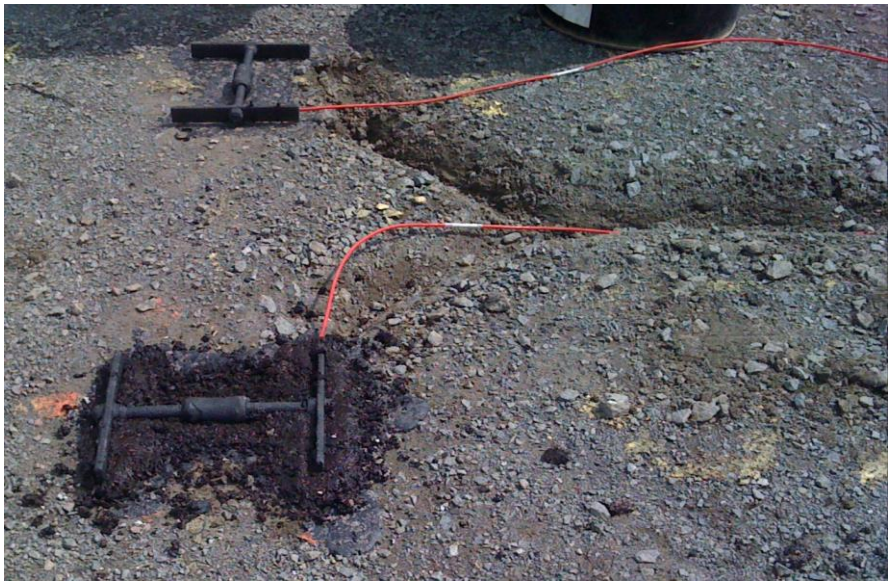

Figure 6.6: H-bar-type strain gauges being placed in the Virginia inverted pavement structure.

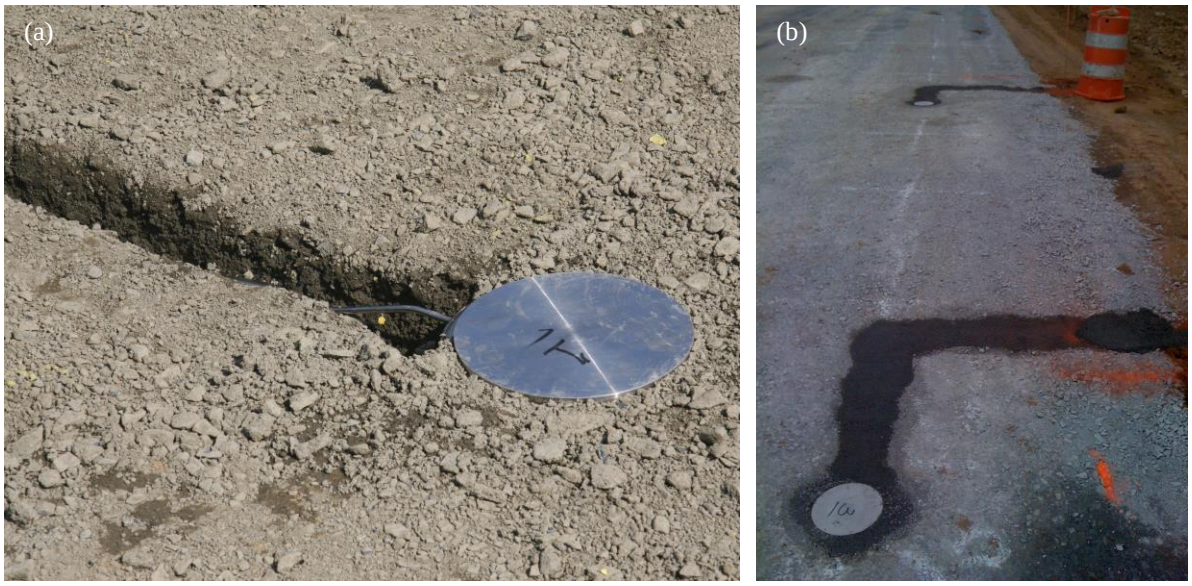

Figure 6.7: Pressure cell installed at the interface between the CTB layer-SG soil (a) and AC-UAB layers (b) in the Virginia inverted pavement structure.

In the Virginia inverted pavement structure, a total of 6 LVDTs were tactically installed to measure deformation at the bottom of the UAB layer. Two sets of LVDTs were placed in three different directions: transverse, longitudinal, and vertical. The placement of the sensors was at both the entry and exit points of the testing pavement segment. Vertical LVDTs were installed by first excavating a trench into the UAB layer and the foundation surface. The moving part of the LVDT was positioned upward and held in place with a conduit. The trench was filled with base layer materials and compacted using a temper. Longitudinal LVDTs were installed with the aluminum disk perpendicular to the outer wheel path line, while transverse LVDTs were installed with the aluminum disk parallel to the outer wheel path line. The LVDT wires were placed in trenches, protected with geotextile and a fine layer of sand, and then backfilled with the same base materials. During the compaction process, the LVDTs were continuously checked with a data acquisition system. Figure 6.8 displays images of the LVDT devices being installed within the UAB layer of the Virginia inverted pavement section.

Figure 6.8: Longitudinal, transversal, and vertical LVDTs installed at the bottom of the UAB layer next to a pressure cell at the Virginia inverted pavement section.

6.1. DCP TESTING RESULTS AND ANALYSIS

Figure 6.9(a) presents the results of the DCP test executed at the top of the UAB layer of the inverted pavement structure at both northbound and southbound lanes per station. The DCP data was collected in terms of the cumulative penetration registered at an increasing number of blow applications. The values of cumulative penetration per station, averaging the dataset of the two lanes, are displayed in Figure 6.9(b). It is evident from the graphs that Stations 55, 56, and 57 exhibited very similar behavior regarding the progression of cumulative penetration with blow counts. By contrast, the variation of cumulative penetration in Station 54 showed a different path characterized by lower penetration values under the same range of the number of blows applied in the other stations. The UAB layer in Station 54 provided better resistance to penetration as compared to the rest of the stations evaluated during DCP testing.

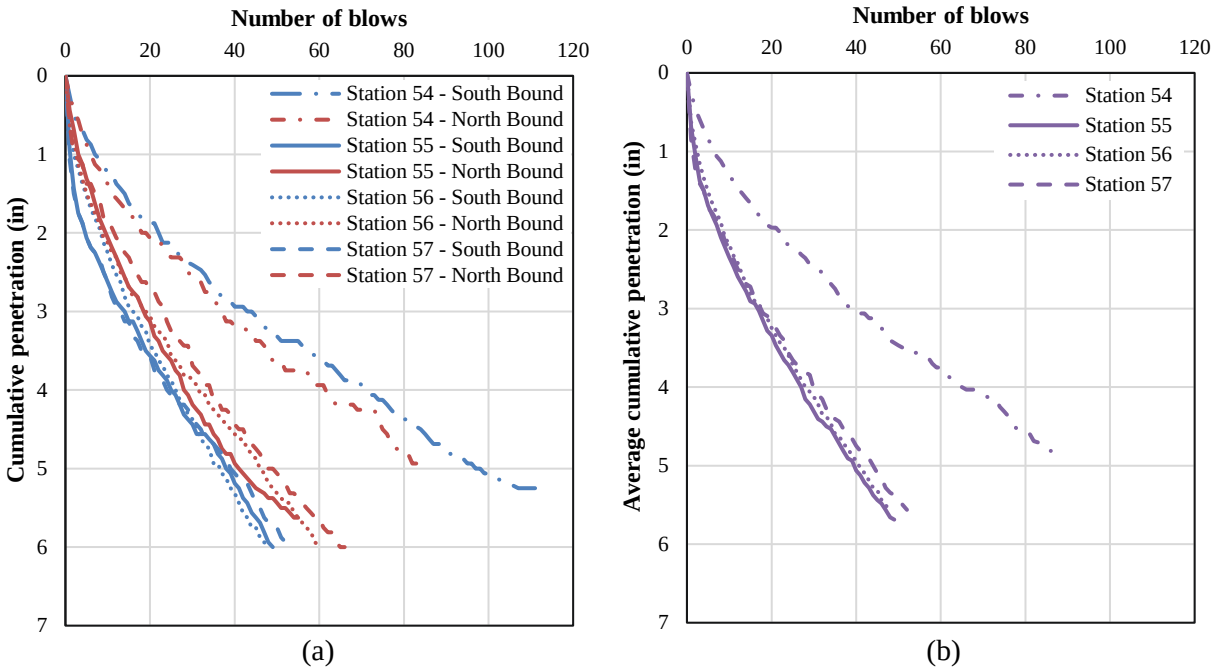

Figure 6.9: Progression of the cumulative penetration with increasing blow applications per type of lane (a) and per station (b) within the UAB layer at the Virginia inverted pavement section.

The relationship between the increasing depth of penetration and the number of applied blows was represented by the graphs shown in Figure 6.10 and Figure 6.11 corresponding to the Northbound and Southbound lanes, respectively, for each of the four evaluated stations. Taking into account the progression of penetration with increasing blow counts, the UAB layer at each testing point was subdivided into top, middle, and bottom layers for a better interpretation of the data. The delimitation of each sublayer was based on the rate of change of the depth of penetration with respect to the number of blow applications. Within each portion of the UAB layer, the ratio of penetration to the number of blows was similar. The best-fit straight lines of the data points from each part of the UAB layer were plotted, and the trendline equations were determined in each lane per station. In the Southbound lanes of Station 55 and Station 56, upper portions of the CTB layer were also considered in the analysis.

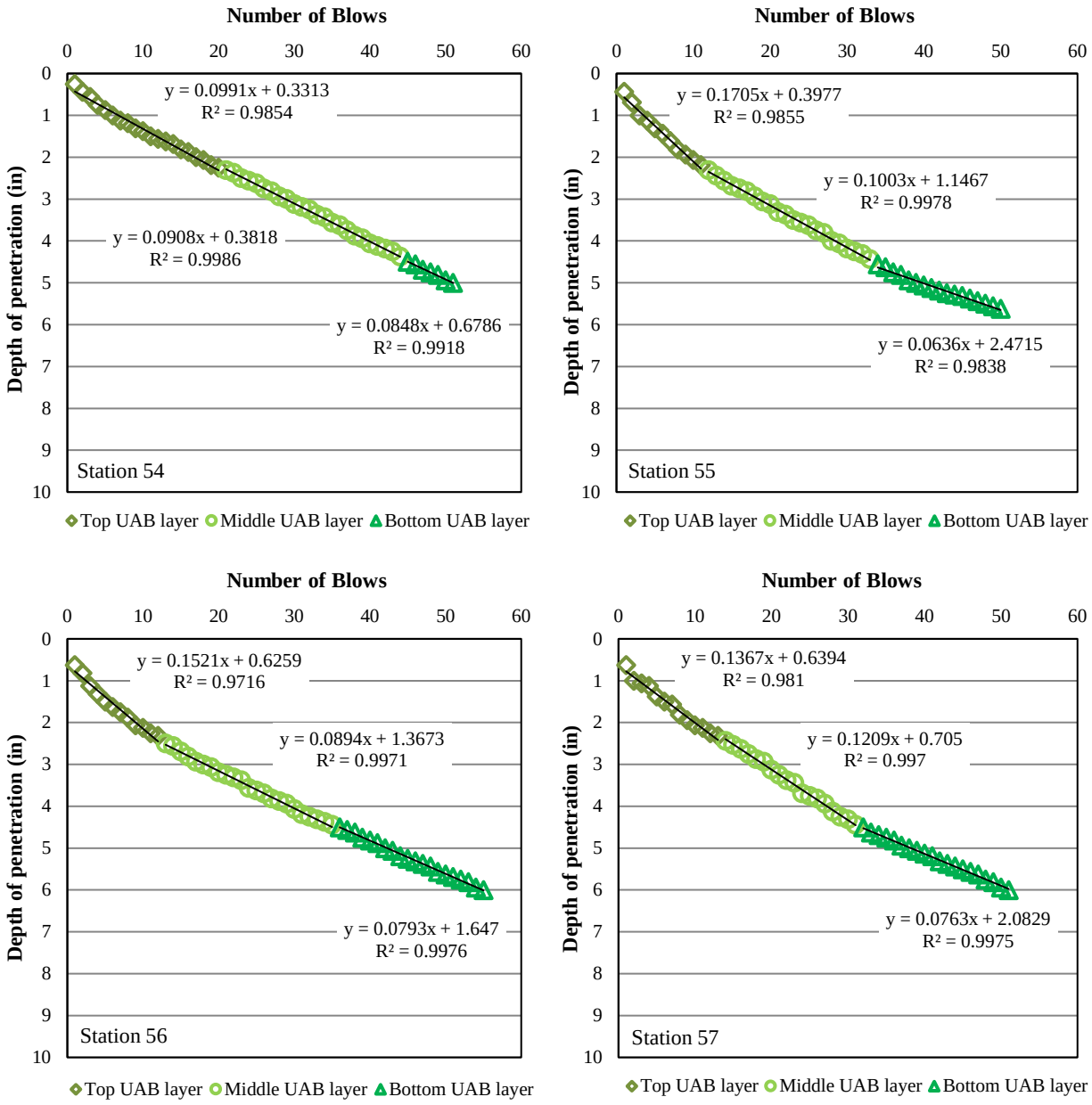

Figure 6.10: Variation of the penetration depth with increments in the number of blows at the top, middle, and bottom portions of the UAB layer during DCP testing at Northbound lanes.

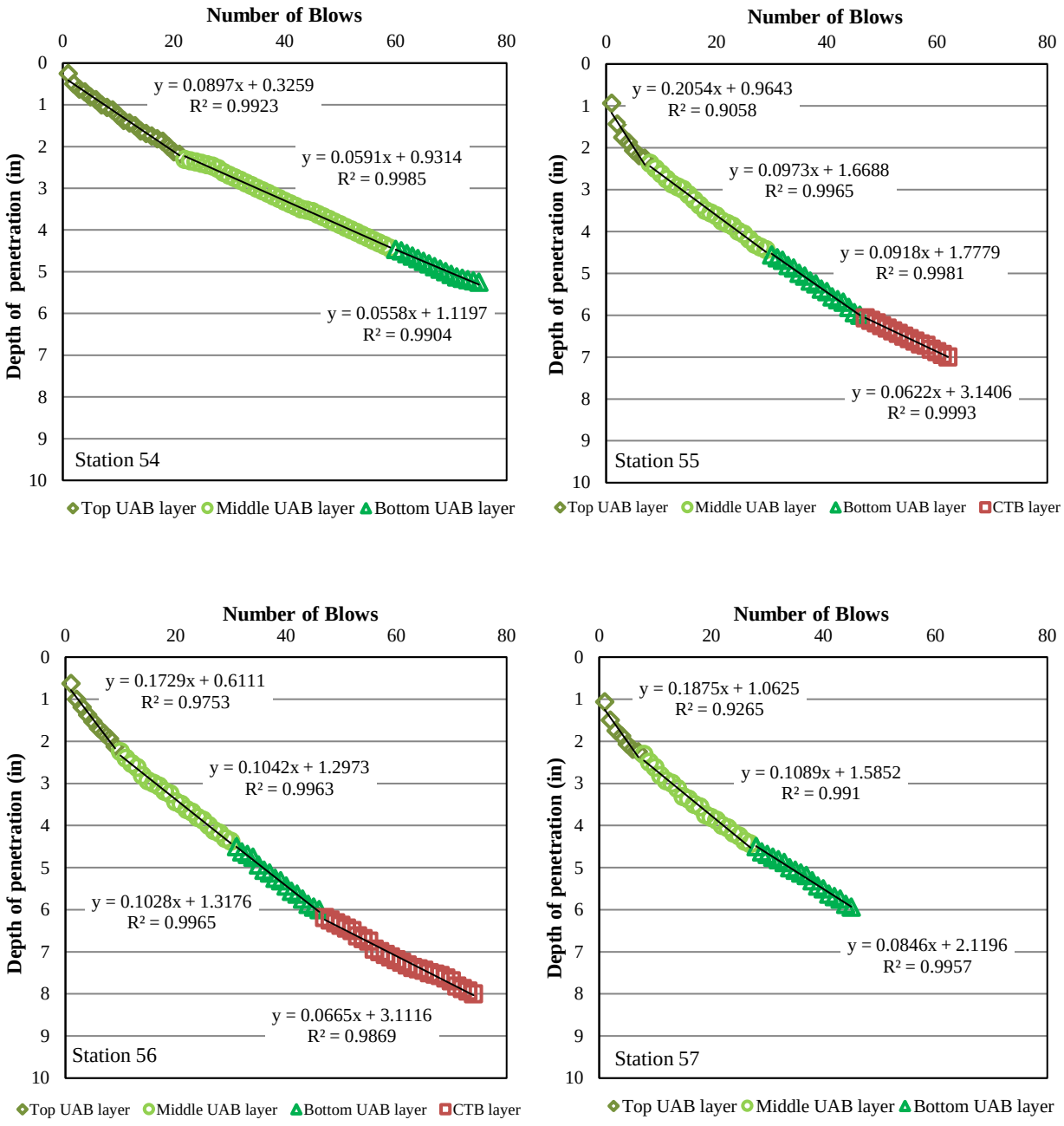

Figure 6.11: Variation of the penetration depth with increments in the number of blows at the top, middle, and bottom portions of the UAB layer during DCP testing at Southbound lanes.

The slopes of the equations of each trendline shown in Figures 6.10 and 6.11 represent the penetration rate in in/blows of the cone throughout the top, middle, and bottom parts of the UAB layer. Lower rates of penetration could be attributed to a granular medium with improved interparticle friction and interlocking effect as compared to a system with higher rates of penetration. As observed in the figures, the penetration rates obtained at deeper levels in the UAB layer tend to decrease, which could signify an enhancement in the orthogonal load-bearing capacity of the mediums at lower depths. In the Southbound lanes of Station 55 and Station 56, decrements in the penetration rate between the bottom of the UAB layer and the underlying CTB layer resulted from improvements in the mechanical properties of the medium when passing from an unbound layer to a highly rigid cementitiously stabilized system.

To visualize the decrease in the cone advance within the UAB layer during DCP testing, penetration rates at the top, middle, and bottom parts of the untreated base were schematically represented in Figure 6.12. The data indicate that in all points of analysis, the penetration rates tend to decline with depth from the surface of the UAB layer down to lower levels closer to the CTB layer. It can be inferred from these results that the cementitiously stabilized layer constitutes a robust platform that contributes to the overlying unbound base layer to achieve better compaction levels, improve the packing of the solid grains, and mitigate deformation.

A critical material property that can be correlated based on the penetration rate of the cone during DCP testing in granular systems is the stiffness of the medium. Chen et al. (2005) proposed an equation to estimate Young's Modulus of a base layer in terms of the penetration rate of the DCP. The inverse relationship between the stiffness of the base layer and the penetration rate during DCP testing is described in Equation 6.1 and has been adapted from the formulation proposed by the same previously mentioned author.

$$E = 9.0962 \cdot (PenRate)^{-0.6645} \quad (6.1)$$

Where:

E: Modulus (ksi)

PenRate: penetration rate (in/blow)

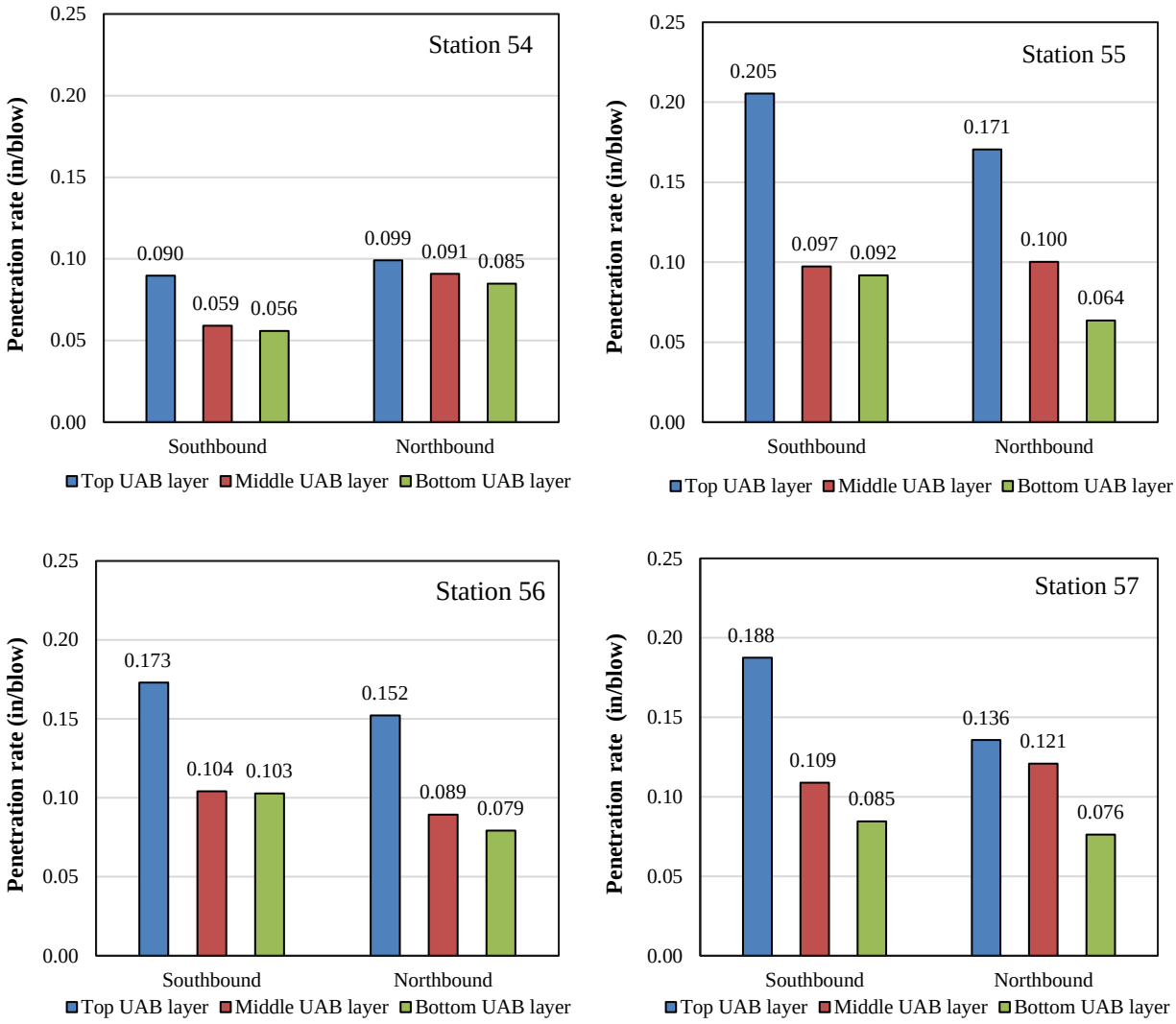

Figure 6.12: Variation of penetration rates at the top, middle, and bottom sublayers of the UAB layer at the Southbound and Northbound lanes.

According to the mathematical formulation indicated in Equation 6.1, the average rigidity values at the top, middle, and bottom parts of the UAB layer were calculated per lane for all four inverted pavement sections. Figure 6.13 illustrates the average Moduli of the UAB sublayers and their corresponding average penetration rates used to estimate the rigidity values. The bar charts reveal the opposite tendencies between the change in penetration rates and the change in stiffnesses at profound levels of the UAB layer. The stiffness at the bottom of the UAB layer is higher compared to the middle and top parts due to the proximity to the robust cement stabilized layer. The closer the untreated aggregate material is to the CTB layer, the lower the penetration rate and higher the Modulus values.

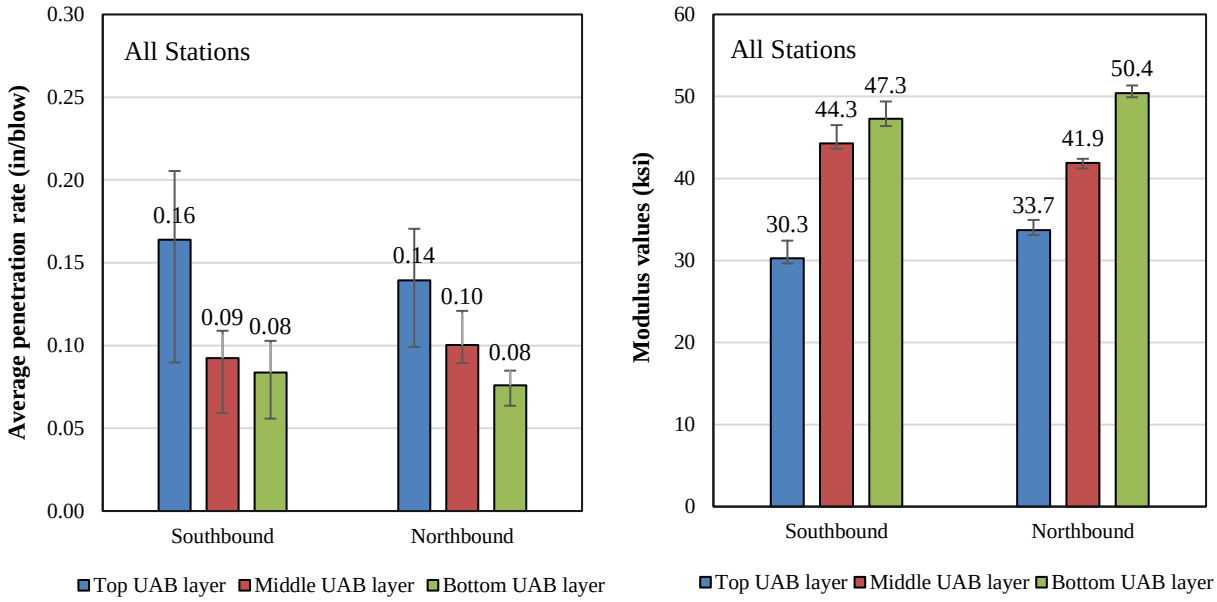

(a) (b)

Figure 6.13: Variation of the average penetration rates (a) and average Moduli (b) at the top, middle, and bottom sublayers of the UAB layer at Southbound and Northbound lanes.

The penetration depths of the DCP at the lower end of the top, middle, and bottom UAB layers were different from one testing point to another, even within the same station. This variability was due to changes in the penetration rate at slightly different depths, which was the criterion for the delimitation of the sublayers. The noncumulative penetration depths at each portion of the UAB layer are graphically summarized in Figure 6.14 for the testing points in which the total depth of analysis covered the entire thickness of the UAB layer. At each point, all three penetration depths were equal to 6 in. Figure 6.14 also includes the percentages with respect to the total final penetration depth within the UAB layer achieved at each sublayer. Both graphs underscore the influence of the proximity to the CTB layer on the penetration into the UAB layer, evidenced by the lowest depths of penetration developed at the bottom sublayer overlying the stabilized medium. An average of 25% of the total penetration into the UAB layer took place at the bottom sublayer. The remaining 75% of the total penetration into the untreated base layer took place at the top and middle portions of the UAB layer. It is evident from these results that the CTB layer constitutes a robust medium that mitigates the penetration of the DCP into the portion of the UAB layer closer to the stabilized system. Further analysis of in situ testing results using the FWD was performed in this dissertation to study the uniformity of compaction of the UAB layer and the deflection responses of the inverted pavement structure under external load applications.

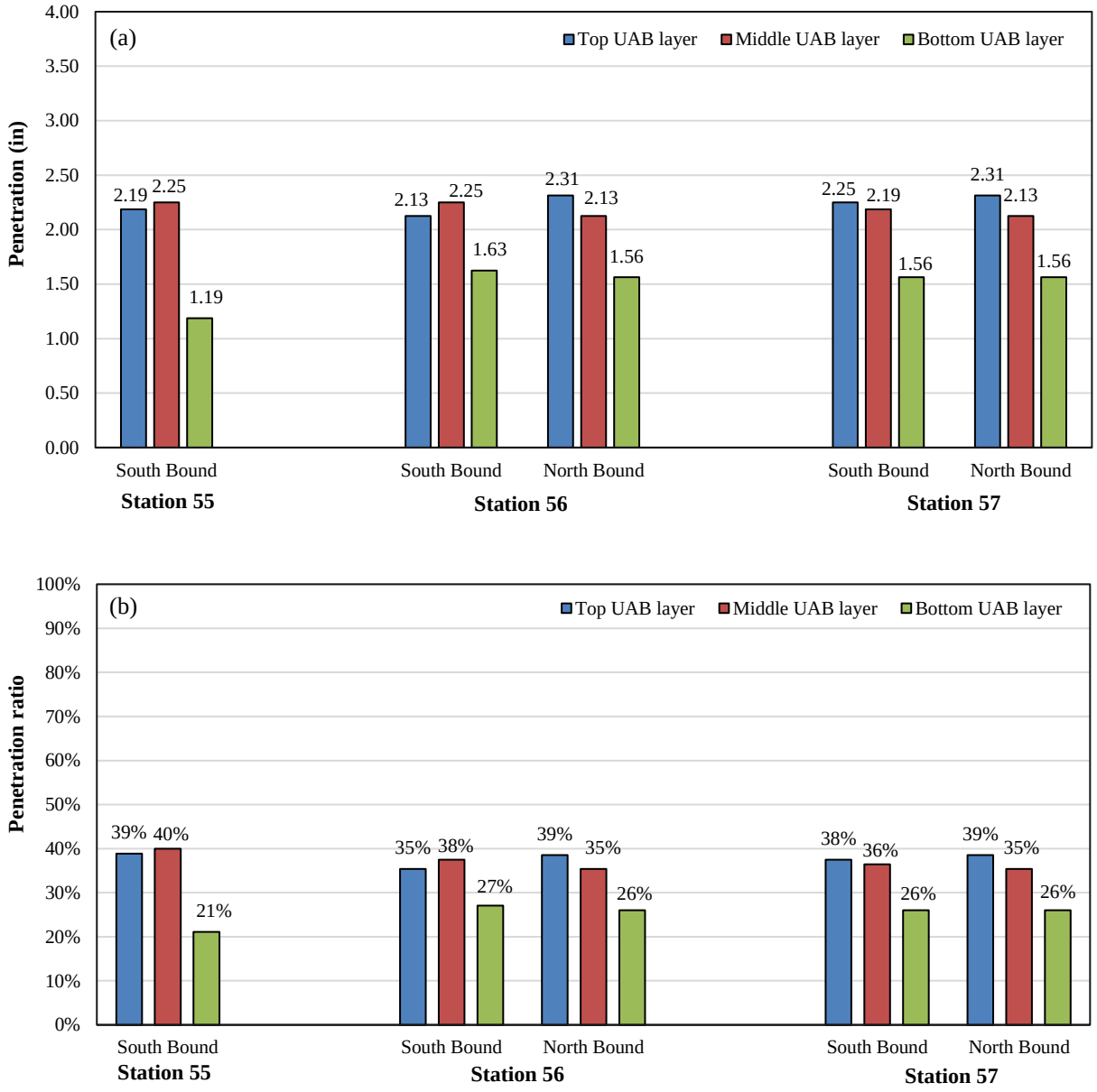

Figure 6.14: Penetration depths (a) and percentages of total penetration (b) achieved in the top, middle, and bottom parts of the UAB layer.

6.2. FWD TESTING RESULTS AND ANALYSIS

Data collected from in-situ FWD testing was also evaluated in this dissertation. The surface deflections registered below the center of the load plate at each station corresponding to the inverted and conventional pavement structures are depicted in Figure 6.15. The deflections resulting from dropping a load of 82 psi one single time over the inverted pavement were compared to the average deflections of two drops of 77 psi applied to the conventional pavement. The results showed that vertical deformations at zero lateral offsets measured in each station of the inverted pavement were lower than the average deflections recorded in the conventional pavement even though the load applied to the inverted structure was greater. The results indicate that the average deflection value of all stations on the inverted pavement (20.22 mils) was approximately 5 times lower than the average deflection value of all stations on the conventional pavement (104.83 mils). In addition, according to the coefficient of variation (COV) and the range of inverted and conventional pavement deflection values registered in each station, there was more data dispersion in the conventional pavement sections. These contrasting behaviors could be attributed to the better structural performance of the inverted pavement layered system. The stiff CTB layer acts as a rigid underlying support of the UAB layer minimizing the vertical deformations and maximizing the rigidity of the untreated granular medium. It is believed that less dispersed deflection values at the inverted pavement structure could be explained due to the better and more uniform compaction levels achieved by the UAB layer as a result of compacting the untreated aggregate base on top of the robust underlying cementitiously stabilized medium.

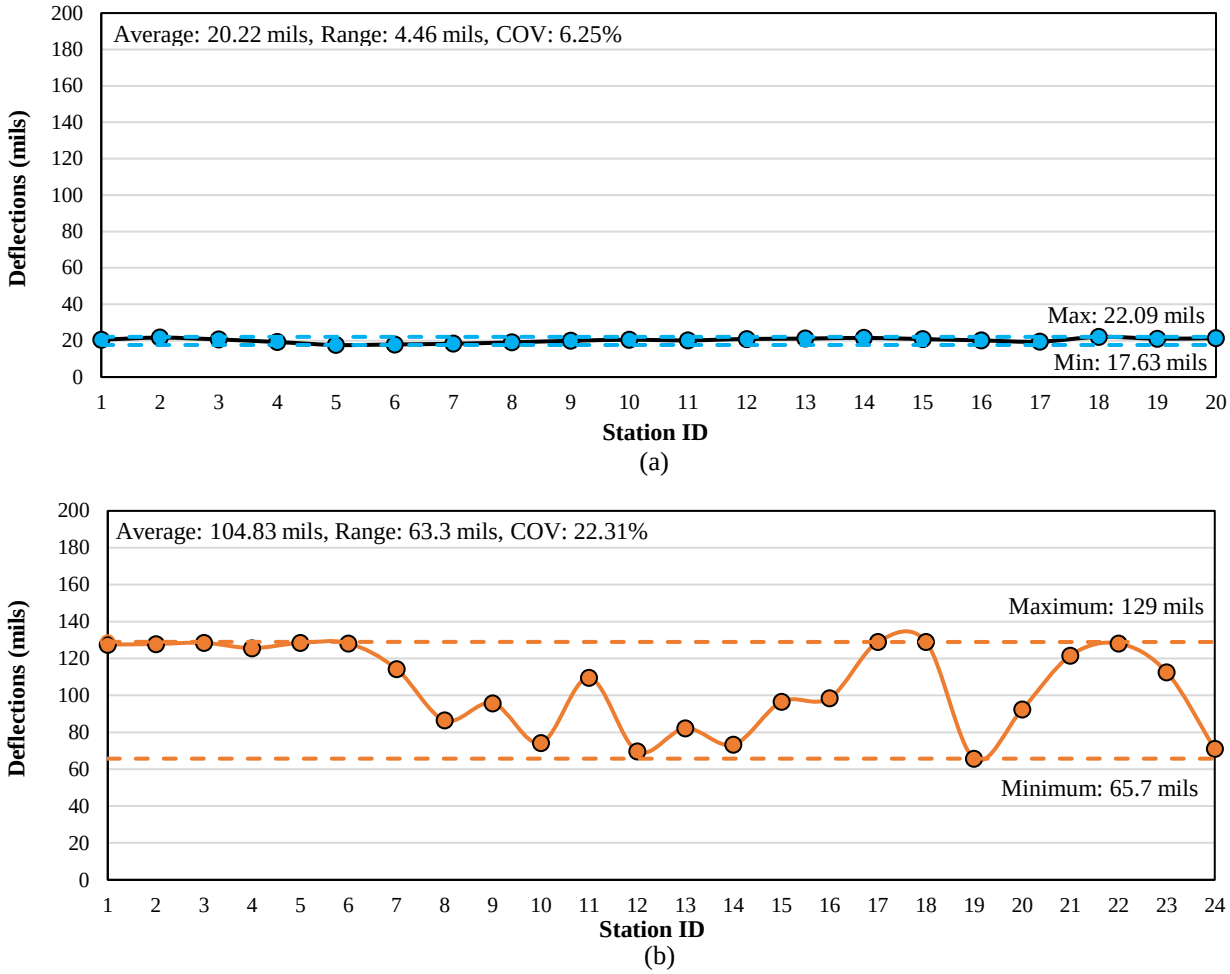

Figure 6.15: Surface deflections measured at the center of the loading plate during FWD testing on the (a) inverted pavement and (b) conventional pavement.

A series of indices were calculated based on the deflection data collected from all geophones used during FWD testing to characterize the mechanical behavior of pavement structures derived from the deflection basin computed at each testing point. Figure 6.16 displays the variation of the Base Layer Index (BLI), Middle Layer Index (MLI), Lower Layer Index (LLI), and F-1 shape factor determined in all stations of the inverted pavement structure. The same indices were estimated in 19 stations of the conventional pavement structure, and the resulting values are summarized in Figure 6.17. The data of five stations from the conventional pavement was excluded from the analysis due to non-descending deflections evidenced at increasing lateral distances from

the point of application of the load. It is essential to highlight that the FHWA recommends the deflection-based indices selected in this research study to assess the structural condition of flexible and rigid pavement structures (Pierce et al. 2017). Also, some researchers (Talvik et al. 2009, Rabbi & Mishra 2021) have recommended using deflection basin parameters from FWD testing as performance indicators for network-level asset management.

The structural conditions of the base, subbase, and subgrade soil in a typical pavement layer configuration can be quantified through the BLI, MLI, and LLI, respectively. The BLI was computed as the difference between the surface deflection at no lateral offset and the surface deflection at a 12-in lateral offset. The MLI was calculated as the difference between the surface deflection at a 12-in lateral offset and the surface deflection at a 24-in lateral offset. Finally, the LLI was determined as the difference between surface deflection at a 24-in lateral offset and the surface deflection at a 36-in lateral offset. The findings presented in Figure 6.16 and Figure 6.17 indicate that considerably lower index values were observed in the inverted pavement structure compared to the conventional pavement structure. Since a lower BLI, MLI, or LLI indicates an improved structural condition, the inverted layered system can be considered structurally superior.

A review of the plots displayed in Figure 6.16 and Figure 6.17 reveals that the F-1 shape factors calculated from the deflection basins of the inverted pavement structure were lower than the F-1 shape factors corresponding to the conventional pavement structure. Equation 6.2 shows the formula used to compute the F-1 shape factor as a function of FWD surface deflection data. Lower F-1 shape factors are an indicator of higher ratios of pavement rigidity to subgrade rigidity; therefore, the stiffness of the inverted layered system is expected to be greater than the stiffness of the conventional layered system. Higher stiffness evidenced by higher Modulus values resulted in lower deflections and improved structural performance of the inverted pavement.

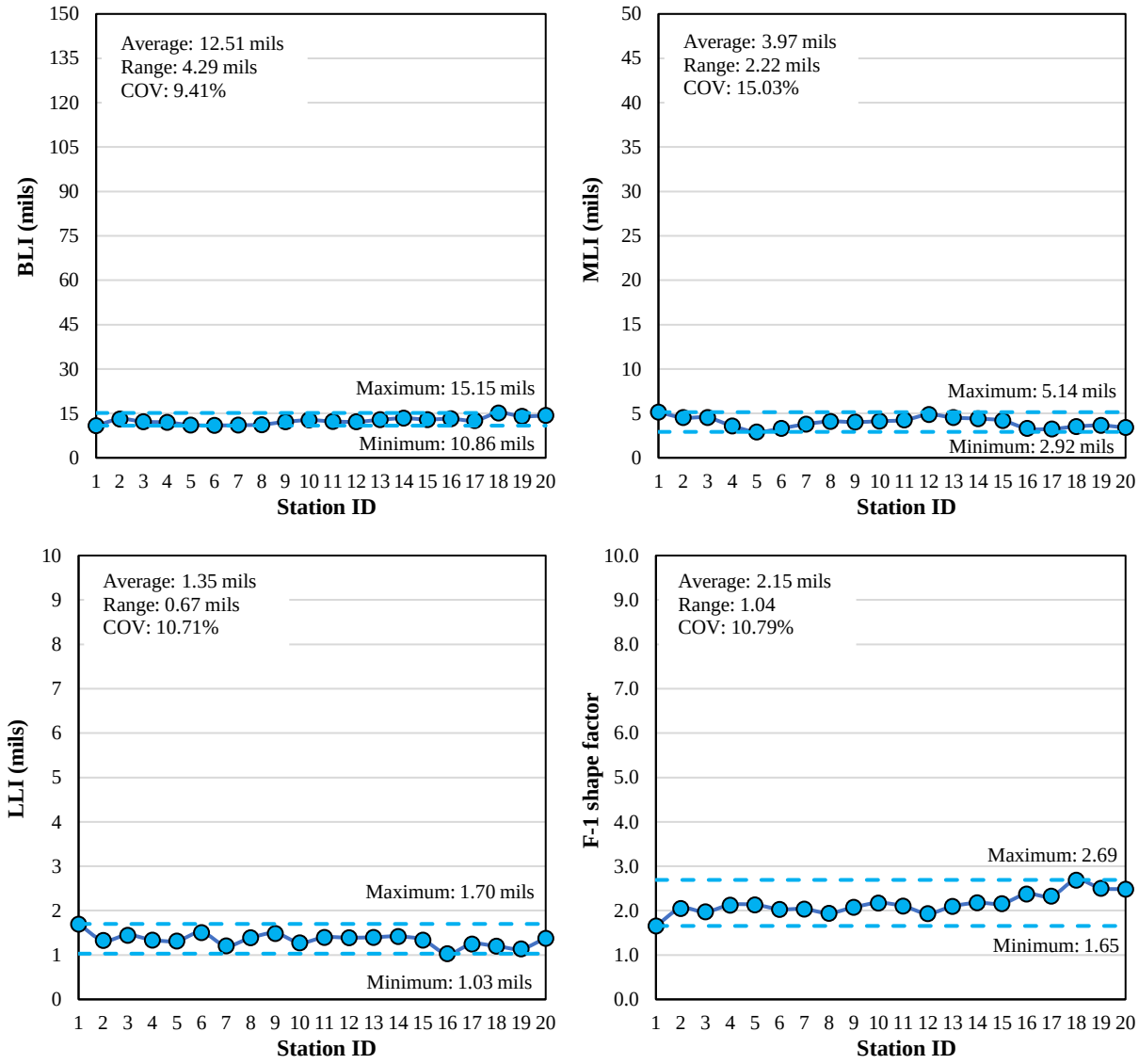

Figure 6.16: Deflection-based indices computed from the FWD data measured on the Virginia inverted pavement structure.

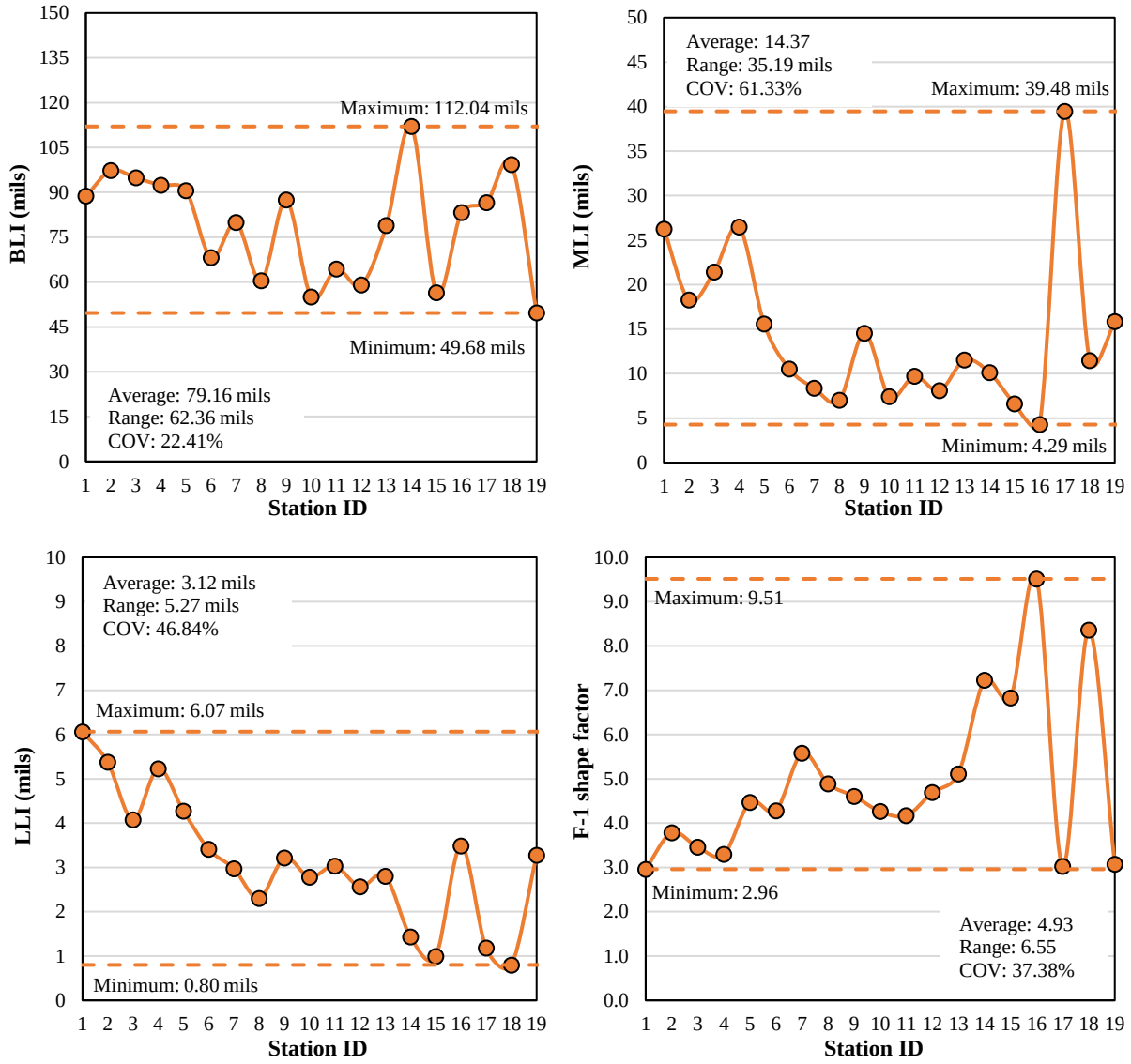

Figure 6.17: Deflection-based indices computed from the FWD data measured on the Virginia conventional pavement structure.

$$F\text{-}1 = \frac{D_0 - D_{60}}{D_{30}} \quad (6.2)$$

Where:

F-1: F-1 shape factor

D_0: surface deflection at no lateral offset

D_{30}: surface deflection at a 12-in lateral offset

D_{60}: surface deflection at a 24-in lateral offset

The AREA value was another parameter derived from the FWD testing that was considered in this dissertation. The AREA value is the normalized area of a cross-sectional slice through the deflection basin that extends from the loading centerline to the farthest sensor. It is calculated by dividing the area of the cross-sectional slice by the maximum surface deflection located beneath the loading plate. To obtain the AREA value, half of the deflection basin section is approximated by a series of right trapezoids, where the deflections of two consecutive sensors serve as bases, and the distance between the sensors acts as the perpendicular height.

Finally, the surface area of the constrained deflection basin was also calculated. This surface area is expressed in in^2 and is limited by half of the two-dimensional deflection basin. To determine this surface area, a similar process to the one described above was followed. However, in this case, the area was not normalized.

Figure 6.18 and Figure 6.19 show the variation of the AREA value and the constraint deflection basin surface for the inverted and conventional pavement structures, respectively. As shown in the figures, the AREA values of the inverted pavement structure were greater than the AREA values of the conventional pavement structure. These results suggest that the conventional layered system is less strong than the inverted pavement structure and, thus, underscore the enhanced structural behavior of the inverted layered system compared to the conventional

pavement structure. In addition, the surface area of the constrained deflection basin for the inverted pavement was found to be lower than that of the conventional pavement. This suggests that the non-traditional layered system experienced less vertical deformation compared to the conventional system.

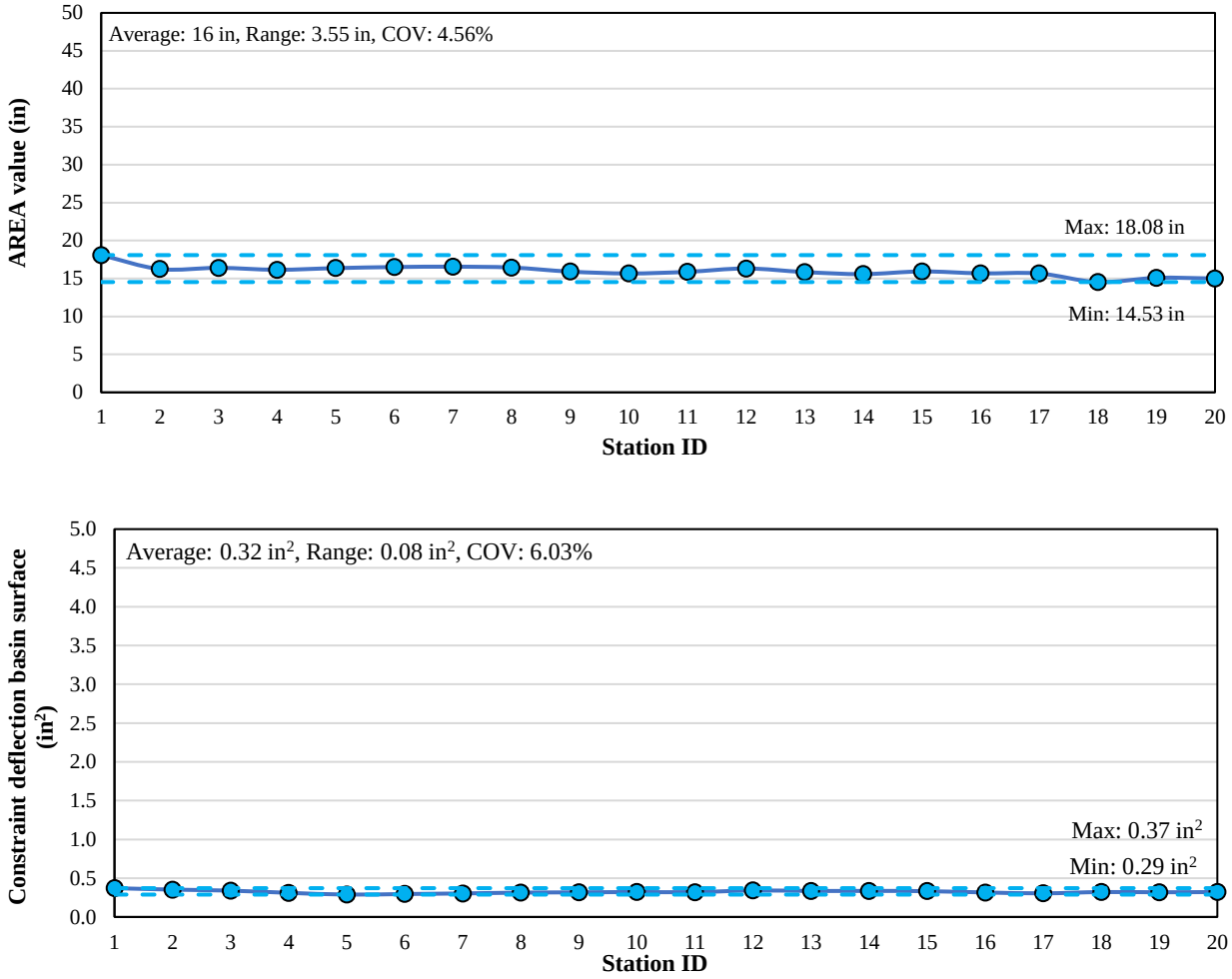

Figure 6.18: AREA value and constraint deflection basin surface from the FWD data measured on the Virginia inverted pavement structure.

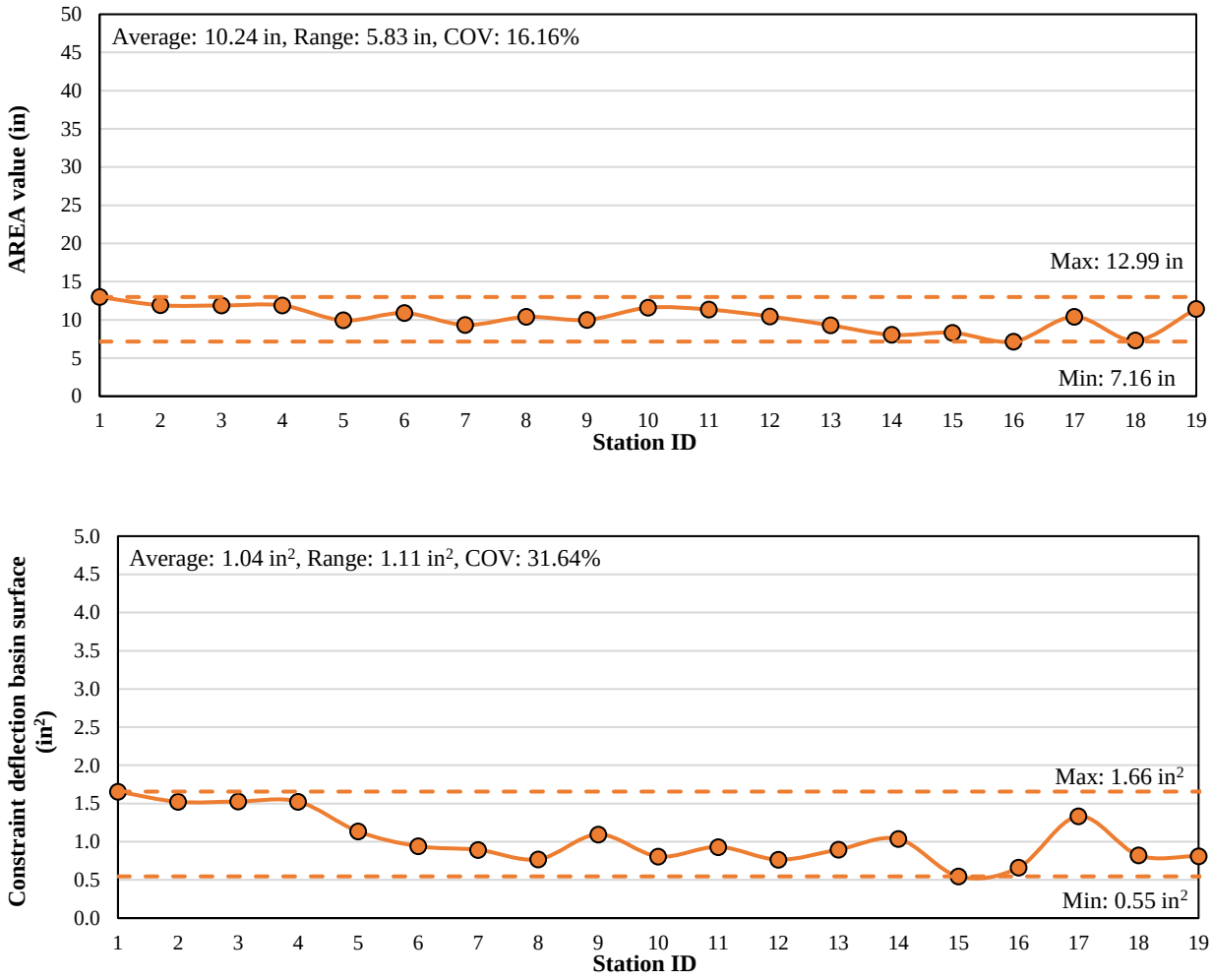

Figure 6.19: AREA value and constraint deflection basin surface from the FWD data measured on the Virginia conventional pavement structure.

From the standpoint of the variability of all deflection-based index values determined throughout the stations of inverted and conventional pavement structures, it is evident that the data points of each index regarding the conventional layered system were more dispersed than the indices related to the inverted layered system. The range and COV are simple statistical measures to quantify the variability of the data points. It is depicted in Figures 6.16, 6.17, 6.18, and 6.19 that the variation of the indices along the stations is significantly less pronounced in the inverted

pavement structure. The rationale behind these results is the homogeneity in the compaction of the UAB layer achieved due to the presence of a robust underlying CTB layer.

As a final analysis, the vertical deformation data measured using the FWD was examined to compare inverted versus conventional pavement structures in terms of the variability in the rate of change of the deflections developed at varying lateral offsets from the load plate center. The deflection basin of an inverted and a conventional pavement station are exhibited in Figure 6.20. As shown in the figure, the deflections recorded by the four geophones closest to the loading centerline were clustered to determine the slope of the trendline as an indicator of the dissipation rate of vertical deformations with respect to the lateral distances where the sensors were located. Similarly, the remaining five geophones were grouped to estimate the slope of the best fitting line of the deflection data points. As a result, the deflection basin was subdivided into two regions: the primary deflection basin defined by the deflections measured by the cluster of four geophones, and the secondary deflection basin defined by the deflections measured by the cluster of five geophones. In each cluster, the highest deflection value was considered the origin for calculating the line of best fit, setting the intercept as zero.

Table 6.1 and Table 6.2 present the slopes of primary and secondary deflection basins from the conventional and inverted pavements, respectively. It is apparent from the tables that the inverted pavement structure presented lower average slope values in both sensor clusters as compared to the conventional pavement structure. These findings imply that the change in the vertical deformations measured by consecutive geophones in each cluster is less prominent in the stations from the inverted layered system. As evidenced through the standard deviation and COV, higher dispersion in the rate of dissipation of the deflections with respect to lateral distances was observed at the conventional pavement structure. The smaller variability in the changing rate of

the vertical deformations developed in the inverted pavement structure could be explained due to the uniformly distributed compaction of the UAB layer. This final analysis demonstrated that the inverted pavement exhibited a more consistent deformation behavior among stations due to the favorable location of the stiff CTB layer during compaction of the overlying UAB layer.

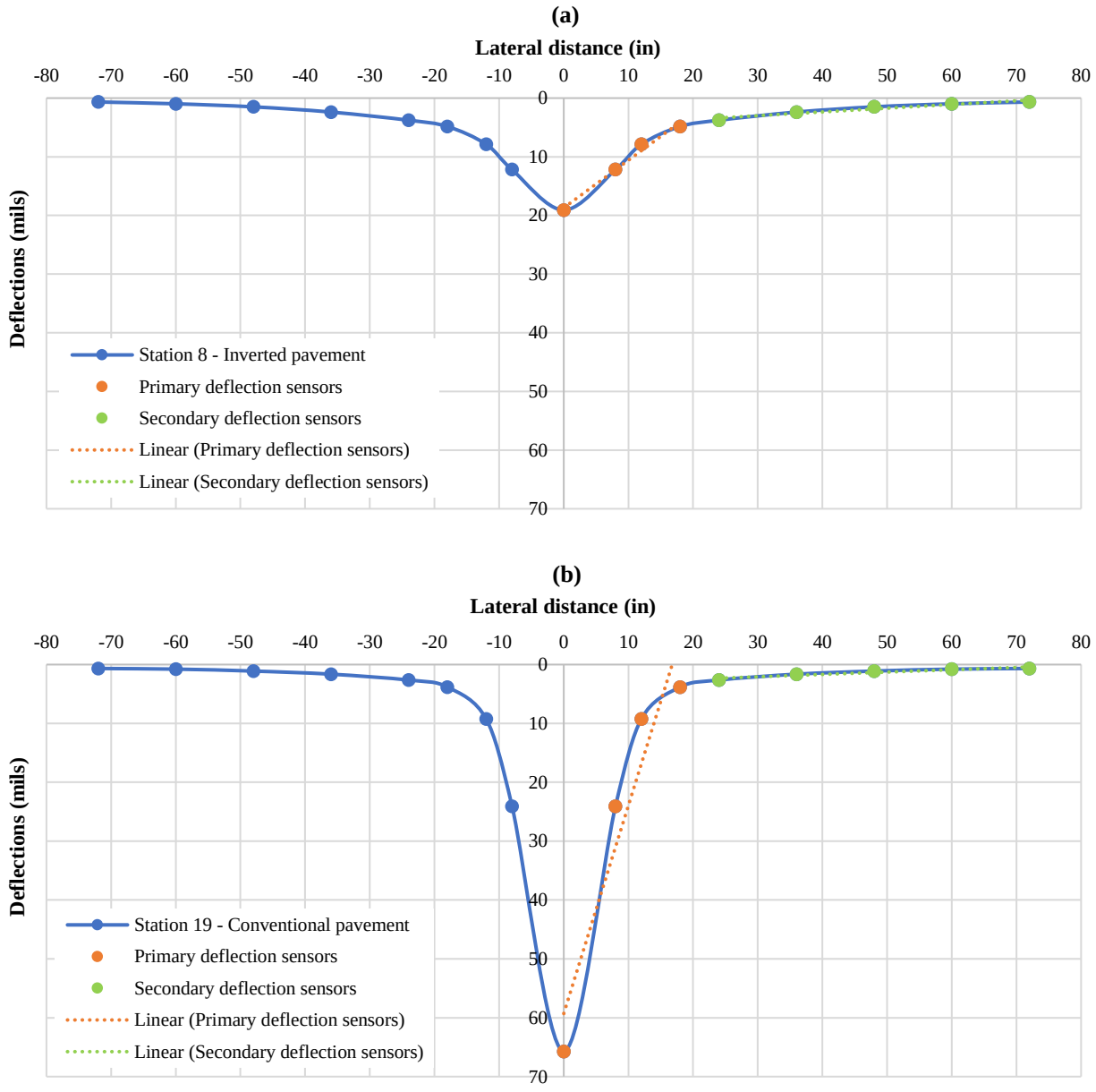

Figure 6.20: Trendline equations of deflections calculated as an example for Station 8 of the inverted pavement (a) and Station 19 of the conventional pavement (b).

Table 6.1: Values and statistics of the slopes of the trendlines of the primary and secondary deflection basins at the Virginia conventional pavement structure.

Station number and statistics	**Slopes of primary deflection basin (mils/in)**	**Slopes of secondary deflection basin (mils/in)**
Station 1	6.1895	0.2664
Station 2	6.6522	0.2570
Station 3	6.6893	0.2242
Station 5	6.4635	0.2137
Station 7	6.4177	0.1792
Station 8	4.7643	0.1588
Station 9	7.1550	0.1878
Station 10	4.2308	0.1439
Station 11	6.1805	0.1660
Station 12	3.7999	0.1387
Station 13	4.5009	0.1579
Station 14	4.1081	0.1275
Station 15	5.6342	0.1311
Station 17	7.9576	0.1502
Station 19	3.9931	0.0484
Station 20	5.8839	0.1193
Station 22	6.6436	0.0291
Station 23	7.0077	0.0404
Station 24	3.6160	0.1203
Average values	5.7682	0.1402
Standard deviation	1.2243	0.0678
COV	21.23%	48.35%

Table 6.2: Values and statistics of the slopes of the trendlines of the primary and secondary deflection basins at the Virginia inverted pavement structure.

Station number and statistics	**Slopes of primary deflection basin (mils/in)**	**Slopes of secondary deflection basin (mils/in)**
Station 1	0.8276	0.0880
Station 2	0.9717	0.0774
Station 3	0.9088	0.0773
Station 4	0.8723	0.0714
Station 5	0.7979	0.0714
Station 6	0.7905	0.0733
Station 7	0.8065	0.0665
Station 8	0.8383	0.0744
Station 9	0.8959	0.0750
Station 10	0.9352	0.0709
Station 11	0.8993	0.0713
Station 12	0.9161	0.0768
Station 13	0.9507	0.0726
Station 14	0.9876	0.0718
Station 15	0.9464	0.0698
Station 16	0.9509	0.0674
Station 17	0.9095	0.0669
Station 18	1.0783	0.0628
Station 19	1.0076	0.0623
Station 20	1.0261	0.0697
Average values	0.9159	0.0719
Standard deviation	0.0785	0.0057
COV	8.57%	7.96%

Chapter 7: Numerical Analysis of the Virginia Inverted Pavement Structure

A set of numerical models of the Virginia inverted pavement section was created to study their mechanical behavior under specific loading conditions. The models were based on the in-situ FWD testing results and field data collected from the inverted pavement section constructed in Virginia. The FE method was used to evaluate the mechanical behavior of the pavement structures. The study compared the inverted pavement model to a conventional design obtained by switching the order of the top second (UAB) and top third (CTB) layers of the inverted pavement section. The critical stresses and strains developed at specific locations within the pavement system were analyzed for both types of pavement structures. Abaqus was the program used for the numerical analysis. The study emphasized on the structural performance of the UAB layer of the inverted section, which plays a crucial role in the load distribution capacity of the pavement system.

7.1. BACKCALCULATION ANALYSIS

In order to estimate the Moduli values of each layer of the pavement structure, including the subgrade soil that supported the layered system, a backcalculation analysis was executed. This analysis took into consideration the deflection data obtained from the field during the FWD testing of the Virginia inverted pavement section. To perform the structural evaluation, the pavement analysis program Elmod 6 from Dynatest was used.

Using the same load plate geometry, the surface deflections of the subgrade were measured based on deflection responses obtained from the FWD test conducted at the top of the soil. The same arrangement of geophones previously described in Chapter 6 was employed to gauge the surface deflections. The field-testing program included a total of 28 stations, covering almost 350 ft. At each testing point, the subgrade soil was subjected to an average pressure of 53 psi applied in three different instances to induce vertical deformation.

Figure 7.1 illustrates the progression of the average deflection values beneath the center of the load plate and the corresponding change of the average backcalculated Moduli from one station to the next. As anticipated, lower deflections correlated with higher Modulus values, while higher deflections resulted in lower Moduli. The final average Modulus value of 7.5 ksi for the subgrade soil was obtained as the output of the backcalculation analysis.

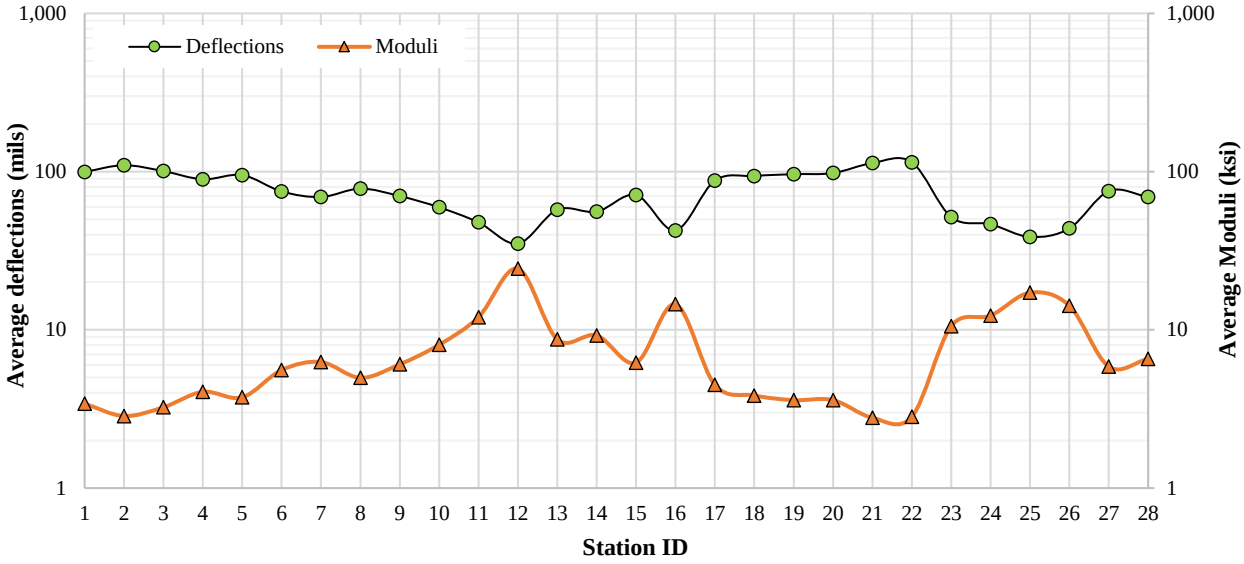

Figure 7.1: Progression of surface deflections measured under the load plate center and resulting backcalculated Moduli of the subgrade soil at the Virginia inverted pavement section.

After the construction of the inverted pavement structure, a non-destructive in-situ test was conducted at the top of the topmost layer using FWD. The deflection data collected from the test was utilized to perform a backcalculation analysis to estimate the Modulus values for each layer of the inverted system resting on top of the subgrade soil. The average backcalculated Moduli were computed for each layer at different stations where the in-situ test was performed.

The variation of Modulus values for the AC layer, UAB layer, and CTB layer, with the stiffness of the subgrade soil maintained at 7.5 ksi, was displayed in Figure 7.2. The resulting average Moduli for the AC layer, UAB layer, and CTB layer were 340 ksi, 67 ksi, and 412 ksi,

respectively. These Modulus values were considered as the main input parameter to characterize the material properties of each layer of the Virginia inverted pavement structure in addition to the stiffness of the subgrade soil.

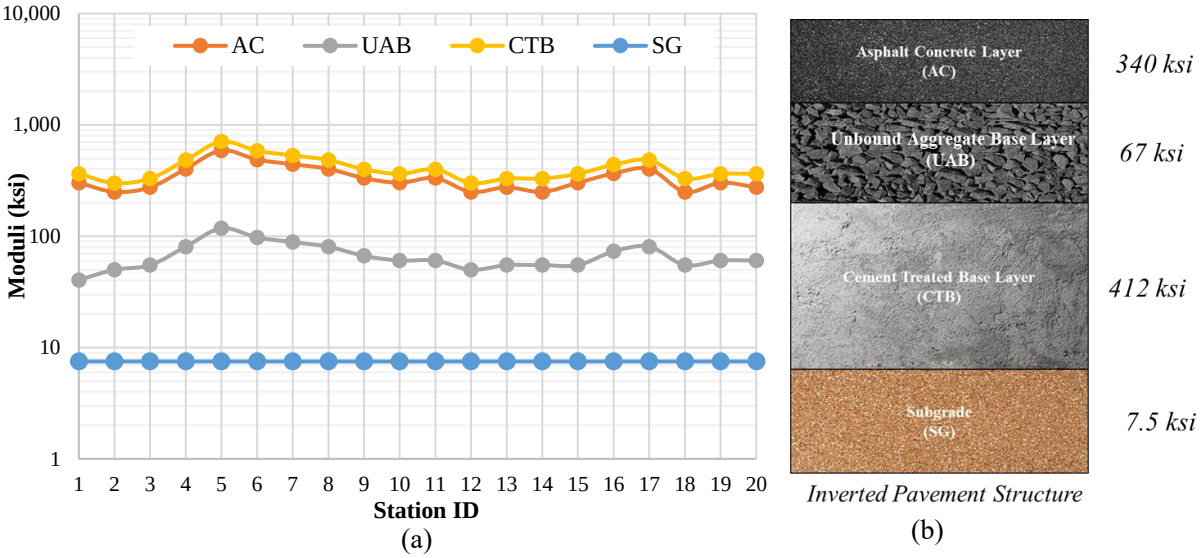

Figure 7.2: Progression of Moduli at the AC layer, UAB layer, CTB layer, and SG soil from the Virginia inverted section (a) and resulting average backcalculated Modulus values (b).

As shown in Figure 7.2, the inverted pavement structure does not follow the conventional design in terms of the decreasing order of layer stiffnesses with depth. Instead, the Modulus of the UAB layer is the lowest among all structural layers and is sandwiched between a robust CTB layer and an overlying AC layer. This configuration aligns with the concept of an inverted pavement.

The cementitiously stabilized medium represents the stiffest layer, situated above the subgrade soil. Consequently, the modular ratio of the CTB layer to the subgrade soil exceeded 50. Additionally, the Modulus values of the AC layer and the CTB layer were approximately five and six times higher than that of the UAB layer, respectively. The findings from the backcalculation analysis are invaluable for the numerical modeling of the inverted layered system. To fully characterize the structural behavior of the pavement layers, an important material property in

addition to the Modulus values is the Poisson's ratio (PR). In this study, reasonable values for the PR were assumed for each layer of the inverted pavement structure, with values of 0.35, 0.25, and 0.20 assigned to the AC layer, UAB layer, and CTB layer, respectively. As for the SG soil, a PR of 0.41 was considered.

7.2. LOADING CONDITIONS

An aggregate haul truck, with a gross weight of 80,580 lb, was instructed to drive at a speed of 30 to 35 miles per hour on both inverted and conventional pavement structures during the loading phase of the full-scale testing road test in Virginia. The truck axle configuration consisted of a steering axle, followed by three single axles, and two dual axles at the rear of the heavy vehicle. Figure 7.3 displays a 3-D representation of the truck used in the road test, featuring the same axle configuration.

Figure 7.3: 3-D representation of an aggregate haul truck featuring the same axle configuration as the vehicle used at the road test in Virginia. Source: Hum3D.

The weight of each axle is summarized in Table 7.1, as well as the measurements of the distances between each axle and the steering axle. The contact area between the wheels and the pavement surface was considered rectangular. Table 7.1 also shows the geometry of the areas of contact of one tire for each axle type. The weight per tire and their corresponding contact areas indicate an inflation pressure of approximately 100 psi for each wheel.

Table 7.1. Weight and geometric characteristics of the axle configuration from the aggregate haul truck used at the road test in Virginia.

Axle type	Axle weight (lb)	Tire weight (lb)	Geometry of contact area (in x in)	Distance with respect to the steering axle (ft and in)
Steering	14,236	7,118.00	11.5 in x 6.1 in	-
Single 1	6,282	3,141.00	8.1 in x 4.5 in	14 ft 8 in
Single 2	6,959	3,479.50	8.1 in x 4.5 in	18 ft 4 in
Single 3	7,507	3,753.50	8.1 in x 4.5 in	21 ft 10 in
Dual 1	21,129	5,282.25	8.7 in x 6.9 in	25 ft 9 in
Dual 2	24,467	6,116.75	8.7 in x 6.9 in	30 ft 1 in

7.3. NUMERICAL SIMULATION

The Virginia inverted pavement structure and its equivalent conventional design were modeled using the FE method. Abaqus, a widely accepted software platform for conducting such simulations, was employed for this purpose. The inverted pavement structure, which includes an AC layer, UAB layer, CTB layer, and subgrade soil, was modeled based on the non-destructive in-situ testing results obtained from the Virginia inverted pavement section. Likewise, the equivalent conventional pavement structure consisting of an AC layer, CTB layer, UAB layer, and subgrade soil was also modeled to facilitate a comparative analysis of the critical pavement responses between the inverted and conventional pavement systems.

To accurately capture the critical responses of both types of pavement structures, data corresponding to the pavement layer thicknesses, layer Moduli, and PR values were incorporated into the developed FE model. These parameters were crucial in enabling a comprehensive evaluation of the structural behavior and performance of both the Virginia inverted pavement structure and its conventional design.

7.3.1. Isotropic Analysis

The simulated pavement structures had a length of 63.5 ft and a width of 21 ft. The total depth of the inverted and conventional systems was determined by the thickness of each layer, namely a 5-in AC layer, a 6-in UAB layer, and a 10-in CTB layer, arranged accordingly depending on the type of pavement configuration. The subgrade soil was modeled with a thickness of 39 in to support the 21-in system adequately. This thickness ensured appropriate stress distribution with depth and prevented any undue influence of bottom boundary conditions on the critical pavement responses. To simulate a realistic scenario, the entire aggregate haul truck was modeled resting on the pavement surface, with appropriate lateral free space considered around the truck to prevent any unrealistic responses influenced by the lateral boundary conditions.

The simulation was meshed appropriately to ensure accurate results. Due to the parallelepiped shape of the pavement structure, C3D20R brick elements were considered suitable for modeling due to its integration capabilities. Two different analyses were performed: a full-truck analysis and an axle analysis. In the full-truck analysis, all axle loads were applied simultaneously, while in the axle analysis, each axle load was applied individually. This approach enabled the evaluation of the influence of the proximity of axles on pavement critical responses. To fully characterize the mechanical behavior of each layer and subgrade, all materials were modeled as linear elastic and required a Modulus and PR as input parameters. Figure 7.4 depicts the mesh, boundary conditions, and pressure applied on the contact areas for each axle.

Figures 7.5 to 7.9 depict a series of plots showcasing specific stresses and strains at the bottom of the AC layer and top of the subgrade soil, as well as the vertical deformation at the surface of the pavement structure. These output responses are essential parameters in determining the fatigue life and permanent deformation of the layered systems.

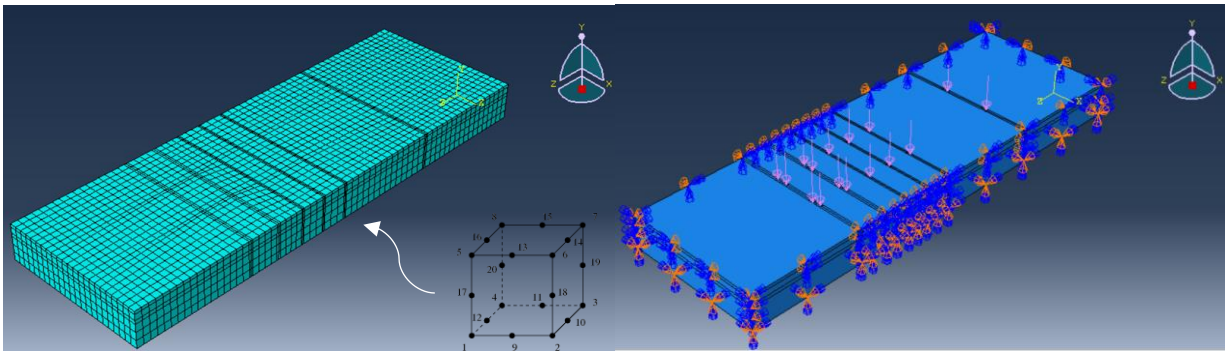

Figure 7.4: Mesh, 20-node brick element, boundaries, and loading conditions considered in the simulation of the Virginia inverted and conventional pavement structures.

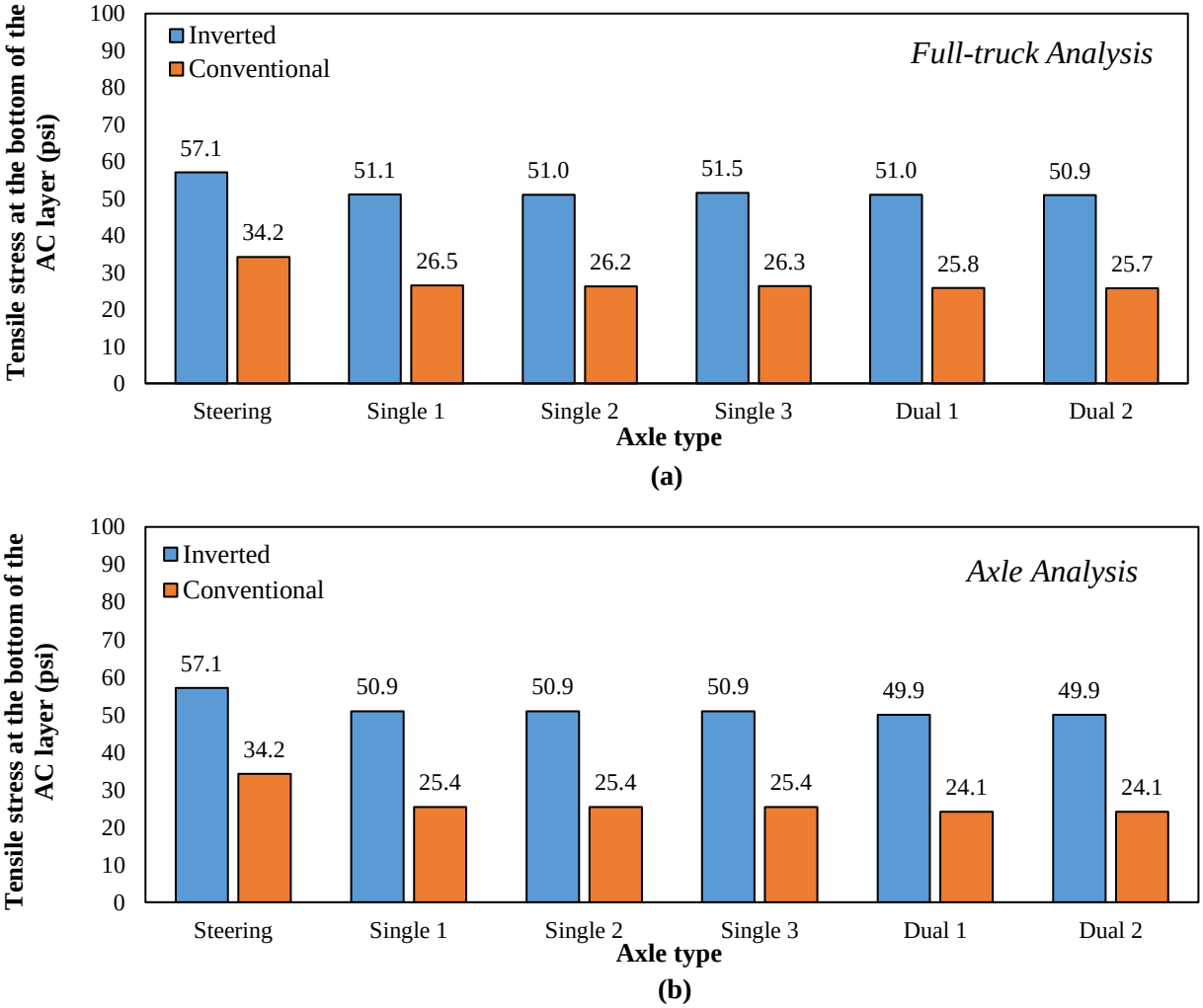

Figure 7.5: Tensile stresses developed at the bottom of the AC layer in the Virginia inverted and conventional pavement structures considering a full truck analysis (a) and axle analysis (b).

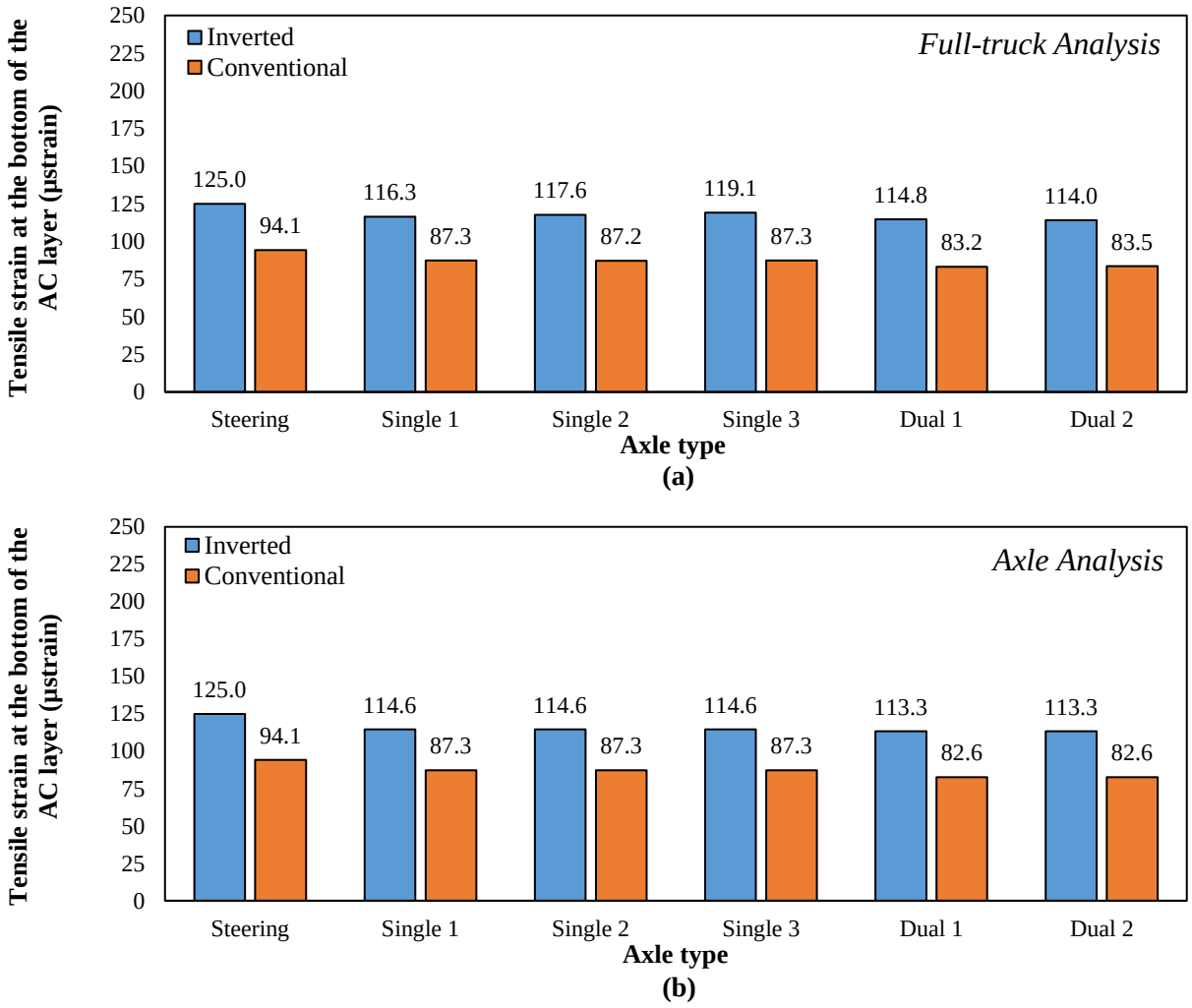

Figure 7.6: Tensile strains developed at the bottom of the AC layer in the Virginia inverted and conventional pavement structures considering a full truck analysis (a) and axle analysis (b).

Figures 7.5 and 7.6 provide a visual representation of the tensile stresses and strains that were developed at the bottom of the AC layer for the Virginia inverted and conventional pavement structures. These bar charts depict the tensile stresses for each axle type and were obtained from both the full-truck and axle analyses. Notably, the inverted pavement structure exhibited higher tensile stresses and strains than the conventional pavement structure in both types of analyses. The reason for this difference lies in the type of layer placed beneath the AC layer. In the conventional pavement, the CTB layer is more rigid than the UAB layer of the inverted structure, limiting the

deformation of the AC layer and resulting in lower tensile stresses and strains at the bottom of the superficial layer. Conversely, the flexible UAB layer in the inverted pavement design allows the upper AC layer to deform under load, resulting in higher tensile stresses and strains at the bottom of the asphaltic layer. The bar charts also show that the full-truck analysis produced slightly higher results, suggesting a small influence of the neighboring axles on the development of tensile stresses and strains at the bottom of the AC layer. Steering axle responses were mostly unaffected by neighboring axles due to their farther position from the immediately adjacent Single 1 axle.

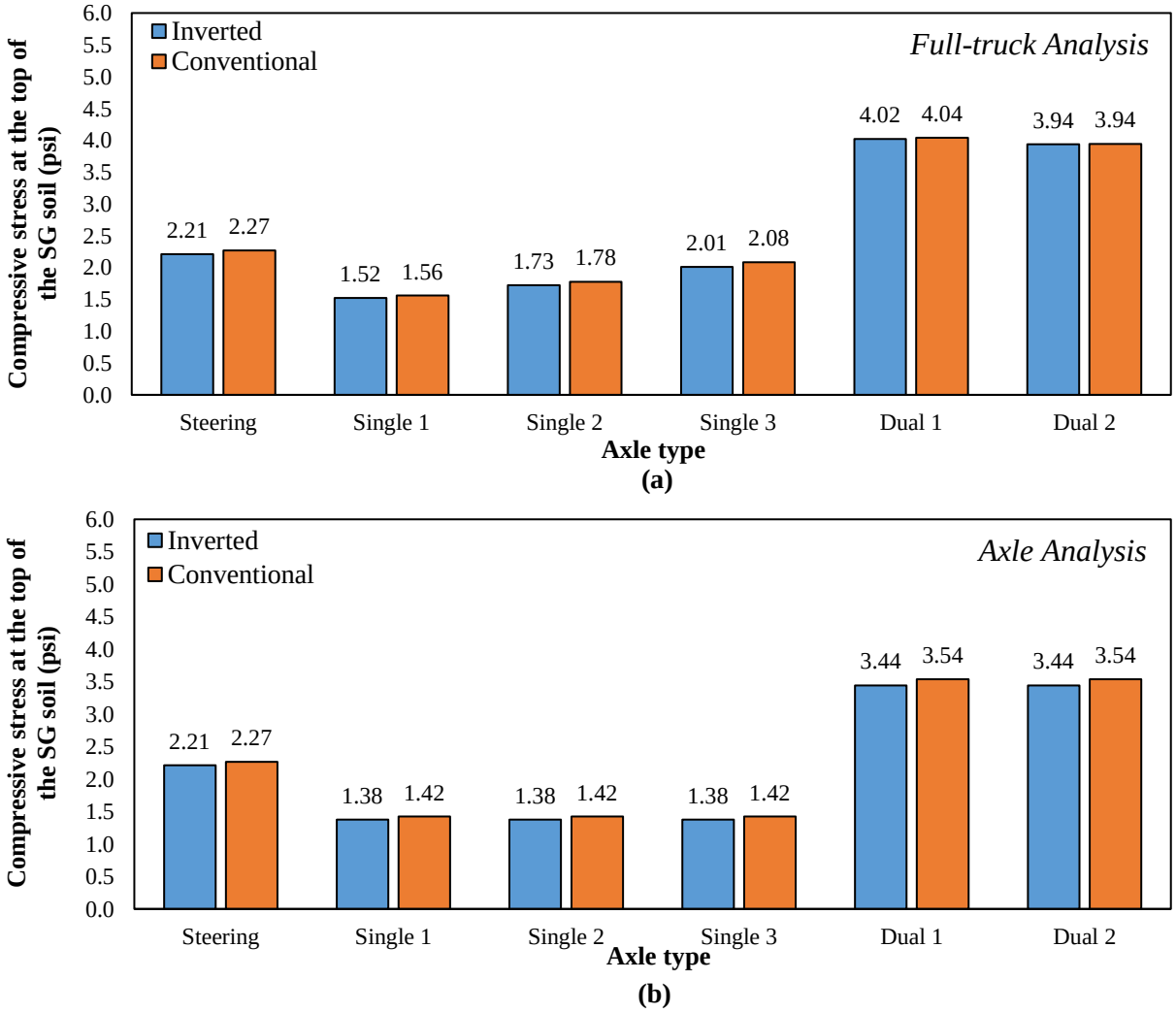

Figure 7.7: Compressive stresses developed at the top of the SG soil in the Virginia inverted and conventional pavement structures considering a full truck analysis (a) and axle analysis (b).

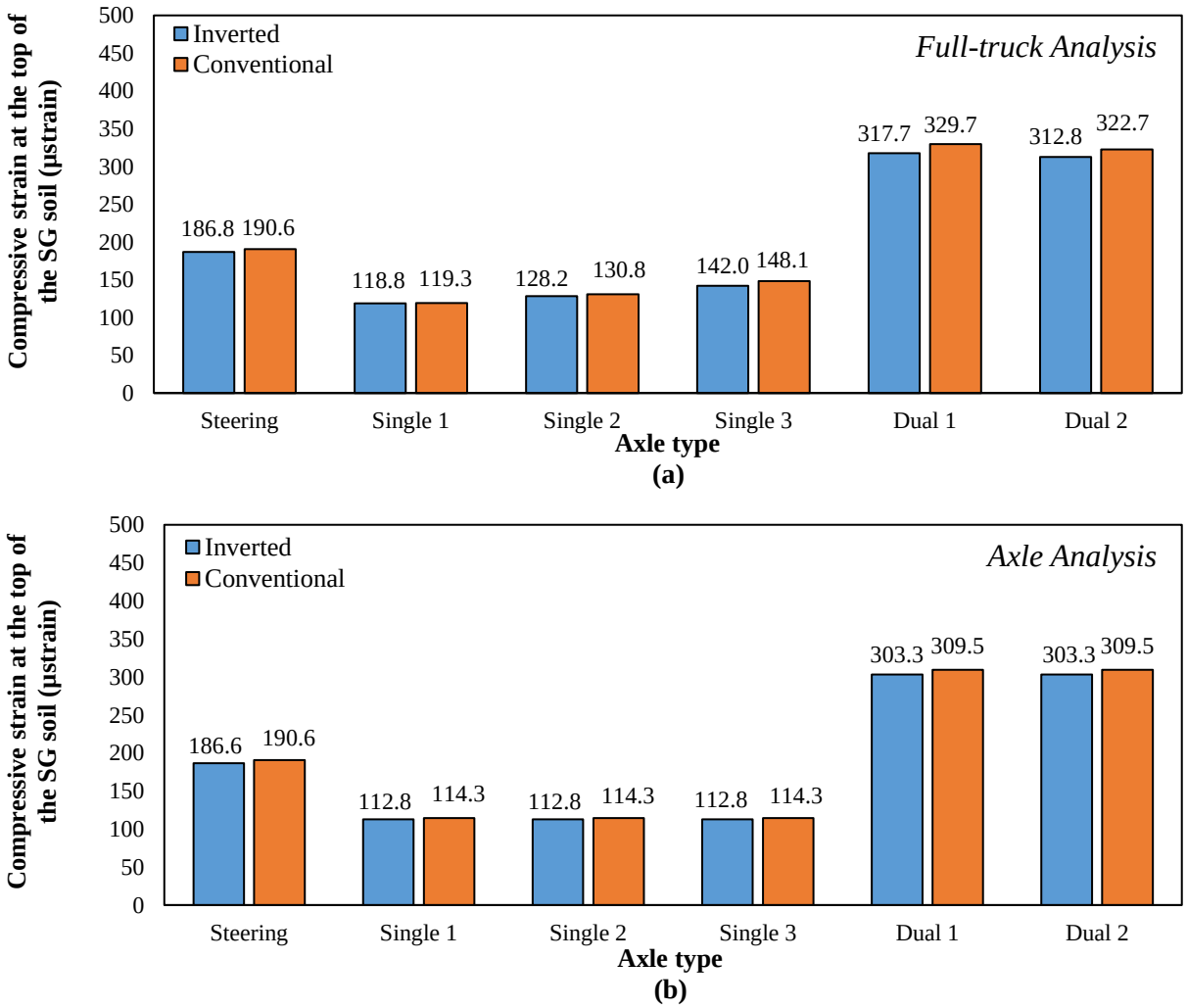

Figure 7.8: Compressive strains developed at the top of the SG soil in the Virginia inverted and conventional pavement structures considering a full truck analysis (a) and axle analysis (b).

In addition to the stresses and strains at the bottom of the AC layer, another critical pavement response is the compressive stress at the top of the subgrade soil. The results summarized in Figure 7.7 showed that the inverted pavement structure performed better in terms of stress dissipation as compared to the conventional pavement structure. It is worth noting that stresses were higher in the full-truck analysis as compared to the axle analysis, indicating an influence of the axles located in the vicinity of one another. Notably, the steering axle responses remained

largely unaffected by neighboring axles due to their position farther away from the immediately adjacent axle (single 1).

The same previous trend was found for the compressive strains developed at the top of the subgrade soil as displayed in Figure 7.8. Lower strains were observed in inverted pavement, with a strain increase in the conventional pavement, and higher strains in the full-truck analysis. These findings suggest that the layer configuration of the inverted pavement design had a better load-distribution capacity evidenced by lower levels of stresses transmitted to the SG soil.

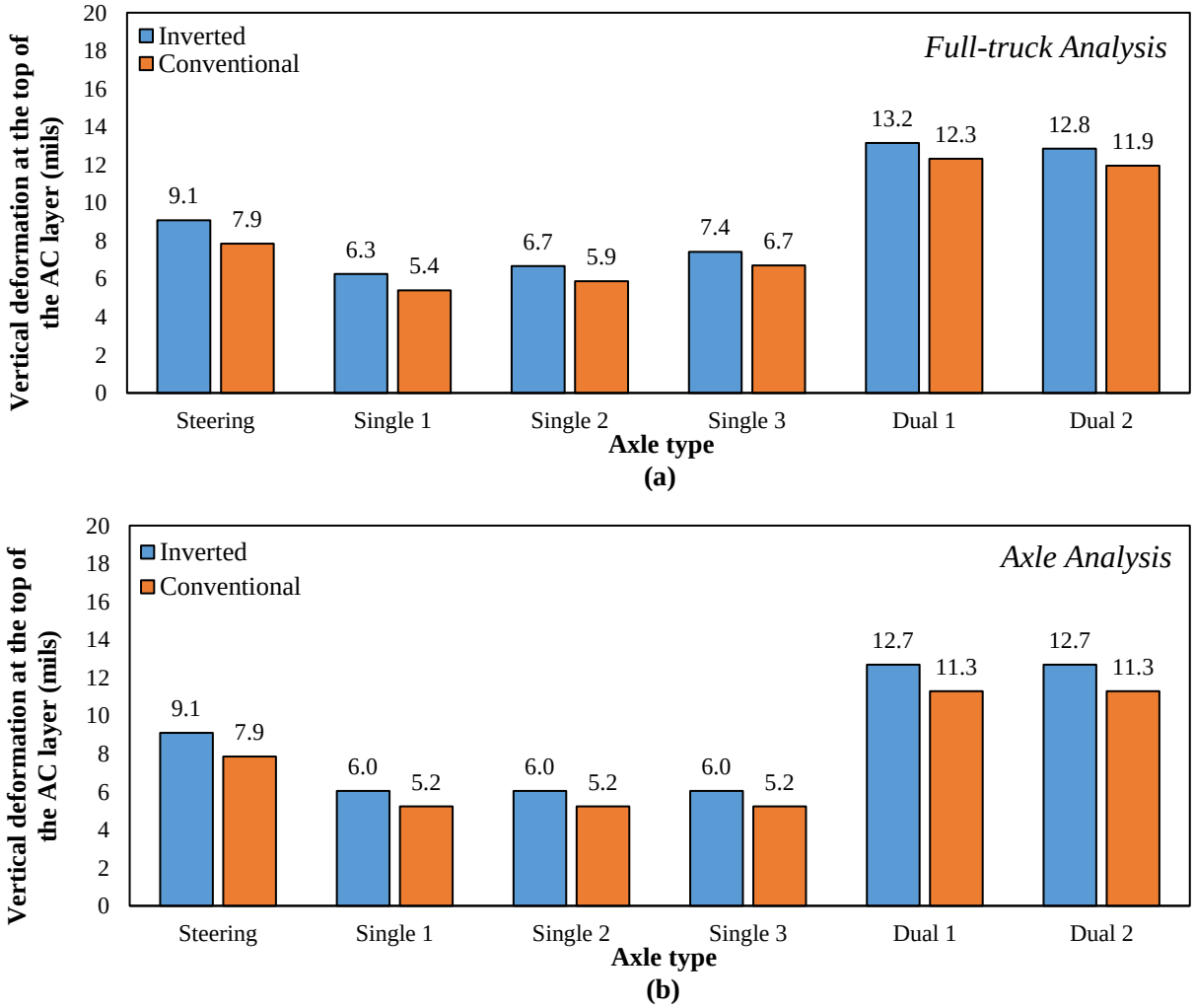

Figure 7.9: Vertical deformation at the top of the AC layer in the Virginia inverted and conventional pavement structures considering a full truck analysis (a) and axle analysis (b).

Figure 7.9(a) illustrates the vertical deformation at the top of the AC layer for both pavement structures under the application of all axles simultaneously, while Figure 7.9(b) displays the same pavement response for each axle applied independently. The results indicate higher deformations in the inverted pavement structure in both analyses, implying that the inverted pavement design is susceptible to rutting. Additionally, the full-truck analysis displayed even higher deformations, indicating that neighbor axles influence the AC surface deflection, increasing the likelihood of the pavement experiencing permanent deformation. These findings align with a previous study conducted on Route 59 in Lufkin, Texas (Moody 1994), which evaluated the performance of a 3-in overlay and a crushed stone interlayer on an existing jointed concrete pavement to minimize reflection cracking. The treatment based on the inverted pavement concept showed no cracking after 2 years but exhibited an initial rut depth of 0.25 in.

Figures 7.10 to 7.15 depict the stress and strain analysis outcomes in the UAB layer. This layer has been chosen as the focus of the study due to its significant role in the load distribution capacity of the inverted pavement structure. The UAB layer in the inverted pavement was compared against its counterpart in the conventional pavement system.

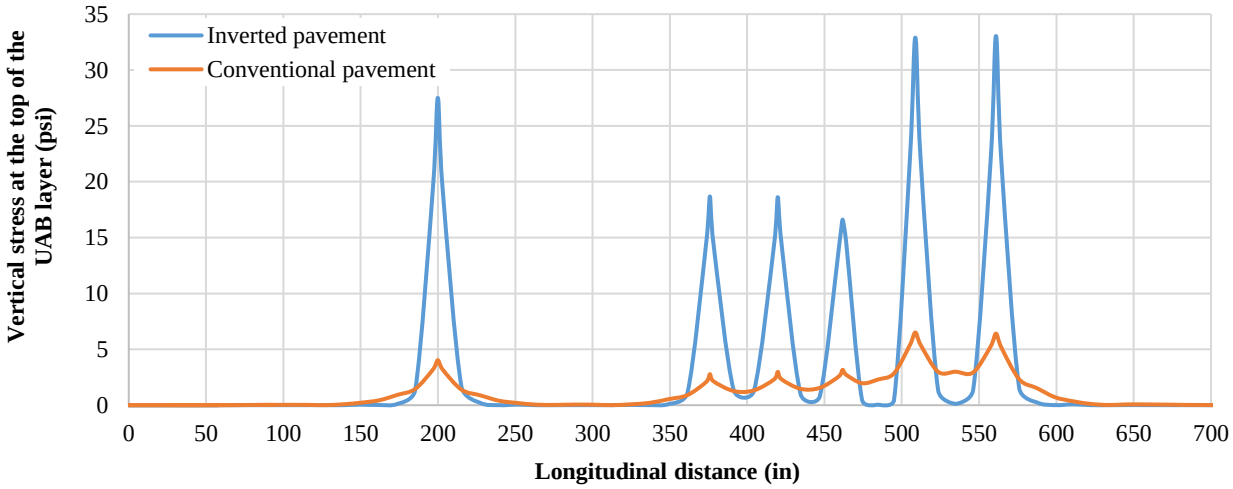

Figure 7.10: Vertical stresses at the top of the UAB layer in the Virginia inverted and conventional pavement structures.

Figure 7.10 presents the vertical stresses at the top of the UAB layer in both inverted and conventional pavement structures. The graph depicts the variation of the vertical stresses along a line passing longitudinally through the tire contact areas at one side of each axle. Each peak in the graph corresponds to the effect of one tire (for steering and single axles) or two tires (for dual axles) located at one side of each axle. The results reveal that the inverted pavement structure experiences higher stresses as compared to the conventional pavement structure due to the proximity of the UAB layer to the surface where the loads are applied.

Moreover, in the inverted pavement structure, the vertical stresses dissipate completely between two consecutive peaks, whereas in the conventional pavement structure, the stresses do not completely dissipate between two consecutive peaks. This difference in behavior can be attributed to the location of the UAB layer in both pavement structures and the extent of the pressure bulb of the stresses being transmitted from the surface down. In the inverted pavement structure, the UAB layer is located closer to the pavement surface, where the extent of the pressure bulb is smaller. This allows for the dissipation of the vertical stresses between two consecutive axles. In contrast, the pressure bulb has a higher extent with depth where the UAB layer of the conventional pavement is located. Therefore, the stresses cannot dissipate completely between two consecutive peak values.

Figure 7.11 visually demonstrates this trend based on the program output. The figure displays the UAB layers isolated from the rest of the pavement structures, with red color representing zero stress values. The inverted pavement structure shows red colors of zero stress between the tire contact areas of the different axles, whereas the conventional pavement structure does not have any red coloring between the peak values where the tire contact areas are located.

This difference in pressure bulbs is due to the location of the UAB layer, which is placed at a different depth depending on the pavement structure type.

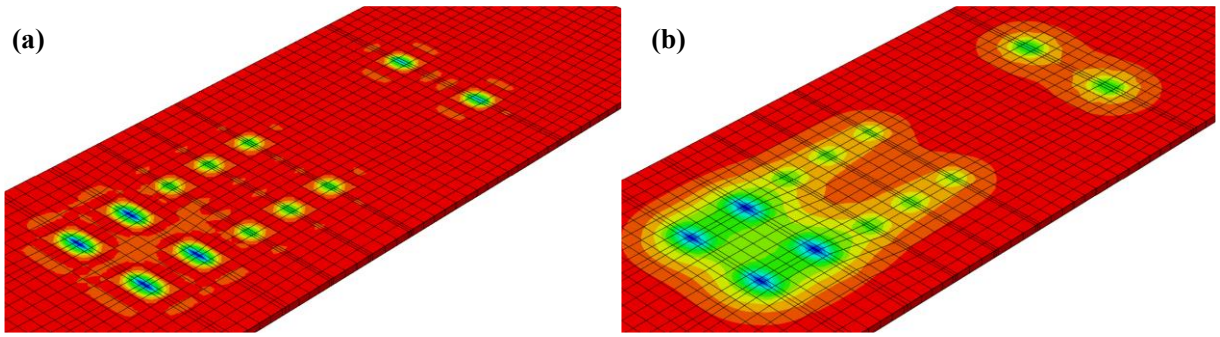

Figure 7.11: Contrasting extent of the pressure bulbs evident at the surface of the UAB layer in the Virginia inverted (a) and conventional (b) pavement structures.

The analysis was continued by examining the shear stresses along the surface of the UAB layer in both the inverted and conventional pavement structures. Two directions were examined - longitudinal and transversal to the direction of traffic. In Figure 7.12, the longitudinal variation of the shear stresses at the top of the UAB layer is presented, where each pair of peak values represents the effect of one or two tires located at one side of each axle. The inverted pavement shows higher shear stresses due to the proximity of the UAB layer to the surface where the loads are applied. In contrast, the conventional pavement exhibits lower shear stresses, as the UAB layer is located at deeper levels away from direct contact with the traffic loads.

Moving on to the transversal direction, Figure 7.13 displays the variation of the shear stresses at the top of the UAB layer for a set of dual axles. Similar to the longitudinal direction, the inverted pavement experiences higher shear stresses compared to the conventional pavement. In both figures, the shear stresses are observed to be higher at the edges of the contact area and are zero directly beneath the tire contact areas for each axle. The differences in the shear stresses observed in the inverted and conventional pavement structures are attributed to the location of the UAB layer and its distance from the surface where the loads are applied.

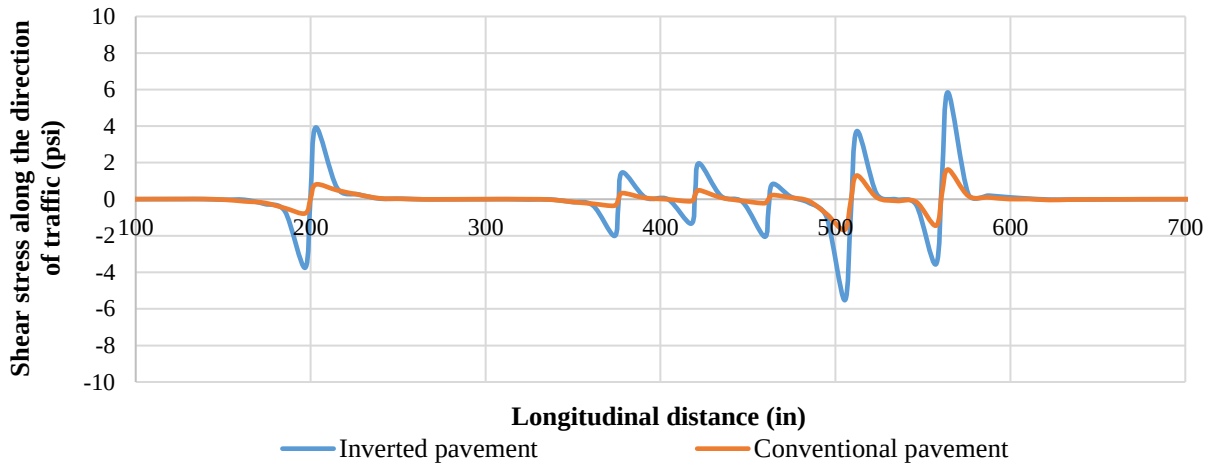

Figure 7.12: Longitudinal shear stresses at the top of the UAB layer beneath one set of tires for all axles in the Virginia inverted (a) and conventional (b) pavement structures.

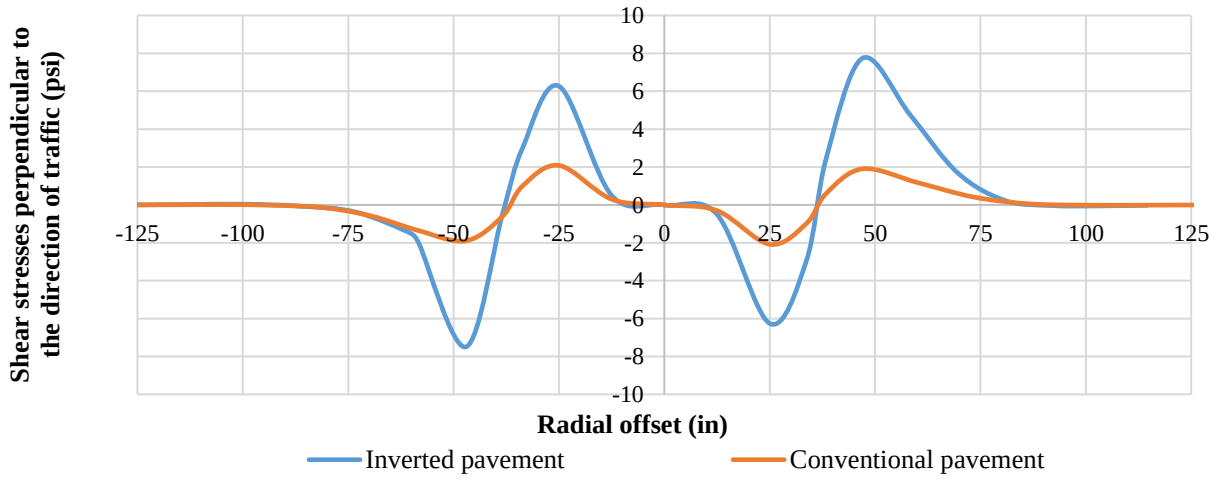

Figure 7.13: Transversal shear stresses at the top of the UAB layer beneath the tires of one set of dual axles in the Virginia inverted (a) and conventional (b) pavement structures.

Once the top surface of the UAB layer in the inverted and conventional pavement structures was evaluated, the study shifted its focus to the dissipation of stress inside the layer. Figure 7.14 presents the vertical stress distribution within the UAB layer below the steering axle for both the inverted and conventional designs. In the displayed figure, the UAB layer is shown in a cross-sectional view, where distinct color bands indicate varying levels of stress. The region with the highest stress magnitude is located at the upper right-hand corner, which vertically aligned with

the superficial points of contact for the applied load. As anticipated, the UAB layer in the inverted pavement structure experiences considerably higher stresses, which can be attributed to its proximity to the surface where the loads are applied.

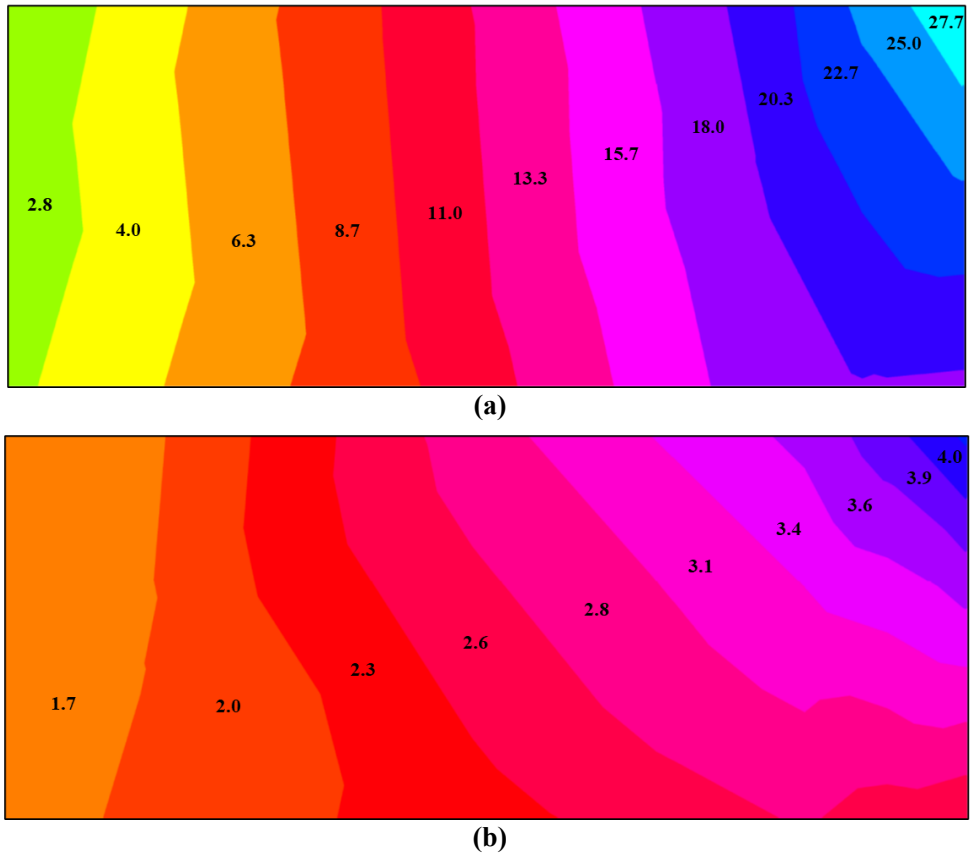

Figure 7.14: Vertical stress distribution within the UAB layer of the Virginia inverted (a) and conventional (b) pavement structures.

Continuing the analysis of the UAB layer in the inverted and conventional pavement structures, Figure 7.15 illustrates the horizontal stress distribution within the layer beneath the middle single axle. Noticeably, the UAB layer of the inverted pavement structure experiences higher stress levels in comparison to the conventional pavement structure. Besides, this graph highlights the inadequacy of assigning isotropic properties to the UAB layer. As depicted, negative stresses are detected at the bottom of the UAB layer, which is an unfeasible outcome since granular materials, like the UAB layer, cannot withstand tensile stresses.

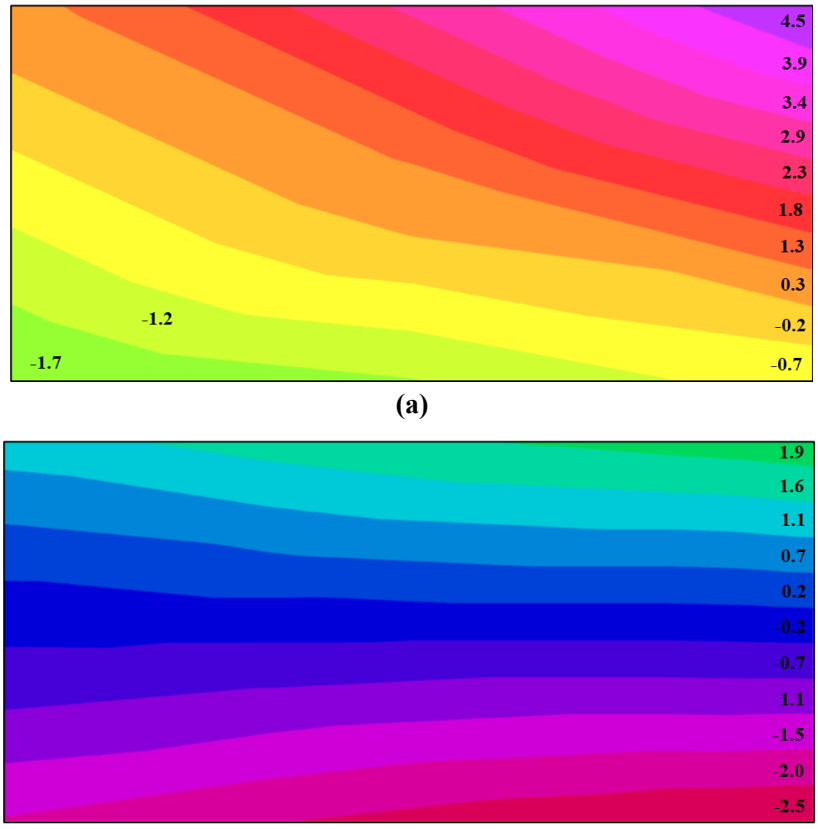

Figure 7.15: Horizontal stress distribution within the UAB layer of the Virginia inverted (a) and conventional (b) pavement structures.

7.3.2. Anisotropic Analysis

Unbound granular mediums exhibit an inherent anisotropy in their material properties, meaning that the properties are directionally dependent. This anisotropy is present even before the layer is subjected to traffic loads and is caused by the random arrangement of particles during compaction. The distribution of interparticle contacts is primarily determined by the geometry of the aggregates and the level of compaction achieved during construction.

In the previous section of this chapter, the isotropic assumption used in the UAB layer simulation was discussed. The isotropic approach considered equal material properties in both the vertical and horizontal directions, which resulted in some interesting findings related to the stress

distribution at the surface and throughout the UAB layer of inverted and conventional pavement structures under the same loading conditions. Specifically, the UAB layer in the inverted pavement structure exhibited significantly higher stresses than the UAB layer in the conventional pavement structure. However, further analysis revealed that the bottom region of the UAB layer was being subjected to tension, which is not plausible in a granular medium properly selected and compacted under ideal moisture conditions.

To address this issue and improve the accuracy of the simulation, the UAB layer was modeled as an anisotropic medium, specifically, as cross-anisotropic with the same material properties in the horizontal plane but different properties in the perpendicular vertical direction to that plane. This cross-anisotropic model was based on the compliance matrix M, which was calculated using the formulation adapted from Main et al. (2019). As displayed in Equation 7.1, the model required four material properties, including the horizontal modulus (E_x), vertical modulus (E_y), and two Poisson's ratios (PR_{xx} and PR_{xy}).

The level of anisotropy was defined as the ratio of the horizontal modulus to the vertical modulus, and two levels of anisotropy were initially evaluated, i.e., E_x/E_y of 0.5 and 0.4. The vertical modulus E_y of 67 ksi was known from the Modulus value obtained through backcalculation analysis, while values for the PR_{xx} and PR_{xy} were assumed to be 0.25 and 0.14, respectively. The resulting stiffness matrix was verified through comparison with pertinent literature on the anisotropic characterization of unbound granular systems, such as Ashtiani (2009) and Al-Qadi et al. (2010).

$$M = \begin{bmatrix} \frac{1}{E_x} & -\frac{PR_{xx}}{E_x} & -\frac{PR_{xy}}{E_y} & 0 & 0 & 0 \\ -\frac{PR_{xx}}{E_x} & \frac{1}{E_x} & -\frac{PR_{xy}}{E_y} & 0 & 0 & 0 \\ -\frac{PR_{xy}}{E_y} & -\frac{PR_{xy}}{E_y} & \frac{1}{E_y} & 0 & 0 & 0 \\ 0 & 0 & 0 & \frac{2(1+PR_{xy})}{E_y} & 0 & 0 \\ 0 & 0 & 0 & 0 & \frac{2(1+PR_{xy})}{E_y} & 0 \\ 0 & 0 & 0 & 0 & 0 & 2\left(\frac{1}{E_x}+\frac{PR_{xx}}{E_x}\right) \end{bmatrix} \quad (7.1)$$

Vertical stress distributions in the UAB layer were computed for both Virginia inverted and conventional pavement structures under different levels of anisotropy (0.5 and 0.4). The analysis compared cross-anisotropic results to their isotropic counterpart (E_x/E_y of 1) to assess the impact of assuming a lower horizontal stiffness in the unbound granular medium. Figures 7.16 to 7.18 display cross-sectional slices of the UAB layer with colored regions representing the stress distribution due to the application of dual axle loads on the top of the AC layer of the pavement structures. The highest stress magnitude was found at the upper right-hand corner, which coincides vertically with the points of contact of the load at the surface.

When the horizontal Modulus is half of the vertical Modulus, as depicted in Figure 7.16(b), it becomes apparent that the UAB layer in the inverted pavement structure experiences greater vertical stresses below the last dual axle compared to the stresses that develop when isotropic properties are assumed. Moreover, when E_x accounts for only 40% of E_y, the vertical stresses in the UAB layer of the inverted pavement structure are even higher, as can be seen in Figure 7.16(c). It follows that a decrease in the ratio of E_x to E_y of the UAB layer leads to higher vertical stresses.

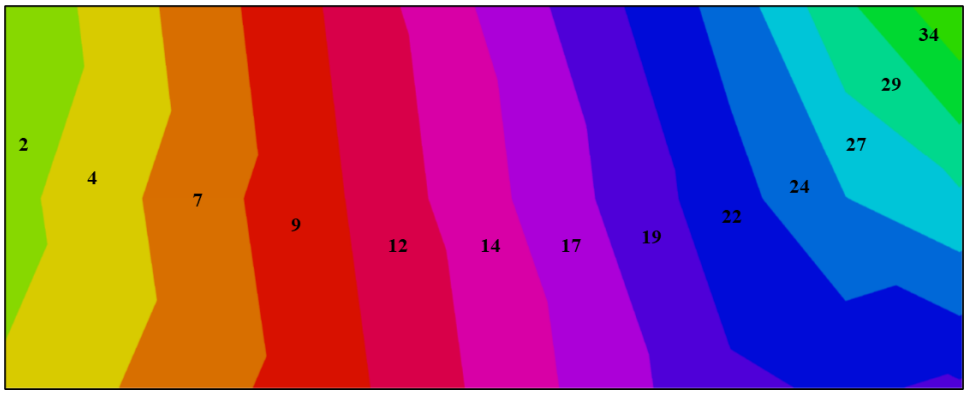

(a)

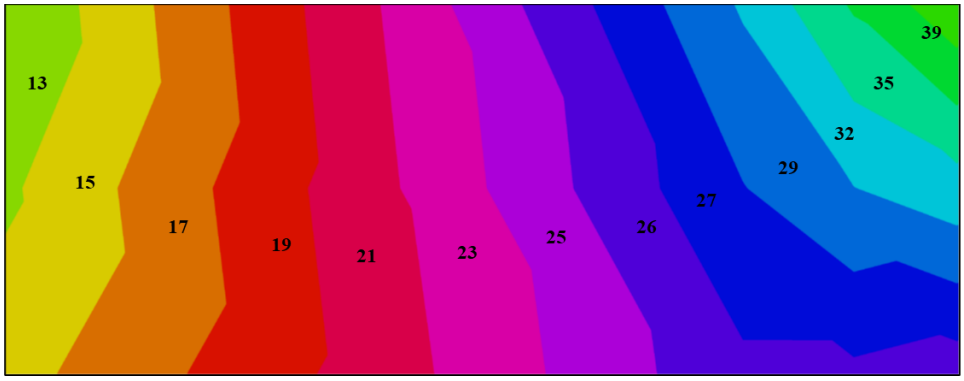

(b)

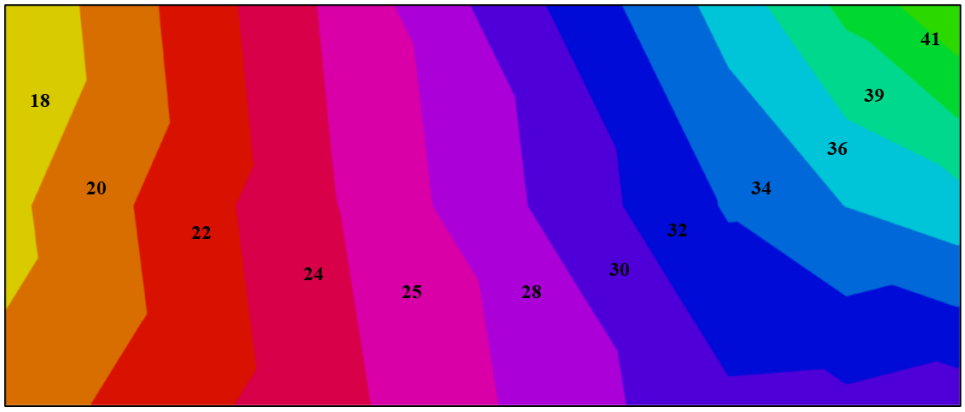

(c)

Figure 7.16: Vertical stress distribution within the UAB layer of Virginia the inverted pavement beneath the dual axle assuming E_x/E_y=1.0 (a), E_x/E_y=0.5 (b), and E_x/E_y=0.4 (c).

Similar to the behavior observed in the inverted pavement structure, the conventional pavement structure also exhibits a comparable trend when examining the vertical stress distribution within the UAB layer under the load from the last set of dual axles. Figure 7.17

demonstrates that as the ratio of E_x/E_y shifts from 0.5 to 0.4, the vertical stresses developed in the granular medium attain greater magnitudes. Conversely, when the ratio is equal to 1, the estimated vertical stresses developed in the UAB layer are at their lowest intensities.

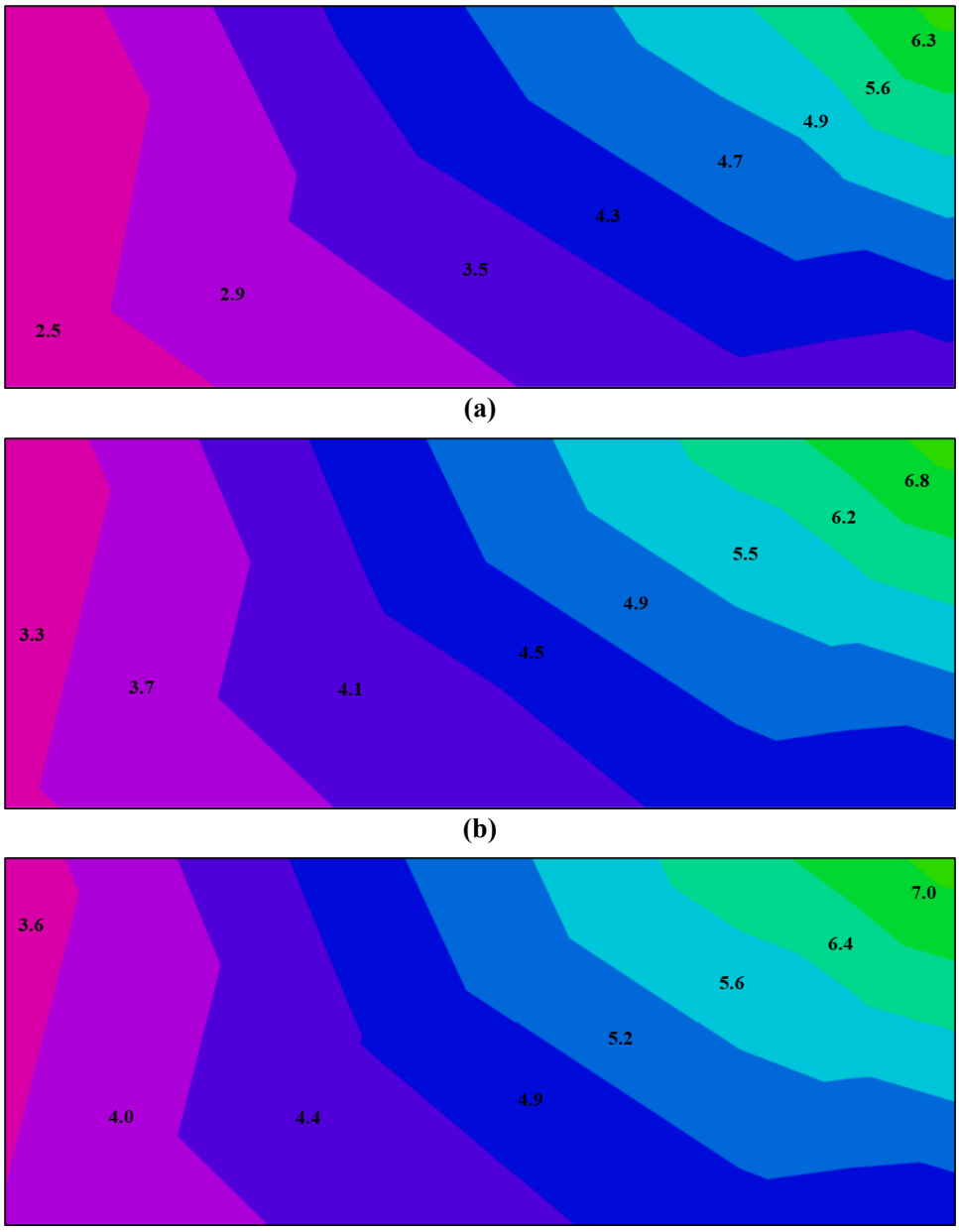

Figure 7.17: Vertical stress distribution within the UAB layer of the Virginia conventional pavement beneath the dual axle assuming E_x/E_y=1.0 (a), E_x/E_y=0.5 (b), and E_x/E_y=0.4 (c).

The evaluation of the dissipation of horizontal stresses within the UAB layer of the inverted pavement structure was conducted for various levels of anisotropy under the loads imposed by the dual axles. Figure 7.18 illustrates that the negative stresses observed at the bottom of the UAB layer under isotropic conditions were eliminated when the layer was assigned with cross-anisotropic properties. Consequently, the entire UAB layer was subjected to compressive stresses, which is in line with the anticipated behavior of a granular medium.

The findings presented in the previous figures demonstrate how the inherent anisotropy of the UAB layer affects the magnitude of stresses transmitted through the medium. Assuming isotropic properties for the UAB layer in both inverted and conventional pavement structures could result in erroneous or underestimated stresses, as anisotropic approaches show higher stress magnitudes developed within the layer. This may lead to an insufficient thickness of the UAB layer, ultimately affecting the overall pavement design and potentially causing structural failure.

7.3.3. Model validation with field measurements

To confirm the accuracy of the numerical simulation of the Virginia inverted pavement section, the results were compared to measurements obtained by instruments embedded within the pavement during data collection at the Bull Run testing site. Although an exact match between the modeled pavement responses and the in-situ measurements is not anticipated, the goal of the analysis is to achieve a reasonable approximation of the simulated values to the measured values to validate the numerical simulation.

The simulated stresses and strains from the Virginia inverted pavement structure were compared with measurements obtained from longitudinal strain gauges positioned horizontally at the bottom of the AC layer and pressure cells installed at the top and bottom of the UAB layer. The simulated pavement responses were obtained by assuming isotropic characteristics for the

UAB layer and by varying the E_x/E_y ratios in increments of 0.1, encompassing nine levels of anisotropy, ranging from 0.1 to 0.9.

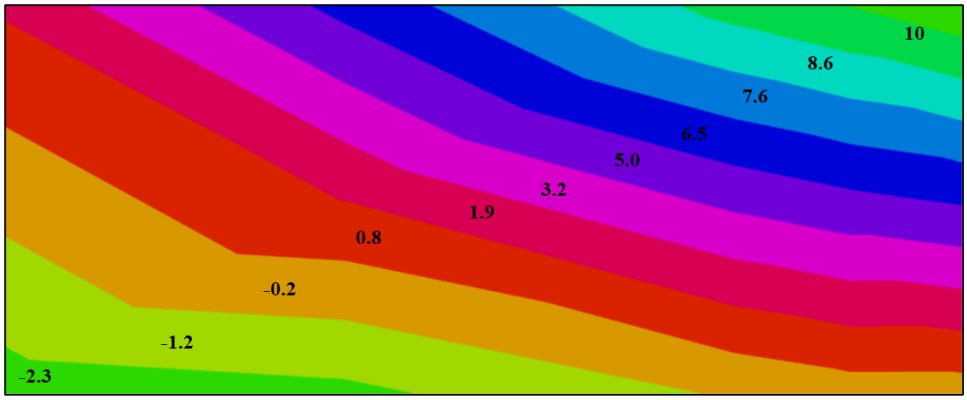

(a)

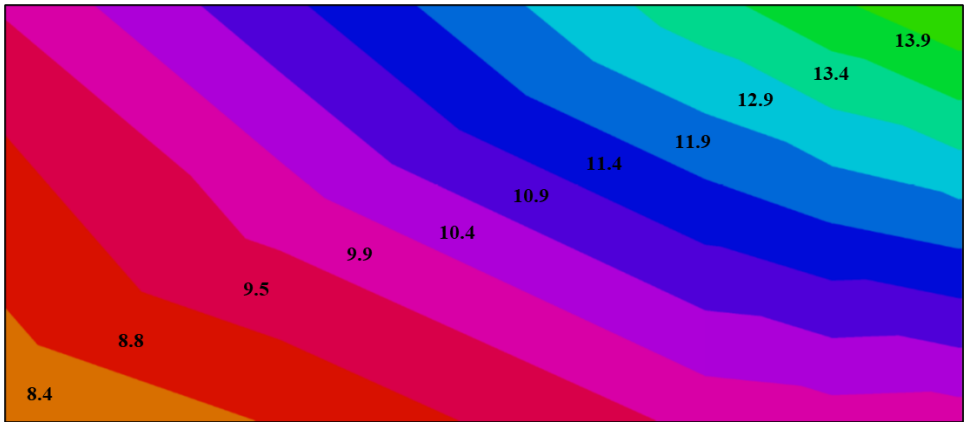

(b)

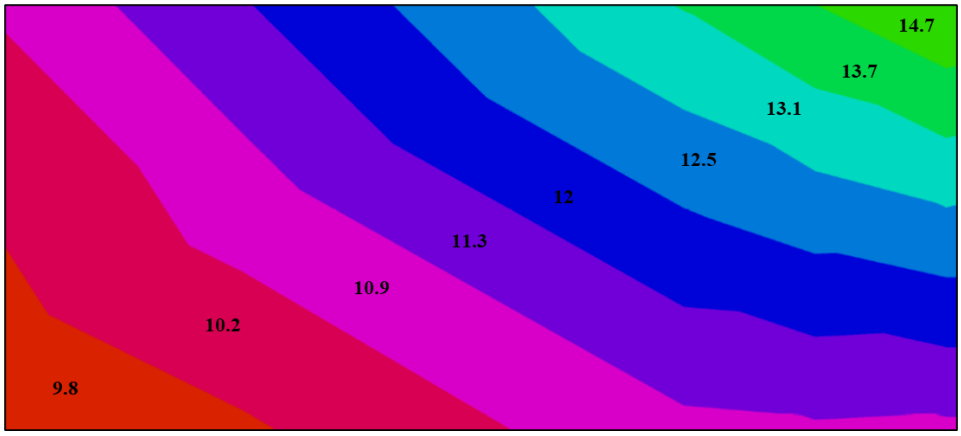

(c)

Figure 7.18: Horizontal stress distribution within the UAB layer of the Virginia inverted pavement beneath the dual axle assuming E_x/E_y=1.0 (a), E_x/E_y=0.5 (b), and E_x/E_y=0.4 (c).

Three strain gauges were installed at the bottom of the AC layer during the data collection process to measure the horizontal longitudinal strains caused by traffic loads. These sensors, identified as SG-2, SG-4, and SG-6, were placed equidistantly from one another at 4 ft intervals. The data was collected in three runs of a truck passing over the area where the instruments were installed. The measurements captured by SG-6 during Runs 2 and 3 are shown in Figure 7.19. The data displayed a high level of noise. Data from Run 1 was not included as the strain gauge failed to collect any measurements.

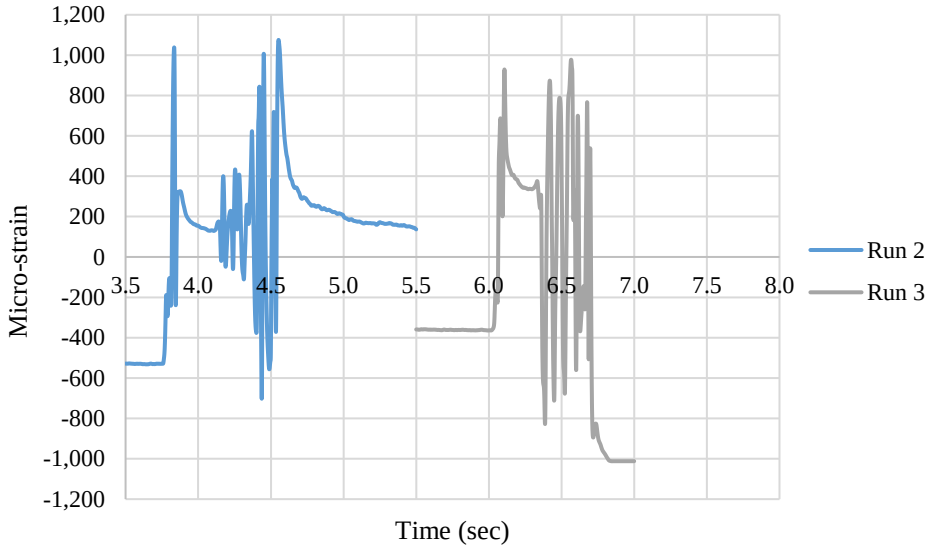

Figure 7.19: Data measured by SG-6 placed longitudinally to the traffic flow below the AC layer of the Virginia inverted pavement section during Runs 2 and 3.

The readings captured by SG-4 at the bottom of the AC layer during the 3 truck runs are displayed in Figure 7.20. The peak values of the readings represent the passing of each axle. Despite the large magnitude of the loads, the readings are small. This may be because the wheel path of the truck did not align with the location of SG-4, as evidenced by the negative values and low strains recorded for the dual axles, indicating compression instead of the expected tensile strains.

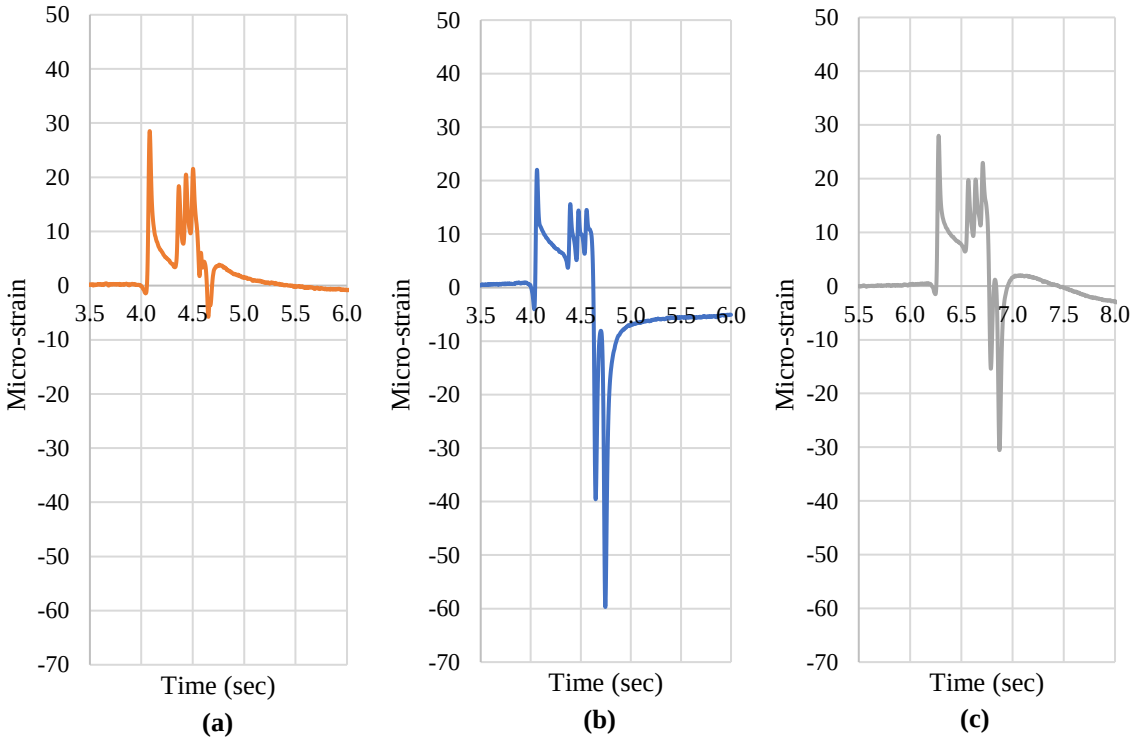

Figure 7.20: Data measured by SG-4 placed longitudinally to the traffic flow below the AC layer of the Virginia inverted pavement section during Run 1 (a), Run 2 (b), and Run 3 (c).

In the analysis, only the strains measured by SG-2 during Runs 1, 2, and 3 were used. Figure 7.21 displays the strain variation while the heavy truck passed over the sensors, and three tables with the measurements for each axle type are also included. The recorded values are reasonable and were compared to the simulated values obtained using the numerical model of the Virginia inverted pavement structure.

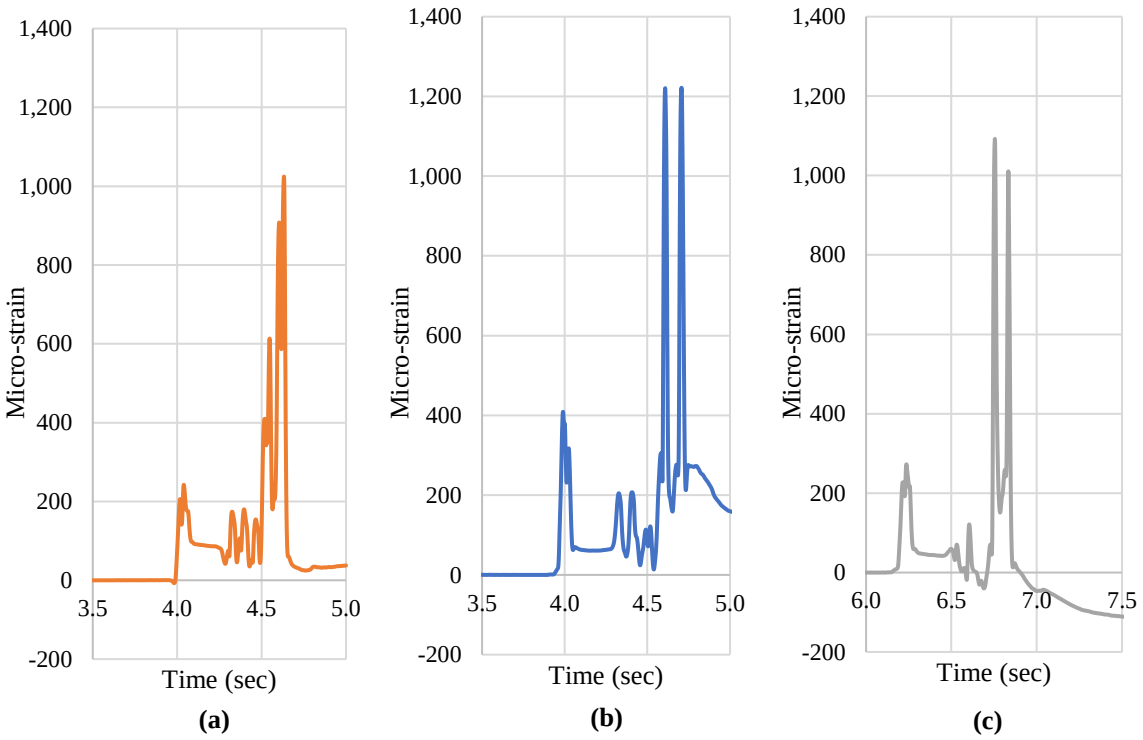

SG-2 Run-1

Axle	*Time*	*Microstrain*
Entrace baseline	3.8510	0.0000
Steering	4.0390	241.9569
Pony 1	4.3260	173.7593
Pony 2	4.3960	179.7715
Pony 3	4.4660	154.0437
Dual 1	4.5480	613.0537
Dual 2	4.6330	1024.2076
Exit baseline	4.9730	36.2373

SG-2 Run-2

Axle	*Time*	*Microstrain*
Entrace baseline	3.6460	0.0000
Steering	3.9900	408.8417
Pony 1	4.3270	204.7362
Pony 2	4.4080	207.1469
Pony 3	4.5180	121.6316
Dual 1	4.6080	1220.6474
Dual 2	4.7070	1221.6609
Exit baseline	5.6300	130.0108

SG-2 Run-3

Axle	*Time*	*Microstrain*
Entrace baseline	5.9900	0.0000
Steering	6.2360	272.6278
Pony 1		
Pony 2		
Pony 3		
Dual 1	6.7550	1092.1497
Dual 2	6.8340	1010.4219
Exit baseline	7.6780	-115.8354

Figure 7.21: Data measured by SG-2 placed longitudinally to the traffic flow below the AC layer of the Virginia inverted pavement section during Run 1 (a), Run 2 (b), and Run 3 (c).

Figure 7.22 presents the horizontal longitudinal strain responses of the inverted pavement at the bottom of the AC layer as calculated by the FE model. In addition to the isotropic analysis, nine different levels of anisotropy were examined. The bar charts in the figure indicate the resulting strains for each axle, with lower E_x/E_y ratios corresponding to higher strains. The values presented in the chart correspond to the pavement responses that resemble those measured in the field.

As summarized in Table 7.2, the strain values calculated at anisotropy levels of 0.3 and 0.2 for the steering axle are close to the measured responses for Run 1. For the Single 1 axle, the strain values calculated at anisotropy levels of 0.2 and 0.1 closely resemble the measured responses for Runs 1 and 2. For the Single 2 axle, the values calculated at anisotropy levels of 0.4, 0.3, 0.2, and 0.1 are similar to the measured responses for Runs 1 and 2. Finally, for the Single 3 axle, the values calculated at anisotropy levels of 0.8, 0.7, and 0.6 closely resemble the measured responses for Run 1.

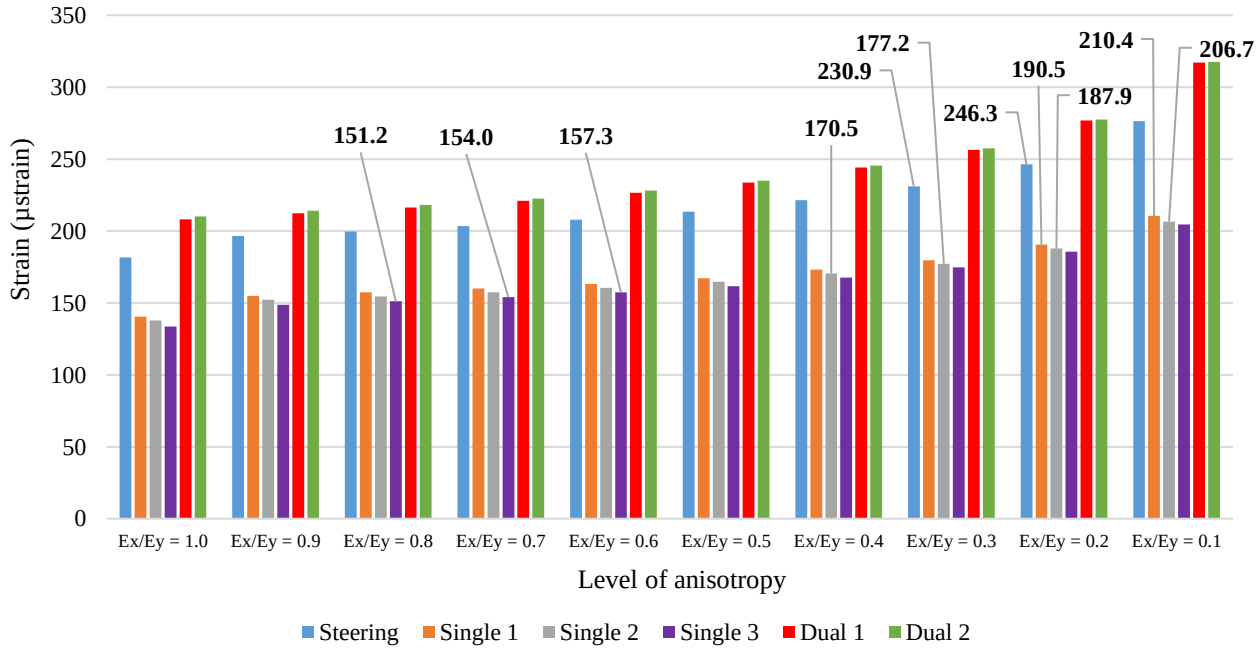

Figure 7.22: Calculated horizontal longitudinal strains developed at the bottom of the AC layer of the Virginia inverted pavement structure.

Table 7.2. Comparison of calculated and measured longitudinal strains at the bottom of the AC layer of the Virginia inverted pavement section.

Axle type	Level of anisotropy	Calculated strains (μstrain)	Measured strains (μstrain)	Run No.
Steering	E_x/E_y=0.3	246.3	241.9	Run 1
	E_x/E_y=0.2	230.9		
Single 1	E_x/E_y=0.2	190.5	173.76	Run 1
	E_x/E_y=0.1	210.4	204.74	Run 2
Single 2	E_x/E_y=0.4	170.5		
	E_x/E_y=0.3	177.2	179.7	Run 1
	E_x/E_y=0.2	187.9	207.1	Run 2
	E_x/E_y=0.1	206.7		
Single 3	E_x/E_y=0.8	151.2		
	E_x/E_y=0.7	154	154	Run 1
	E_x/E_y=0.6	157.3		

Two pressure cells i.e., PC-1 and PC-6, were installed at the top of the UAB layer to measure the vertical stresses induced by traffic loads during data collection. They were installed 26 ft apart from one another, and data was collected in three runs of the truck over the area where the instruments were installed. Figure 7.23(a) shows an example of the data collected by a pressure cell, with each peak value indicating the vertical stresses induced by each axle of the truck. While PC-1 was able to register the responses induced by all axles, excessive noise was recorded by the pressure cell on certain occasions, as shown in Figure 7.23(b), making it impossible to estimate the vertical stress. This was the case for Run 3 of PC-1. In other cases, as shown in Figure 7.23(c), some axle responses could not be captured by the device, such as the Single 1 axle not being measured by PC-6 in Run 1.

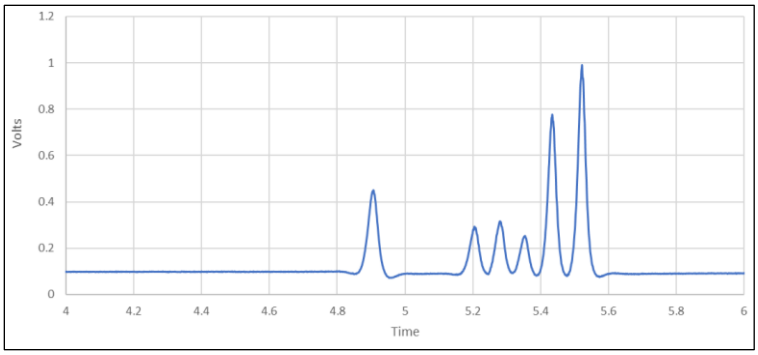

(a)

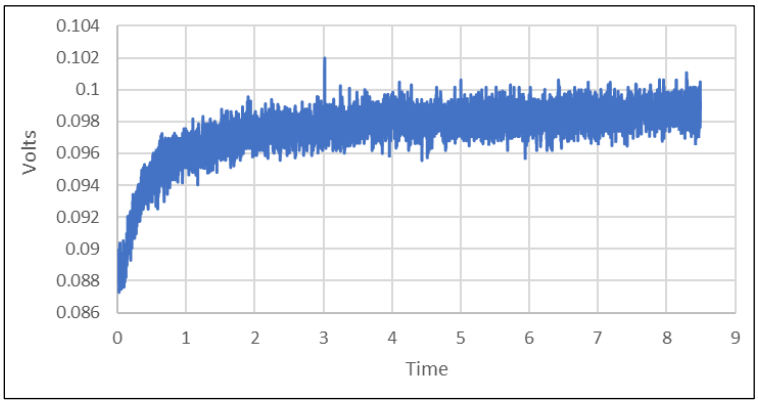

(b)

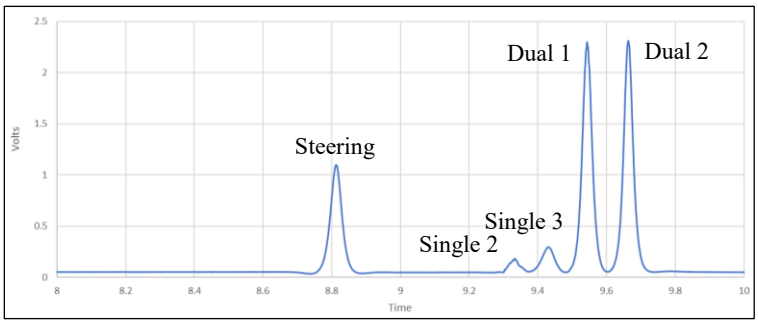

(c)

Figure 7.23: Data measured by the following pressure cells installed at the top of the UAB layer of the Virginia inverted pavement section: (a) PC-1/Run 2, (b) PC-1/Run 3, and (c) PC-6/Run 1.

Two pressure cells i.e., PC-3 and PC-4, were installed at the bottom of the UAB layer to measure vertical stress induced by the truck. These pressure cells were positioned 18 ft apart from each other. The responses of all pressure cells in all three runs are compiled in Table 7.3.

Table 7.3. Data measured by pressure cells installed at the top and bottom of the UAB layer of the Virginia inverted pavement section.

Axle type	Pressure Cell	Vertical stress (psi)		
		Run 1	Run 2	Run 3
Steering	PC1	36.26	7.11	Not recorded
	PC6	20.88	7.34	Not recorded
	PC3	19.84	6.43	Not recorded
	PC4	24.55	10.40	Not recorded
Single 1	PC1	Not recorded	4.39	Not recorded
	PC6	Not recorded	4.34	3.61
	PC3	Not recorded	3.93	Not recorded
	PC4	Not recorded	5.53	4.84
Single 2	PC1	4.26	4.74	Not recorded
	PC6	4.47	4.65	2.98
	PC3	2.92	3.99	Not recorded
	PC4	5.67	6.21	3.86
Single 3	PC1	7.05	3.70	Not recorded
	PC6	6.57	4.32	3.59
	PC3	5.00	3.51	Not recorded
	PC4	8.33	6.09	5.12
Dual 1	PC1	43.35	12.74	Not recorded
	PC6	42.32	14.65	7.81
	PC3	22.82	9.65	Not recorded
	PC4	30.88	17.40	10.68
Dual 2	PC1	47.75	16.4	Not recorded
	PC6	42.55	15.72	8.28
	PC3	24.79	11.65	Recorded
	PC4	30.15	18.77	10.87

Figure 7.24 shows the vertical stress responses developed at the top of the UAB layer of the inverted pavement calculated by the FE model. Besides the isotropic analysis, 9 levels of anisotropy were evaluated. It can be seen that the lower the E_x/E_y ratio, the higher the resulting stresses in each axle. The values indicated in the bar charts correspond to those pavement responses similar to the measured values from the field. As displayed in Table 7.4, for the case of the steering axle, the vertical stress values calculated at levels of anisotropy of 0.4, 0.3, and 0.2 are close to the measured responses for PC-1/Run 1. For the case of the Dual 1 axle, the stress values calculated at levels of anisotropy of 0.4, 0.3, and 0.2 are close to the measured responses for PC-1/Run 1 and

PC-6/Run 1. For the case of the Dual 2 axle, the values calculated at levels of anisotropy of 0.4, 0.3, 0.2, and 0.1 are close to the measured responses for PC-1/Run 1 and PC-6/Run 1.

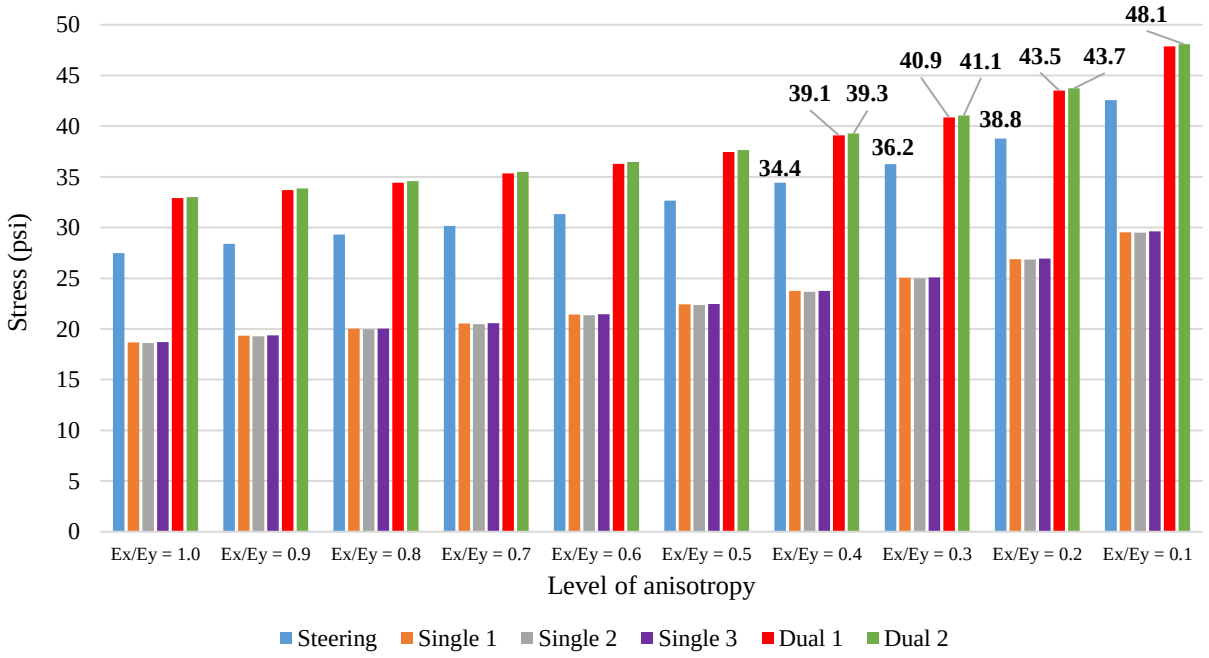

Figure 7.24: Calculated vertical stresses developed at the top of the UAB layer of the Virginia inverted pavement structure.

Table 7.4. Comparison of calculated and measured vertical stresses at the top of the UAB layer of the Virginia inverted pavement section.

Axle type	Level of anisotropy	Calculated vertical stress (psi)	Measured vertical stress (psi)	Pressure cell No.	Run No.
Steering	E_x/E_y=0.4	34.4	36.3	PC-1	Run 1
	E_x/E_y=0.3	36.2			
	E_x/E_y=0.2	38.8			
Dual 1	E_x/E_y=0.4	39.1	43.3	PC-1	Run 1
	E_x/E_y=0.3	40.9	42.3	PC-6	Run 1
	E_x/E_y=0.2	43.5			
Dual 2	E_x/E_y=0.4	39.3	47.7	PC-1	Run 1
	E_x/E_y=0.3	41.1	42.4	PC-6	Run 1
	E_x/E_y=0.2	43.7			
	E_x/E_y=0.1	48.1			

Figure 7.25 shows the vertical stress responses developed at the bottom of the UAB layer of the inverted pavement calculated by the FE model. Besides the isotropic analysis, 9 levels of anisotropy were evaluated. It can be seen that the lower the E_x/E_y ratio, the higher the resulting stresses in each axle. The values indicated in the bar charts correspond to those pavement responses similar to the measured values from the field. As summarized in Table 7.5, for the case of the steering axle, the vertical stress values calculated at levels of anisotropy of 0.5, 0.4, and 0.3 are close to the measured responses for PC-3/Run 1 and PC-4/Run 1. For the case of the Dual 1 axle, the stress values calculated at levels of anisotropy of 0.4, 0.3, 0.2, and 0.1 are close to the measured responses for PC-3/Run 1, and PC-4/Run 1. For the case of the Dual 2 axle, the values calculated at levels of anisotropy of 0.3, 0.2, and 0.1 are close to the measured responses for PC-3/Run 1 and PC-4/Run 1.

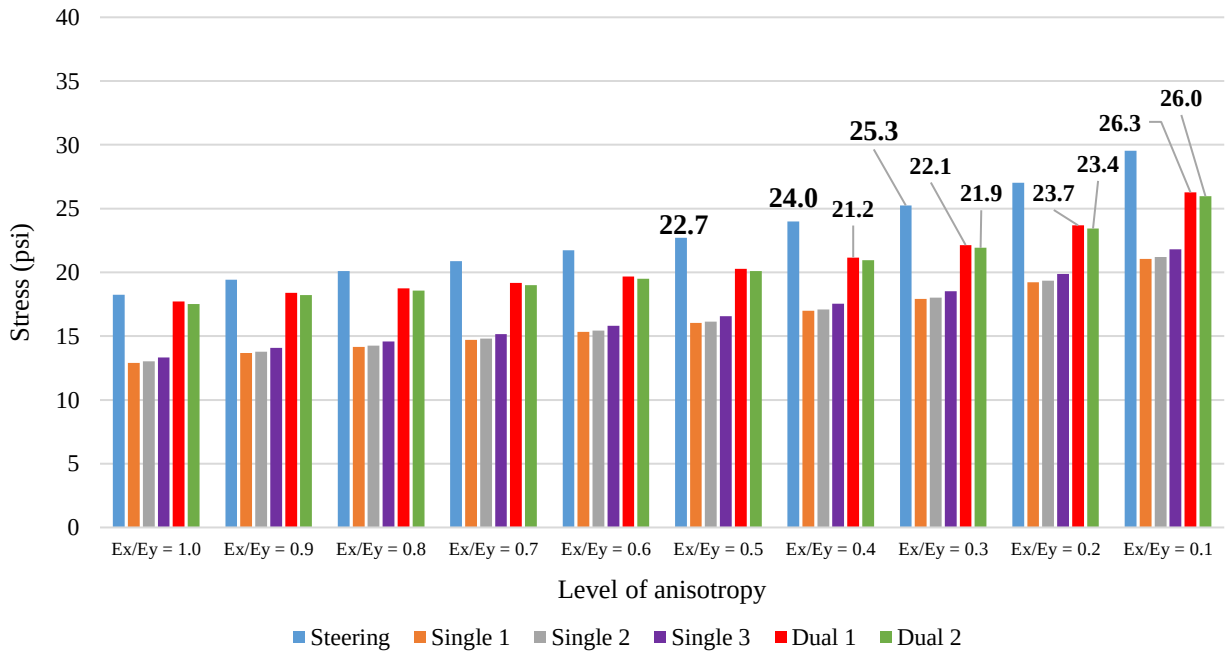

Figure 7.25: Calculated vertical stresses developed at the bottom of the UAB layer of the Virginia inverted pavement structure.

Table 7.5. Comparison of calculated and measured vertical stresses at the bottom of the UAB layer of the Virginia inverted pavement section.

Axle type	Level of anisotropy	Calculated vertical stress (psi)	Measured vertical stress (psi)	Pressure cell No.	Run No.
Steering	E_x/E_y=0.5	22.7	19.8	PC-3	Run 1
	E_x/E_y=0.4	24.0	24.5	PC-4	Run 1
	E_x/E_y=0.3	25.3			
Dual 1	E_x/E_y=0.4	21.2	22.8	PC-3	Run 1
	E_x/E_y=0.3	22.1	30.9	PC-4	Run 1
	E_x/E_y=0.2	23.7			
	E_x/E_y=0.1	26.3			
Dual 2	E_x/E_y=0.3	21.9	24.8	PC-3	Run 1
	E_x/E_y=0.2	23.4	30.2	PC-4	Run 1
	E_x/E_y=0.2	26.0			

The results demonstrate that there is a correspondence between the computed responses obtained from the FE-based simulation and the responses obtained from the field measurements when assuming a level of anisotropy near E_x/E_y of 0.3. This discovery aligns with the research of Masad et al. (2006), who compared measured pavement surface deflections against predictions derived from the FE method by supposing anisotropy levels of 0.3, 0.4, and 0.5 for two non-treated granular layers situated on top of the subgrade soil and beneath the asphalt concrete layer. The authors concluded that the best agreement between the projected and measured deflections was attained when the ratio of horizontal modulus to vertical modulus was 0.3.

Differences between the measured and calculated pavement responses could be attributed to the dynamic nature of the load during field testing and the static nature of the load in the numerical simulation. In addition, errors during data collection in the field and the wandering effect of the loading aggregate haul truck when passing over the sensors may have also contributed to the differences. It appears that Run 1 was the most accurate in terms of the proximity of the sensors to the location where the truck passed, as evidenced by the high number of calculated pavement responses that were similar to the values measured by the sensors during that run.

Chapter 8: Numerical Analysis of the Texas Inverted Pavement Structure

An inverted pavement section was constructed in two segments of State Highway SH-123 located in Corpus Christi, which is a heavily trafficked roadway belonging to the Eagle Ford Shale Area, an energy developing region of East Texas. The construction plan specified a 52 ft wide and approximately 23,318 ft long inverted pavement section consisting of an AC layer at the top, an UAB layer at the bottom, and an underlying CTB layer, all of which were resting on top of the subgrade soil. Two years after the construction, GPR testing was conducted on the inverted pavement section to confirm the thickness of each layer of the system as per the design plans. Additionally, an in-situ FWD test was conducted at the top of the pavement surface using backcalculation analysis to estimate the Moduli of each layer.

Using data obtained from the field, a series of numerical models were developed to investigate the mechanical response of the Texas inverted pavement section to specific loading scenarios. The FE method was utilized to analyze the structural behavior of the pavement. The study also involved comparing the inverted pavement model to a conventional design, in which the order of UAB and CTB layers was reversed. Critical stresses and strains in specific areas of the pavement system were examined for both pavement designs using Abaqus software. The investigation focused on the load distribution capacity of the UAB layer, which is a crucial structural component of the layered system.

8.1. FIELD DATA TESTING RESULTS

The location of SH-123, which spans from Interstate 35 in San Marcos to US 181 in Karnes City, is depicted in Figure 8.1. An inverted pavement configuration was used to construct two segments of SH-123, namely from station 79+92 to station 189+80 and from station 501+90 to

station 625+20. The design plans specified a 3-layered system consisting of a 5-in AC layer, an 8-in UAB layer, and an 8-in CTB layer, all placed on top of the subgrade soil.

Figure 8.1: Location of SH-123 between Karnes City and San Marcos in Texas.

Validation of the layer configuration and thicknesses was conducted using GPR results, as depicted in Figure 8.2, which displays typical GPR readings obtained from the Texas inverted pavement section. Generally, the layer interfaces were identifiable except for the interface between the CTB layer and the SG soil, as the GPR cannot penetrate effectively beyond 20 in. The GPR image also revealed that the AC layer thickness varied between 4 to 6 in, and the base layer thickness was around 8 in, consistent with the construction project design plans.

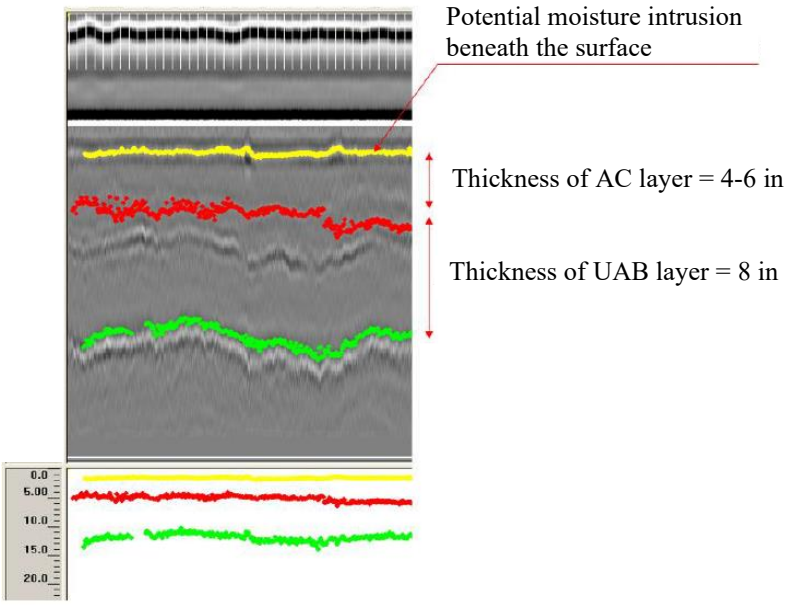

Figure 8.2: Data sample from GPR readings performed in the Texas inverted pavement structure.

Continuing the analysis, an FWD test was conducted on the Texas inverted pavement section by applying an average pressure of 90 psi on the AC layer. Seven geophones were placed at lateral offset values of 0, 8, 12, 18, 24, 36, and 60 in to measure the resulting surface deflections. The vertical deformations were then used for a backcalculation analysis to estimate the Modulus values of each layer and the subgrade soil. Figure 8.3 illustrates the stiffness values of each layer in the inverted pavement structure. Using the backcalculated Modulus values, a conventional pavement design was defined by switching the order of the two layers below the AC layer in the inverted configuration. The layer configuration of the conventional pavement design is also presented in Figure 8.3. The conventional pavement follows the standard design approach, with decreasing stiffness values from top to bottom, where the layer closest to the surface has the highest load-bearing capacity and quality. Conversely, in the inverted pavement, the UAB layer is sandwiched between two stiffer layers, with the AC layer having the highest Modulus value.

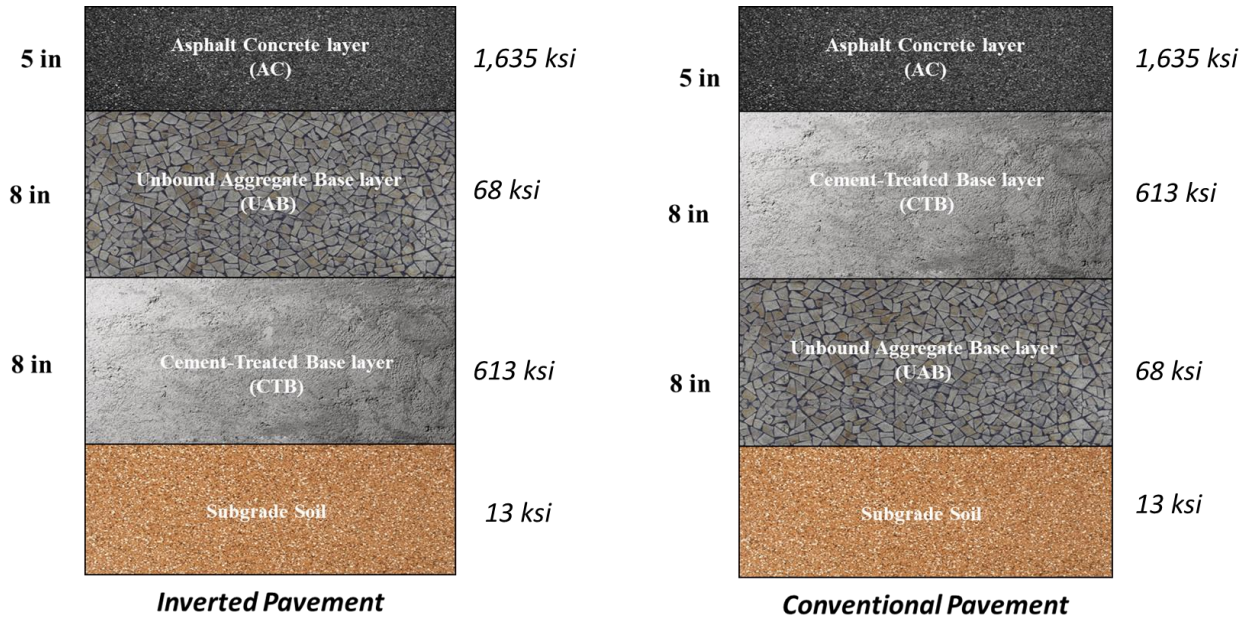

Figure 8.3: Backcalculated Modulus values of each layer of the Texas inverted and conventional pavement sections.

8.2. NUMERICAL ANALYSIS CONSIDERATIONS

Based on the numerical model of the Virginia inverted pavement section, which was validated with real pavement responses measured from the field, the Texas inverted pavement structure was simulated following the same modeling considerations. The response of the Texas inverted pavement structure was evaluated considering the same axle load configuration and weights of the aggregate haul truck, as well as the contact areas per tire used in the Virginia inverted pavement model.

The approach utilized for the Virginia inverted pavement simulation was adopted for modeling the Texas inverted pavement. This involved defining the surface area dimensions of the pavement block or parallelepiped volume where the truck loads were perpendicularly applied. Further criteria involved determining the suitable thickness of the subgrade soil and accounting for the lateral free space around the truck to ensure that the stress distribution was appropriate and there were no adverse effects from the surrounding boundary conditions on the critical pavement

responses. In addition to the modeling criteria previously mentioned, further considerations were inherited from the Virginia inverted pavement simulation, specifically regarding the choice of element type for meshing the pavement structure.

The Texas inverted pavement section was simulated in accordance with the thicknesses and stiffnesses outlined in Figure 8.3, using assumed PRs of 0.35, 0.25, 0.20, and 0.40 for the AC layer, UAB layer, CTB layer, and SG soil, respectively. In order to account for the effects of neighboring axles on the stress and strain distributions, a full-truck analysis was conducted. To provide a comprehensive understanding of the mechanical behavior of each layer and SG soil, all materials were initially modeled as linear elastic and subsequently transitioned to an anisotropic analysis.

8.3. ISOTROPIC ANALYSIS

Figure 8.4 visually represents the tensile stresses and strains at the bottom of the AC layer for both the Texas inverted and conventional pavement structures. These charts indicate the tensile stresses for each axle type obtained from the full-truck analyses i.e., all axles acting simultaneously. As expected, the inverted pavement structure showed higher tensile stresses and strains. The reason for this difference can be attributed to the type of layer beneath the AC layer. The more rigid CTB layer in the conventional pavement restricts the deformation of the AC layer, resulting in lower tensile stresses and strains at the bottom of the surface layer. On the other hand, the flexible UAB layer in the inverted pavement design permits greater deformation of the AC layer, resulting in higher tensile stresses and strains at the bottom of the asphaltic layer.

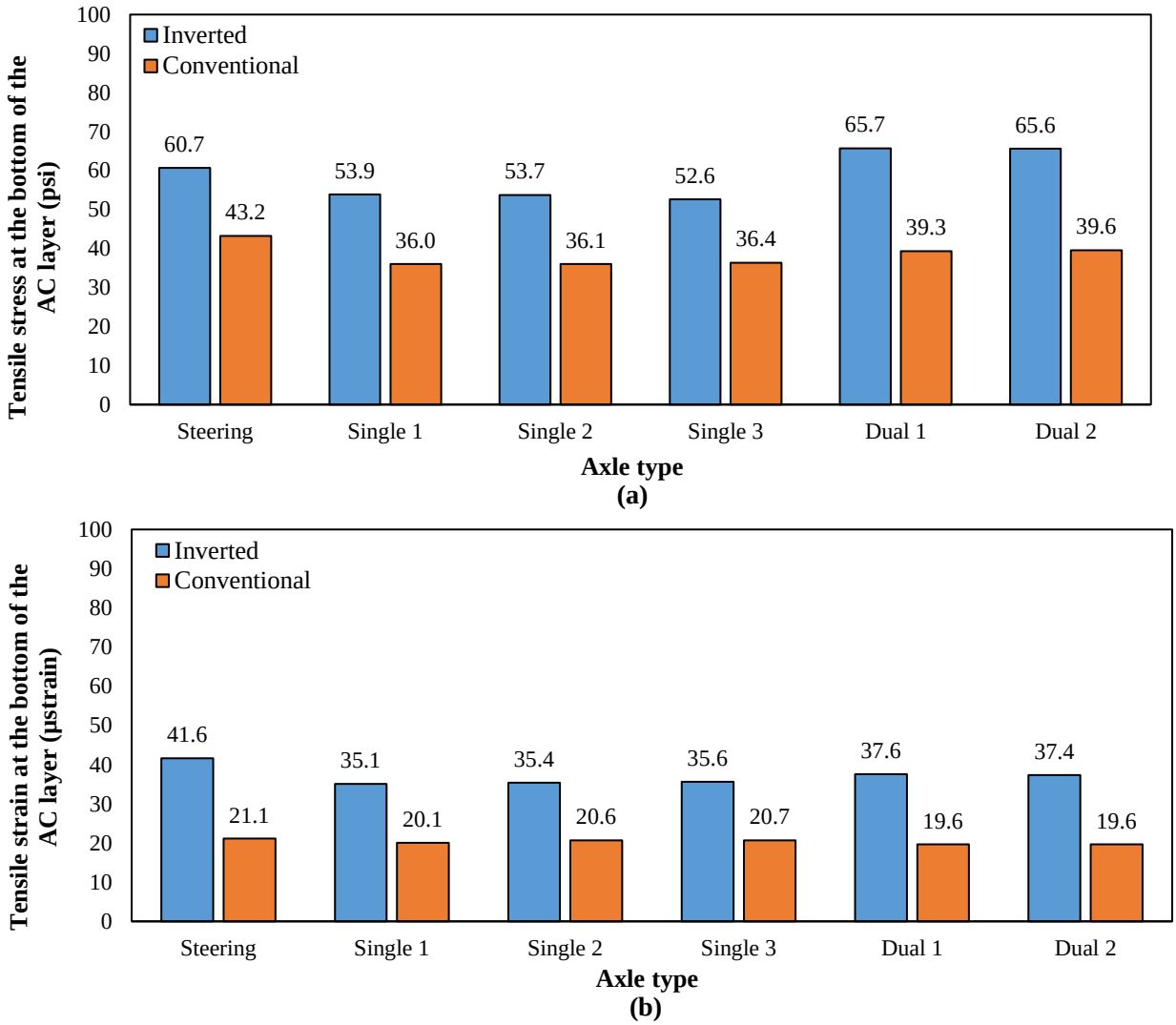

Figure 8.4: Tensile stresses (a) and strains (b) developed at the bottom of the AC layer in the Texas inverted and conventional pavement structures considering a full truck analysis.

In addition to the aforementioned pavement responses, the analysis also considered the compressive stresses and strains at the top of the SG soil, which were found to be lower in the inverted pavement structure for all axle types. As depicted in Figure 8.5, these results suggest that the layer configuration of the inverted pavement design was more effective in distributing the load, resulting in lower levels of stresses and strains transmitted to the SG soil from the pavement surface.

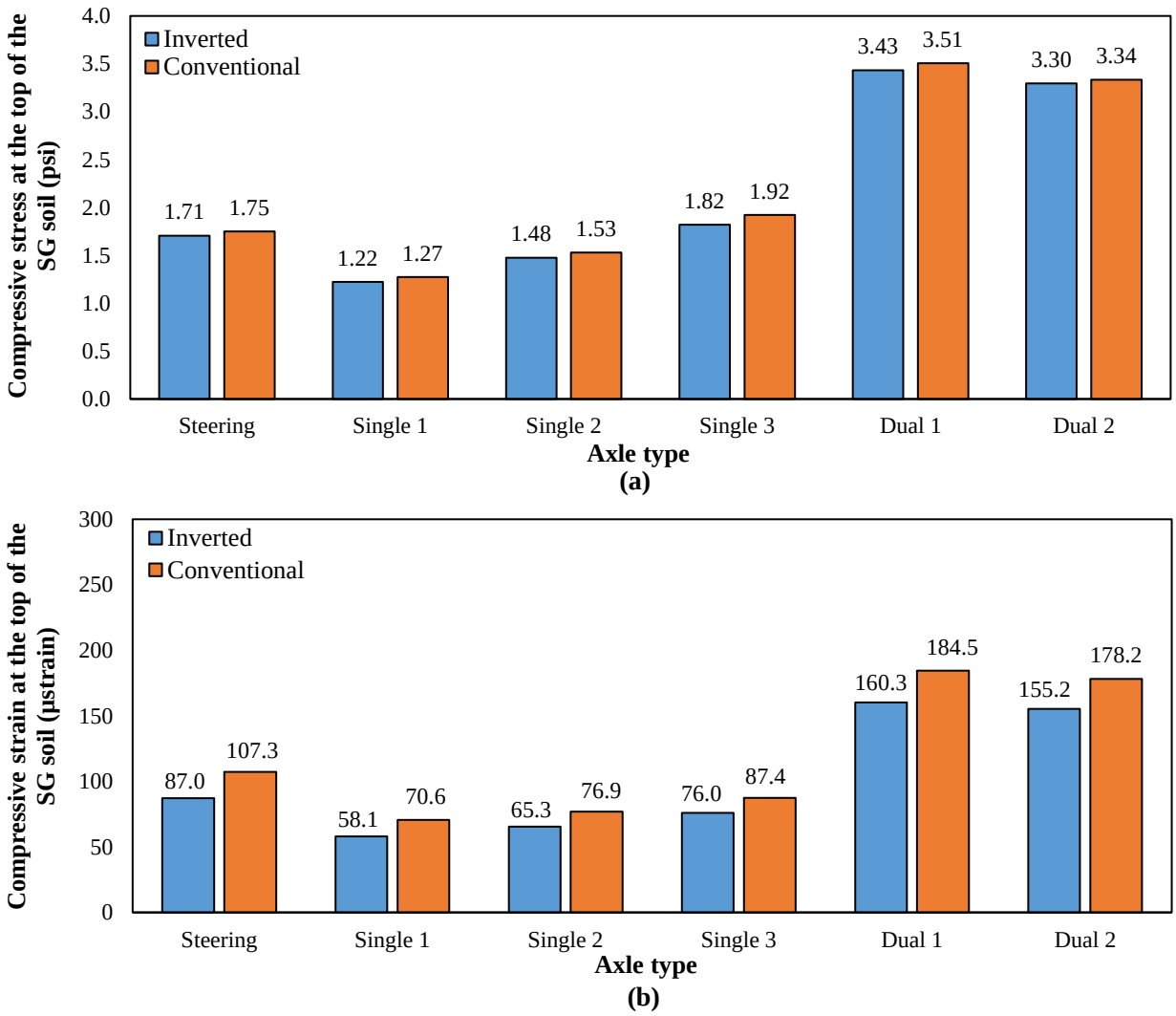

Figure 8.5: Compressive stresses (a) and strains (b) developed at the top of the SG soil in the Texas inverted and conventional pavement structures considering a full truck analysis.

Figure 8.6 presents a comparison of the vertical deformation at the top of the AC layer of both inverted and conventional pavement structures under the application of all axles at the same time. The results show that the inverted pavement structure has higher deformations, indicating its higher susceptibility to experiencing rutting or permanent deformation.

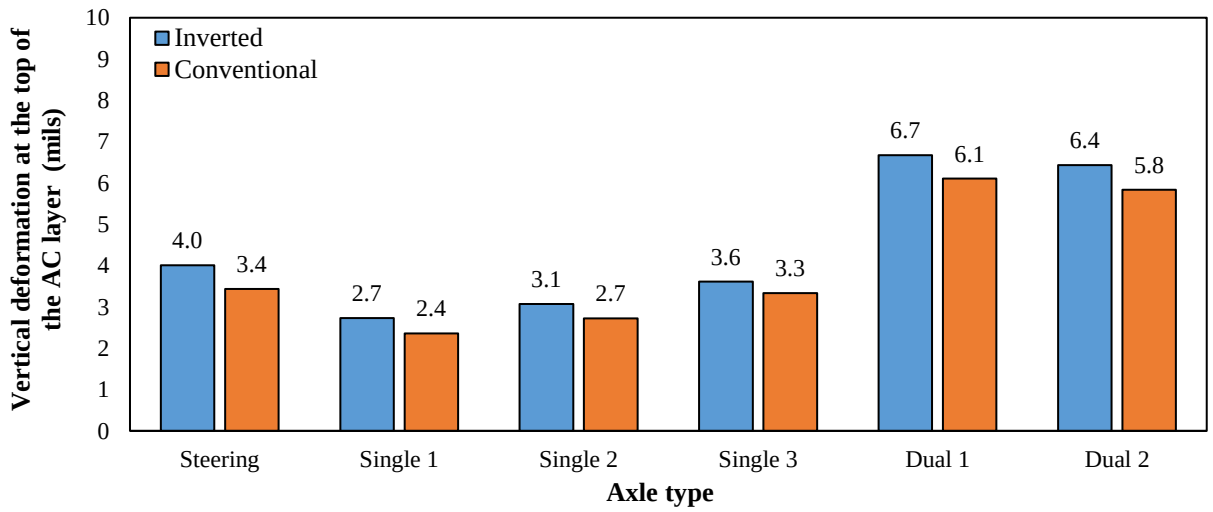

Figure 8.6: Vertical deformation at the top of the AC layer in the Texas inverted and conventional pavement structures considering a full truck analysis.

Focusing on the UAB layer of the inverted pavement structure, Figure 8.7 shows the vertical stresses at the top of that layer in both pavement structures. The graph displays the variation of vertical stresses along a line passing through the tire contact areas on one side of each axle, with each peak corresponding to the effect of one or two tires, depending on the axle type. The results demonstrate that the inverted pavement structure experiences higher stresses than the conventional pavement structure due to the closeness of the UAB to the pavement surface where loads are applied.

Furthermore, the dissipation of vertical stresses between two consecutive peaks differs between the inverted and conventional pavement structures. This dissimilarity is attributed to the location of the UAB layer and the extent of the pressure bulb of the stresses transmitted from the surface downwards. In the inverted pavement structure, the UAB layer is located closer to the surface, resulting in a smaller extent of the pressure bulb. Consequently, the vertical stresses dissipate completely between two consecutive peaks. On the other hand, the conventional

pavement structure has a higher extent of the pressure bulb at greater depths where the UAB layer is located. Thus, the vertical stresses do not dissipate completely between two consecutive peaks.

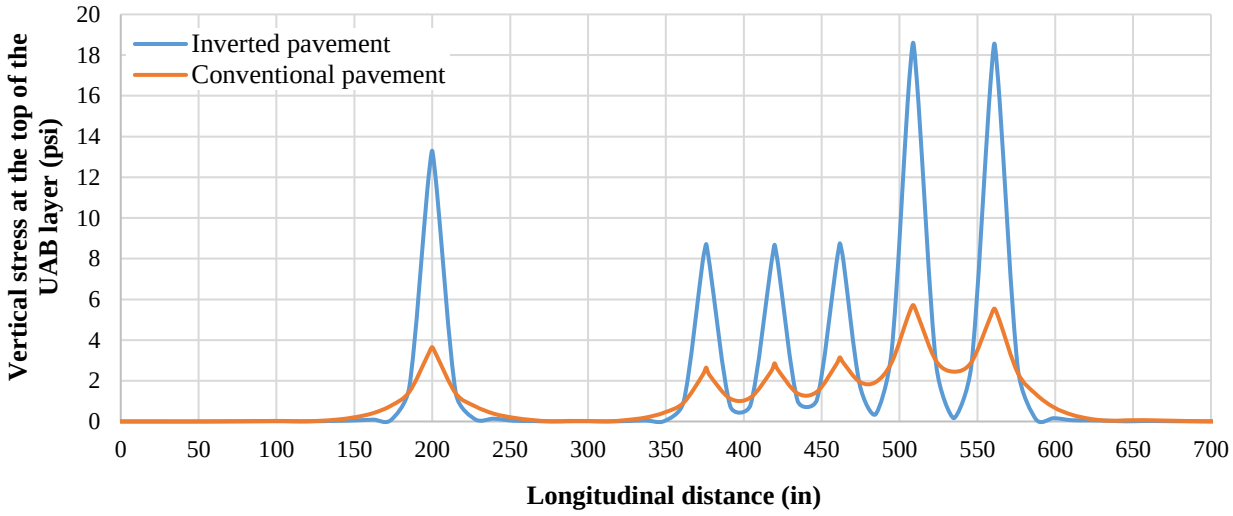

Figure 8.7: Vertical stresses at the top of the UAB layer in the Texas inverted and conventional pavement structures.

The analysis was extended to investigate the shear stresses along the surface of the UAB layer in both the inverted and conventional pavement structures. Figure 8.8(a) illustrates the longitudinal variation of the shear stresses at the top of the UAB layer, where each peak value corresponds to the effect of one or two tires located at one side of each axle. The results indicate that the inverted pavement structure experiences higher shear stresses compared to the conventional pavement structure. This can be attributed to the fact that the UAB layer in the inverted pavement structure is located closer to the surface where the loads are applied, resulting in higher stresses. In contrast, the conventional pavement structure exhibits lower shear stresses as the UAB layer is located at deeper levels away from direct contact with traffic loads.

Moving onto the transversal direction, Figure 8.8(b) demonstrates the changes in shear stresses at the top of the UAB layer for one of the dual axles. Similar to the longitudinal direction, the inverted pavement experiences elevated shear stresses when compared to the conventional

pavement. In both diagrams, the shear stresses are seen to be greater at the edges of the contact area and remain zero directly underneath the tire contact area for each axle. The disparities in the shear stresses observed between the inverted and conventional pavement structures are attributed to the location of the UAB layer and its distance from the surface where the loads are applied.

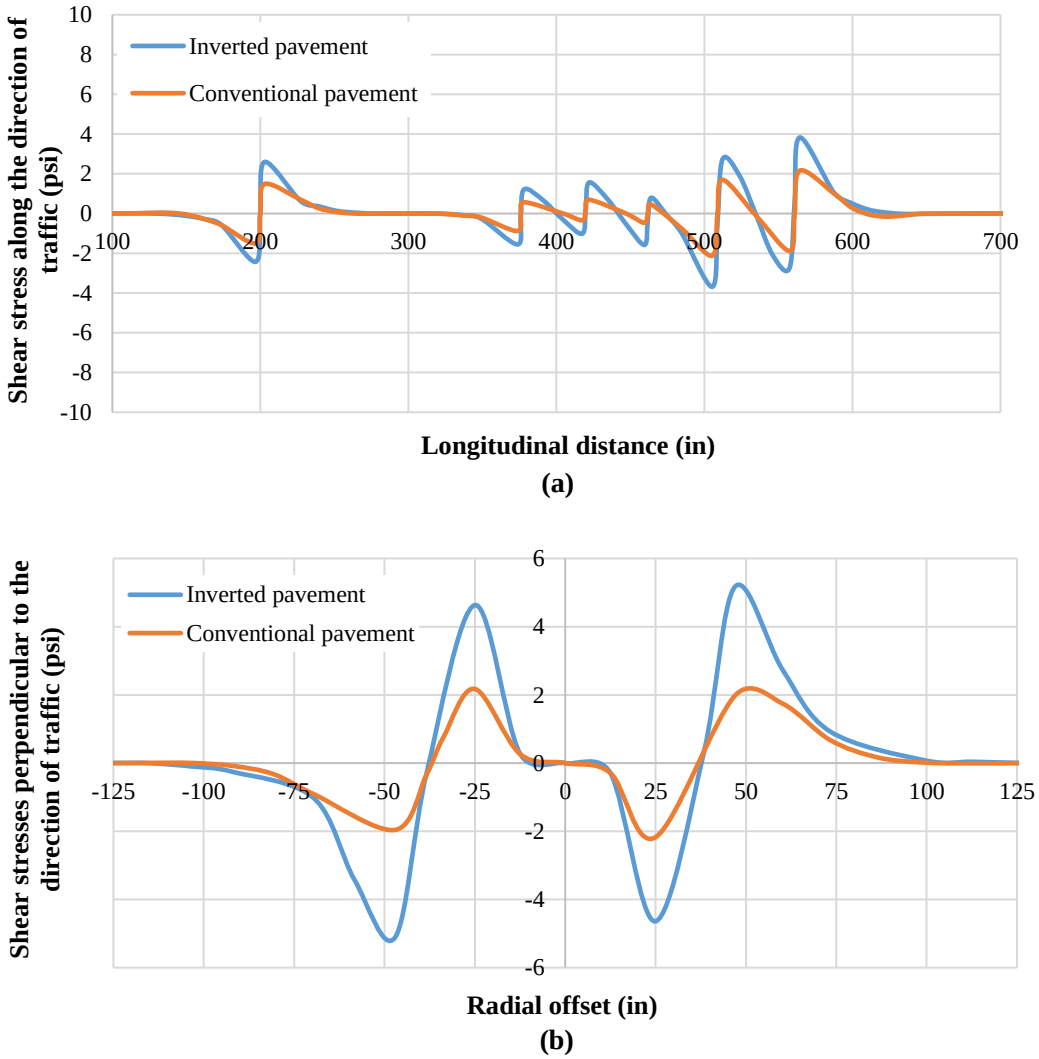

Figure 8.8: Longitudinal shear stresses at the top of the UAB (a) and transversal shear stresses at the top of the UAB (b) in the Texas inverted and conventional pavement structures.

After analyzing the top surface of the UAB layer in both the inverted and conventional pavement structures, the study proceeded to investigate the dissipation of stress inside the layer. Figure 8.9 depicts the distribution of vertical stress within the UAB layer beneath the steering axle for both pavement designs. The stress levels are indicated by different color bands, with the highest stress magnitude located at the upper right-hand corner, which aligns vertically with the superficial contact points of the applied load. As anticipated, the UAB layer in the inverted pavement structure experiences significantly higher stresses due to its proximity to the surface where the loads are applied.

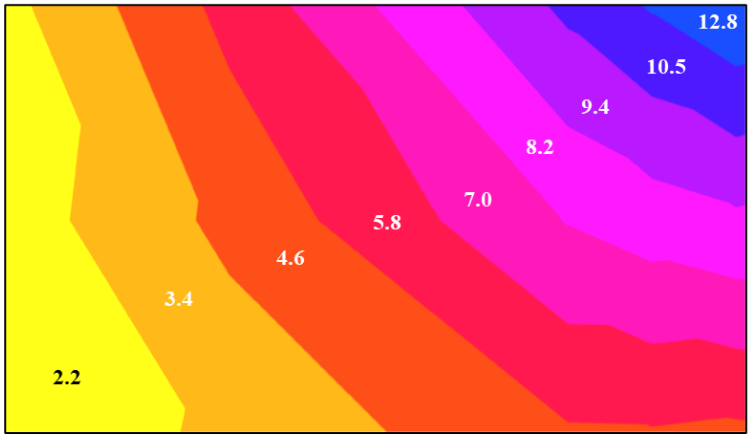

(a)

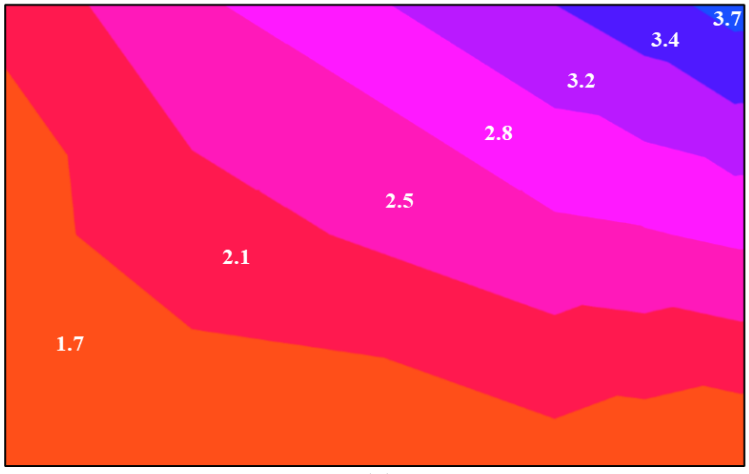

(b)

Figure 8.9: Vertical stress distribution within the UAB layer of the Texas inverted (a) and conventional (b) pavement structures.

The analysis of the UAB layer in both inverted and conventional pavement structures was furthered by examining the horizontal stress distribution beneath the middle single axle, as presented in Figure 8.10. It is evident from the graph that the UAB layer in the inverted pavement structure experiences higher stress levels than that of the conventional pavement structure. Additionally, the graph highlights the inaccuracy of assigning isotropic properties to the UAB layer. The presence of negative stresses at the bottom of the UAB layer in the conventional pavement structure is an impossible outcome since granular materials, such as the UAB layer, cannot resist tensile stresses.

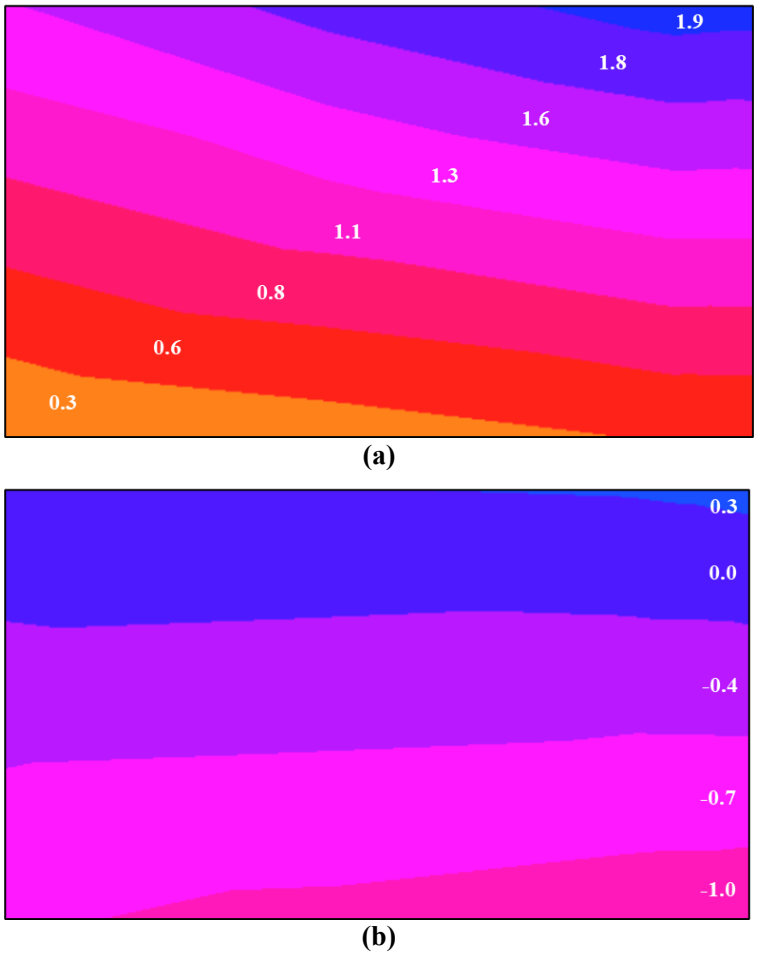

Figure 8.10: Horizontal stress distribution within the UAB layer of the Texas inverted (a) and conventional (b) pavement structures.

8.4. ANISOTROPIC ANALYSIS

The UAB layer in the Texas inverted and conventional pavement section was simulated as a cross-anisotropic medium utilizing the stiffness matrix obtained from the inverse of the compliance matrix M displayed in Equation 7.1. The study evaluated two levels of anisotropy, namely E_x/E_y of 0.5 and 0.25. The vertical modulus, Ey, was determined as 68 ksi through backcalculation analysis, while PR_{xx} and PR_{xy} were assumed to be 0.25 and 0.14, respectively.

To evaluate the effect of assuming a lower horizontal stiffness in the unbound granular medium, the vertical stress distributions in the UAB layer were calculated and compared between the cross-anisotropic and isotropic (E_x/E_y of 1) assumptions. The stress distribution resulting from the last dual axle loads is presented in Figures 8.11 to 8.14, where the colored regions indicate the varying stress levels. The upper right-hand corner exhibited the highest stress values, which aligned with the points of contact of the load on the surface. This analysis aimed to provide insights into the impact two different levels of anisotropy on the stress distribution of the UAB layer.

Figure 8.11(b) reveals that when the horizontal Modulus is 50% of the vertical Modulus, the UAB layer in the inverted pavement structure experiences more significant vertical stresses below the last dual axle compared to when isotropic properties are applied. Additionally, in Figure 8.11(c), where E_x is 25% of E_y, the vertical stresses in the inverted pavement structure are even more pronounced. The data confirms that reducing the E_x to E_y ratio of the UAB layer leads to an increase in vertical stresses.

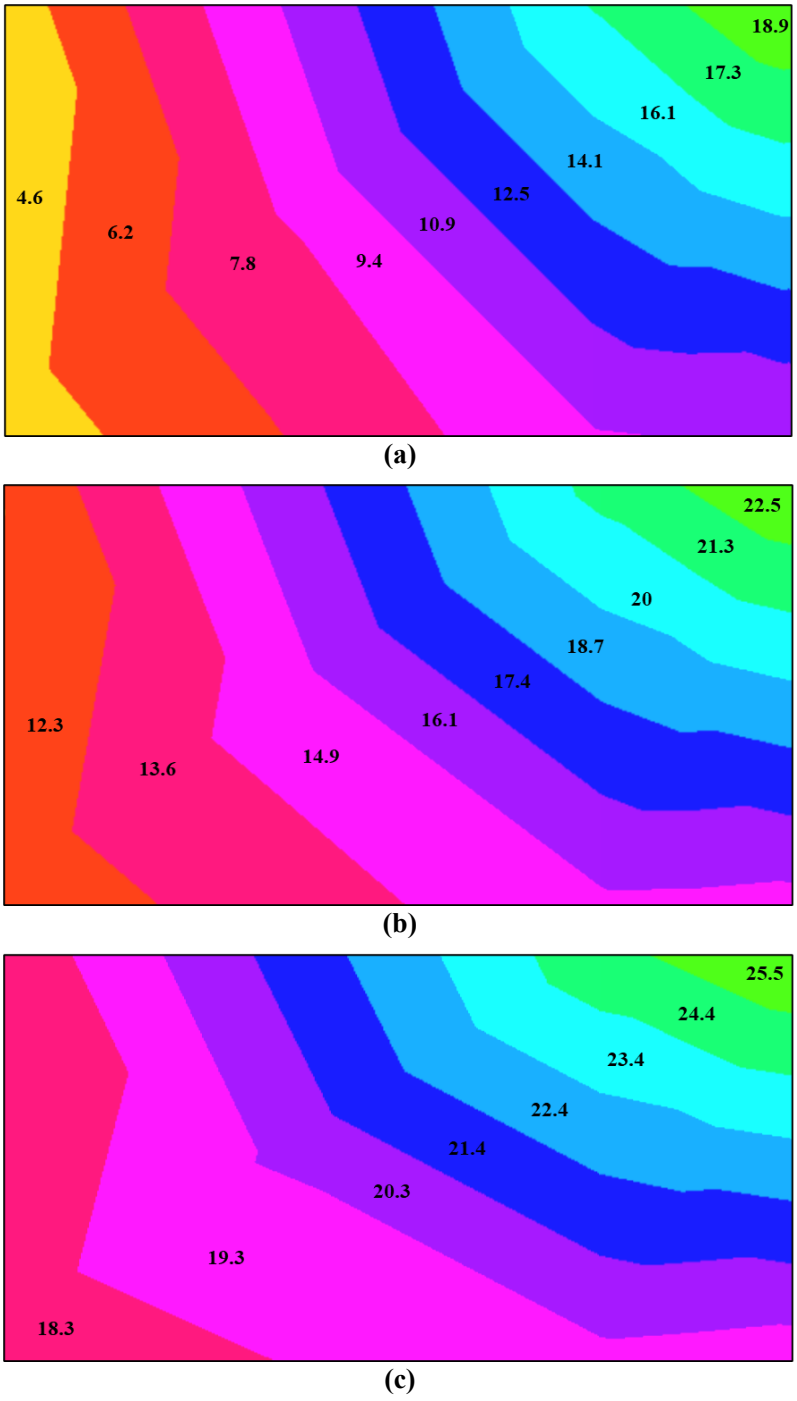

Figure 8.11: Vertical stress distribution within the UAB layer of the Texas inverted pavement structure beneath the last dual axle assuming E_x/E_y=1.0 (a), E_x/E_y=0.5 (b), and E_x/E_y=0.25 (c).

Likewise, the conventional pavement structure displays a similar pattern when it comes to the vertical stress distribution within the UAB layer under the load from the last set of dual axles. Figure 8.12 reveals that the UAB layer experiences higher vertical stresses as the ratio of E_x/E_y decreases from 0.5 to 0.25. Conversely, the vertical stresses in the UAB layer are at their lowest magnitudes when the ratio is equal to 1.

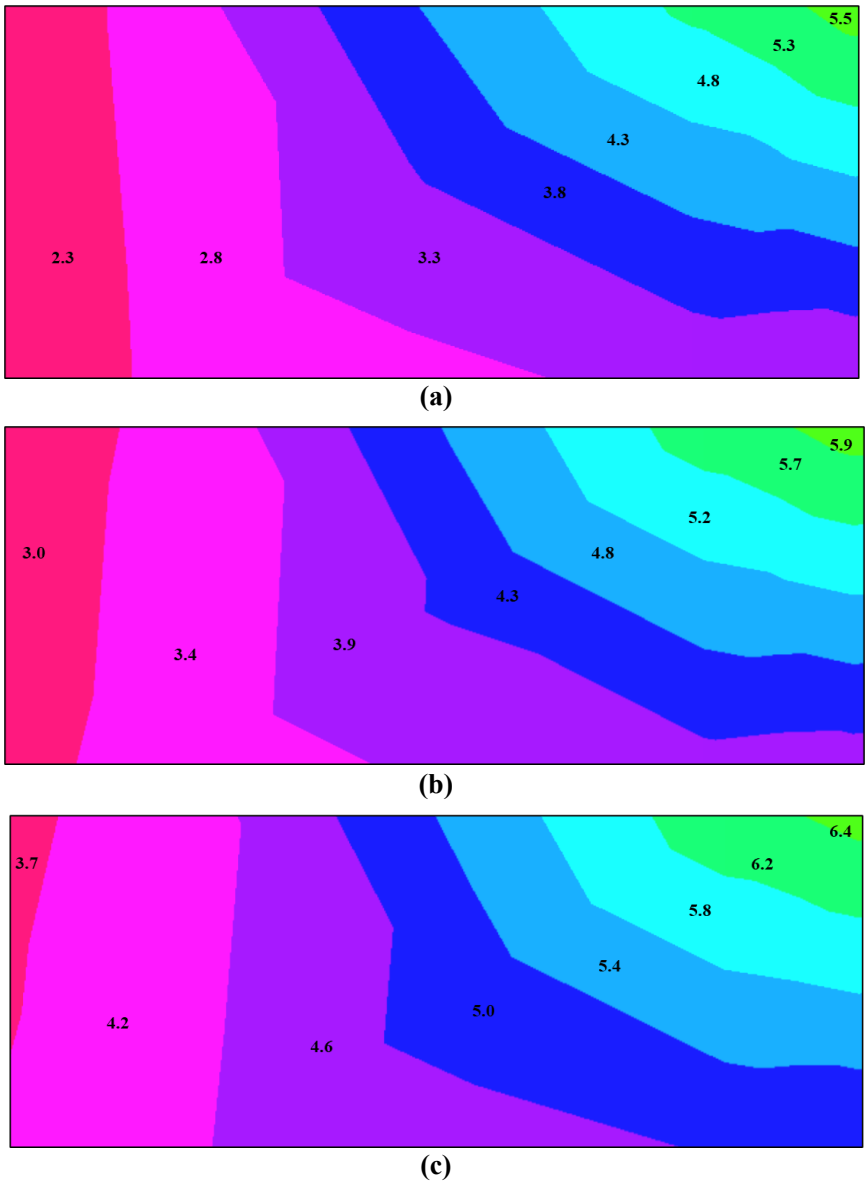

Figure 8.12: Vertical stress distribution within the UAB layer of the Texas conventional pavement beneath the dual axle assuming E_x/E_y=1.0 (a), E_x/E_y=0.5 (b), and E_x/E_y=0.25 (c).

To assess the dissipation of horizontal stresses within the UAB layer of the inverted pavement structure, the same two levels of anisotropy were evaluated under the last set of dual axles. Figure 8.13 indicates that the stresses present in the UAB layer under anisotropic conditions were greater compared to the stresses observed when isotropic properties were utilized.

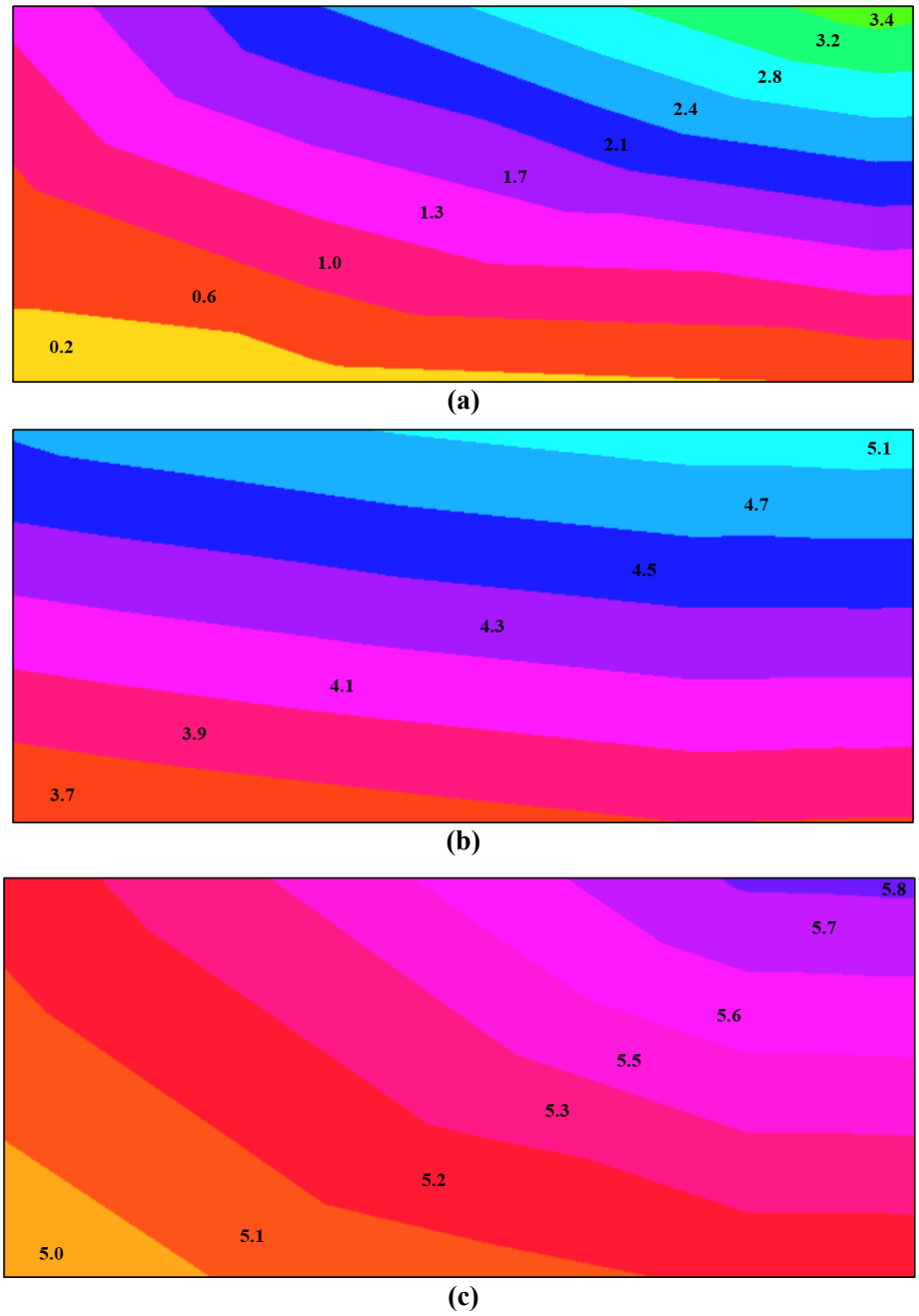

Figure 8.13: Horizontal stress distribution within the UAB layer of the Texas inverted pavement beneath the dual axle assuming E_x/E_y=1.0 (a), E_x/E_y=0.5 (b), and E_x/E_y=0.25 (c).

The same pattern identified in the UAB layer of the inverted pavement structure is also evident in the Texas conventional pavement structure, as depicted in Figure 8.14. The application of cross-anisotropic properties to the granular medium increases the horizontal stresses, leading to the elimination of negative horizontal stresses at the bottom of the layer and transforming them into compression. This outcome is consistent with the behavior of a granular medium that is not capable of withstanding tensile stresses.

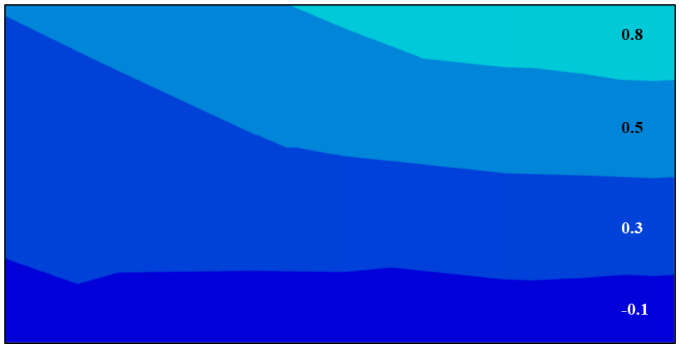

(a)

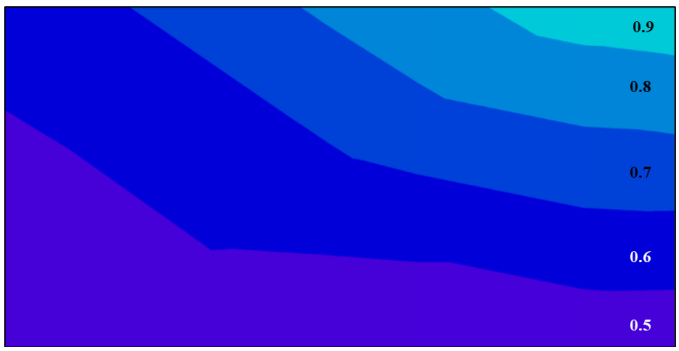

(b)

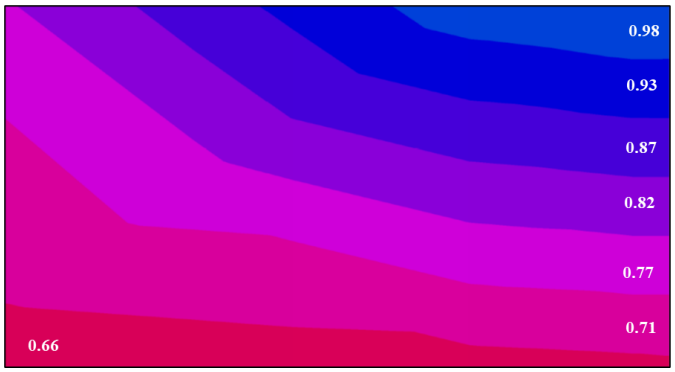

(c)

Figure 8.14: Horizontal stress distribution within the UAB layer of the Texas conventional pavement beneath the dual axle assuming E_x/E_y=1.0 (a), E_x/E_y=0.5 (b), and E_x/E_y=0.25 (c).

The previous figures clearly indicate that the natural anisotropy of the UAB layer significantly impacts the transmitted stress magnitude through the medium. Overlooking the anisotropic nature of the UAB layer in both inverted and conventional pavement structures may result in miscalculations or underestimation of stress levels. Anisotropic modeling, on the other hand, reveals higher stress values developed within the UAB layer, which is critical information for pavement design. Neglecting such an essential factor could lead to an inadequate UAB layer thickness, affecting the overall pavement design, and eventually leading to a decrease in the service life of the infrastructure.

To highlight the impact of decreased E_x/E_y ratios on the mechanical response of the UAB layer in the Texas inverted pavement configuration, Figure 8.15 presents a plot demonstrating the variation of vertical and horizontal strains at the top of the UAB layer under two levels of anisotropy. The results indicate that, for each axle, the strains increase as the degree of anisotropy transitions from isotropic to lower E_x/E_y ratios.

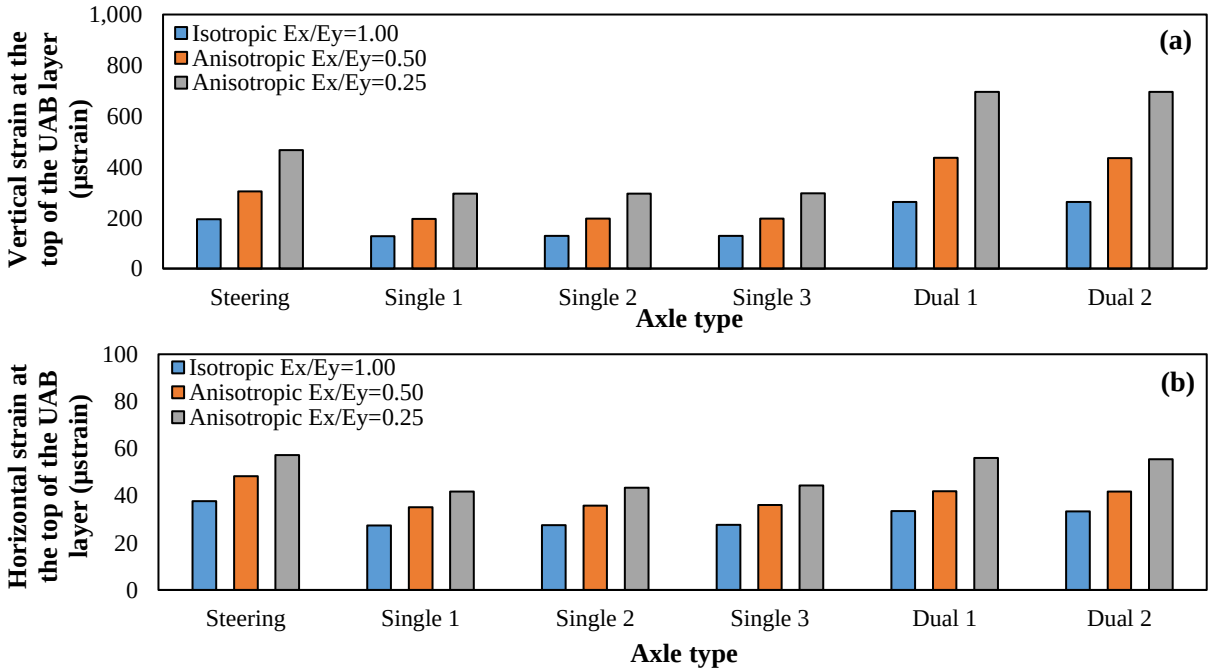

Figure 8.15: Vertical and horizontal strain at the top of the UAB layer of the Texas inverted pavement structure for all axles at isotropic and anisotropic conditions.

Chapter 9: Stability Analysis of Unbound Granular Mediums in Pavement Structures

The UAB layer plays a crucial role in an inverted pavement structure, as demonstrated by the results presented in previous chapters. Compared to a conventional pavement structure, the UAB layer in an inverted pavement is subjected to significantly higher stresses and strains. Moreover, the directional dependence of the material properties in the UAB layer, as defined by the differences in vertical and horizontal Modulus, contributes substantially to the load-bearing capacity of the pavement structure.

The level of anisotropy of the UAB layer significantly affects critical pavement responses in both inverted and conventional structures. As demonstrated in previous findings, the magnitude of stresses and strains developed within the UAB layer varies depending on the E_x/E_y ratio, which highlights the close relationship between the load-bearing capacity of the granular system and the cross-anisotropic nature of its strength. The anisotropic behavior of the UAB layer arises from its inherent nature, characterized by the random distribution of grains with distinct geometries that are properly compacted to form a structural layer with load-distribution capabilities.

This chapter focuses on exploring an additional source of directional dependency in the UAB layer, specifically the stress-induced anisotropic nature of the unbound granular system. To achieve this, a new set of numerical models will be developed based on both Virginia and Texas inverted and conventional pavement designs, subjected to specific loading conditions. Additionally, the stress states in the UAB layer will be compared in terms of the first invariant of the stress tensor (I_1) and the second invariant of the deviatoric stress tensor (J_2) at different points within the layer. The resulting I_1 vs. J_2 plots will be overlaid with the stress paths specified in the Standard Method of Test for Determining the Resilient Modulus of Soils and Aggregate Materials AASHTO T-307 (AASHTO, 2003) and the Harmonized Test Methods for Laboratory

Determination of Resilient Modulus for Flexible Pavement Design NCHRP 1-28A (Witczak, 2003), which are accepted protocols for characterizing the strength properties of unbound materials. The objective is to evaluate whether laboratory tests of granular materials are conducted under similar loading conditions as expected for an unbound granular base layer in an inverted pavement structure.

A stability analysis will also be conducted to investigate the relationship between the cohesion and angle of internal friction of the untreated unbound aggregate base layer and the invariants of the stress tensor and deviatoric stress tensor that arise due to traffic loads. Anisotropic properties will be assigned to the granular medium, and the stability analysis will compare the susceptibility of the UAB layer in both inverted and conventional pavement designs to develop high plastic deformations that could compromise the structural integrity of the entire pavement system under traffic loads.

9.1. NUMERICAL SIMULATIONS

Various models were generated using the Abaqus software to simulate the inverted pavement systems of the Virginia and Texas designs. Equivalent traditional pavement designs were also taken into account and simulated in the same FE program. Each model from the Virginia inverted and conventional pavements, as well as from the Texas inverted and conventional structures, was subjected to the same load and modeled according to the same criteria (i.e., boundary conditions, finite element type, surface area, subgrade thickness, etc.). To evaluate the impact of heavier loads such as those exceeding the threshold for overweight trucks in Texas, which are frequently present in the pavement segment of SH-123 studied in this dissertation, an additional set of models were created for the Texas inverted and conventional pavement structures maintaining the modeling criteria previously specified.

For the development of the new set of models, the material properties and layer thicknesses for the inverted pavement structures constructed in Virginia and Texas, as explained in Chapter 7 and Chapter 8, were retained. The conventional pavements were structured in a top-down order with an AC layer, CTB layer, UAB layer, and SG soil. In contrast, the inverted pavements were arranged with an AC layer, UAB layer, CTB layer, and SG soil. An anisotropic UAB layer with an E_x to E_y ratio of 0.3 was incorporated into all pavement structures.

In the Virginia inverted and conventional pavement models, a single type of loading condition was examined. Specifically, the simulation was focused on the impact of a single wheel load from the steering axle of the aggregate haul truck that was utilized during the field tests. As the effect of the complete set of axles has already been extensively studied in previous chapters of this dissertation, the analysis in this instance will only take into account one tire of the steering axle in contact with the pavement surface, providing a pressure of approximately 100 psi.

Two different loading conditions were considered for the Texas inverted and conventional pavement models. Firstly, the models were subjected to a 100-psi pressure from a single wheel of the steering axle of the same aggregate haul truck used in Virginia. Secondly, two additional inverted and conventional models were simulated with a pressure of 180 psi applied in a rectangular contact area of 50 in^2, representing a super heavy load (SHL). This condition was encountered in a study conducted on SH-123, where portable weight-in-motion devices were used to collect traffic data and quantify the frequency and magnitude of SHLs in the Eagle Ford Shale and Permian Basin regions. These areas are renowned for their oil and gas extraction and refining operations, resulting in the transportation of heavily loaded trucks with gross weights in excess of 254,300 lb, commonly referred to as SHLs (Ashtiani et al., 2019).

To simulate the pavement structures, a 3.3 ft x 3.3 ft surface area was used for all models, with the tire contact area placed symmetrically in the center. The entire pavement block had a thickness of 60 in, which was divided into a 21-in 3-layer system and a 39-in thick SG soil. The specific details of the 21-in system varied based on the thickness of each layer in the Virginia and Texas inverted and conventional pavement structures. This geometric configuration ensured appropriate stress distribution and prevented any undue influence of boundary conditions on the critical pavement responses.

The meshing of the Virginia inverted and conventional pavement models was defined using cubical elements with a side length of 3 in. Meanwhile, for the Texas inverted and conventional pavement models, a smaller cubical element with a side length of 2.67 in was utilized to mesh each layer of the system. In all cases, C3D20R brick elements were chosen for their integration capabilities in modeling. An exaggerated deformed shape of the Texas inverted pavement model analyzed under the aforementioned modeling criteria can be seen in Figure 9.1.

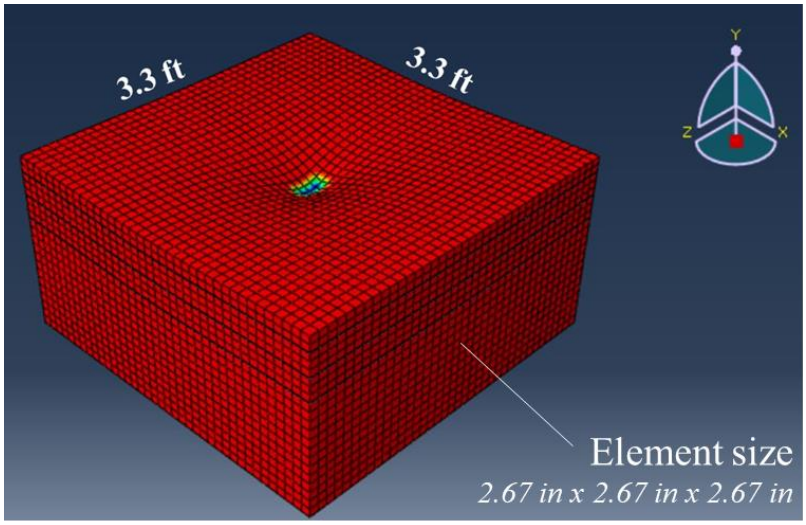

Figure 9.1: Mesh of the Texas inverted pavement model in Abaqus generated using 2.67-in sided cubic elements.

9.2. STRESS-INDUCED ANISOTROPY

The location of external wheel loads in relation to the point of analysis within an unbound granular layer of a pavement structure introduces an additional component to the directional dependence of stiffness properties in the UAB layer. The application of a moving wheel load induces nonlinear shear stresses on the pavement structure, which results in the accumulation of plastic strain in the UAB layer. These shear stresses cause the rotation of the principal plane, which is the plane on which the shear stresses are zero. The orientation of this plane can be determined by calculating the rotation angle that results in zero components of shear stresses, using Equation 9.1, which employs the Mohr circle failure criterion (Ashtiani 2009).

$$\theta = \frac{1}{2}\, tan^{-1}\left(\frac{2\tau_{xy}}{\sigma_x - \sigma_y}\right) \tag{9.1}$$

Where:

θ: orientation of the principal plane

τ_{xy}: shear stress

σ_x: horizontal stress

σ_y: vertical stress

To determine the rotation of the principal plane, the UAB layer at the top of the inverted and conventional pavement structures was assessed along a longitudinal line aligned with the center of the wheel path in the direction of traffic flow. To calculate the vertical, horizontal, and shear stresses within the UAB layer and to realistically determine the orientation of the principal plane (θ), cross-anisotropic properties were assigned to the UAB layer.

The orientation of the principal plane varies longitudinally as the wheel load moves, as shown in Figure 9.2. The origin of the plot represents the point where the top of the UAB layer

aligns vertically with the centerline of the wheel load. As the plot shows, the inclination of the principal plane is zero at the centerline, meaning that the stresses directly under the centerline of the wheel load are principal stresses, and there are zero shear stresses. This finding is consistent with the shear stress plots in Figures 7.13 and 8.8, which indicate that the shear stresses at the top of the UAB layer are zero below the centerline of the tire contact area and reach their maximum value at the edge of the tire contact area.

From Figure 9.2, it is evident that the UAB layer of the inverted pavement structures experiences higher stress states, resulting in higher θ angles in both Virginia and Texas inverted pavement designs. Equation 9.1 relates shear stresses with vertical and horizontal stresses, which are all relatively lower in magnitude for the conventional pavement structures in Virginia and Texas. As a result, the relationship between stresses and θ causes a change in inclination, as seen in the graph. During the passage of a wheel load, the inclination of the principal plane increases up to a certain point, after which it decreases as the shear stresses dissipate. At radial distances close to the tire edge, the inclination of the principal plane is significant, while it becomes negligible at a certain distance away from the wheel load. Therefore, it is imperative to consider stress-induced anisotropy in the mechanistic design and analysis of the UAB layer in inverted pavement structures.

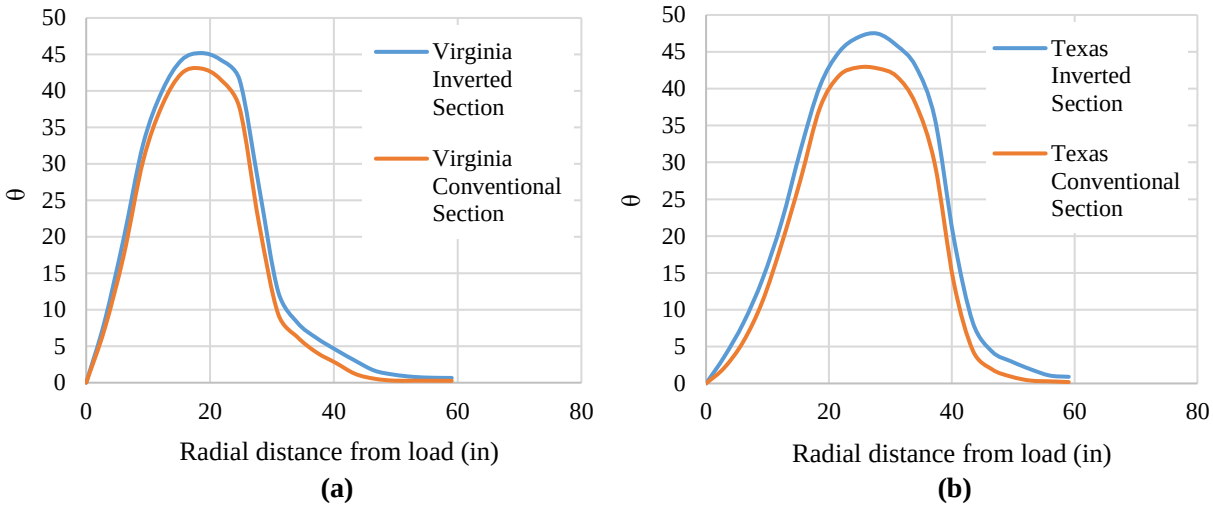

Figure 9.2: Rotation of the principal plane at the top of the UAB layer for the Virginia (a) and Texas (b) inverted and conventional pavement structures.

9.3. STRESS-PATH ANALYSIS

Accurately simulating the stress states created by traffic loads is of utmost importance in the mechanistic design and analysis of pavement structures. Two widely used laboratory protocols, AASHTO T-307 and NCHRP 1-28A, are employed to evaluate the resilient properties of untreated granular materials for future pavement design. This dissertation is focused on examining the stress states experienced by specimens in the laboratory as compared to the actual stress states undergone by the granular medium, including the UAB layer in inverted and conventional pavement structures, when subjected to loading.

The subsequent sections will provide a brief overview of the main features of both the AASHTO T-307 and NCHRP 1-28A procedures. The AASHTO T-307 standard provides a comprehensive approach for preparing and testing untreated base materials and SG soils to determine their M_r under traffic load conditions in flexible pavements. The protocol begins by classifying aggregates based on their grain size distribution and plasticity index (PI). Granular specimens are then placed in a triaxial cell and subjected to repeated cycles of haversine stress

pulses with a duration of 0.1 sec and resting periods of 0.9 sec. A constant confining pressure is applied as the vertical stress increases in each sequence, with confinement ranging from 3 psi to 20 psi and vertical stress ranging from 3 psi to 40 psi. Specimens are prepared for testing using a 6-in diameter mold for coarse-grained materials compacted with a vibratory hammer and a 2.8-in diameter mold for fine-grained materials compacted by impact. The protocol also specifies a minimum L/D ratio to reduce variability in the measured responses.

The NCHRP 1-28A protocol divides aggregate systems into two groups based on their grain size distribution and PI. To fabricate the specimens in the laboratory, the protocol recommends using impact or vibratory compaction methods for coarse-grained specimens with a 4-in diameter and vibratory compaction for fine-grained specimens with a 6-in diameter. Testing is performed using a triaxial chamber that applies repeated cycles of a haversine-shaped pulse lasting 0.1 sec with a 0.9-sec resting period for base or subbase layers, and a 0.2-sec loading time and 0.8-sec resting period for SG soil. The protocol subjects the specimens to six stress paths with five stress states in each sequence, resulting in the application of 30 stress combinations on the sample. Increasing confining pressures are applied as the vertical stress increases in each sequence, with confinement ranging from 3 psi to 20 psi and vertical stress ranging from 2 psi to 144 psi.

9.3.1. Virginia inverted pavement section stress path analysis

Usually, stress paths are plotted on a p-q graph, with p representing the mean of the principal stresses and q equal to twice the radius of the Mohr circle, i.e., difference between the major principal stress and the minor principal stress. A set of p-q plots were generated based on the stress responses developed in the UAB layer of the inverted and conventional pavement structures from Virginia.

P-q stress values were extracted from the UAB layer of both the Virginia inverted and conventional pavement models. The values were obtained from 189 points in total, distributed across three levels: top, middle, and bottom. To collect the data, three planes perpendicular to the direction of traffic were selected at three different distances from the tire contact area i.e., beneath, at the edge, and 3 in away from the rectangular surface. Each plane contains 63 points or nodes. Figure 9.3 illustrates the location of these planes and the nodes on each plane where the stresses were evaluated.

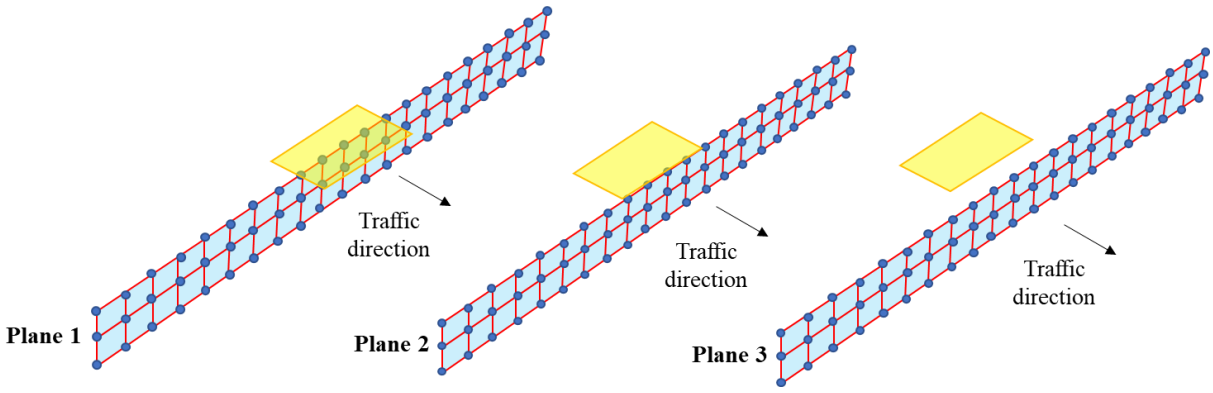

Figure 9.3: Schematic of the 189 nodes distributed in Planes 1, 2, and 3, respectively located beneath, at the edge, and at 3 in away from the tire contact area highlighted in yellow.

Figure 9.4 illustrates the p-q plot obtained from the stress states computed for the 189 nodes located at various transversal planes within the UAB layer of the Virginia inverted pavement structure. The nodes were categorized based on their corresponding planes, with Plane 1 situated beneath the tire contact area. The scatterplot reveals that the highest p and q values were observed in Plane 1, while Planes 2 and 3, which are located farther from the tire contact area, exhibited lower maximum p-q values at lower x and y coordinates. Although the p-q values at the bottom of the plot appear to be zero, they are not because the model does not exhibit isotropic conditions. The horizontal and vertical stresses are comparable but not identical. The p-q values in each plane increase as the shear stresses at the points of analysis increase. The trendlines of the p-q values in

each plane depict the progression of the stress paths. The steepest slope was observed in the p-q values from Plane 1, indicating the most critical conditions, while Plane 3 exhibited the shallowest slope of the p-q values, indicating that the ascending to failure could occur at a slower rate.

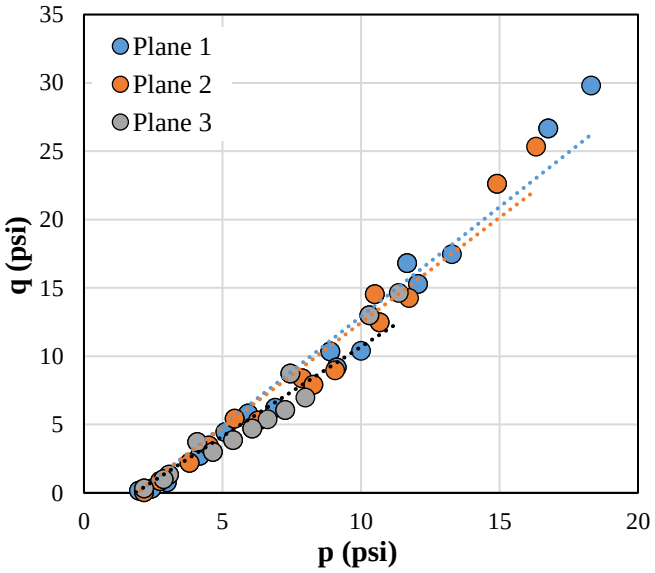

Figure 9.4: P-q plot from the stresses calculated at three transversal planes within the UAB layer of the Virginia inverted pavement structure.

Figure 9.5 presents the p-q values derived from the stresses of 189 nodes within the UAB layer for each type of pavement structure i.e., Virginia inverted and conventional sections, without any categorization based on planes. The results for each pavement structure were combined for all three planes. It is evident that the highest p-q values were recorded for the inverted pavement design. This increase in p-q values is more noticeable in the inverted design as the UAB layer experiences significantly higher stress magnitudes. In contrast, lower p-q values were observed in the conventional design, along with lower slopes for the increase in p-q values.

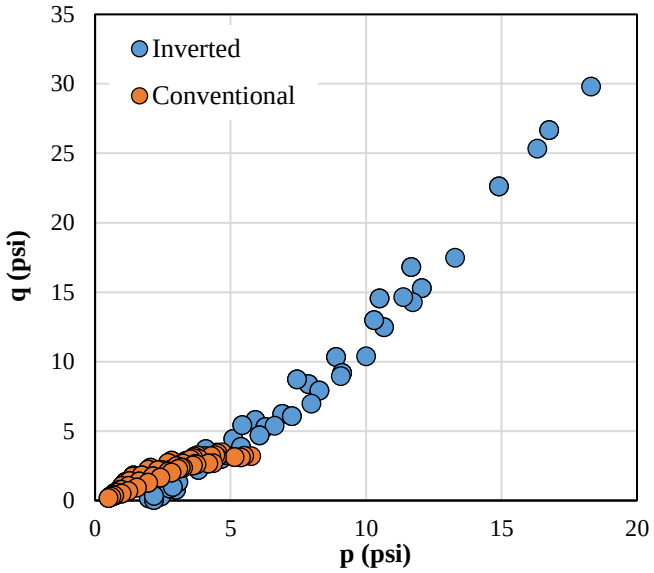

Figure 9.5: P-q plot from the stresses calculated within the UAB layer of the Virginia inverted and conventional pavement structures.

To conduct a thorough analysis of the stress states experienced by the UAB layer of the Virginia inverted and conventional pavement structures, stress invariants were computed for each node per plane. Equations 9.2 and 9.3 show the expressions used to determine the first invariant of the stress tensor (I_1) and the second invariant of the deviatoric stress tensor (J_2) in terms of the principal stresses (σ_1, σ_2, and σ_3).

$$I_1 = \sigma_1 + \sigma_2 + \sigma_3 \tag{9.2}$$

$$J_2 = \frac{1}{6}\left[(\sigma_1 - \sigma_2)^2 + (\sigma_1 - \sigma_3)^2 + (\sigma_2 - \sigma_3)^2\right] \tag{9.3}$$

The scatterplot in Figure 9.6 displays the I_1 vs J_2 plot of all 189 nodes analyzed in the UAB layer of the Virginia inverted pavement structure. The nodes were categorized based on their location in three planes, namely, Plane 1, Plane 2, and Plane 3, and based on their depth within the UAB layer, i.e., top, middle, and bottom. As expected, higher stresses were observed in Plane 1, which is located closer to the tire contact area, as evidenced by the decreasing trend of the

maximum I_1-J_2 values when moving from Plane 1 to Plane 3. Furthermore, the nodes located closer to the surface of the UAB layer exhibited higher I_1-J_2 values in each plane due to the higher stresses developed. The trendlines of each node category, which represent the increase of the stress paths, displayed higher slopes in the top nodes in each plane. A steeper slope signifies more critical conditions, where the progression towards the failure surface could occur at a faster rate.

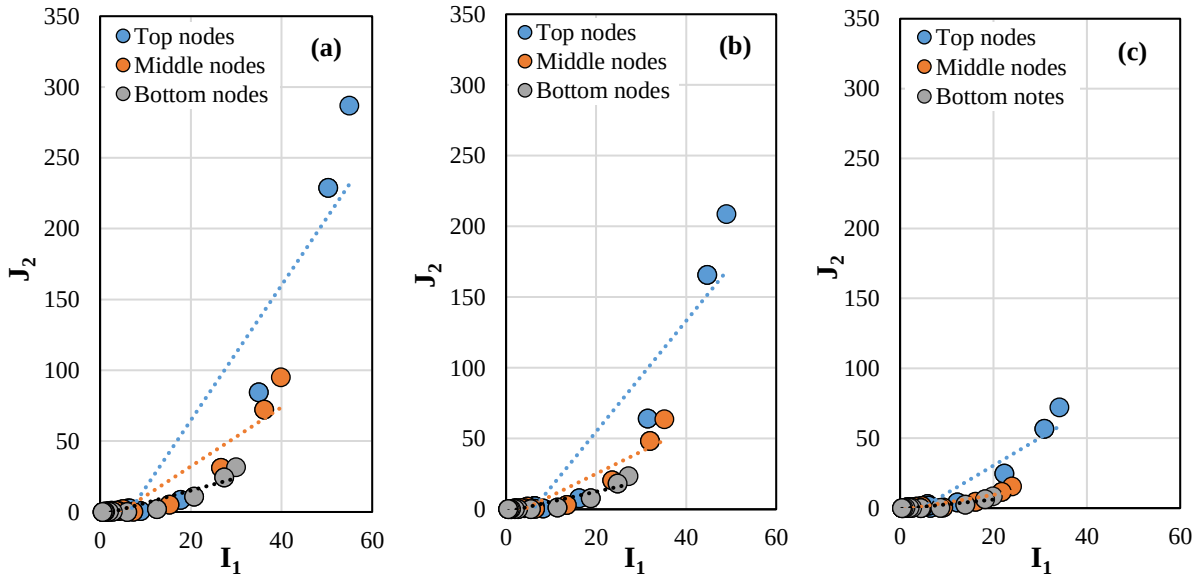

Figure 9.6: I_1-J_2 plots from the stresses calculated within the UAB layer of the Virginia inverted pavement structure for Plane 1 (a), Plane 2 (b), and Plane 3 (c).

Figure 9.7 illustrates the I_1 vs J_2 plots of a total of 378 nodes analyzed in the UAB layer of the Virginia inverted and conventional pavement structures. For each type of pavement design, 189 nodes were evaluated. The I_1-J_2 values derived from the stress states specified in AASHTO T-307 and NCHRP 1-28A were superimposed on these data points. The stress envelopes for AASHTO T-307 and NCHRP 1-28 A are also plotted. As shown in Figure 9.7, the NCHRP protocol imposes more demanding stress states than the AASHTO protocol. AASHTO T-307 cannot subject granular base materials to certain stress states experienced by the UAB layer of an inverted pavement structure like the one built in Virginia. This is evident in the points that fall

outside the stress envelope defined by the stress limits specified in the AASHTO standard. However, the NCHRP protocol appears to better capture all stress states experienced by the UAB layer of the inverted pavement structure. Both protocols fail to subject the aggregate systems to very low stress levels, but the likelihood of transitioning to critical conditions at those low stress intensities is low. It is worth mentioning that both protocols can simulate the stress levels that the UAB layer of a conventional pavement structure will experience.

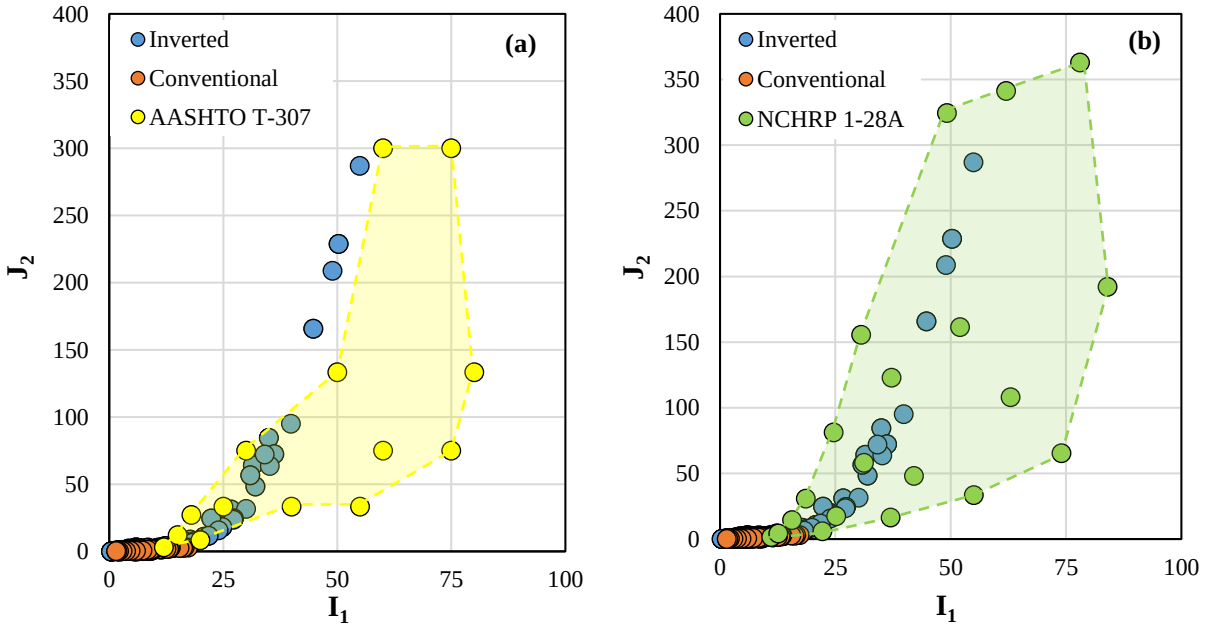

Figure 9.7: I_1-J_2 plots from the stresses calculated within the UAB layer of the Virginia inverted and conventional pavement structures compared to (a) AASHTO T-307 and (b) NCHRP 1-28A.

9.3.2. Texas inverted pavement section stress path analysis for conventional loads

P-q plots were generated to represent the stress responses in the UAB layer of the inverted and conventional pavement structures in Texas, under conventional loading conditions. Stress values were obtained from a total of 252 points, which were distributed among three levels, namely top, 2.67-inch depth, 5.33-inch depth, and bottom. The data was collected from three planes perpendicular to the traffic direction, located at varying distances from the tire contact area, namely

beneath, at the edge, and 2.67 inches away from the rectangular surface. Each plane consisted of 84 nodes, where stress values were evaluated. The location of these planes and the nodes on each plane where stresses were obtained is shown in Figure 9.8.

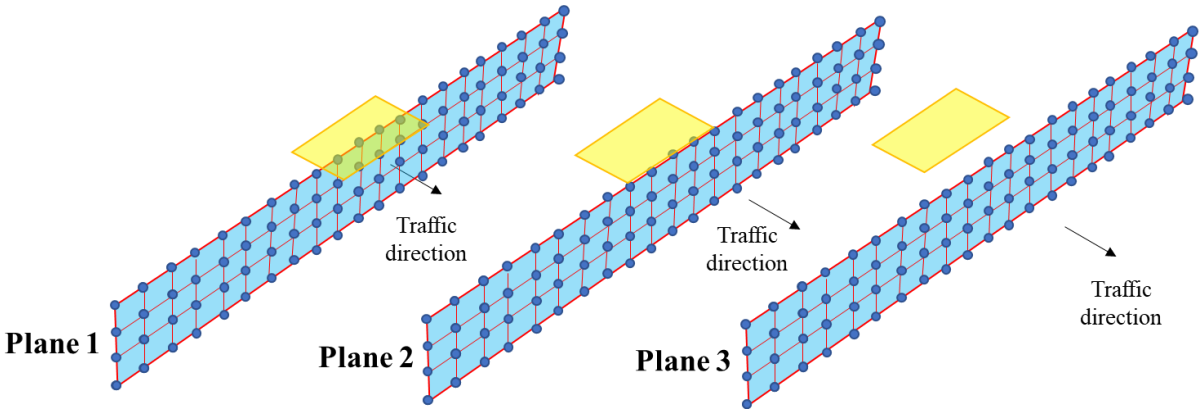

Figure 9.8: Schematic of the 252 nodes distributed in Planes 1, 2, and 3, respectively located beneath, at the edge, and at 3 in away from the tire contact area highlighted in yellow.

The p-q plot obtained from the computed stress states for the UAB layer of the Texas inverted pavement structure is shown in Figure 9.9. The 252 nodes were located on different transversal planes, with Plane 1 situated below the tire contact area. Each plane contained 84 nodes. The scatterplot shows that the maximum p and q values were observed in Plane 1, which is closest to the tire contact area, while Planes 2 and 3, located farther from the tire contact area, exhibited lower maximum p-q values. Although the bottom of the plot appears to have zero p-q values, this is not the case as the model does not have isotropic conditions. The p-q values in each plane increased as the shear stresses at the points of analysis increased. The trendlines of the p-q values in each plane depicted the progression of the stress paths, with the steepest slope observed in Plane 1 and the shallowest slope observed in Plane 3. This indicates that failure could occur more rapidly in Plane 1 compared to Plane 3.

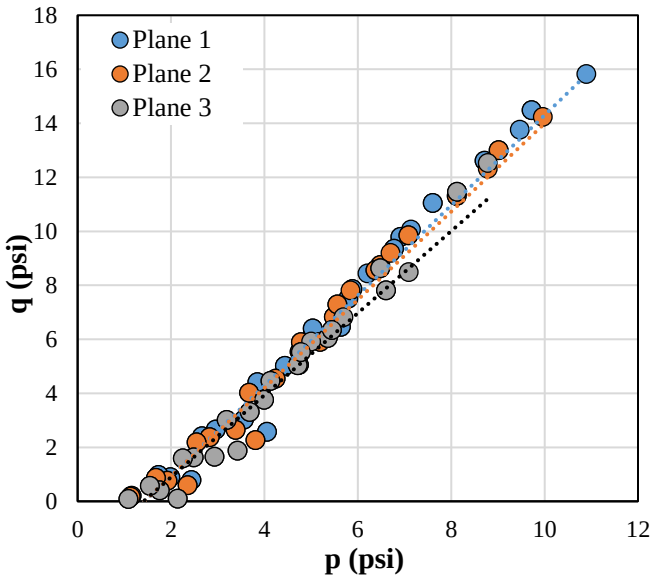

Figure 9.9: P-q plot from the stresses calculated at three transversal planes within the UAB layer of the Texas inverted pavement structure.

Figure 9.10 displays the p-q values obtained from stress analysis of 252 nodes within the UAB layer of both the Texas inverted and conventional pavement structures subjected to conventional loads, without any categorization based on planes. The results for each pavement structure were combined for all three planes. It is apparent that the Texas inverted pavement structure exhibits higher p-q values compared to the conventional design. This increase in p-q values is more prominent in the inverted design, as the UAB layer experiences significantly higher stress magnitudes. Conversely, lower p-q values were observed in the conventional design, with lower slopes for the increase in p-q values.

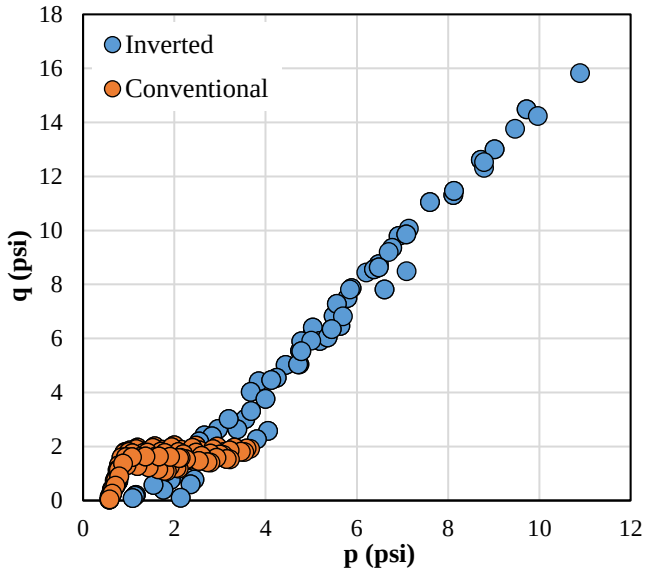

Figure 9.10: P-q plot from the stresses calculated within the UAB layer of the Texas inverted and conventional pavement structures.

The stress states experienced by the UAB layer of the Texas inverted and conventional pavement structures subjected to conventional loads were analyzed by computing stress invariants for each node per plane. Figure 9.11 presents a scatterplot of the I_1 vs J_2 plot of all 252 nodes analyzed in the UAB layer of the Texas inverted pavement structure. The nodes were categorized based on their location in three planes and their depth within the UAB layer. Higher stresses were observed in Plane 1, which is located closer to the tire contact area, as evidenced by the decreasing trend of the maximum I_1-J_2 values when moving from Plane 1 to Plane 3. Additionally, nodes located closer to the surface of the UAB layer showed higher I_1-J_2 values in each plane due to the higher stresses developed. The trendlines of each node category, which represent the increase of the stress paths, displayed higher slopes in the top nodes in each plane. A steeper slope signifies more critical conditions, where the progression towards the failure surface could occur at a faster rate.

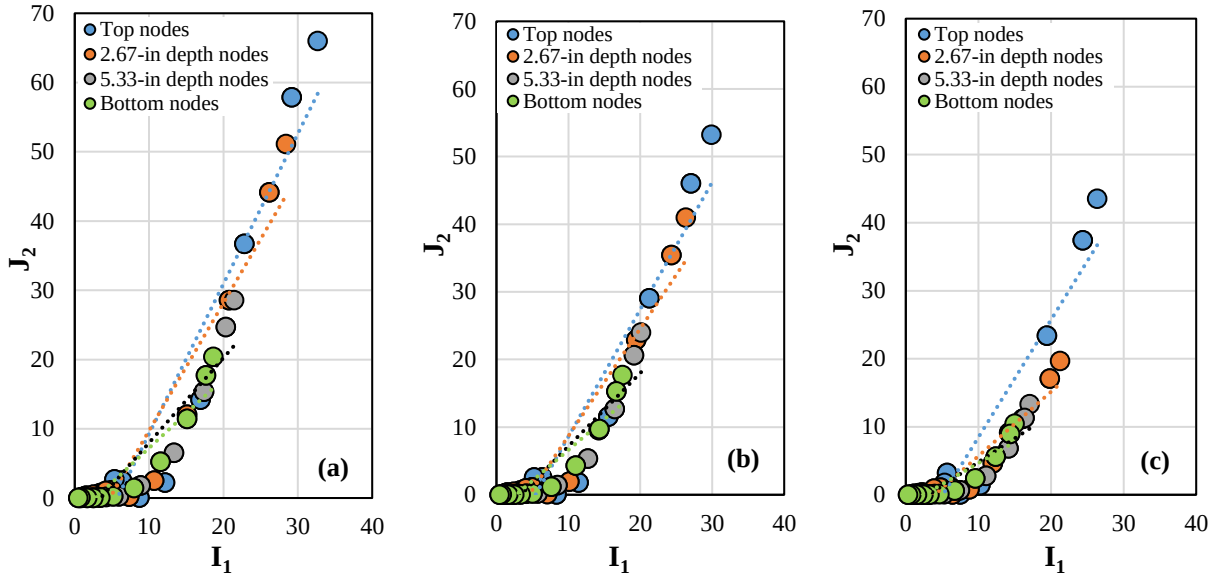

Figure 9.11: I_1-J_2 plots from the stresses calculated within the UAB layer of the Texas inverted pavement structure for Plane 1 (a), Plane 2 (b), and Plane 3 (c).

In Figure 9.12, the I_1-J_2 plots of a total of 504 nodes within the UAB layer of the Virginia inverted and conventional pavement structures are shown. For each type of pavement design, 252 nodes were evaluated, and the I_1-J_2 values obtained from stress states specified in AASHTO T-307 and NCHRP 1-28A were superimposed on the data points. The stress envelopes for both protocols were also plotted. It can be observed that both protocols can cover all stress states experienced by the UAB layer of the inverted pavement structure. However, they are unable to subject the aggregate systems to very low stress levels, but the likelihood of reaching critical conditions at those stress levels is low. It is worth noting that both protocols can simulate the stress levels experienced by the UAB layer of the Texas inverted and conventional pavement structures when subjected to conventional loads.

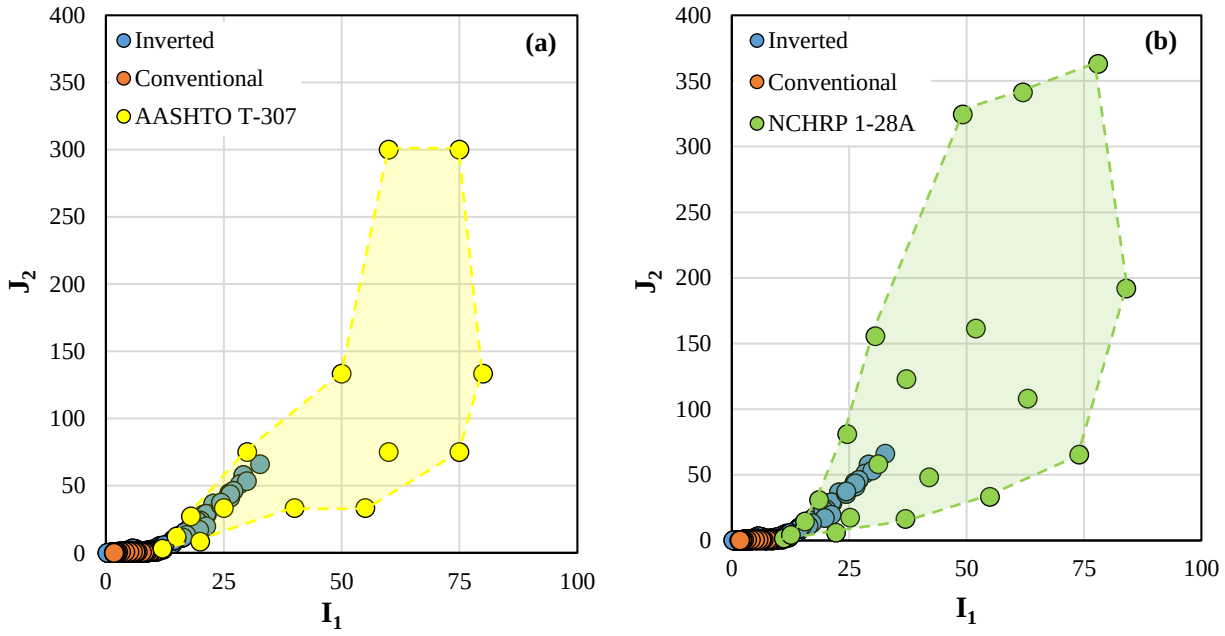

Figure 9.12: I_1-J_2 plots from the stresses calculated within the UAB layer of the Texas inverted and conventional pavement structures compared to (a) AASHTO T-307 and (b) NCHRP 1-28A.

9.3.3. Texas inverted pavement section stress path analysis for super heavy loads

P-q plots were generated to illustrate the stress responses of the UAB layer in the inverted and conventional pavement structures from Texas under the influence of super heavy loads. The data was collected from the same three planes perpendicular to the traffic direction and 84 nodes per plane specified in Figure 9.8.

Figure 9.13(b) displays the p-q plot that represents the stress states computed for the 252 nodes in the UAB layer of the Texas inverted pavement structure subjected to SHLs. The nodes were divided into three planes based on their location, with Plane 1 being the closest to the tire contact area. The scatterplot indicates that the highest p and q values were found in Plane 1, while Planes 2 and 3, which are farther from the tire contact area, exhibited lower maximum p-q values at lower x and y coordinates. Although the p-q values at the bottom of the plot appear to be zero, they are not because the model does not exhibit isotropic conditions. The p-q values in each plane

increase as the shear stresses at the points of analysis increase. The trendlines of the p-q values in each plane depict the progression of the stress paths. The steepest slope was observed in the p-q values from Plane 1, indicating the most critical conditions, while Plane 3 exhibited the shallowest slope of the p-q values, suggesting that the ascending to failure could occur at a slower rate. When comparing Figure 9.13(a), which displays the p-q plot of the UAB layer of the Texas inverted pavement structure under the loading conditions of a conventional aggregate haul truck, to the p-q plot obtained under super heavy load conditions, it is apparent that the p-q values are greater when exposed to the heavier loads.

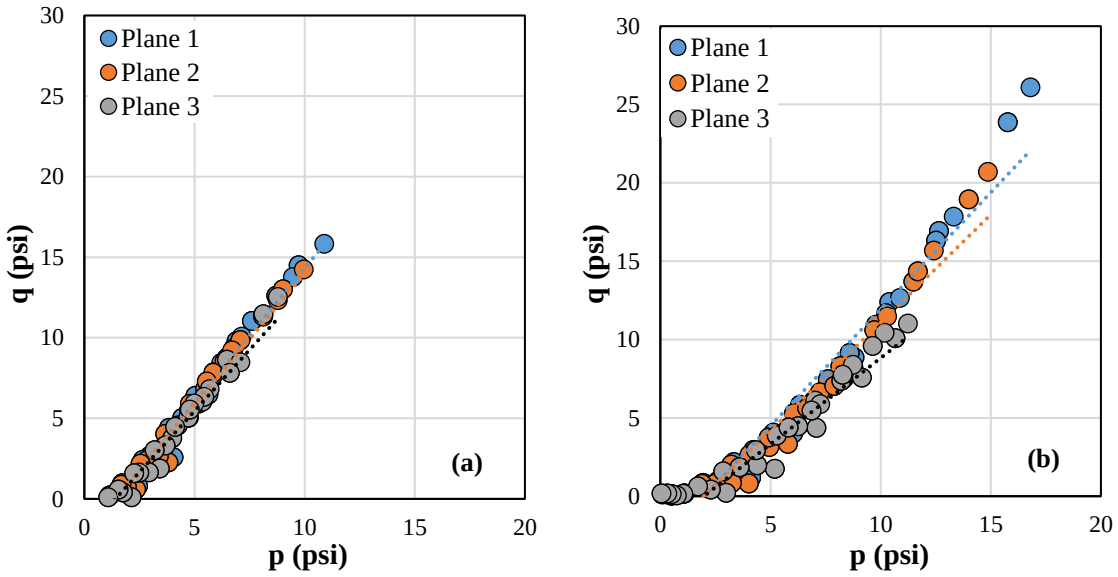

Figure 9.13: P-q plots from the stresses calculated at three transversal planes within the UAB layer of the Texas inverted pavement structure subjected to conventional loads (a) and SHLs (b).

Figure 9.14(b) displays the p-q values obtained from stress analysis of 252 nodes within the UAB layer of both the Texas inverted and conventional pavement structures, subjected to SHLs without any categorization based on planes. The results for each pavement structure were combined for all three planes. It is apparent that the Texas inverted pavement structure exhibits higher p-q values compared to the conventional design. This increase in p-q values is more

prominent in the inverted design, as the UAB layer experiences significantly higher stress magnitudes. Conversely, lower p-q values were observed in the conventional design, with lower slopes for the increase in p-q values. By comparing the p-q values in Figure 9.14(a) computed from stress analysis in the UAB layer of the Texas inverted and conventional pavement structures under conventional loads, it can be seen that the stress states increase significantly when subjected to SHLs, as shown in Figure 9.14(b).

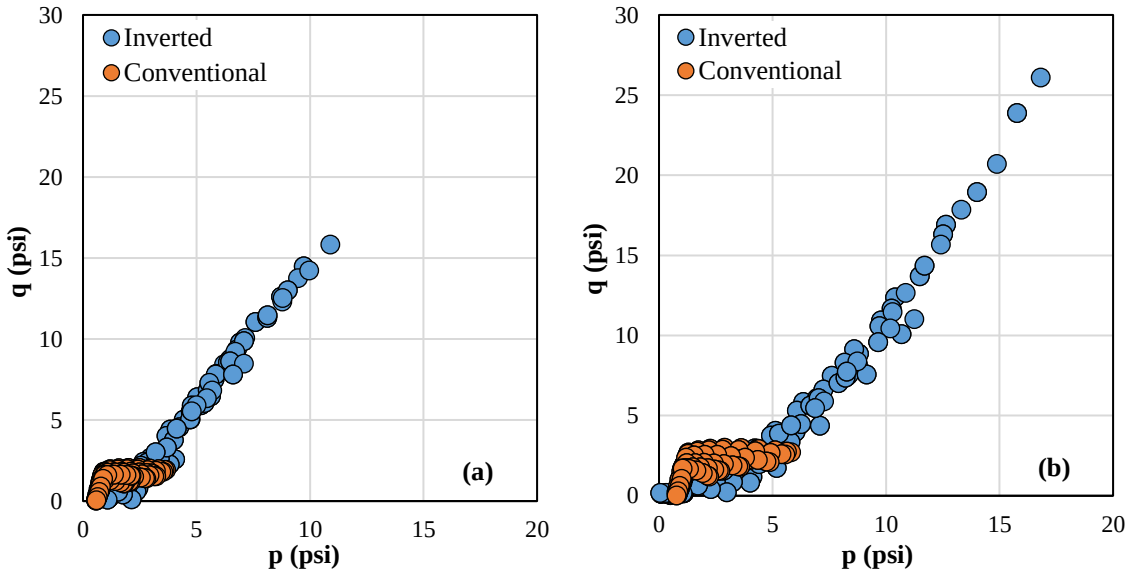

Figure 9.14: P-q plots from the stresses calculated within the UAB layer of the Texas inverted and conventional pavement structures subjected to conventional loads (a) and SHLs (b).

To analyze the stress states experienced by the UAB layer of the Texas inverted and conventional pavement structures under super heavy loads, stress invariants were calculated for each node per plane. Figure 9.15 depicts a scatterplot of the I_1 vs J_2 plot of all 252 nodes analyzed in the UAB layer of the Texas inverted pavement structure, categorized based on their location in three planes and their depth within the UAB layer. The results showed that Plane 1, situated closer to the tire contact area, exhibited higher stresses, with a decreasing trend of the maximum I_1-J_2 values observed when moving from Plane 1 to Plane 3. Additionally, the nodes closer to the surface

of the UAB layer displayed higher I_1-J_2 values in each plane due to the higher stresses developed. The trendlines of each node category demonstrated higher slopes in the top nodes in each plane, signifying more critical conditions and indicating that the progression towards the failure surface could occur at a faster rate. The I_1-J_2 plots obtained when SHLs are applied reveal that the UAB layer experiences much higher stress states, as compared to the plots obtained when conventional loads are applied, as shown in Figure 9.11.

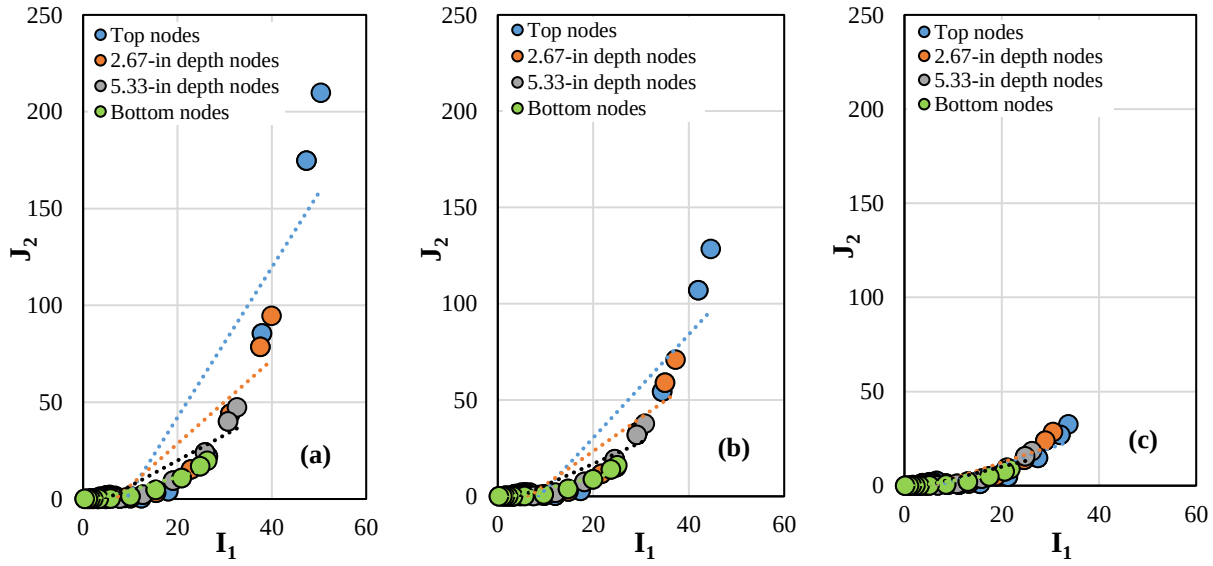

Figure 9.15: I_1-J_2 plots from the stresses calculated within the UAB layer of the Texas inverted pavement structure subjected to SHLs for Plane 1 (a), Plane 2 (b), and Plane 3 (c).

Figure 9.16 depicts the I_1 vs J_2 plots of 504 nodes analyzed in the UAB layer of the Texas inverted and conventional pavement structures subjected to SHLs, with 252 nodes evaluated for each type of pavement design. The I_1-J_2 values obtained from the stress states specified in AASHTO T-307 and NCHRP 1-28A were superimposed on the data points, along with the stress envelopes for each protocol. It is observed that AASHTO T-307 fails to subject granular base materials to certain stress states experienced by the UAB layer of an inverted pavement structure similar to the one constructed in Texas, as indicated by the points outside the stress envelope

defined by the stress limits specified in the standard. On the other hand, the NCHRP protocol appears to better capture all stress states experienced by the UAB layer of the Texas inverted pavement structure, even when SHLs are applied. Both protocols do not subject the aggregate systems to very low stress levels, but the likelihood of transitioning to critical conditions at those low stress intensities is low. It is worth noting that both protocols can simulate the stress levels that the UAB layer of a conventional pavement structure will experience.

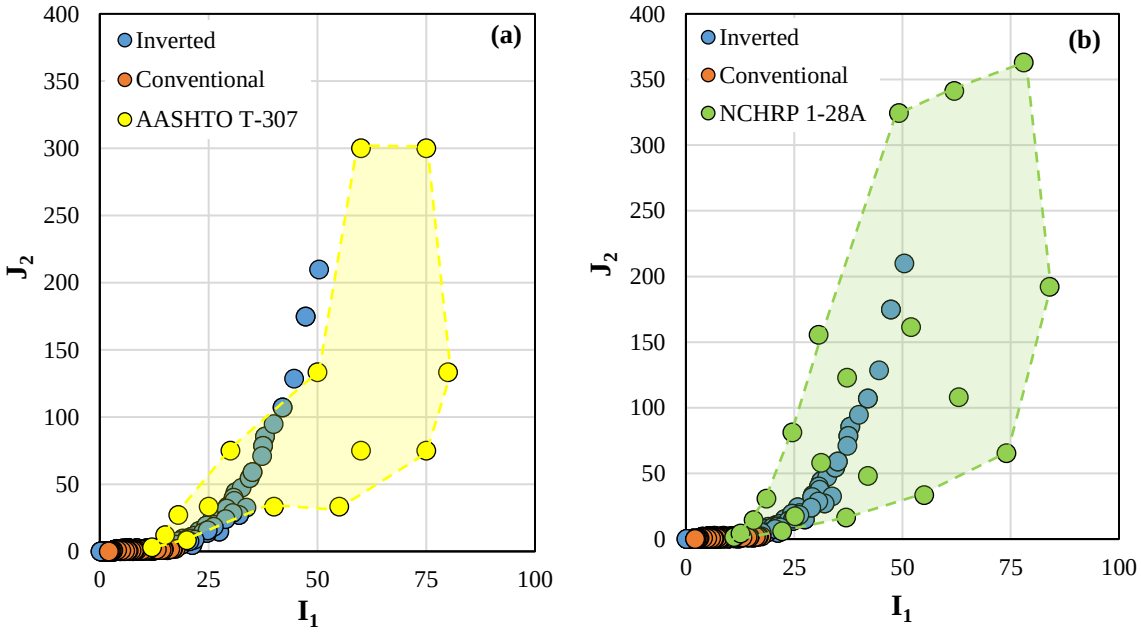

Figure 9.16: I_1-J_2 plots from the stresses calculated within the UAB layer of the Texas inverted and conventional pavement structures subjected to SHLs compared to (a) AASHTO T-307 and (b) NCHRP 1-28A.

9.4. FAILURE FUNCTION ANALYSIS

The objective of this analysis is to assess the stability of the UAB layer in both inverted and conventional pavement structures, considering the stress states that the layer will experience during loading. To ensure that these stresses are within an acceptable range, a failure function is typically used to control the design and evaluate the probability of failure in unbound granular materials.

To maintain the stability of the UAB layer in both inverted and conventional pavement structures, the Mohr-Coulomb yield function will be used. This function, expressed in terms of stress invariants, is presented in Equation 9.4 (Ashtiani 2009). The failure function is defined based on the stress states (i.e., I_1, J_2, third invariant of the deviatoric stress tensor, and the angle of similarity) induced by traffic loads, as well as the strength of the material, which is characterized by the cohesion (c) and the angle of internal friction (φ). By using this function, it is possible to control the design and assess the likelihood of failure in unbound granular mediums.

$$f = \frac{I_1}{3} sin\,\varphi + \sqrt{J_2}\, sin\left(\theta + \frac{\pi}{3}\right) + \frac{\sqrt{J_2}}{3} cos\left(\theta + \frac{\pi}{3}\right) sin\,\varphi - c\, cos\,\varphi \quad (9.4)$$

Where:

θ: Angle of similarity, $cos\ 3\theta = \frac{3\sqrt{3}}{2}\ \frac{J_3}{J_2^{1.5}}$

J_3: third invariant of the deviatoric stress tensor = $\left[\sigma_1 - \frac{I_1}{3}\right]\left[\sigma_2 - \frac{I_1}{3}\right]\left[\sigma_3 - \frac{I_1}{3}\right]$

Choosing appropriate materials is a critical aspect of constructing a UAB layer that can withstand traffic loads. The strength of the base layer material is determined by two key factors: cohesion and the angle of internal friction. Cohesion refers to the plasticity, stickiness, and moldability of the fine-grained portion of the granular mixture, while the angle of internal friction is influenced by the interparticle friction and interlocking effect of the coarse-grained particles in contact. Both the fine and coarse portions of the granular mixture contribute to the strength and load-distribution capacity of the medium.

To evaluate the potential for damage in the UAB layer of inverted and conventional pavement structures, the failure function was assessed at specific points in a plane within the UAB layer transverse to the traffic direction, similar to the locations shown in Figures 9.3 and 9.8 for the Virginia and Texas models, respectively. The calculated values of the failure function serve as

a measure of the probability of failure in the UAB layer. A zero value of the failure function indicates that yielding is taking place, whereas a negative value implies an unlikely probability of failure. On the other hand, a positive value of the failure function indicates that the UAB layer is susceptible to experiencing high plastic deformations.

9.4.1. Virginia inverted pavement section failure function analysis

The material used to construct the UAB layer of the Virginia inverted pavement section was assumed to be a mixture of selected coarse-grained and fine-grained aggregates, producing a cohesion of 8 psi and an angle of internal friction of 32°. Figure 9.17 displays surfaces that depict the computed values of the failure function for all 189 nodes in each respective plane transversal to the traffic flow (63 nodes per plane) located at three specific positions relative to the tire contact area within the UAB layer of the Virginia inverted pavement structure. The value of the failure function is presented on the vertical axis, while the horizontal plane is determined by the depth and offset used to locate each analyzed node.

The results presented in Figure 9.17 demonstrate that the failure function values for all nodes in each plane (top, middle, and bottom) of the Virginia inverted pavement structure were negative, indicating that the structure could withstand traffic loads without experiencing plastic deformation. The plots in Figure 9.17 also reveal that as the depth of the layer increases, the value of the failure function becomes more negative, indicating that the stresses dissipate through the depth of the layer. Similarly, the values of the failure function decrease as the lateral offset from the tire contact area increases. This means that smaller stress states at radial distances from the tire contact area result in less critical conditions. The maximum value of the failure function occurs at the surface and at a lateral offset of zero from the wheel load. Therefore, it can be concluded that

the selected material properties of c = 8 psi and φ = 32° ensure the stability of the UAB layer of the Virginia inverted pavement and minimize the risk of plastic deformation.

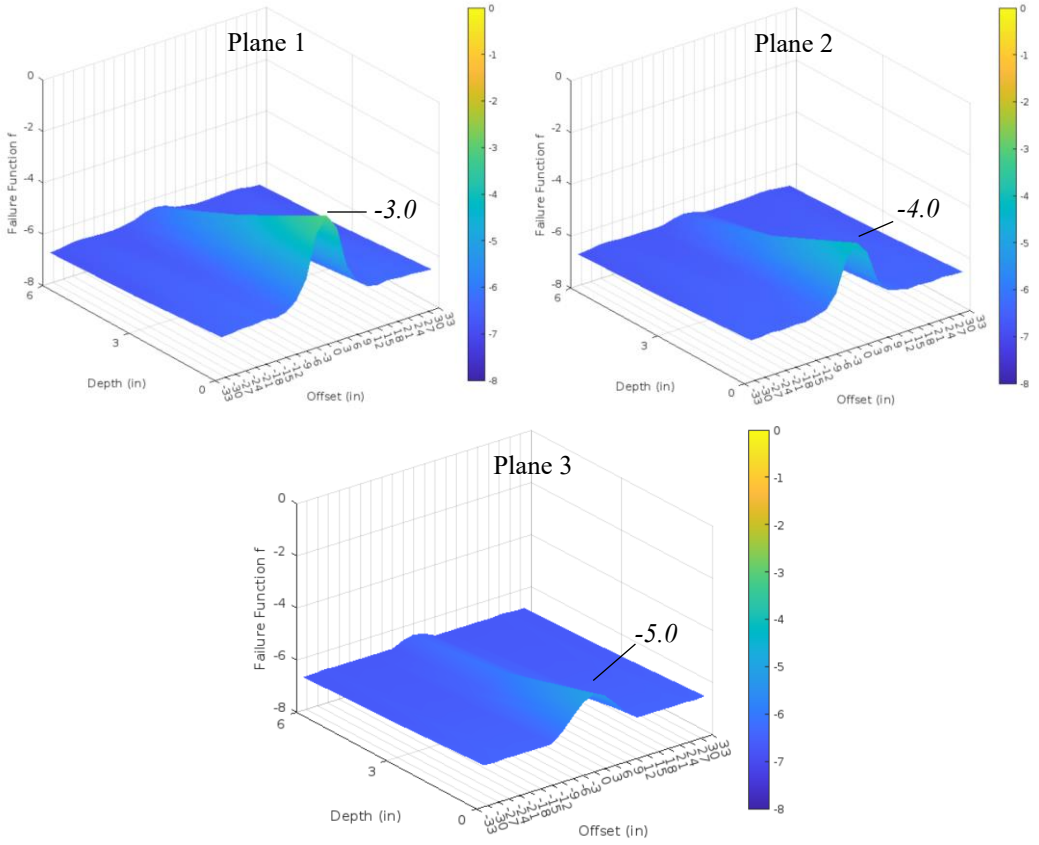

Figure 9.17: Failure function f values in the three planes of analysis within the UAB layer of the Virginia inverted pavement section assuming material properties of c = 8 psi and φ = 32°.

The analysis continued by assigning different strength properties to the UAB layer of the Virginia inverted and conventional pavement structures, with a c value of 3.5 psi and a φ value of 35°. Subsequently, new failure functions were computed for 63 nodes within the most critical plane. The stability of the UAB layer was then compared between the inverted and conventional designs based on the values of the failure function.

The two surfaces resulting from the 3-D plot showing the location of nodes in depth and offset distances with respect to the values of the failure function are presented in Figure 9.18. It is evident that the surface for the inverted design is situated below zero, indicating that the UAB

layer is in a stable condition. However, for the conventional design, the surface reaches positive values close to the tire contact area and the surface, indicating that the material strength in this case leads to unstable conditions for the UAB layer of the Virginia conventional pavement structure. Therefore, the conventional pavement system is likely to undergo plastic deformations when subjected to the corresponding stress states.

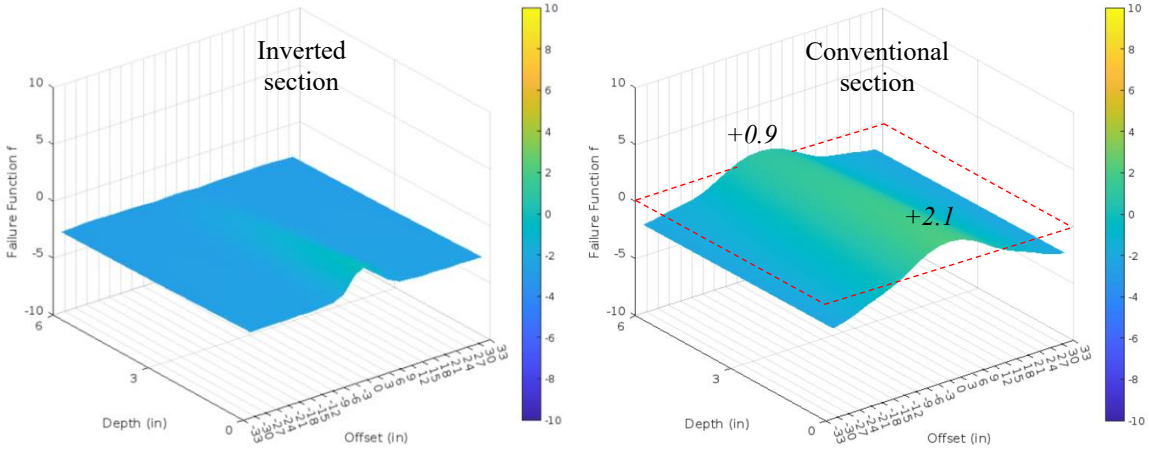

Figure 9.18: Failure function f values in Plane 1 within the UAB layer of the Virginia inverted and conventional pavement sections assuming material properties of c = 3.5 psi and φ = 35°.

To assess the impact of the cohesion and angle of internal friction of aggregates on the stability of the UAB layer of the Virginia inverted pavement section, an analysis was conducted with nodes located at zero lateral offset and zero depth. The cohesion values ranged from 5.5 psi to 8 psi, and the angle of internal friction ranged from 33° to 40°. Figure 9.19 displays the surface representing the combined effect of c and φ on the failure function. The figure demonstrates that as cohesion and angle of internal friction increase, the failure function decreases, indicating a lower probability of the UAB layer failing. This is a logical result, as stronger materials tend to perform better under loading.

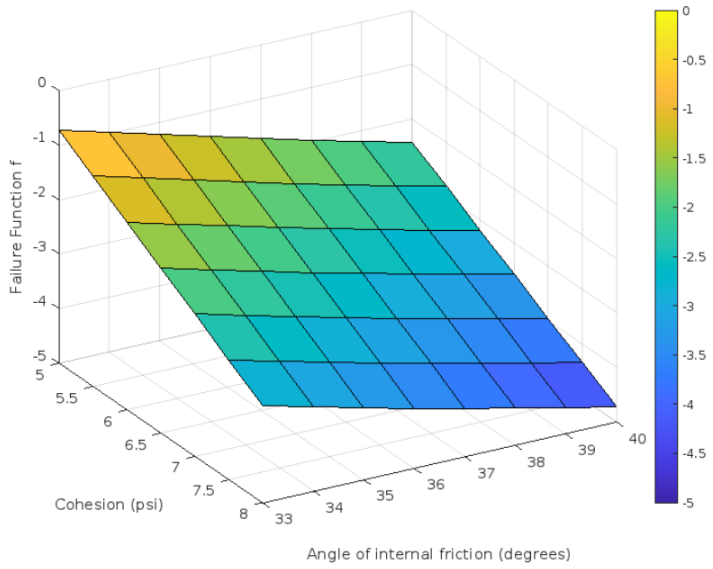

Figure 9.19: Influence of c and φ on the failure function f values in a point located at 0-in depth and 0-in offset from the tire contact area within the UAB layer of the Virginia inverted section.

9.4.2. Texas inverted pavement section failure function analysis for conventional loads

The UAB layer in the Texas inverted pavement section was assumed to be constructed using a combination of coarse-grained and fine-grained aggregates, resulting in a cohesion of 5 psi and an angle of internal friction of 33°. Figure 9.20 illustrates surfaces that exhibit the computed values of the failure function for all 252 nodes in each respective plane situated transversely to the traffic flow (84 nodes per plane) at three specific positions with respect to the tire contact area within the UAB layer of the Texas inverted pavement structure. The value of the failure function is presented on the vertical axis, while the depth and offset used to locate each analyzed node determine the horizontal plane.

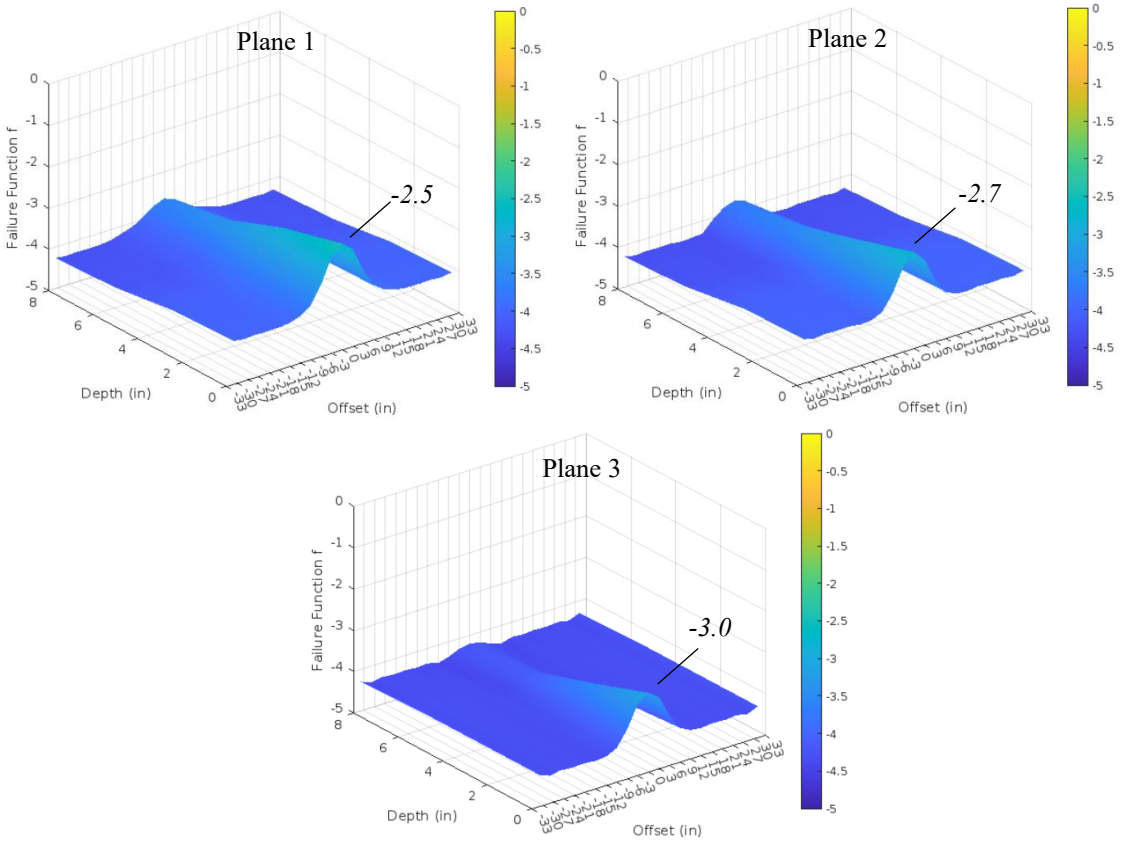

Figure 9.20: Failure function f values in the three planes of analysis within the UAB layer of the Texas inverted pavement section assuming material properties of c = 5 psi and φ = 33°.

The findings depicted in Figure 9.20 show that the failure function values of the Texas inverted pavement structure were negative for all nodes in each plane (top, middle, and bottom). This indicates that the structure can handle traffic loads without undergoing plastic deformation. The plots reveal that as the depth of the layer increases, the failure function value becomes more negative, suggesting that the stresses dissipate through the depth of the layer. Similarly, as the lateral offset from the tire contact area increases, the failure function values decrease, indicating that smaller stress states at radial distances from the tire contact area result in less severe conditions. The maximum failure function value occurs at the surface and at a lateral offset of zero from the wheel load. Therefore, it can be inferred that the selected material properties of c = 5 psi

and φ = 33° ensure the stability of the UAB layer of the Texas inverted pavement and minimize the risk of plastic deformation.

Next, the analysis progressed to assigning distinct strength properties to the UAB layer of the Texas inverted and conventional pavement structures, with c and φ values of 3.5 psi and 35°, respectively. Afterward, new failure functions were computed for 84 nodes located within Plane 1, situated beneath the tire wheel. The stability of the UAB layer was then compared between the inverted and conventional designs, based on the failure function values.

Figure 9.21 displays the two surfaces obtained from the 3-D plot, which depicts the relationship between the failure function values and the location of nodes in depth and offset distances. The surface corresponding to the inverted design is located below zero, suggesting that the UAB layer is stable. In contrast, the surface for the conventional design reaches positive values near the tire contact area and the surface, indicating that the material strength in this case leads to unstable conditions for the UAB layer of the Texas conventional pavement structure. Hence, the conventional pavement system is expected to experience plastic deformations when subjected to the corresponding stress states.

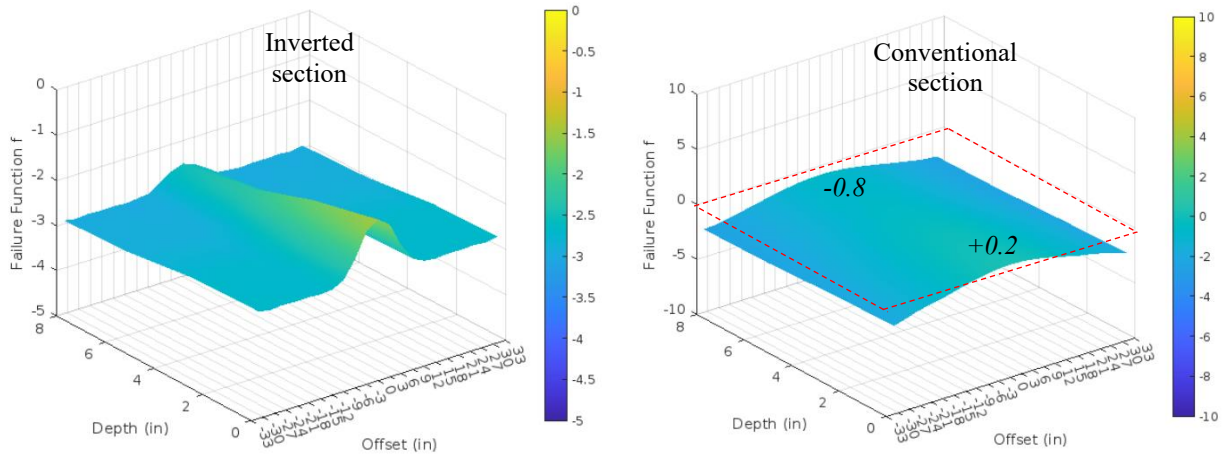

Figure 9.21: Failure function f values in Plane 1 within the UAB layer of the Texas inverted and conventional pavement sections assuming material properties of c = 3.5 psi and φ = 35°.

To investigate how the stability of the UAB layer of the Texas inverted pavement section is affected by the cohesion and angle of internal friction of aggregates, an analysis was carried out using nodes located at zero lateral offset and depth. The same range of cohesion and angle of internal friction as the one used for the Virginia model was applied to the Texas model. The results are presented in Figure 9.22, which shows the surface representing the combined effect of c and φ on the failure function. The figure clearly indicates that as the cohesion and angle of internal friction increase, the failure function decreases, implying a lower probability of the UAB layer failing. This is a reasonable outcome since stronger materials generally exhibit better performance under loading.

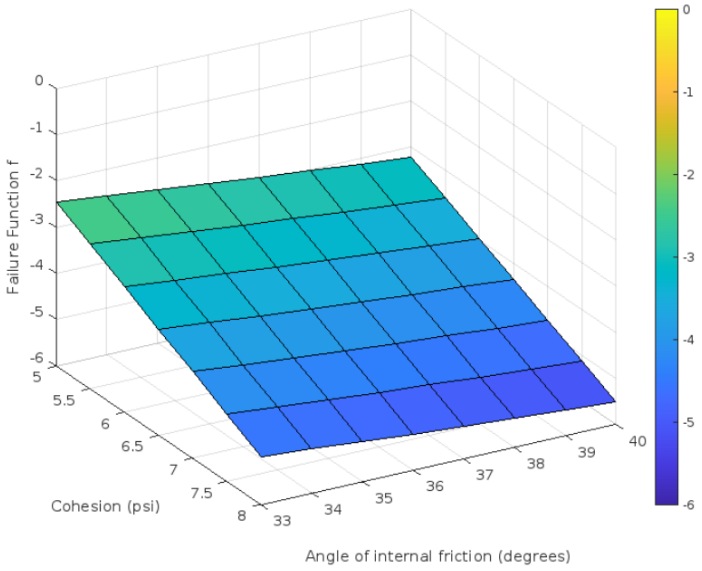

Figure 9.22: Influence of c and φ on the failure function f values in a point located at 0-in depth and 0-in offset from the tire contact area within the UAB layer of the Texas inverted section.

9.4.3. Texas inverted pavement section failure function analysis for super heavy loads

The Texas inverted pavement structure was evaluated under two different types of loads: one load representing conventional trucks and the other one representing the SHL. For the conventional loading, a pressure of 100 psi was applied, while for the SHL, a pressure of 180 psi

was considered. The material for the UAB layer of the inverted pavement structures was considered to exhibit a strength characterized by a cohesion of 5 psi and an angle of internal friction of 33°. Under these material properties, a surface was generated representing the failure function values of the UAB layer in a plane located beneath the tire contact area, which is the most critical plane of analysis.

The surface plot presented in Figure 9.23 depicts the failure function values computed for the UAB layer of the inverted pavement structure under two loading conditions: a conventional aggregate haul truck and a SHL. The plane of analysis is located beneath the tire contact area and includes the 84 nodes situated at four different depths with respect to the layer surface (i.e., 0 in, 2.67 in, 5.33 in, and 8 in). The UAB layer of the Texas inverted pavement section remains stable without experiencing plastic deformation in both scenarios. However, the peak failure function value is closer to zero for the SHL load compared to the conventional load, indicating that the UAB layer under SHL loads is more susceptible to exhibit plastic deformations.

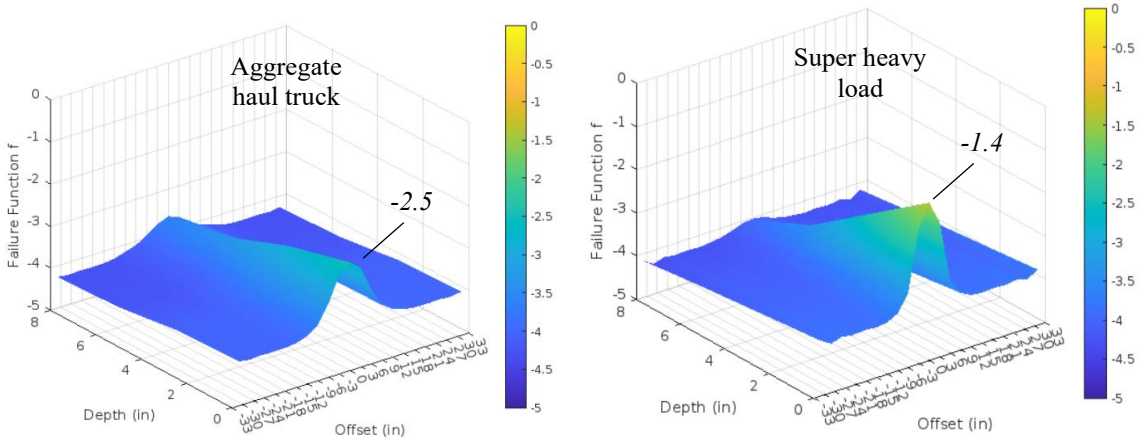

Figure 9.23: Failure function f values in Plane 1 within the UAB layer of the Texas inverted pavement section subjected to conventional loads and SHLs assuming material properties of cohesion and angle of internal friction of 5 psi and 33°, respectively.

For the purpose of evaluating the stability of the UAB layer under different material properties, a new case was studied by assigning a cohesion of 3 psi and an angle of internal friction of 30° to the layer. Similar to the previous analysis, new failure function values were computed for the critical plane within the UAB layer of the Texas inverted pavement structure. The results are presented in Figure 9.24, where it is noticeable that the UAB layer under SHL loading displays positive failure function values, indicating instability and a high probability of plastic deformation at the surface and 0 in of offset from the tire contact area. In contrast, for the UAB layer under the aggregate haul truck load, all failure function values are negative, indicating stable conditions under loading. This inverted pavement design does not meet the demands of the stressful states produced by SHLs.

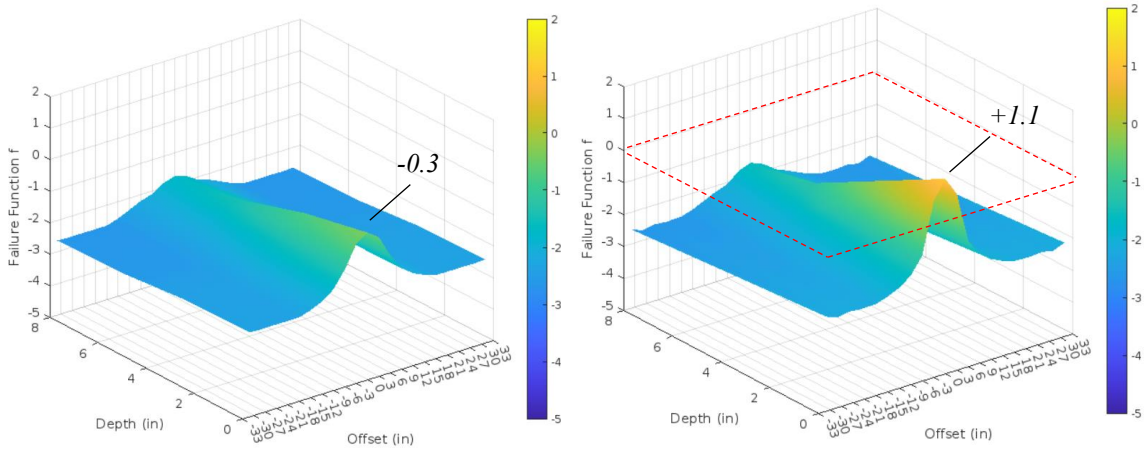

Figure 9.24: Failure function f values in Plane 1 within the UAB layer of the Texas inverted pavement section subjected to conventional loads and SHLs assuming material properties of cohesion and angle of internal friction of 3 psi and 30°, respectively.

Chapter 10: Summary of Findings and Conclusions

10.1. MATERIAL MODELS FOR THE DESIGN OF CEMENTITIOUSLY STABILIZED LAYERS

This dissertation aimed to investigate the inter-relations between the IDT strength and UCS and the relationships between the M_r and UCS of cementitiously stabilized virgin and reclaimed materials. To fulfill this objective, a comprehensive experimental program was designed and executed in the laboratory, underscoring the fabrication, and testing of cement-stabilized specimens. The experiment design included the use of limestone and gravel as virgin materials, and RCA and FDR aggregates as reclaimed materials, to study the influence of the mineralogical properties and surface characteristics on the mechanical performance of cement-treated systems. Three levels of cement dosage ranging from 2% to 4% were incorporated into the mixtures to examine the behavior of lightly to moderately stabilized mediums. The laboratory compaction process involved using the IH, VH, TGC, and SGC methods to fabricate cylindrical specimens of different sizes. Before undergoing mechanical testing, the samples were subjected to two different curing/conditioning methods to evaluate the susceptibility of aggregate to moisture retention and transport. The strength and resilient properties of the specimens were characterized using the UCS test, IDT strength test, and M_r test, performed at SRs of 25% and 50%.

The results of the laboratory analysis showed a positive correlation between the IDT strength and the UCS, with a simplified linear relationship indicating that the IDT strength was approximately 10% of the UCS when all experiment design permutations were incorporated into the model development. The variation in trendline slopes and the different ranges of strength achieved by each material emphasized the impact of aggregate type on the tensile and compressive behavior of virgin and reclaimed cementitiously stabilized systems. Additionally, the UCS-IDT strength relationship was highly sensitive to the H/D ratio of the cylindrical laboratory-compacted

specimens. Apart from specimen size, the compaction energy applied during the fabrication process also influenced the orthogonal strength properties of the specimen. Based on these findings, a set of material models were developed to predict IDT strength as a function of the UCS, H/D ratio, and cement dosage. The regression coefficients of the IDT strength models varied according to the moisture/conditioning and compaction procedures adopted during the specimen preparation phase of the study. The consideration of four material types, three levels of cement dosages, four compaction methods, three H/D ratios, and two moisture/conditioning procedures led to the generalization of the material models, resulting in satisfactory forecasting capabilities.

The results from the laboratory experiments showed a clear relationship between the UCS and M_r of cement-stabilized specimens, particularly for low cement content. The variation in the slopes of the trendlines and the different ranges of M_r and UCS for each material type emphasized the impact of aggregate type on the resilient and compressive behavior of both virgin and reclaimed materials. The amount of cement added to the mixtures also had a significant effect on the spread of the M_r-UCS data points around the mean, with lighter stabilization showing a tighter distribution compared to moderate stabilization. The influence of the SR during the M_r testing was also considered in the analysis. Lower SR values resulted in higher M_r, while higher stress paths led to increased strains and decreased M_r across all permutations of the experiment. These findings highlight the importance of strain dependency in the responses and its implications for the design of stabilized highway pavements in high-traffic areas.

10.2. INFLUENCE OF LABORATORY COMPACTION METHODS ON THE MICROSTRUCTURE AND STRENGTH PROPERTIES OF CEMENTITIOUSLY STABILIZED MATERIALS

The objective of this dissertation was to investigate the effect of impact, vibratory, and gyratory compaction methods on the microstructural features and strength properties of virgin and reclaimed materials stabilized with cement. To achieve this objective, a complete laboratory program was designed, considering four aggregate sources, three dosages of cement, and four different compaction procedures. The microstructural analysis included the fabrication of limestone specimens treated with 3% cement and compacted using the IH, VH, and SGC. For the strength analysis, limestone, gravel, RCA, and FDR materials were mixed with 2%, 3%, and 4% cement to fabricate a set of cementitiously stabilized cylindrical specimens compacted under three different mechanisms, including impact, vibratory, and gyratory methods. After 7-day curing, the specimens were subjected to compressive and tensile testing to determine the UCS and IDT strength of the cement-treated systems.

It was found from the X-ray computerized tomographic imaging results that the specimen compacted with the SGC presented a more homogeneous internal structure with lower porosity values as compared to impact-compacted and vibratory-compacted specimens. The predominant uniformity in the microstructure of the gyratory-compacted specimen can be attributed to the fact that the SGC imparted the compaction energy through the combined action of kneading, vibration, and static pressure with the absence of lifts. Moreover, the gyratory compaction mechanism eliminated any bedding error and trapped air voids close to the inner perimeter of the mold, resulting in high-quality laboratory-compacted specimens.

Supplementary to the microstructural analyses, the influence of compaction methods on the UCS and IDT strength properties of cementitiously stabilized virgin and reclaimed aggregate

base materials was also investigated in this dissertation. The compressive strength results indicated that gyratory-compacted specimens exhibited higher UCS values than specimens fabricated using the impact compaction method. Regarding the IDT strength results, all specimens fabricated with the gyratory compaction method tend to have higher tensile strength values than the specimens prepared with impact and vibratory hammers. Higher compressive and tensile strength values in specimens compacted with the SGC can be explained due to more uniform microstructures with less amounts of voids and thus improved interparticle friction and interlocking effect.

On the previous subject matter, compaction energies imparted by impact, vibratory, and gyratory compaction methods have proven to exert a considerable influence on the compressive and tensile strength properties of cementitiously stabilized specimens. Based on the UCS and IDT strength data obtained in this study, the strength of a specimen does not consistently increase with a higher amount of compaction energy. As a complement to the amount of energy that equipment is capable of providing, a crucial factor is the mechanism of transmission of the compaction energy to the specimen. For example, in most cementitiously stabilized specimens, higher IDT strength values were obtained in specimens compacted with the SGC, despite the fact that its compaction energy was approximately 34% lower than that of the VH. These findings could be attributed to the fact that a significant amount of energy was lost during compaction with the VH. During compaction with the SGC, the synergistic effects of compressive pressure, shearing forces, and kneading are responsible for generating specimens with the highest IDT strength values. Similar conclusions can be drawn based on the comparison of UCS results of impact-compacted and vibratory-compacted specimens. In more than half of the cementitiously stabilized blends, higher UCS strength values were obtained in specimens compacted with the IH, despite the fact that its compaction energy was approximately 82% lower than that of the VH.

Additional testing is required to confirm the laboratory results of air void distribution and orthogonal strength properties of virgin and reclaimed cementitiously stabilized specimens fabricated using different compaction methods. It is necessary to use a different database and compare the results of laboratory-compacted specimens with those of field core samples to establish suitable correlations between compaction methods and strength results. These studies will help provide insights into the fabrication of uniform cementitiously stabilized specimens and reduce the variability in mechanical testing results caused by poor-quality specimen preparation in the laboratory.

10.3. THE BULL RUN INVERTED PAVEMENT ROAD TEST: DEFLECTION ANALYSIS AND DEFORMATION CHARACTERIZATION FROM FIELD TESTING RESPONSES

The inverted pavement road test located on Bull Run Route 659 in Chantilly, Virginia, was conceived as a full-scale testing site to study the interaction between the different layers of the non-conventional structural system and their mechanical properties under dynamic traffic loading conditions. Data extracted from the in-situ test program is relevant to comprehending the structural conception of inverted pavements and establishing the basis for the development of numerical simulations.

This dissertation focused on the deflection analysis of the inverted pavement section, as well as the deformation characterization of inverted and conventional pavement structures measured from in-situ test evaluations performed on the Bull Run testing site. DCP tests were executed at the top of the UAB layer at the inverted pavement structure, while FWD tests were conducted at the most superficial layers in both inverted and conventional pavement structures.

According to the analysis of the data collected from the field, the DCP testing results, expressed in the form of cumulative penetration in correspondence to a rising number of blows, showed a similar progression of the vertical penetration of the cone within the UAB layer in three out of four of the evaluated inverted pavement stations per lane. The station with a distinctive trend in the evolution of the cumulative deformation exhibited lower penetrations per lane, suggesting an improved resistance to the cone being driven into the layer. It was also found that the rate of penetration into the UAB layer tended to decrease at more profound levels closer to the underlying CTB layer. Moreover, correlations between the cone penetration rate and stiffness indicate that in the proximities to the stabilized medium, the Moduli values of the UAB layer were greater compared to the rigidities at the upper levels of the UAB layer farther from the CTB layer. As a final analysis of the DCP field data, partial penetration depths in each UAB sublayer were calculated. It was noted that an average of 75% of the total penetration within the UAB layer took place at the upper and middle UAB sublayers. The behavior of the UAB layer under penetration can be attributed to the non-stabilized granular layer compacted on top of a significantly stiffer medium. This unconventional arrangement of layers resulted in a higher compactibility at the bottom of the UAB layer, as well as lower plastic deformations within the system, evidenced by the high stiffness values and lower rates and depths of penetration developed in the UAB layer overlying the CTB layer, especially in the parts of the UAB layer closer to the cementitiously stabilized layer.

Based on the FWD testing results, the inverted pavement structure presented considerably lower deflections measured below the loading plate as compared to the vertical deformations at zero lateral offset in the conventional pavement structure. Additionally, significantly less dispersion in the deflection data was observed on the inverted pavement structure due to the

positive influence of the stiff underlying CTB layer on the homogeneity of compaction of the UAB layer. Five indices, i.e., BLI, MLI, LLI, F-1 factor, and AREA value, were computed based on the deflection data from all nine geophones used during FWD testing in inverted and conventional layered systems. The values of the indices adopted by the inverted pavement structure denoted an enhanced structural condition and a lower dispersion of the data. This behavior can be attributed to the uniformity of compaction of the UAB layer due to the underlying CTB layer. This stabilized layer served as a rigid platform for the untreated aggregate medium and contributed to the increase in stiffness, better compactability, homogeneity in the compaction, and reduction of the vertical deformations in the UAB layer of the inverted pavement structure. Lastly, a deflection basin analysis was performed involving the calculation of the slope of the trendline from the vertical deformations registered by a group of geophones located closer to the loading plate, called the primary deflection sensors, and another group of geophones located more distantly called the secondary deflection sensors. Low variability in the dissipation rate of the deflections at a higher lateral offset on both clusters of sensors was evident in the inverted pavement structure, underscoring the favorable influence of the CTB layer on the uniformity of compaction of the UAB layer, capable of generating a more homogeneous rate of change of the vertical deformations in consecutive sensors within each cluster.

10.4. NUMERICAL ANALYSIS OF INVERTED PAVEMENT STRUCTURES

The Virginia and Texas inverted pavement structures along with their conventional counterparts were modeled employing the FE method. Input parameters essential for defining the numerical models were derived from field test results. The simulated pavement models were subjected to the same loading conditions, and their resulting responses were analyzed and compared.

10.4.1. Isotropic Analysis

Findings revealed that the inverted pavement structure experienced higher stresses and strains at the bottom of the AC layer compared to the conventional pavement structure. This phenomenon can be attributed to the more flexible UAB layer placed beneath the AC layer in the inverted design. The UAB layer allows for the upper AC layer to deform and deflect when subjected to loads, resulting in higher tensile stresses and strains at the bottom of the asphaltic layer. In contrast, the CTB layer of the conventional pavement design is stiffer and restrains the deformation of the AC layer, leading to lower stresses and strains at the bottom of the superficial layer. Therefore, the design of inverted pavements should consider the higher stresses and strains that the AC layer will undergo, and an appropriate thickness and asphaltic mix should be chosen accordingly. Controlling the reduction of the fatigue life due to bottom-up cracking can be achieved by appropriately designing the AC layer of the inverted pavement structure to resist the expected higher tensile stresses and deformations under loading.

The compressive stress at the top of the SG soil was another critical pavement response, along with stresses and strains at the bottom of the AC layer, analyzed in this dissertation. Results show that the inverted pavement structure performed better than the conventional pavement structure in terms of stress distribution capacity and lower strains. Overall, the inverted pavement design had better load-bearing capacity and lower levels of stresses transmitted to the subgrade soil as compared to the equivalent conventional pavement configuration.

The vertical deformation at the top of the AC layer was also analyzed as a pavement response for both inverted and conventional structures. The results showed that the inverted pavement system had higher deformations, indicating that it is more susceptible to developing permanent deformation. This is consistent with a previous study where an inverted pavement

design exhibited evidence of rutting after two years of traffic loads. Suitable mixture designs capable of providing adequate rutting resistance in the AC layer must be taken into account during the design of inverted pavement systems. The timely application of an overlay during the life cycle of the inverted pavement structure is another alternative for addressing minor surface defects such as early-stage rutting.

The location of neighboring axles had a significant impact on the tensile stresses and strains at the bottom of the AC layer, compressive stresses, and strains at the top of the subgrade soil, and vertical deformation at the top of the surface layer. Specifically, the stresses and deformations measured in a given axle were influenced by those developed in adjacent axles. However, the steering axle was found to be an exception in all cases due to its distance from the Single 1 axle, which prevented any influence on the stresses, strains, and vertical deformations developed in the critical locations. To accurately capture the overlapping effects of stresses, strains, and deformations, it is recommended to always consider the axles located in close proximity to the axle of interest.

Focusing on the UAB layer of inverted and conventional pavement structures, higher vertical stresses were registered at the top of the untreated medium of the inverted pavement due to the proximity of the UAB layer to the surface where loads are applied. Additionally, vertical stresses dissipate completely between two consecutive peaks below the tire contact areas in the inverted pavement, but not in the conventional pavement. The location of the UAB layer and the extent of the pressure bulb explain this difference in behavior. The UAB layer is closer to the surface in the inverted pavement, where the pressure bulb is smaller, allowing for stress dissipation. In contrast, the UAB layer of the conventional pavement is located deeper, resulting in incomplete stress dissipation due to the higher extent of the pressure bulb.

Shear stresses along the surface of the UAB layer in both inverted and conventional pavement structures were analyzed in two directions i.e., longitudinal and transversal to the direction of traffic. Results showed that the inverted pavement experienced higher shear stresses due to its proximity to the surface where loads are applied. All shear stresses were higher at the edges of the contact area and were zero beneath the tire contact areas for each axle. These findings suggest that the location of the UAB layer plays a crucial role in stress distribution, resulting in significant differences in shear stresses between the two types of pavement structures.

After analyzing the top surface of the UAB layer in the inverted and conventional pavement structures, the study focused on stress dissipation inside the layer. The findings indicate that the UAB layer experiences considerably higher stresses in the inverted pavement structure due to its proximity to the load surface. It can be observed that a similar behavior is evident when comparing the horizontal stresses developed within the UAB layer. The results of this study underscore the critical role of proper material selection, compaction, and design in determining the thickness of the UAB layer for an inverted pavement structure. These findings are particularly relevant as the UAB layer in this type of pavement is subjected to significantly higher vertical, horizontal, and shear stresses than that of a conventional pavement system. Therefore, it is essential to carefully consider these factors during the design and construction of an inverted pavement to ensure its long-term durability and performance.

10.4.2. Anisotropic Analysis

The simulation of the UAB layer in pavement structures using an isotropic assumption has been found to result in inaccurate or underestimated stresses, which could potentially cause failure of the pavement structure. To address this issue, the UAB layer in inverted and conventional pavement structures has been simulated as an anisotropic medium. Anisotropy refers to the

directional dependence of material properties and is present in unbound granular mediums due to the random arrangement of particles during compaction, even before the layer is subjected to traffic loads.

When cross-anisotropic properties were assigned to the UAB layer, it resulted in increased vertical and horizontal stresses as well as vertical and horizontal strains within the medium. This indicates that the level of anisotropy, which is determined by the ratio of horizontal Modulus to vertical Modulus, is an important factor in determining the stresses within the layer. To accurately understand the behavior of the UAB layer under loading, its directional dependency must be taken into account. As such, the design of inverted pavement structures should consider the directional dependency of the material properties of the UAB layer to ensure that it can withstand the actual stresses it will experience.

In accordance with relevant literature, this study has identified that a level of anisotropy around 0.3 is appropriate for characterizing granular materials, specifically the UAB layer of an inverted pavement structure. This conclusion was drawn by comparing measured pavement responses from the Virginia inverted section, such as longitudinal strain at the bottom of the AC layer and vertical stress at the top and bottom of the UAB layer, to calculated pavement responses obtained from the numerical simulation. The results showed that the measured and estimated values were similar when the horizontal Modulus was assumed to be 30% of the vertical Modulus. This finding is significant because it sheds light on the necessary level of anisotropy required to model the mechanical behavior of unbound granular systems subjected to loads in pavement structures. Consequently, it can be concluded that the numerical model developed based on the Virginia inverted pavement section and then replicated for the Texas inverted pavement section is a valuable tool for future design and analysis of this particular type of design.

The level of anisotropy of the UAB layer has a significant impact on critical pavement responses in both inverted and conventional structures. Findings of this dissertation demonstrate that the stresses and strains developed within the UAB layer change depending on the level of anisotropy. This relationship highlights the close connection between the cross-anisotropic level of the unbound medium and its load-bearing capacity that impacts the performance of the entire pavement structure.

10.5. STABILITY ANALYSIS OF UNBOUND AGGREGATE SYSTEMS IN PAVEMENT STRUCTURES

In this chapter, multiple models were generated using the Abaqus software to simulate inverted pavement systems of the Virginia and Texas designs, along with equivalent traditional pavement designs. To assess the impact of heavier loads, additional models were created for the Texas inverted and conventional pavement structures. The material properties and layer thicknesses for the inverted pavement structures constructed in Virginia and Texas were retained, while an anisotropic UAB layer with an E_x to E_y ratio of 0.3 was incorporated into all pavement structures. In the Virginia models, the simulation focused on the impact of a single wheel load from the steering axle of an aggregate haul truck. Two different loading conditions were considered for the Texas models, including a pressure of 100 psi from a single wheel of the steering axle of the same aggregate haul truck used in Virginia and a pressure of 180 psi representing a super heavy load (SHL). FE modeling approach enabled the assessment of critical pavement responses under various loading conditions for different pavement designs, providing valuable insights into the performance of inverted and conventional pavement structures.

The study highlights the importance of considering stress-induced anisotropy in the mechanistic design and analysis of the unbound granular layer in pavement structures. The analysis shows that the location of external wheel loads in relation to the point of analysis introduces an

additional directional dependence of stiffness properties in the UAB layer. The inclination of the principal plane varies longitudinally as the wheel load moves, resulting in higher stress states in the UAB layer of inverted pavement structures. Neglecting stress-induced anisotropy could result in premature pavement failure and suboptimal performance. By accounting for these factors in pavement design and analysis, engineers can improve the durability and longevity of pavement structures and reduce the need for costly repairs and maintenance.

In pavement engineering, it is crucial to understand the stress states developed within the pavement layers due to traffic loading. One way to visualize and analyze these stress states is by plotting stress paths on a p-q graph or on a I_1 vs J_2 plot. The study analyzed the stress states experienced by the UAB layer of the Virginia and Texas inverted and conventional pavement structures. The study found that the inverted pavement design experienced higher stress magnitudes, stress paths with steeper slopes, and more critical conditions than the conventional pavement design. The comparison between the stress envelopes defined by the AASHTO T-307 and NCHRP 1-28A protocols reveals that the latter imposes more demanding stress states on the UAB layer of the inverted pavement structure. This suggests that the NCHRP protocol is better suited to simulate the stress conditions experienced by the UAB layer of an inverted pavement structure. However, both protocols can capture the stress levels experienced by the UAB layer of a conventional pavement structure. The data points that fall outside the stress envelope defined by the AASHTO standard highlight the limitations of this protocol in capturing all stress states experienced by the UAB layer of an inverted pavement structure. Although both protocols do not apply very low stress levels to the aggregate systems, the probability of reaching critical conditions at those stress intensities is low and can be disregarded.

The stability of the UAB layer was also studied in both inverted and conventional pavement structures by considering the stress states that the layer will experience during loading. The Mohr-Coulomb yield function is a reliable tool for controlling the design and evaluating the probability of failure in unbound granular materials. By expressing the function in terms of stress invariants and material strength parameters such as cohesion and angle of internal friction, the failure function can be defined based on the stress states induced by traffic loads. Using this function, it was possible to assess the likelihood of failure and evaluate the stability of the UAB layer in both pavement structures.

The failure functions of various base layer materials were computed under different scenarios, with specific cohesion and angle of internal friction values assumed. Additionally, the stress states of the UAB layer in both inverted and conventional pavement structures of Virginia and Texas were taken into account for the calculation of the failure function values. These values were presented in a 3-D surface plot, with the depth and offset distances determining the horizontal plane.

If the failure function surface was located on the negative side of the vertical axis, it indicated that the UAB layer could sustain traffic loads without experiencing any plastic deformation. The shape of the surface showed that as the depth of the layer increased, the failure function value became more negative, indicating that stresses dissipated through the depth of the layer. Similarly, as the lateral offset from the tire contact area increased, the failure function value decreased, meaning that smaller stress states at radial distances from the tire contact area resulted in less critical conditions. The highest value of the failure function occurred at the surface and at a lateral offset of zero from the wheel load. Based on the different scenarios evaluated, the UAB layers of the inverted pavement structures demonstrated better stability performance than the UAB

layers of the conventional pavements, which exhibited positive values of failure function at surface points closer to the tire contact area, indicating more probability to undergo plastic deformation.

When subjected to SHLs, the UAB layer of the Texas inverted pavement structure experiences higher stress states, as evidenced by the increased values seen in the p-q and I_1 vs J_2 plots when compared to conventional traffic loads on an unbound granular medium. Evaluation of the failure function for the UAB layer, based on the assigned values of cohesion (c) and angle of internal friction (φ), indicates that the granular material fails and experiences plastic deformation at critical conditions that are closer to the tire contact area. This suggests that inverted pavement designs may not be the most effective solution for resisting SHLs, as the UAB layer is prone to unstable conditions such as fracture of the material and breaking of the coarser aggregate. Therefore, a detailed analysis should be conducted to evaluate the stability of the UAB layer when subjected to high-stress conditions, such as those observed in the Permian Basin area in Texas.

Lastly, the analysis of the impact of the cohesion and angle of internal friction of aggregates on the stability of the UAB layer of the inverted pavement sections showed that as these properties increase, the failure function decreases, indicating a lower probability of the UAB layer failing. However, caution must be exercised when increasing cohesion as the percentage of fine-grained soil in the mix should not exceed 2%. The presence of more than 2% fines can result in moisture susceptibility and volumetric instability, leading to increased swelling and shrinkage potential as well as freezing and thawing potential, which can compromise the structural integrity of the UAB layer of the pavement structure.

References

Al-Qadi, I., Wang, H., and Tutumluer, E., (2010) "Dynamic Analysis of Thin Asphalt Pavements by Using Cross-Anisotropic Stress-Dependent Properties for Granular Layer." *Transportation Research Record*, No. 2154, pp. 156–163.

American Association of State Highway and Transportation Officials, AASHTO. (2003) "Standard Method of Test for Determining the Resilient Modulus of Soils and Aggregate Materials." *AASHTO T 307*, Washington, DC.

Arabani, M. and Karami, M. (2007) "Geomechanical Properties of Lime Stabilized Clayey Sands." *The Arabian Journal for Science and Engineering*, 32 (1B), pp 11-25.

Arabali, P., et al. (2018) "Application of Superpave Gyratory Compactor for Laboratory Compaction of Unbound Granular Materials." *International Conference on Transportation and Development*, American Society of Civil Engineers, pp. 359-370.

Arcement, B.J., and Wright, S.G. (2001) "Evaluation of Laboratory Compaction Procedures for Specification of Densities for Compacting Fine Sands." *Report No. FHWA/TX-02/1874-1*, Federal Highway Administration.

Arrieta, J., Batista, E., dos Santos, R., and Lundgren, J. (2018) "Empirical Relationships with Unconfined Compressive Strength and Split Tensile Strength for the Long Term of a Lime-Treated Silty Soil," *Journal of Materials in Civil Engineering*, 30(8): 06018008.

Ashtiani, R. (2009) "Anisotropic Characterization and Performance Prediction of Chemically and Hydraulically Bounded Pavement Foundations." *Thesis (Ph.D.)*, Texas A&M University.

Ashtiani, R., Morovatdar, A., Licon, C., Tirado, C., Gonzales, J., and Rocha, S. (2019) "Characterization and Quantification of Traffic Load Spectra in Texas Overweight Corridors and Energy Sector Zones," *Report No. FHWA/TX-19/0-6965-1*, The University of Texas at El Paso, TX.

Ashtiani, R., and Tarin, J. (2016) "Testing Procedure for Long Life Heavy Duty Stabilized Bases." *Report No. FHWA/TX-20/0-6812-1*, The University of Texas at El Paso, TX.

Ashtiani, R.S., Rashidi, M., Rodriguez, E., Ordaz, M., Cruz H., Garay, G., and Rocha, S. (2020) "Establishing Best Practices for Construction and Design of Cement Treated Materials." *Report No. FHWA/TX-19/0-6949-0*, The University of Texas at El Paso, Austin, TX.

Babic, B. (1987) "Relationships Between Mechanical Properties of Cement Stabilized Materials." *Journal of Materials and Structures*, 20, pp 455-460.

Barenberg, E. (1977) "Evaluating Stabilized Materials." *Contract No. HR 63-4-1*, National Cooperative Highway Research Program, NCHRP.

Barksdale, R.D. (1984) "Performance of Crushed Stone Base Courses." *Transportation Research Record 954*, Transportation Research Board, Washington, DC.

Browne, M.J. (2006) "Feasibility of using a Gyratory Compactor to Determine Compaction Characteristics of Soil." *Thesis (MSc)*, Montana State University.

Buchanan, S. (2010) "Inverted Pavements-What, Why, and How?" *AFTRE Industry Education Webinar*. Aggregates Foundation for Technology, Research, and Education. Alexandria, VA.

Cerni, G., and Camilli, S. (2011) “Comparative Analysis of Gyratory and Proctor Compaction Processes of Unbound Granular Materials.” *Road Materials and Pavement Design*, 12(2), pp. 397-421.

Chen, D., Lin, D., Liau, P., and Bilyeu, J. (2005) “A Correlation Between Dynamic Cone Penetrometer Values and Pavement Layer Moduli.” *Geotechnical Testing Journal*, 28(1), pp. 42-49.

Cortes, D.D. and Santamarina, J.C. (2013) “The LaGrange Case History: Inverted Pavement System Characterization and Preliminary Numerical Analyses.” *International Journal of Pavement Engineering*, 14(5), pp. 463–471.

Dempsey, B., Janssen, B., Thomas, J., Frey, P., Ioannides, A., and Elliott, N. (1984) “Development of a Preliminary Stabilized Material Pavement Analysis System.” *Report No. ESL-TR-83-34*, University of Illinois at Urbana-Champaign, IL.

Du, Y., et al. (2018) “Preliminary Investigation of the Feasibility of Using a Superpave Gyratory Compactor to Design Cement-Treated Aggregate Mixture.” *Applied Sciences*, 8(6), 946.

Georges, T. (2007) “Falling Weight Deflectometer (FWD) Test Results: Entrance Road of the Lafarge Quarry in Morgan County, GA.” *Final Report*, Georgia Department of Transportation.

Gnanendran, C. and Piratheepan, J. (2010) “Determination of Fatigue Life of a Granular base Material Lightly Stabilized with Slag Lime from Indirect Diametrical Tensile Testing.” *Journal of Transportation Engineering*, 136 (8), pp 736-745.

Grau, R.W. (1973) “Evaluation of Structural Layers of Flexible Pavements.” *Miscellaneous Paper S-73-26*, U.S. Army Engineer Waterways Experiment Station, Vicksburg, Mississippi.

Hossain, M. and Kim, W. (2015) “Estimation of Subgrade Resilient Modulus Using Unconfined Compression Test.” *Transportation Research Record*, 2473, pp 126-135.

Hoskins, B.E., McCullough, B.F., and Fowler, D.W. (1991) “The Development of a Long-Range Rehabilitation Plan for US-59, in District 11.” *Research Report No. 987-1*, Austin, TX.

Johnson, C.W. (1960) “Comparative Studies of Combinations of Treated and Untreated Bases and Subbase for Flexible Pavements.” *Highway Research Board*, Bulletin 289, National Research Council, Washington, DC.

Kang, X., Kang, G., Chang, K., and Ge, L. (2014). “Chemically Stabilized Soft Clays for Road-Base Construction.” *Journal of Materials in Civil Engineering*, 27(7): 04014199.

Kaya, Z., et al. (2012) “Effect of Compaction Method on Mechanical Behavior of Graded Aggregate Base Materials.” *GeoCongress 2012*, American Society of Civil Engineers, pp. 1486-1494.

Kennedy, T. and Hudson, R. (1973) “Tensile Properties of Subbases for Use in Rigid Pavement Design.” *Report No. 98-14F*, University of Texas at Austin, TX.

Kim, W., and Labuz, J.F. (2007) “Resilient Modulus and Strength of Base Course with Recycled Bituminous Material.” *Report No. MN/RC-2007-05*, Minnesota Department of Transportation.

Lee, W., Bohra, N., Altscbaeffl, A., and White, T. (1997) “Resilient Modulus of Cohesive Soils.” *Journal of Geotechnical and Geoenvironmental Engineering*, 123(2), pp 131-136.

Lee, et al. (2019) “Application of Superpave Gyratory Compactors for Flexible Base and Subgrade.” *Report No. FHWA/TX-17/0-6883-R1*, Federal Highway Administration.

Lewis, D. (2006) “Inverted Base Pavement at Lafarge Quarry Entrance Road: 445 Five-Year Field Evaluation.” *Final Report*. Georgia Department of Transportation (GDOT), Georgia, 2006.

Lewis, D.E., Ledford, K., Georges, T., and Jared, D.M. (2012) “Construction and Performance of Inverted Pavements in Georgia.” *Paper No. 12-1872*, Poster Presentation in Session 639, 91st Annual Meeting of the Transportation Research Board, Washington, DC.

Li, C., White, D.J., and Vennapusa, P. (2015) “Moisture-Density-Strength-Energy Relationships for Gyratory Compacted Geomaterials.” *Geotechnical Testing Journal*, 38(4), pp. 461-473.

Little, D., Scullion, T., Kota, P., and Bhuiyan, J. (1994) “Identification of Structural Benefits of Base and Subgrade Stabilization,” *Report No. TX-94/1287-2*, Texas A&M University.

Masad, S., Little, D., and Masad, E. (2006) “Analysis of Flexible Pavement Response and Performance Using Isotropic and Anisotropic Material Properties.” *Journal of Transportation Engineering*, 132 (4), pp. 342-349.

Mokwa, R., Cuelho, E., and Browne, M. (2008) “Laboratory Testing of Soil Using the Superpave Gyratory Compactor.” *Transportation Research Board 87th Annual Meeting*, Washington, DC., pp 1-14.

Moody, E.D. (1994) “Field Investigations of Selected Strategies to Reduce Reflective Cracking in Asphalt Concrete Overlays Constructed over Existing Jointed Concrete Pavements.” *Transportation Research Record 1449*, Transportation Research Board, Washington, DC.

Papadopoulos, E. and Santamarina, J.C. (2017) “Inverted Base Pavements: Construction and Performance.” *International Journal of Pavement Engineering*, 20(6), pp. 697-703.

Pierce, L.M., Bruinsma, J.E., Smith, K.D., Wade, M.J., Chatti, K., Vandenbossche, J.M. (2017) "Using Falling Weight Deflectometer Data with Mechanistic-Empirical Design and Analysis, Volume III: Guidelines for Deflection Testing, Analysis, and Interpretation." *Research Report FHWA-HRT-16-011*, Washington, DC.

Ping, W.V., et al. (2003) "Evaluation of Laboratory Compaction Techniques for Simulating Field Soil Compaction (Phase II)." *Report No. FL/DOT/RMC/BB-890(F)*, Florida A&M University-Florida State University.

Piratheepan, J. and Gnanendran, C. (2008) "Dynamic Modulus and Fatigue Testing of Lightly Cementitiously Stabilized Granular Pavement Materials" *Airfield and Highway Pavements*, American Society of Civil Engineers.

Rashidi, M., Ashtiani, R., Si, J., Izzo, R., and McDaniel, M. (2018) "A Practical Approach for the Estimation of Strength and Resilient Properties of Cementitious Materials." *Transportation Research Record*, 2672 (52), pp 152-163.

Rasoulian, M., Becnel, B., and Keel, G. (2000) "Stone Interlayer Pavement Design." *Transportation Research Record 1709*, Transportation Research Board, Washington, DC.

Scullion, T., Sebesta, S., Estakhri, C., Harris, P., Shon, C., Harvey, O., and Rose-Harvey, K. (2012) "Full-Depth Reclamation: New Test Procedures and Recommended Updates to Specifications." *Report No. FHWA/TX-11/0-6271-2*, Texas A&M University.

Sebesta, S., and Harris, P. (2005) "Investigation of Methods for Improved Precision of Test Method TEX-113-E." *Report No. FHWA/TX-05/0-5135-1*, Federal Highway Administration.

Sebesta, S., Harris, P., and Liu, W. (2008) “Improving Lab Compaction Methods for Roadway Base Materials.” *Report No. FHWA/TX-07/0-5135-2*, Federal Highway Administration.

Texas Department of Transportation, TxDOT. (2008) “Compacting Specimens Using the Texas Gyratory Compactor (TGC).” *Tex-206-F*.

Texas Department of Transportation, TxDOT. (2011) “Laboratory Compaction Characteristics and Moisture-Density Relationship of Base Materials.” *Tex-113-E*.

Thompson, M. (1965a) “Split-tensile Strength of Lime-Stabilized Soils.” *Highway Research Record*, 92, pp 69-82.

Thompson, M. (1965b) “Shear Strength and Elastic Properties of Lime-Soil Mixtures.” *Highway Research Record*, pp. 1-14.

Titi, H., Rasoulian, M., Martinez, M., Becnel, B., and Keel, G. (2003) “Long-Term Performance of Stone Interlayer Pavement.” *Journal of Transportation Engineering*, 129 (2), pp. 118–126.

Tutumluer, E. (2013) “Practices for Unbound Aggregate Pavement Layers.” *NCHRP Synthesis 445*, Transportation Research Board, Washington, DC.

Virginia Department of Transportation, VDOT. (2022) “2022 Road and Bridge Specifications.” Richmond, VA.

Wang, M. and Huston, M. (1972) “Direct-tensile Stress and Strain of a Cement-Stabilized Soil.” *Highway Research Record*, 379, pp 19-24.

Wen, H., Muhunthan, B., Wang, J., Li, X., Edil, T., and Tinjum, J. (2014) “Characterization of Cementitiously Stabilized Layers for Use in Pavement Design and Analysis.” *NCHRP Report No. 789*, Washington State University and University of Wisconsin at Madison.

Weingart, R. (2018) “Turning Pavement Design Upside Down.” *Kent Seminar Lecture*, Department of Civil and Environmental Engineering, The University of Illinois at Urbana-Champaign.

Witczak, M.W. (2003) “Harmonized Test Methods for Laboratory Determination of Resilient Modulus for Flexible Pavement Design.” *NCHRP 1-28A*, Volume I: Unbound Granular Material.

Yaghoubi, E., et al. (2018) “Impact of Compaction Method on Mechanical Characteristics of Unbound Granular Recycled Materials.” *Road Materials and Pavement Design*, 19(4), pp. 912-934.

Vita

Edgar Rodriguez is a Peruvian civil engineer born in Piura in 1986. He graduated from the University of Piura in 2008 with a Bachelor of Science in Civil Engineering and obtained his professional licensure the following year. His thesis project, titled "Calculation of Pavement Condition Index in Luis Montero Avenue, District of Castilla," demonstrated his expertise in pavement design and evaluation.

After graduation, Edgar joined the faculty of the University of Piura as a professor of several undergraduate courses, including Statics, Geology Applied to Civil Engineering, Soil Mechanics, and Pavement Design. In 2011, he participated in the Inca Engineering Expedition in Cuzco, a research project funded by the National Science Foundation and the Pan-American Advanced Studies Institute, where he contributed to the study of the Inca Road. Edgar's dedication to research took him to the Road Research Center of the National Technological University in La Plata, Argentina, in 2012, where he completed an academic internship focused on the structural evaluation of asphalt pavements.

In 2016, Edgar pursued a Master of Science Program in Civil Engineering at the University of Texas at El Paso (UTEP) in the United States. During his graduate studies, he participated in several research projects sponsored by the National Cooperative Highway Research Program, the Texas Department of Transportation, and the Metropolitan Transportation Commission of California. After completing his master's degree, he continued his academic career at UTEP, where he is currently a Ph.D. candidate.

Edgar's research interests include pavement material characterization, pavement structure modeling, and transportation asset management. He has published articles on topics such as laboratory pavement material characterization, pavement structure design and analysis, mathematical applications in Civil Engineering, and education in Engineering. His expertise in these areas has earned him a position as a reviewer for the American Society of Civil Engineers Journal of Transportation, Part B-Pavements.